



**HAL**  
open science

# Nonlinear control and visual guidance of underwater vehicles

Lam Hung Nguyen

► **To cite this version:**

Lam Hung Nguyen. Nonlinear control and visual guidance of underwater vehicles. Automatic. CO-MUE Université Côte d'Azur (2015 - 2019), 2019. English. NNT : 2019AZUR4095 . tel-03092317

**HAL Id: tel-03092317**

**<https://theses.hal.science/tel-03092317>**

Submitted on 2 Jan 2021

**HAL** is a multi-disciplinary open access archive for the deposit and dissemination of scientific research documents, whether they are published or not. The documents may come from teaching and research institutions in France or abroad, or from public or private research centers.

L'archive ouverte pluridisciplinaire **HAL**, est destinée au dépôt et à la diffusion de documents scientifiques de niveau recherche, publiés ou non, émanant des établissements d'enseignement et de recherche français ou étrangers, des laboratoires publics ou privés.

# THÈSE DE DOCTORAT

## Contrôle non-linéaire et guidage visuel de véhicules sous-marins

**Lam Hung NGUYEN**

Laboratoire: CNRS-I3S

**Présentée en vue de l'obtention  
du grade de docteur en Automatique,  
Traitement du Signal et des Images  
de l'Université Côte d'Azur**

**Dirigée par:**

Minh Duc Hua (Encadrant principal),  
Tarek Hamel (Directeur de thèse)

**Soutenu le:** 28 Novembre 2019

**Devant le jury, composé de:**

Pascal Morin, Professeur, ISIR CNRS-Sorbonne Université

Carlos J. F. Silvestre, Professeur, Université de Macao

Vincent Creuze, MCF (HDR), LIRMM CNRS-UM

Guillaume Allibert, MCF, I3S CNRS-UCA

Minh Duc Hua, Chargé de recherche, I3S CNRS-UCA

Tarek Hamel, Professeur, I3S CNRS-UCA

Alain Fidani, Directeur Recherche et Innovation, ECA  
Group

Yann Le Page, Directeur Technique, Alseamar Alcen



# THÈSE DE DOCTORAT

UNIVERSITÉ CÔTE D'AZUR

ÉCOLE DOCTORALE STIC

Sciences et Technologies de l'Information et de la Communication

Laboratoire I3S-CNRS

## **Contrôle non-linéaire et guidage visuel de véhicules sous-marins**

Thèse pour obtenir le grade de

Docteur en Automatique, Traitement du Signal et des Images

Présentée par

**Lam Hung NGUYEN**

Soutenue publiquement le 28 Novembre 2019 devant le jury composé de:

**Président et rapporteur**

Pascal Morin, Professeur, ISIR CNRS-Sorbonne Université

**Rapporteur**

Carlos J. F. Silvestre, Professeur, Université de Macao

**Examineurs**

Vicent Creuze, MCF (HDR), LIRMM CNRS-UM

Guillaume Allibert, MCF, I3S CNRS-UCA

**Encadrant principal**

Minh Duc Hua, Chargé de recherche, I3S CNRS-UCA

**Directeur de thèse**

Tarek Hamel, Professeur, I3S CNRS-UCA

**Invités**

Alain Fidani, Directeur Recherche et Innovation, ECA Group

Yann Le Page, Directeur Technique, Alseamar Alcen



# Abstract

Recent advances in technology have led to a growing interest in underwater robotic applications. Historically, payload constraints have severely limited the development of scale-model underwater vehicles. They are small; their dynamics are highly nonlinear, subjected to complex and imprecise hydrodynamic effects and to disturbances commensurable with the control actions. Consequently, they provide an ideal testing ground for sophisticated nonlinear control techniques. Classical control techniques applied to these vehicles seem to be inadequate in dealing with their highly nonlinear dynamics, model uncertainties and external disturbances. Another key arising issue is the difficulty of navigation in cluttered environments and close to obstacles without precise positioning with respect to the environment and without velocity measurements.

In the present thesis, two research topics have been considered. Firstly, two novel dynamic visual servoing controllers exploiting the so-called homography matrix for fully-actuated vehicles (without measuring the linear velocity) have been proposed. These two approaches are derived for two different camera configurations: downward-looking and forward-looking. The key contribution here is the non-requirement of costly Doppler Velocity Log (DVL) velocity sensor. The control performance has been validated over simulations and via practical trials in a real challenging environment. The experimental platform as well as the software was built over the period of the thesis. Secondly, a novel trajectory tracking algorithm for a class of underactuated vehicles with axisymmetric slender body has been developed. The proposed approach makes use of a new nonlinear dynamic model of the vehicle, and exploits the symmetry of the vehicle in control design. The control performance and its robustness have been validated via simulations using a realistic model of an underwater vehicle.

**Keywords:** AUV, Visual servoing, Homography-based control, Station keeping, Trajectory tracking, Underactuated vehicles, Nonlinear control



# Résumé

Les récents progrès technologiques ont suscité un intérêt croissant pour les applications robotiques sous-marines. Historiquement, les contraintes liées à la charge utile ont fortement limité le développement des véhicules sous-marins à modèle réduit. Ils sont petits, leur dynamique est très non linéaire, soumis à des effets hydrodynamiques complexes et imprécis et à des perturbations proportionnables aux actions de contrôle. Par conséquent, ils constituent un terrain d'essai idéal pour les techniques de contrôle non-linéaire sophistiquées. Les techniques de contrôle classiques appliquées à ces véhicules semblent inadéquates pour faire face à leur dynamique hautement non-linéaire, aux incertitudes des modèles et aux perturbations externes. Une autre question clé qui se pose est la difficulté de la navigation dans des environnements encombrés et à proximité d'obstacles sans positionnement précis par rapport à l'environnement et sans mesure de vitesse.

Dans la présente thèse, deux sujets de recherche ont été considérés:

1) Deux nouveaux schémas de contrôle par asservissement visuel dynamique (sans mesure de la vitesse linéaire) pour les véhicules sous-marins complètement actionnés ont été proposés. Ces deux contrôleurs ont été développés pour deux configurations différentes de la caméra : pointant vers le bas et vers l'avant. La principale contribution ici est de s'en passer du coûteux capteur de vitesse (DVL) utilisé pour mesurer la vitesse linéaire. Les performances des deux algorithmes de contrôle ont été validées par des simulations et via des essais pratiques dans un environnement très difficile. La plateforme expérimentale ainsi que le logiciel de développement a été conçue sur la période la thèse.

2) Nous avons proposé un nouvel algorithme de poursuite de trajectoire pour une classe de véhicules sous-déclenchés ayant une forme axisymétrique allongée. La méthode proposée utilise un nouveau modèle dynamique non linéaire du véhicule et exploite la symétrie du véhicule pour la synthèse de la conception des commandes. La performance de la loi de contrôle élaborée et sa robustesse ont été validées via des simulations en utilisant un modèle réaliste d'un véhicule sous-marin.

**Keywords:** AUV, asservissement visuel, contrôle basé sur l'homographie, maintien en position, suivi de trajectoire, véhicules sous-actionnés, contrôle non linéaire



# Summary in French

- **Chapitre 1: Motivations, contributions et structure de la thèse.**

Comme indiqué sur le titre, ce chapitre de **Partie I: Introduction** tout d'abord brièvement présente les motivations et les objectifs de ce projet de thèse. Ensuite, les contributions principales sont fournies. En fin, la section de structure de la thèse présente brièvement le contenu de tous les chapitres.

- **Chapitre 2: Une nouvelle tendance dans la robotique sous-marine.**

Tout d'abord, ce chapitre discute sur le développement de la communauté mondiale de petits robots sous-marins, puis sur la technologie des petits ROV (véhicule télécommandé) et AUV (véhicule sous-marin autonome) de pointe. Enfin, certaines technologies récentes utilisées pour les véhicules sous-marins de petite taille et à faible coût sont présentées.

- **Chapitre 3: Modèle mathématique des véhicules sous-marins.**

Ce chapitre rappelle la modélisation de la dynamique complexe des véhicules sous-marins selon l'approche lagrangienne. Divers phénomènes hydrodynamiques et hydrostatiques affectant la dynamique des véhicules sous-marins sont discutés. La formulation finale du modèle non linéaire 6 degrés de liberté est dérivée.

- **Chapitre 4: Préliminaires sur l'estimation de l'homographie et les techniques de contrôle basées sur l'homographie.**

Ceci est le premier chapitre de **Partie II: Contrôle asservissement visuel basé sur l'homographie (HBVS) d'AUVs complètement actionnés sans mesures de vitesse linéaire**. Tout d'abord, ce chapitre rappelle la définition de l'homographie, puis discute de certaines techniques d'estimation de l'homographie et de méthodes existantes de contrôle du HBVS.

- **Chapitre 5: Contrôle dynamique HBVS d'AUVs complètement actionnés sans mesures de vitesse linéaire: le cas d'une caméra orientée en bas.**

Une nouvelle approche de contrôle dynamique du HBVS développée pour les véhicules sous-marins complètement actionnés équipés d'une caméra observant une cible visuelle (presque) plane et texturée. Tout d'abord, la formulation du problème et les idées de base de la conception des contrôles sont présentées. En suite, la conception du contrôle sous forme d'une architecture de contrôle en cascade est fournie avec des analyses rigoureuses de la stabilité et de la convergence. Les performances et la robustesse du contrôleur proposé sont d'abord vérifiées par simulation basée

sur un modèle réaliste de véhicule sous-marin, puis validées expérimentalement par des essais dans un environnement réel de lac en utilisant la plate-forme I3S-UV. Enfin, des extensions potentielles sont proposées pour élargir les fonctionnalités de l'application de maintien de poste.

- **Chapitre 6: Contrôle dynamique HBVS d'AUVs complètement actionnés sans mesures de vitesse linéaire: le cas d'une caméra orientée vers l'avant.**

Une nouvelle approche de contrôle dynamique du HBVS est développée pour le cas plus difficile dans lequel le sous-marin considéré est complètement actionné. Le robot est équipé d'une caméra qui est orientée vers l'avant en observant une cible visuelle plane et (presque) verticale. Les performances du contrôleur proposé sont d'abord validées par simulation, puis par des expériences préliminaires dans une cuve d'eau.

- **Chapitre 7: Développement de la plate-forme expérimentale I3S-UV.**

Ce chapitre explique la nécessité pour l'équipe I3S-OSCAR d'avoir d'une plate-forme sous-marine pour valider expérimentalement les algorithmes de contrôle et d'estimation développés. Tous les processus de développement en termes de la conception électro-mécanique et de logiciel de contrôle sont présentés en détail.

- **Chapitre 8: Suivi de trajectoire de véhicules sous-marins sous-actionnés et axisymétriques à forme allongée.**

Ce chapitre se trouve dans **Partie III: Contrôle des véhicules sous-marins sous-actionnés**. Un nouveau contrôleur est développé pour le problème de suivi de trajectoire de véhicules sous-marins à forme allongée et (presque) axisymétrique par rapport à leur axe longitudinal. La conception des commandes exploite la dynamique 3D des véhicules et certaines propriétés particulières héritées de leur forme en termes de résistance et de masse ajoutée. Les performances et la robustesse du contrôleur proposé sont vérifiées par simulation basée sur un modèle réaliste d'un véhicule sous-marin.

*To my whole beloved family*



## *Acknowledgements*

I would like to express my deepest gratitude to my supervisors, CR. Minh Duc HUA and PR. Tarek HAMEL, for academic guidance during my PhD project. My grateful thanks are also extended to DR. Claude SAMSON, who together with PR. Tarek HAMEL has providing me opportunities to work in the OSCAR team of the I3S laboratory, starting by supervising me within my masters' internship. They all bring me to a new horizon of knowledge: nonlinear control and nonlinear observers. These tools with powerful mathematical insight make me astonishing by efficient solutions for many practical problems.

I would like to thank Guillaume ALLIBERT, And  ANGLADE, Ninad MANERIKAR, Simeone De MARCO and Jean-Marie KAI for all their supports to complete my work successfully. I am also grateful to other friends who are or are used to be at the I3S: Fernando IRETA MUNOZ, Jos  Henrique GOULART, Myriana RIFAI, Yousef ALF, Arnaud TANGUY. Thank you all for the time we spend together.

I would like to particularly thank my wife and my daughters for being with me in such a long journey. I really appreciate how patient you were while I worked on this PhD project. I am grateful for my parents and parents-in-law for continuously supporting my life and study.

Finally, I gratefully acknowledge the financial support which has made my research possible. This funding has come from the Vietnam International Educational Development (VIED) and the projects: ANR EQUIPEX Robotex, FUI GREENEXPLORER (2017-2021), and ANR Astrid CONGRE (2019-2021).



# Nonlinear control and visual guidance of underwater vehicles

Lam-Hung NGUYEN



# Contents

<b>Notation</b>	<b>xix</b>
<b>I Introduction</b>	<b>1</b>
<b>1 Motivations, contributions and thesis structure</b>	<b>3</b>
1.1 Motivations and contributions . . . . .	3
1.2 Thesis structure . . . . .	8
<b>2 A new trend in underwater robotics</b>	<b>11</b>
2.1 Recent small underwater robots . . . . .	13
2.1.1 Small ROVs . . . . .	14
2.1.2 Small AUVs . . . . .	19
2.1.3 Small hybrid vehicles . . . . .	22
2.2 Review on the technologies used for small underwater robots . . . . .	23
2.2.1 Brushless thruster . . . . .	23
2.2.2 Camera . . . . .	26
2.2.3 Depth sensor and single-beam echo sounder . . . . .	27
<b>3 Mathematical model of underwater vehicles</b>	<b>29</b>
3.1 Reference frames . . . . .	30
3.2 Kinematics . . . . .	31
3.3 Dynamics . . . . .	32
3.3.1 Rigid body dynamics . . . . .	32
3.3.2 Added mass . . . . .	33

3.3.3	Body-fluid dynamics . . . . .	34
3.4	External forces and torques . . . . .	35
3.4.1	Restoring forces . . . . .	35
3.4.2	Drag . . . . .	35
3.4.3	Propulsion system . . . . .	36
3.4.4	Current . . . . .	37
3.5	Complete nonlinear model . . . . .	38

## **II Dynamic Homography-Based Visual Servo (HBVS) control of fully-actuated AUVs without linear velocity measurements 39**

<b>4</b>	<b>Preliminaries on homography estimation and homography-based control techniques 43</b>
4.1	Homography definition . . . . . 44
4.2	Existing feature-based homography estimation techniques . . . . . 46
4.2.1	A classical algebraic algorithm of homography estimation . . . . . 48
4.2.2	A state-of-the-art nonlinear homography observer on $SL(3)$ . . . . . 49
4.2.2.1	Observer on $SL(3)$ based on direct point correspondences 49
4.2.2.2	Observers with partially known group velocity . . . . . 50
4.3	Discussions on existing HBVS controllers . . . . . 52
4.3.1	HBVS kinematic controllers based on homography decomposition 52
4.3.2	HBVS kinematic controllers without homography decomposition . 59
4.3.3	HBVS dynamical controllers without homography decomposition 59
<b>5</b>	<b>Dynamic HBVS control of fully-actuated AUVs without linear velocity measurements: the case of downward-looking camera 65</b>
5.1	Problem formulation . . . . . 66
5.2	Simplified model for control design . . . . . 67
5.3	Basic ideas of control design . . . . . 68
5.4	Control design . . . . . 69
5.4.1	Outer-loop control design . . . . . 70
5.4.1.1	Force control design . . . . . 70
5.4.1.2	Control design of the reference yaw angular velocity . . 75
5.4.2	Inner-loop control design . . . . . 75
5.5	Comparative simulation results . . . . . 79
5.6	Experimental validations . . . . . 83
5.6.1	Experimental setup . . . . . 83
5.6.2	Experimental results . . . . . 84

5.7	Conclusion . . . . .	89
<b>6</b>	<b>Dynamic HBVS control of fully-actuated AUVs without linear velocity measurements: the case of forward-looking camera</b>	<b>91</b>
6.1	Problem formulation . . . . .	92
6.2	Control design . . . . .	93
6.2.1	Outer-loop control design . . . . .	94
6.2.1.1	Heave control design . . . . .	97
6.2.1.2	Surge-and-sway control design . . . . .	97
6.2.1.3	Control design of the reference yaw angular velocity . . . . .	100
6.2.2	Inner-loop control design . . . . .	100
6.2.3	Analyses for Chapter 6 . . . . .	100
6.2.3.1	Proof of Lemma 2 . . . . .	100
6.2.3.2	Proof of Proposition 6 . . . . .	102
6.3	Simulation results . . . . .	103
6.4	Experimental validations . . . . .	106
6.4.1	Experimental setup . . . . .	106
6.4.2	Preliminary experimental results . . . . .	109
6.5	Conclusion . . . . .	113
<b>7</b>	<b>Development of the I3S-UV platform</b>	<b>115</b>
7.1	3D design of I3S-UV . . . . .	116
7.2	Software system . . . . .	120
7.2.1	Homography estimation . . . . .	122
7.2.2	High level control . . . . .	124
7.2.3	Low level control . . . . .	127
7.2.3.1	Control allocation . . . . .	127
7.2.3.2	PWM lookup table . . . . .	130
7.2.3.3	Depth measurement for depth control . . . . .	131
7.3	I3S-UV Product data sheet . . . . .	131
<b>III</b>	<b>Control of underactuated underwater vehicles</b>	<b>135</b>
<b>8</b>	<b>Trajectory tracking of slender-body axisymmetric underactuated underwater vehicles</b>	<b>137</b>
8.1	Modeling . . . . .	139
8.1.1	System modeling . . . . .	139
8.1.2	Model for control design . . . . .	140

8.2	Trajectory tracking control design . . . . .	141
8.2.1	Basic developments . . . . .	141
8.2.2	Outer-loop control design . . . . .	144
8.2.3	Outer-loop control design with integral term . . . . .	148
8.3	Simulation results . . . . .	150
8.4	Conclusion . . . . .	156
	<b>Conclusion</b>	<b>157</b>
	<b>Bibliography</b>	<b>160</b>

# Notation

*Scalar quantities* are denoted by regular font lower-case letters. Bold font is used to mark **vectors** and **matrices**. Matrices are usually denoted by capital letters.

## Constants, variables and symbols

$\mathbb{Z}^+$	the set of positive integer numbers
$\mathbb{R}$	the set of real numbers
$\{\mathbf{e}_1, \mathbf{e}_2, \mathbf{e}_3\}$	the canonical basis of $\mathbb{R}^3$
$\mathbf{I}_n$	the identity of $\mathbb{R}^{n \times n}$ , $n \in \mathbb{Z}^+$
$\mathbf{0}_n$	the zero matrix of $\mathbb{R}^{n \times n}$ , $n \in \mathbb{Z}^+$
$\{\mathcal{A}\}$	the inertial reference system
$\{\mathcal{B}\}$	the reference system attached to the center of buoyancy of the mobile robot (non-inertial)
$\{\mathcal{C}\}$	the reference system attached to the on-board camera (non-inertial)
$m$	mass
$\mathbf{J}_0$	moment of inertia tensor around the center of gravity
$\mathbf{V}$	body-fixed linear velocity vector, $\mathbf{V} = [V_1, V_2, V_3]^\top$
$\boldsymbol{\Omega}$	angular velocity vector
$\text{SL}(3)$	the Special Linear group, the set of all real valued $3 \times 3$ matrices with unit determinant
$\mathfrak{sl}(3)$	Lie-algebra of $\text{SL}(3)$ , the set of matrices with trace equal to zero
$\text{SO}(3)$	the Special Orthogonal group of the orthogonal $3 \times 3$ matrices with unit determinant
$\mathbf{R}$	rotation matrix, $\mathbf{R} \in \text{SO}(3)$
$g$	the gravity constant

## Operators and functions

$\mathbf{v}$	the Euclidean norm of vector $\mathbf{v} \in \mathbb{R}^n$
$(\cdot)^\top$	the transpose operator on a matrix or vector
$\mathbf{u}_\times$	the skew-symmetric matrix associated with the cross product by vector $\mathbf{u} \in \mathbb{R}^3$ , i.e., $\mathbf{u}_\times \mathbf{v} = \mathbf{u} \times \mathbf{v}$ , $\forall \mathbf{v} \in \mathbb{R}^3$
$\text{vex}(\cdot)$	an operator such that $\text{vex}(\mathbf{u}_\times) = \mathbf{u}$
$ \cdot $	the Euclidean norm in $\mathbb{R}^n$
$\ \cdot\ $	the Frobenius norm in $\mathbb{R}^{n \times n}$
$\text{diag}(\lambda_1, \lambda_2, \lambda_3)$	diagonal matrix with the main diagonal values defined by the arguments,
	$\begin{bmatrix} \lambda_1 & 0 & 0 \\ 0 & \lambda_2 & 0 \\ 0 & 0 & \lambda_3 \end{bmatrix}$
$\text{sat}^\delta(\cdot) \in \mathbb{R}^n$ , with $\delta > 0$	the classical saturation function, i.e., $\text{sat}^\delta(\mathbf{x}) \triangleq \mathbf{x} \min(1, \delta/ \mathbf{x} )$ , $\forall \mathbf{x} \in \mathbb{R}^n$

## **Part I**

# **Introduction**



# 1

## Motivations, contributions and thesis structure

### 1.1 Motivations and contributions

Offshore operations are always extremely challenging and classically addressed by Remotely Operated Vehicles (ROVs). However, the use of ROVs is very costly, complicated and inefficient in deep sea and in presence of obstacles. Automatization of surveillance and inspection tasks relying on Autonomous Underwater Vehicles (AUVs) is thus highly relevant. Nevertheless, for such systems to be reliable and used in daily-routine applications, several fundamental and technological challenges must be overcome. For instance, the dynamics of AUVs are highly nonlinear and the translational and rotational dynamics are highly coupled, essentially due to added mass effects. The complexity of hydrodynamic effects often impedes to obtain a precise dynamic model, and the magnitude of external perturbations can become commensurable with the available actuation power. Thus, robust nonlinear control design is of prime importance. Existing control approaches, generally based on the modeling framework proposed by Fossen [19], often make use of a minimal parametrization of the system (Euler angles for example),

leading to very complex equations involving mathematical singularities in the dynamic representation of the system. The resulting control laws are either too simplistic (only dealing with linear tangent behaviors) or too complex (not allowing for taking into account the natural physics of the system such as passivity and dissipativity of external forces). Typically, the 6-degree of freedom (d.o.f) vehicle model is decoupled into two reduced dynamical systems that are a “depth-pitch” model for the motion in the vertical plane and a “plane-yaw” model for the motion in the horizontal plane, by neglecting the interactions between the two types of motion and/or the Coriolis effects. Such a simplification may be meaningful for the class of box-shaped AUVs moving at low speed, since the hydrodynamic Coriolis forces can be dominated by the damping forces. However, for slender-body AUVs moving with some forward speed, this assumption is far from realistic. Stability and performance then suffer significantly when strong sea currents or aggressive maneuvers excite the effects of complex hydrodynamics and strong dynamic couplings. Moreover, control design for underactuated AUVs (by conception) as in the case of torpedo-shaped AUVs propelled by a single thruster (and 2 or 3 control torques) is more involved than the case of (almost) fully-actuated AUVs. For instance, there does not exist any time-invariant feedback controllers capable of stabilizing a fixed reference pose (i.e. position and orientation) asymptotically – a fact known to the automatic control community as a consequence of a theorem due to Brockett [12]. On the other hand, AUVs may navigate in cluttered areas where global acoustic positioning systems are unusable or insufficiently precise for safe navigation. These vehicles may also be required to navigate relatively to their environment so as to carry out inspection and surveillance tasks. In these situations, their perception and navigation rely heavily on embarked exteroceptive sensors and sensor-based control techniques. However, sensor-based control (and in particular vision-based control) of highly nonlinear dynamical systems is usually difficult due to the fact that the vehicle’s pose estimate may be unavailable for feedback control (as in the case of image-based visual servoing or homography-based visual servoing), and that indirect and coupled information about the state and the environment provided by sensor data has to be exploited in the control design process. The fact that linear velocity sensors such as Doppler Velocity Log (DVL) may not be available in small and/or low-cost AUVs due to their high price and weight even amplifies the degree of complexity of sensor-based control design, especially for highly nonlinear and dynamically complex systems like AUVs. In addition, multiple factors specific to underwater environment cause most of sensors and communication means that are widely used in ground and aerial robotics not to work under water. Last but not least, AUV platform and sensor costs, together with requirements for experimental setups such as test area, logistic support, etc., have never been easily accessible for any robotics laboratory.

This PhD project has been carried out within a more global research activity in Underwater Robotics of the I3S-OSCAR team that aims to develop theoretical fundamentals of robust nonlinear control, sensor-based control and nonlinear observers in order to provide the AUVs with a significantly improved overall performance, enabling the offshore automatic inspection and surveillance operations. The different dynamics of underwater vehicles with respect to the ones of aerial vehicles (due to their different ambient fluids) and the differences in capacity of exteroceptive sensors in an underwater environment compared to an aerial environment (e.g. the range of cameras under water is much more limited than that in air) represent new challenges, opportunities and sources of inspiration for the team to apply our knowledge (theoretical and practical) in nonlinear and sensor-based control and nonlinear observer design (that has been developed for two decades in Aerial Robotics) to the field of Underwater Robotics. Within this global research panorama in Underwater Robotics of the I3S-OSCAR team, my PhD project focuses on the two following research topics:

1. **Dynamic homography-based visual servoing of fully-actuated underwater vehicles without relying on linear velocity measurements:** Vision-based stabilization and positioning functionality is useful for AUV navigation in close proximity to underwater infrastructures or a seafloor with many potential applications such as high-resolution imaging, monitoring, inspection, manipulation, station keeping, and docking, etc. In the case of monocular camera, this problem has been mostly addressed in the literature by relying on the assumption of (local) planarity of the visual target and by exploiting the so-called homography –an invertible mapping relating two camera views of the same planar scene. For instance, the  $2\frac{1}{2}$ -D visual servoing control approach proposed by Malis et al. [55] is one of the most successful visual servoing control paradigms. That approach, however, requires a homography decomposition process which is often computationally expensive and highly sensitive to measurement noise. To deplete the need of homography decomposition, Benhimane and Malis [8] proposed a more advanced kinematic Homography-based Visual Servoing (HBVS) control algorithm. That work has inspired the members of I3S-OSCAR team to develop a dynamic HBVS control approach which takes the full dynamics of fully-actuated AUVs into account and, consequently, ensures a large provable domain of stability [44]. In this thesis work, we extended the prior work of the team [44] to the case where linear velocity measurements are not available. One of the main motivations behind this effort is related to the development of a low-cost but efficient solution for the stabilization of AUVs without the need of a costly DVL velocity sensor. More precisely, the proposed solutions make use of a minimal and inexpensive sensor suite consisting of an Inertial Measurement Unit

(IMU) and an embedded video camera. Two algorithms have been successfully developed, with the support of rigorous Lyapunov-based stability analyses, for two different camera configurations: **downward-looking** and **forward-looking**. In particular, the novel visual error used for the second case is also an original contribution. The development of a low-cost and man-portable underwater vehicle called **I3S-UV** during my PhD project, together with the development of the homography estimation library called **HomographyLab**<sup>®</sup> by the I3S-OSCAR team, is a defining factor to the successful experimental validations of these algorithms.

- 2. Trajectory tracking of slender body underactuated underwater vehicles:** Slender body underwater vehicles are often used for data acquisition applications that require them to move at high speed. The slender shape is conceived for reducing hydrodynamic drag along a nominal axis and thus energy consumption. However, this design leads to highly nonlinear dynamics of the system due to added mass and hydrodynamic effects since the total mass can no longer be considered as proportional to identity and the resulting hydrodynamic force also strongly depends on the vehicle's orientation. On the other hand, when traveling forward at high speed, the lateral thrusters in sway and heave directions can be ineffective, leading any fully actuated vehicle to behave like an underactuated one. By considering this fact together with cost effective and weight/volume, slender body underwater robots are often underactuated by conception with the main thruster mounted at the back and control surfaces employed for orientation control. Control design for underactuated AUVs is challenging and still remains an everlasting source of inspiration for applying new control techniques. When the control objective concerns the tracking of a reference position trajectory, whose velocity does not vanish for all time, various classical control design techniques can be applied. For instance, classical methodologies, linear and nonlinear, have been applied on the basis of linear approximations of the two simplified subsystems "depth-pitch" and "plane-yaw" about nominal operating points. The main limitation of these approaches is the local nature of the control design and analysis. Moreover, stability and performance can suffer significantly when strong sea currents or aggressive manoeuvres excite the complex hydrodynamic and added-mass effects. To overcome some of these limitations, nonlinear Lyapunov-based control designs have been recently investigated first for the trajectory tracking problem in a horizontal plane using a simplified and reduced "plane-yaw" 3-d.o.f model and then for the motion in 3D space. A nonlinear high-gain backstepping-based controller proposed in [4] allows for exponential convergence of the position error to a small neighborhood of the origin, which means that asymptotic stabilization to zero is not fulfilled. Moreover,

the attitude is not explicitly controlled but guided by the closed-loop system's zero dynamics, thus possibly resulting in undesirable attitude dynamics. High-gain controllers are also known to be sensitive to measurement noise and time delays of control inputs. Nonlinear robust control design for underactuated AUVs thus remains an active research topic. My work on this topic has been motivated by the extension of the thrust direction control paradigm initially developed for underactuated aerial vehicles by the members of the I3S-OSCAR team [31, 70, 39] to underactuated underwater vehicles, making a step towards a unified control approach for both aerial and underwater vehicles. This work addresses the trajectory tracking control design for slender-body underactuated AUVs, whose body shape is symmetric with respect to the longitudinal axis, using a full 6-d.o.f model. The main objective of this study is to find an appropriate methodology to deal with added mass and hydrodynamic effects. In this work, we have proposed various modifications and adaptations, resulting in a modified apparent force independent of the vehicle's orientation and subsequently a nonlinear system with a triangular control structure. To compensate for unavoidable model uncertainties and external disturbances, the proposed controller is also complemented with bounded integral correction actions via a novel formalism. Future extensions to other control objectives and applications such as path following, vision-based pipeline following, etc. should benefit from this study.

Most of the theoretical contributions and experimental validation results reported in this thesis were published in (or submitted to) the following research papers:

- **Nguyen, L.-H.**, Hua, M.-D., Allibert, G., and Hamel, T. (2017). *Inertial-aided homography-based visual servo control of Autonomous Underwater Vehicles without linear velocity measurements*. In proceedings of 21st International Conference on System Theory, Control and Computing (ICSTCC), pp. 9–16, Sinaia, Romania. [62]
- **Nguyen, L.-H.**, Hua, M.-D., and Hamel, T. (2019). *A nonlinear control approach for trajectory tracking of slender-body axisymmetric underactuated underwater vehicles*. In proceedings of European Control Conference, **Invited Paper**, pp. 4053–4060, Naples, Italy. [64]
- **Nguyen, L.-H.**, Hua, M.-D., Allibert, G., and Hamel, T. (2019). *A homography-based dynamic control approach applied to station keeping of Autonomous Underwater Vehicles without linear velocity measurements. First revision of submission to IEEE Transactions on Control Systems Technology*. [63]
- **Nguyen, L.-H.**, Hua, M.-D., and Hamel, T. (2019). *A homography-based dynamic control approach of Autonomous Underwater Vehicles observing a (near) vertical target*

*without linear velocity measurements.* Submitted to European Control Conference (ECC'20), St Petersburg, Russia. [65]

In addition, I am the main contributor to the development (construction from scratch) of the I3S-UV underwater platform and of the control software system that includes a modified open-source PX4 autopilot and a high level control package in ROS. The robot can be easily upgraded for future needs.

## 1.2 Thesis structure

The present thesis is organized in three parts and partitioned in eight chapters.

- **Chapter 1 - Motivations, contributions and thesis structure.** As dedicated in the title, this chapter in **Part I: Introduction** first briefly presents the motivations and objectives of this thesis work. The main contributions are then provided. The thesis structure section briefly introduces the content of all chapters.
- **Chapter 2 - A new trend in underwater robotics.** This chapter discusses first about the development of worldwide community of small underwater robots, then about state-of-the-art small ROVs and AUVs. Finally, some recent technologies used for small and low-cost underwater vehicles are presented.
- **Chapter 3 - Mathematical model of underwater vehicles.** This chapter recalls the modeling of the complex dynamics of underwater vehicles following Lagrange approach. Various hydrodynamics and hydrostatics phenomena affecting the dynamics of underwater vehicles are discussed. The final formulation of the nonlinear 6 d.o.f model is derived.
- **Chapter 4 - Preliminaries on homography estimation and homography-based control techniques.** This is the first chapter in **Part II: Homography-based visual servo (HBVS) control of fully-actuated AUVs without linear velocity measurements.** This chapter first recalls the homography definition and then discusses about some relevant homography estimation techniques and existing HBVS control approaches.
- **Chapter 5 - Dynamic HBVS control of fully-actuated AUVs without linear velocity measurements: the case of downward-looking camera.** A novel dynamic HBVS control approach is developed for fully-actuated underwater vehicles equipped with a downward-looking camera observing a (near) planar and textured visual target. The problem formulation and basic ideas of control design are first presented. Control design in form of a cascade control architecture are then provided

with the support of rigorous stability and convergence analyses. The performance and robustness of the proposed controller are first verified by simulation based on a realistic underwater vehicle model, and then experimentally validated through trials in a challenging real lake environment by employing the I3S-UV platform. Finally, potential extensions are proposed to enlarge the functionalities of station-keeping application.

- **Chapter 6 - Dynamic HBVS control of fully-actuated AUVs without linear velocity measurements: the case of forward-looking camera.** A novel dynamic HBVS control approach is developed for a more challenging case when the considered fully-actuated underwater robot is equipped with a forward-looking camera observing a (near) vertical planar visual target. The performance of the proposed controller is first validated by simulation and then by preliminary experiments in a small water tank.
- **Chapter 7 - Development of the I3S-UV platform.** This chapter discusses the need of the team to possess an underwater platform for facilitating experimental validations of the developed control and estimation algorithms. All the development process in terms of electro-mechanical design and control software system are presented in detail.
- **Chapter 8 - Trajectory tracking of slender-body axisymmetric underactuated underwater vehicles.** This chapter is in **Part III: Control of underactuated underwater vehicles**. A novel controller is developed for the trajectory tracking problem of slender-body underwater vehicles whose shape is (almost) axisymmetric with respect to their longitudinal axis. The control design exploits the full 3D dynamics of the vehicles and some particular properties inherited from their shape in terms of drag and added mass. The performance and robustness of the proposed controller is verified by simulation using a realistic model of an underwater vehicle.



# 2

## A new trend in underwater robotics

**T**HE last two decades have witnessed significant technology advancements resulting in more powerful microprocessors and companion computers, more robust IMUs, and longer endurance and higher capacity batteries in more compact forms, together with more reliable and more precise navigation systems, all at extremely reasonable costs. Along with the development of advanced control techniques, all these technological factors have led to the development of more powerful and versatile Unmanned Aerial Vehicles (UAVs). In parallel, the expansion of the Internet and social networks has revolutionized the way that information and knowledge could be stored and transmitted on a large scale and with a much faster speed. Due to this, not only open-source software but open-hardware also become popular. In addition, worldwide e-commerce websites and delivery companies allowed one to easily acquire all the necessary components to build their robots even with a modest budget. These exceptional and favorable conditions led to the formation of a huge community of DIY<sup>1</sup> in Aerial Robotics. The development of aerial robots was no more carried out only in the industrial or research/educational environments. A modern era of aerial robotics and of the development of small non-military UAVs had been started. In fact, the development of this DIY community in the inverse sense helped to stimulate the development of UAV

---

<sup>1</sup>DIY stands for do-it-yourself.

---

research in academic environments. It is because of this fact that an UAV system in the sense of hardware and software could be built from scratch in a much shorter period of time by using open resources available in DIY forums. Thus, the researchers could focus on advanced problems such as navigation and control algorithms or image processing, etc. This is especially important for a newcomer who would like to get himself acquainted quickly in the UAV domain.

For underwater vehicles, the surrounding condense environment often results in strong actions to the vehicles. The resulting dynamics are highly nonlinear and complex, and obtaining a precise model for control design is quite challenging. In addition, acoustic navigation systems are often expensive and acoustic communication systems have limited bandwidth. Moreover, components used for building underwater vehicles require waterproof and high pressure resistance. They are thus much more expensive in comparison with components used for building aerial vehicles. All these difficulties prevent a wide participation of the DIY community to the underwater robotics field. However, because of these complexities and difficulties, and of practical needs, the research community always showed their interest to this specific domain. Fortunately, in recent years the same trend that appeared in Aerial Robotics has also occurred in the field of Underwater Robotics. It is partly because many researchers have changed their focus onto underwater environment after aerial robotics has gained considerable achievements. In addition, many electronic components and technologies previously used for aerial robots or robots in a general sense could now be reused for underwater robots such as autopilots, flight controllers, Robot Operating System (ROS), etc. Moreover, there are more companies providing essential components required for building underwater robots. One can consider Blue Robotics<sup>2</sup> as one of the pioneers. These companies not only sell their products, but also provide support to their customers to build and operate their own robots through a large number of free tutorials with open forums and free open-source autopilot firmware.

A more “romantic” reason for having stimulated the development of the DIY community in underwater robotics may be linked to the beautiful underwater world that has often been accessed only by a small group of people possessing enough financial support and diving skills. Small and low-cost underwater robots equipped with a tethered link to the operator (i.e. ROVs) in this case would be an ideal solution for those without these resources.

Here again, the DIY community, affordable components and open source autopilot firmwares ease the involvement of newcomers to the underwater robotics community. The capability of owning small experimental platforms allows researchers to easily and proactively test their theoretical works since less support is required in terms of trans-

---

<sup>2</sup><https://bluerobotics.com>

portation and operational cost. In the past, research groups which did not come from an underwater robotics background often needed collaboration with the ones from the field in order to have access to their vehicles. But nowadays, due to the availability of low cost experimental platforms which are easy to build and assemble, a large number of research groups and individuals (even though not in the field) are able to apply their knowledge to develop new applications. This stimulates the development of research works in the field of underwater robotics, and allows to create more startup companies, especially spin-off ones.

In recent years, there has been a significant increase in the number of small underwater robots developed by worldwide companies or start-ups. These systems can perform a wide range of applications such as underwater photography, hull inspection, treasure hunting, etc. Giants in underwater systems such as Kongsberg Maritime with its subsidiary Hydroid <sup>3</sup> or General Dynamics <sup>4</sup> provide to the market a large choice of small underwater robotic vehicles. While these small systems with simple deployment and retrieval can significantly reduce the budget needed for their operation, they are still relatively expensive. It seems that the market of professional applications is monopolized by a limited number of companies in the field. However, starting by ROV products for hobby/entertainment purposes, start-up companies now show their endeavor to gain market share of ROVs in some specific industrial applications such as underwater surveillance, hull inspection, etc. in areas of shallow water because of less technological barriers. We believe that with the continuous development of many related technologies, the modern underwater robots with smaller dimensions and more intelligence will play an extremely significant role in military, industrial and civil activities in the near future.

In this thesis we focus our attention to the class of small underwater robots, which can be man-portable and are easily to be deployed and retrieved. We will provide detailed insights on the state of the art of small underwater robots in the next section. Here the term small underwater robots stands for Remotely Operated Vehicles (ROVs) and Autonomous Underwater Vehicles (AUVs) in mini (around 16 *kg*) or micro (around 3 *kg*) sizes.

## 2.1 Recent small underwater robots

In this section, we present some recent small underwater robots with discussions on their innovative features.

---

<sup>3</sup><https://www.hydroid.com>

<sup>4</sup><https://gdmissionsystems.com>

## 2.1. Recent small underwater robots

---

### 2.1.1 Small ROVs

In practice, ROVs often work at low speed and are normally used for observation tasks with limited capability of intervention. The potential of low-cost ROVs has been envisioned very early. One of the pioneers is Hydrovision, a subsidiary of SeaBotix which was initially founded in 1986 aiming to this market. The basic guidelines of Hydrovision include capability of real work in real environment, intuitiveness to be simple to operate, ruggedness enough to withstand the harsh environments, and thus its products bring value to the user. In order to increase the portfolio capability to access this market segment, Teledyne Technologies has incorporated Seabotix over M & A activities to form Teledyne Seabotix in 2001. Nowadays, Teledyne Seabotix provides a wide range of mini ROVs, as illustrated in Fig. 2.1 and 2.2. From a general view, it can be seen that all ROVs have modular design including main body skid and additional skids for crawler, grabber, sonar sensor and acoustic system. The main body skids have different depth ratings, thrusters' configuration and tether length. For some ROV models, the additional crawler skids together with attractor can be used to perform crawler inspection mode on hard surfaces (e.g. ship hull). Along with ROVs, there is a large selection of accessories and options allowing Teledyne Seabotix mini ROVs to have a wide range of applications. It is noteworthy to remark from Tab. 2.1 that sonar sensors and acoustic system are all provided by other producers. In addition, SeaBotix also provides simulator software powered by GRi Simulations Inc. for pilot training, and navigation & control software powered by GreenSea (c.f. Fig. 2.3).

Accessories		Producer
AUV/ROV Thrusters		SeaBotix
External LED Lighting		
Grabber Attachments		
Three Jaw Grabber		
Integrated Navigation Control Console		
Laser Scaling		
Altimeter/Echosounder	Tritech Micron Echo Sounder	Tritech
Multibeam Sonar	DIDSON sonar	Sound Metrics
	Tritech Gemini 720i	Tritech
Scanning Sonar	1171 Series OC ROV sonar	Kongsberg Mesotech
	Tritech Super SeaPrince	Tritech
	Tritech Micron	Tritech
Thickness Gauge	Multiple Echo Ultrasonic Digital Thickness Gauge	Cygnus Instruments
USBL Tracking System	Tritech Micron Nav USBL	Tritech

Table 2.1: Teledyne SeaBotix accessories and options



Figure 2.1: Teledyne Seabotix ROVs (Source: <http://www.teledynemarine.com>)

Now, we will introduce VideoRay micro and mini ROVs which are in smaller size in comparison with Teledyne SeaBotix mini ROVs. The VideoRay LLC company has been established in 1999. It offers a series of ROVs evolutionized in time in terms of rating depth, thruster's power, hydrodynamic design, capabilities of software platform and control modes. VideoRay ROVs have depth rating ranging from 76 *m* up to 1000 *m* with also a large set of accessories and options (c.f. Tab 2.2). Their applications are various, including: aquaculture & fishery operations; forensics & crime scene investigation; search & rescue missions; port security operations; recreational yachting; sport fishing &

## 2.1. Recent small underwater robots



Figure 2.2: Teledyne Seabotix ROVs (Source: <http://www.teledynemarine.com>)

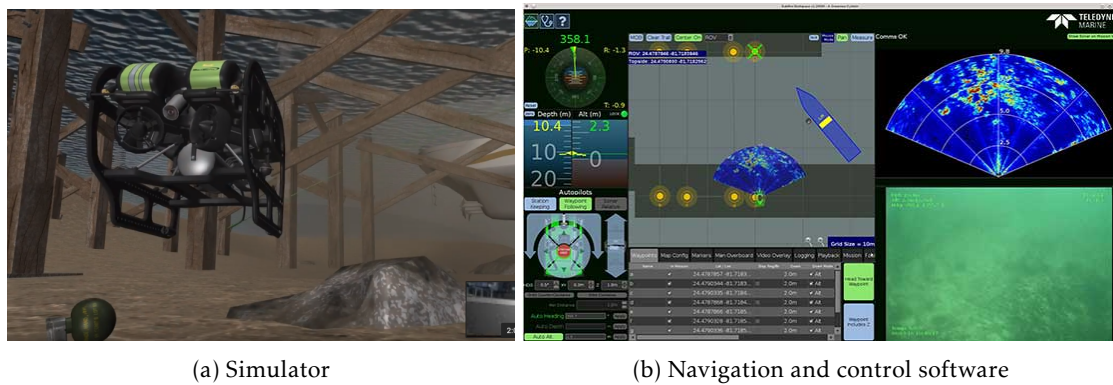


Figure 2.3: Teledyne Seabotix softwares (Source: <http://www.teledynemarine.com>)

underwater marine life observation; shipwreck & treasure exploration; science, research and marine habitat mapping; inland dam inspection; offshore oil & gas rig observation; etc. Nowadays, VideoRay LLC becomes the world's largest volume producer of ROVs

and the global leader in micro ROV technology. As of July 2018, more than 3,000 VideoRay ROVs have been delivered worldwide <sup>5</sup>.

It can be seen from Fig. 2.5d and 2.5e that recent VideoRay ROVs belong to mini class instead of mico one, and they are designed in box-shaped forms. The VideoRay Mission Specialist Defender with enhanced depth rating of 1000 *m* seems to be a strategic step of VideoRay LLC to gain market share of deeper depth applications. The box-shaped form which is a popular ROV design in fact provides advantages since it gives more space simplifying mounting/replacing additional accessories. By employing this design, the configuration of ROVs can be easily customized for specific missions. This fact can be seen in view of Fig. 2.1 and 2.2 where all Teledyne Seabotix ROVs are in this shape.

It is interesting that VideoRay Mission Specialist Defender (Fig. 2.5d) can be upgraded with navigation package which includes a DVL, Greensea control program upgrade, MAX-M8W GPS MAST and (optional) USBL. The DVL is used for measuring linear velocity and consequently distance traveled can be estimated. Therefore, the current position can be calculated with dead-reckoning navigation techniques. When the vehicle is on the surface, a GPS antenna can be used to correct the vehicle's position. This upgrade package allows the vehicle to perform station keeping, requisition, mission planning and dynamic positioning. In the case when the sea bottom exceeds the operational range of the DVL, a USBL system is required for mission profiles. The upgraded VideoRay Mission Specialist Defender indeed can be equivalent to work class ROVs. In practice, for reducing workload of operator, work class ROVs often have the autonomous capabilities. For instance, if the vehicle can perform station keeping in front of a offshore structure then operator can focus only on surveillance or intervention tasks. However, the cost of this upgrade package can be guessed to be quite expensive since the main DVL included in the package exceeds €15,000.

The aforementioned Teledyne SeaBotix mini ROVs and micro/mini VideoRay ROVs are often used for professional applications. They are often go with various accessories, guarantee, technical supports and training. In order to buy them, it is required to contact authorized regional distributors. Their total prices are often very expensive.

Following the trend of mini ROVs aiming toward professional applications as well for entertainment purposes, it has been witnessed a recent startup company named Blueeye founded in 2015. Its first commercial mini ROV named Blueeye Pioneer was announced in 2018. The mini ROV has weight of 9 *kg*, depth rating of 150 *m* and a replaceable battery of 2 *hours* endurance. The vehicle is connected to the surface unit by tether. The surface unit plays the role of wired router or wifi rounter with at least 15 *m* distance in open area. By using a tablet/smartphone installed Blueeye App to connect wirelessly to the surface unit, one can control Blueeye Pioneer ROV.

---

<sup>5</sup>[https://en.wikipedia.org/wiki/VideoRay\\_UROVs](https://en.wikipedia.org/wiki/VideoRay_UROVs)

## 2.1. Recent small underwater robots

---



(a) VideoRay, launched in 2000. Weight: 3.6 kg. Depth rating: 152 m



(b) VideoRay Pro II, launched in 2002. Added more 80% thrust, new lighting, enhanced hydrodynamic performance, upgraded camera and lowered power consumption.



(c) VideoRay Pro 3, launched in 2004. Upgraded lighting, camera and thrusters. New 9-pin accessory plug for optional capabilities. Introduced control through a laptop PC which allow data can be gathered and analyzed.



(d) VideoRay Deep Blue, launched in 2004. Enhanced depth rating up to 305 m. Featured a Tritech SeaSprite scanning sonar.

Figure 2.4: VideoRay ROVs (Source: <http://www.videoray.com>)

In the sequel, let us introduce several mini ROVs used for education/development and entertainment purposes whose prices are relatively cheaper. The BlueROV2 platform presented in Fig. 2.7 can be used for developers with the availability of a wide range of accessories provided by Blue Robotics and opensource autopilot firmware ArduSub. For one who would like to dive and/or take underwater images, IBUBBLE mini ROV illustrated in Fig. 2.8 can be an interesting choice, especially "hands-free" version.



(a) VideoRay Pro 3 GTO, launched in 2005. More powerful thrusters allow increasing speed from 2.6 to 4.1 *knots*



(b) VideoRay Pro 4 , launched in 2009. Improved hydrodynamic performance, camera and ballast adjustment. New control software platform for pilot. Increased vertical and horizontal thrust. Weight: 6.1 *kg*. Depth rating 305 *m*.



(c) VideoRay CoPilot by Seebyte, launched in 2012. Featured autonomous control. CoPilot provides effortless and automatic navigation to underwater locations all while following a pre-defined mission regardless of changing currents and rough sea conditions.



(d) VideoRay Mission Specialist Defender , launched in 2017. Modular design of platform allows easily customizable to adapt to specific missions. Depth rating: 1000 *m*. Weight: 17.2 *kg*.



(e) VideoRay Pro 5 , launched in 2018. System of interchangeable, modular components. Forward speed: 4.4 *knots*. Weight: 10 *kg*. Depth rating: 305 *m*.

Figure 2.5: VideoRay ROVs (Source: <http://www.videoray.com>)

### 2.1.2 Small AUVs

AUVs in general sense stand for underwater vehicles operating without tether. They often travel at higher speed than ROVs, and designed in form of slender body to reduce drag. However, in this section we will discuss only vehicles with propulsor system. Gliders, a subset of AUVs, are out of scope of our discussions.

It is curious that successful startups in this product line have almost been acquired by worldwide conglomerates. One can name Hydroid founded in 2001 then incorporated to Kongsberg over M&A in 2007, Bluefin founded in 1997 then merged to General Dynamics

## 2.1. Recent small underwater robots

Accessories		Producer
Crawler		VideoRay LLC
Rotating Manipulator Arm		
Laser Scaler		
Manipulator Arm		
External SD Camera		Inuktun
MSS Cavitation Cleaner	Model 122 E60 Cavi Blaster	CaviDyne LLC
Positioning System	DVL	Nortek
	Smart tether	KCF Technologies
	MicronNav USBL	Tritech
Water quality sonde	YSI EXO2	YSI
Sonar	Tritech Gemini 720 Series (720ik, 720im, 720is)	Tritech
	Micron DST Scanning Sonar	
	BlueView V Series 2D imaging sonars	Teledyne
	Oculus Multibeam Sonars (M370S, M750d, M1200d)	BluePrint
Video enhancement	LYYN Real Time Video Enhancement	LYYN
Thickness gauge	Ultrasonic Metal Thickness Gauge	Cygnus Instruments
Option		
Navigation package	DVL, Greensea Upgrades, MAX-M8W GPS MAST and USBL (optional)	

Table 2.2: Teledyne SeaBotix accessories and options

in 2011, and recently Riptide Autonomous Solutions purchased by BAE Systems in June 2019. This trend reflects the increasing market for these vehicles as well as technology competition between the giants in the field.

Small AUVs are often design in form of two-man or one-man portable. In Figure 2.9, Bluefin-9 AUV of Bluefin Robotics in shape of two-man portable is illustrated. It has modular design with removable data storage and replaceable Li-ion battery. It has a navigation sensors including DVL and GPS (working only on the water surface). For communication purpose, it is equipped with acoustic modem, and Wifi & Iridium (working only on the water surface). High definition captured images, video and sonar data can be accessed quickly when retrieving the vehicle. The mission endurance is 8 *hours* when traveling at three knots speed. The maximum forward speed is 6 *knots*. The depth rating is 200 *m*. It requires only 30 *minutes* to exchange data storage and replace the battery before redeploying. Equipped with camera and water probe sensor, it can be used for surveying environment, measuring water quality, searching and recovering, or



Figure 2.6: Blueye Pioneer, launched in 2008. The total price of system including ROV, Wireless Surface Unit, 75 m cable, battery & charger, wireless controller, Blueye App, tools & spare parts is US\$9,878 (ex. VAT) (Source:www.blueyerobotics.com)

performing other tactical intelligence missions. Its weight is 70 kg. The propulsion system includes a gimbaled and ducted thruster. It has dimensions: 23.8 cm (W) x 26.4 cm (H) x 241.8 cm (L).

The Bluefin-9 AUV requires at least a group of 3 persons to deploy and retrieve. However, for a smaller one, for instance one-man portable Riptide  $\mu$ UUV, these tasks can be significantly simplified. As can be seen in Fig. 2.10, the vehicle can be easily carried since its weight is around 11.3 kg. However, its speed can be up to 10 knots and depth rating is 300 m. It has several energy options including Lithium ion (80 hours endurance) and Aluminum Seawater Battery (400 hours endurance). It has all the means of communication and navigation as in Bluefin-9, except DVL is optional. In general, Riptide  $\mu$ UUV is not only smaller, but faster and longer endurance in comparison with Bluefin-9.

The small AUVs, especially vehicles belonging to one-man portable class are quite challenging in terms of high pressure resistance and system integration. It is because of the fact that several essential components (e.g. DVL) are quite heavy and voluminous.

## 2.1. Recent small underwater robots

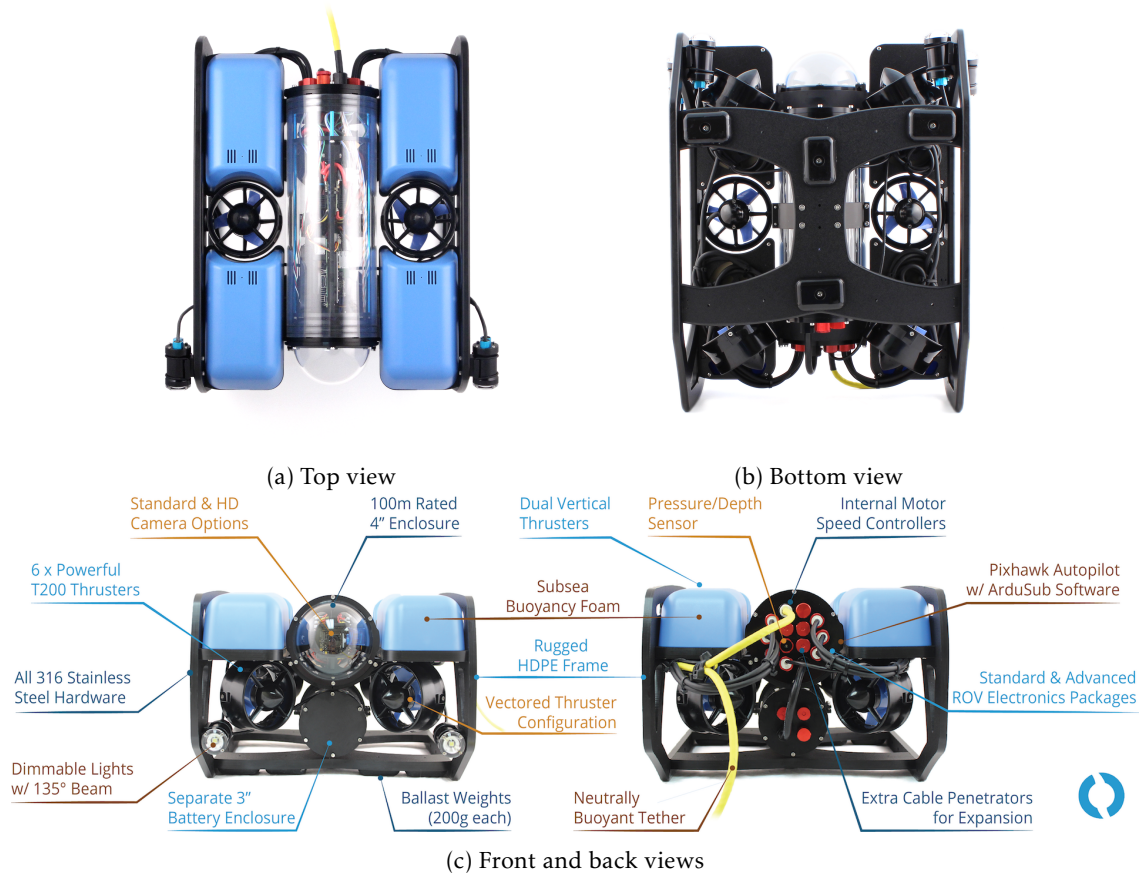


Figure 2.7: BlueROV2, mini ROV for developer, launched in 2016. The total price of system including ROV, 100 m tether cable and battery & charger is around US\$4,000 (ex. VAT). Dimensions: 33.8 cm (W) x 25.1 cm (H) x 45.7 cm (L). Weight: approximate 11 kg. (Source:www.bluerobotics.com)

### 2.1.3 Small hybrid vehicles

For some tactical missions, it is important to quickly access to a far underwater scene and transmit high definition images/video, sonar data or other measurements back to ground station as fast as possible. In this case, ROV is not a good selection, since it travel rather slow. In the contrary, AUV has faster speed but the underwater acoustic communication has very low bandwidth. In order to overcome that issue, AUV can be connected with the ground station by optical fiber. With the development of modern technologies, optical fiber which is rather fragile now can be coated by highly resisted material and consequently it becomes relevant to the task. The AUV in this case is in fact a hybrid vehicle, which can work either in autonomous (if the communication is broken) or remotely control. Nowadays, hybrid vehicles are becoming more popular since their exceptional performance allows for implementing many specific tasks.



Figure 2.8: IBUBBLE, launched preview in October 2019. The total price of "Hands-free" version is around US\$5,400 while for premium one including 100 m tether cable, 2 extra batteries & 2 battery charger, and hardcase is around US\$8,400 (prices inc. VAT). The weight of the vehicle is 9 kg. (Source: [www.ibubble.camera](http://www.ibubble.camera))

## 2.2 Review on the technologies used for small underwater robots

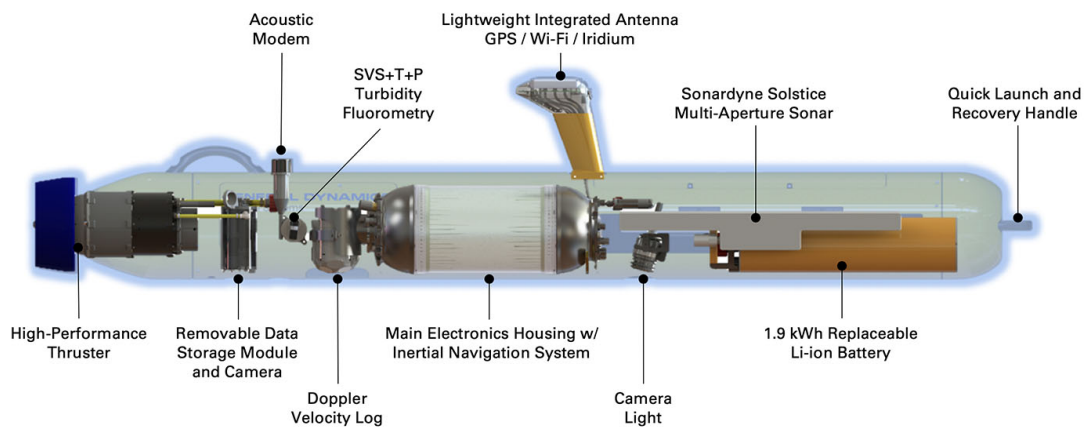
### 2.2.1 Brushless thruster

Thrusters always remain troublesome for ones who desired to build their own robots. While the in-house thrusters (e.g. hack-pump thruster) are not reliable, the industrial (e.g. SeaBotix thrusters) are significant expensive (at least US\$550 per item). Moreover, they are required periodical maintenance. Many people tried to overcome these issues but were not successful. It was the founder of Blue Robotics, Rustom Jehangir with his friends had noticed these facts when intended to build a small GPS-guided solar-powered boat that can travel autonomously from Los Angeles to Hawaii. They then decided to design new thruster which resists well to saltwater, operating continuously and reliably. However, the thruster must be affordable for everyone who would like to explore the ocean. After introducing the prototype of their first thruster (namely T100)

## 2.2. Review on the technologies used for small underwater robots



(a) Redesigned Bluefin-9 in field trial  
Bluefin9inside.jpg



(b) Inside view of components of Bluefin-9

Figure 2.9: Two-man portable Bluefin-9 AUV of Bluefin Robotics (Source: [www.gdmissionsystems.com](http://www.gdmissionsystems.com))

in May 2014, they quickly got the attention of the community. On August 12th 2014, they launched a kickstarter program for the target of US\$35,000 for funding the cover of the rest of the cost of thruster construction. After one month, they got US\$102,685 or 293% of their goal. That is the begin of T100 brushless thruster that runs completely



Figure 2.10: One-man portable Riptide AUV (source: [www.defensenews.com](http://www.defensenews.com))

immersed in water without corrosion or shorting and the need of traditional pressure limitations and Blue Robotics company. Nowadays, Blue Robotics provided to the market more powerful T200 thruster and recently M200 brushless underwater motor (for general purposes) (c.f. 2.11). As reported in [2], Blue Robotics has sold worldwide more than 35 thousands thrusters since 2014. Among the users are a large number of startups and research institutions. It is not too exaggerated to say that the appearance of T100 and Blue Robotics is a milestone in the history of underwater robotics community. Start from their own thrusters, nowadays Blue Robotics provides to the market a large choice of more than 250 essential components and sensors for underwater robotics applications, offers versatility for companies looking to integrate their own systems.

A T200 thruster of US\$169.00 together with ESC of US\$25.00 (all exc. VAT) can provide a thrust of 5 *kgf*. By providing pwm signal, it is quite simple and reliable to control each thruster. Our in-house underwater robot is indeed equipped with T200 thrusters. From our practical experiments, we have observed the high performance of this thruster.



(a) T100 and T200 have almost the same design, however the latter is more powerful

(b) General purpose underwater motor M200

Figure 2.11: Blue Robotics thrusters and motor (Source: [www.bluerobotics.com](http://www.bluerobotics.com))

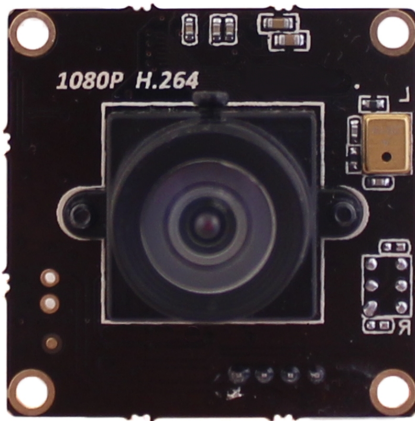
### 2.2.2 Camera

Small underwater robots are mainly used for observation applications. Thus, camera is one of the most important sensor. From diving sport, goPro<sup>6</sup> camera box which can withstand to 60 *m* underwater can be a nice choice to protect the inside camera. Another low-cost solution can be implemented by employing water tight tube (acrylic), end cap and dome end cap, which can be purchased from Blue Robotics to create camera box. This kind of camera box can resist up to 100 *m* underwater. Another issue when working with camera in underwater environment is lighting. Since below 10 *m* depth underwater, the light is very poor. Thus, one needs to have artificial lighting, which can be now easily performed by employing underwater LED lamp (c.f. 2.12b). Also from Blue Robotics, one can purchase Low-light HD camera (c.f. 2.12a) for improving the quality of images captured in low lighting underwater conditions.

In fact, water turbidity has strong influence on the quality of captured images. In order to deal with this issue, histogram equalization, a method in openCV dedicated for contrast adjustment can be employed for enhancing image quality before carrying out other tasks, for example homography estimation. Practically, this method showed the effectiveness in processing underwater images. In addition, the red wave in the light is absorbed by water. The color of captured image is thus strongly effected. One can use red filter for solving this issue.

---

<sup>6</sup><https://gopro.com/fr/fr/shop/cameras/>

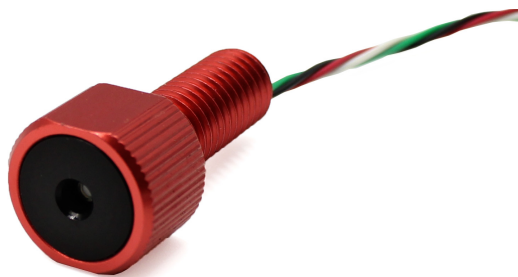


(a) Low light camera



(b) Lumen Subsea Light for ROV/AUV

Figure 2.12: Blue Robotics low light camera and Lumen Subsea Light (Source: [www.bluerobotics.com](http://www.bluerobotics.com))



(a) Depth sensor



(b) Ping sonar altimeter and echo sounder

Figure 2.13: Blue Robotics pressure sensor and single-beam echo sounder (Source: [www.bluerobotics.com](http://www.bluerobotics.com))

### 2.2.3 Depth sensor and single-beam echo sounder

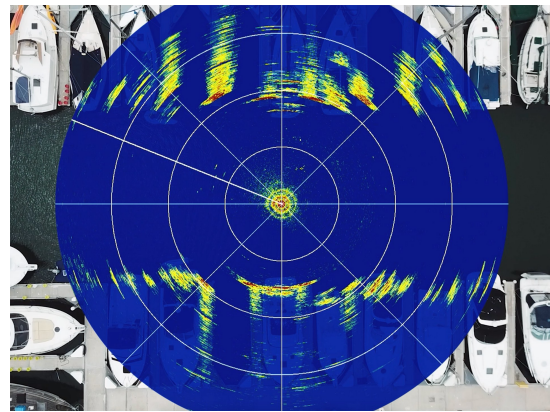
For underwater vehicle, depth sensor (c.f. 2.13a) is important to measure submerged depth while single beam echo sounder (c.f. 2.13b) is useful for measuring distance from the vehicle to the seabed or obstacle. For vehicles working in low-visibility water conditions, the mechanical scanning imaging sonar (Ping360 scanning sonar, c.f. 2.14) can be employed for navigation. This sensor is also useful for applications such as inspection, obstacle avoidance, target location and tracking, autonomous systems development, etc. These sensors with reasonable prices allow developers to implement many interesting functionalities for small underwater robots.

## 2.2. Review on the technologies used for small underwater robots

---



(a) Ping360



(b) Scanning imaging sonar monitor

Figure 2.14: Blue Robotics Ping360 sonar system (source: [www.bluerobotics.com](http://www.bluerobotics.com))

# 3

## Mathematical model of underwater vehicles

**G**OOD knowledge about the mathematical model of an AUV is important for control design and its validations by simulation. By numerically integrating ordinary differential equations of the model using, for instance, Runge-Kutta method, the vehicle's motion can be observed under the action of external effects and control inputs. With a modern computer and a simple code written, e.g., in Matlab/Simulink, such a simulation task may be performed efficiently within a very short time scale. A standard model of an AUV, commonly considered as a rigid body immersed in a condense and viscous environment, includes kinematic and dynamic equations. The former describes geometrical relations between the differentiation of the vehicle's pose (i.e. position and orientation) and its velocities (translational and angular) that can be expressed in different reference frames. The latter presents accelerating or decelerating translational (resp. rotational) motion of the vehicle under the action of all forces (resp. torques) acting on it.

Originally formalized in his thesis manuscript [18], the model formulation of ships and underwater vehicles proposed by T. I. Fossen using the notation of Society of Naval Architects and Marine Engineers (SNAME) is particularly popular since his well-known

book [19] is the foundation of a large number of marine vehicle control works. Inspired by manipulator model formulation, this nonlinear mathematical model has been developed on the basis of Euler angles, a minimal parametrization of the vehicle's orientation (i.e. attitude). The use of a minimal attitude parametrization allows for straightforward linearization of the system equations about any desired equilibrium trajectory and, thus, enabling the application of any linear control technique on the resulting linearized system. However, Euler angles, alike any other minimal attitude parametrization, suffer from artificial and unnecessary singularity when the pitch angle reaches  $\pm\pi/2$ .

Due to the aforementioned reason, in this work rotation matrix which is an element of the Special Orthogonal group  $SO(3)$  is adopted for attitude parametrization so that singularity issue can be avoided. As for the dynamic equations, the dynamic formulation proposed lately by N. E. Leonard [46] is preferred due to its compact form and physical interpretation related to the translational and rotational momentums of the body-fluid system. However, the interested reader can find the equivalent transformation between the Leonard model and the Fossen model in [43].

In this chapter the basics of AUV modeling are recalled. First, reference frames used for representing the vehicle's motion are introduced. Then, kinematic and dynamic equations are provided. Since the AUV is submersed in a fluid, hydrodynamic effects in terms of added mass and drag are carefully investigated. The effect of sea current can be considered as external perturbation.

### 3.1 Reference frames

Before deriving the equations of motion, it is important to define the reference frames used for that purpose. Classically, the dynamic equations of the vehicle are derived in the body-fixed coordinates because the expressions of hydrodynamic and control terms are much simple. It is well-known that the principal axes of symmetry of the vehicle are often chosen as the coordinate axes since the resulting inertia matrix can be relatively simplified. The body-fixed, mobile reference frame  $\{\mathcal{B}\}$  is chosen such that  $\vec{e}_3^b$  pointing towards the design "bottom" of the vehicle, while  $\vec{e}_1^b$  points towards its bow and  $\vec{e}_2^b$  towards its starboard. The coordinate vector representing the position of the Center of Gravity (CG) in  $\{\mathcal{B}\}$  is denoted as  $\mathbf{r}_G \in \mathbb{R}^3$ .

For the one observing the AUV's motion on Earth, it is convenient to define an Earth-fixed reference frame. Following SNAME convention, the Earth-fixed coordinate system  $\{\mathcal{A}\}$  is a North-East-Down (earth fixed reference frame convention) (NED) reference frame, with its base vector  $\vec{e}_3^a$  aligning the gravitational direction. The notation of two coordinate systems as depicted in Fig. 3.1 are summarized in Table. 3.1.

Reference	$\{\mathcal{A}\}$	$\{\mathcal{B}\}$
Base vectors	$\{\vec{e}_1^a, \vec{e}_2^a, \vec{e}_3^a\}$	$\{\vec{e}_1^b, \vec{e}_2^b, \vec{e}_3^b\}$
Attached to	Origin of inertial frame	Center of Buoyancy (CB) of the vehicle

Table 3.1: Reference frames used in this thesis

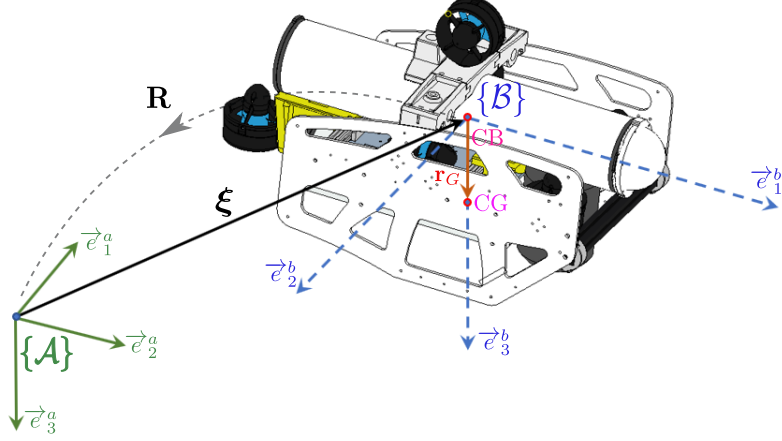


Figure 3.1: An AUV with reference frames and notation

### 3.2 Kinematics

Since the AUV is considered as a rigid body moving in a 3 dimensional space, the method of attitude parameterization should be carefully noticed. In this thesis the notion of rotation matrix is used in model formulation. Unit quaternions are used for efficient computational calculations since they have less parameters and require less computation cost to renormalize after each integration step due to rounding errors than the rotation matrix. Euler angles, despite their singularity issue, are still useful for visualization purposes due to their intuitive interpretation. The transformation between different attitude parametrizations including rotation matrix, Euler angles and unit quaternions can be found in [10, 28].

The orientation of the body-fixed reference frame  $\{\mathcal{B}\}$  with respect to the inertial  $\{\mathcal{A}\}$  is represented by a rotation matrix  $\mathbf{R} \in \text{SO}(3)$ . Let us denote the coordinate vector representing the position of the CB in the inertial frame  $\{\mathcal{A}\}$  as  $\xi \in \mathbb{R}^3$ .

The rate of change of the vehicle's position represents the velocity vector that relates to the body-referenced velocity  $\mathbf{V} \in \mathbb{R}^3$  by

$$\dot{\xi} = \mathbf{R}\mathbf{V} \quad (3.1)$$

### 3.3. Dynamics

---

The kinematics of the rotation matrix of the vehicle [23] satisfy:

$$\dot{\mathbf{R}} = \mathbf{R}\boldsymbol{\Omega}_\times \quad (3.2)$$

## 3.3 Dynamics

In comparison with any heavier-than-air aerial vehicle, the dynamics of an underwater vehicle are remarkably different because the surrounding environment of the vehicle is more dense and viscous. In the sequel the vehicle's dynamic equations are linear superposed of the rigid body and of the surrounding liquid.

### 3.3.1 Rigid body dynamics

Let us denote  $\mathbf{J}_0 \in \mathbb{R}^{3 \times 3}$  the inertia matrix of the rigid body in a body-fixed frame whose axes are aligned with the ones of  $\{\mathcal{B}\}$  and whose origin coincides with the CG. In most of the cases,  $\mathbf{J}_0$  can be approximately described by a diagonal positive-definite matrix:

$$\mathbf{J}_0 = \begin{bmatrix} J_x & 0 & 0 \\ 0 & J_y & 0 \\ 0 & 0 & J_z \end{bmatrix} \quad (3.3)$$

For the inertia matrix  $\mathbf{J} \in \mathbb{R}^{3 \times 3}$  expressed in  $\{\mathcal{B}\}$ , it can be deduced based on  $\mathbf{J}_0$  by applying the parallel axis theorem [41]:

$$\mathbf{J}_B = \mathbf{J}_0 - m\mathbf{r}_{G \times}^2 \quad (3.4)$$

Denote  $\mathbf{P} \in \mathbb{R}^3$  and  $\boldsymbol{\Pi} \in \mathbb{R}^3$  the translational and rotational momentums expressed in  $\{\mathcal{B}\}$ , respectively. In view of (3.4), the expressions of the quantity of momentum of the rigid body in the frame  $\{\mathcal{B}\}$  are given by

$$\begin{cases} \mathbf{P} = m\mathbf{V} - m\mathbf{r}_{G \times}\boldsymbol{\Omega} \\ \boldsymbol{\Pi} = \mathbf{J}_B\boldsymbol{\Omega} + m\mathbf{r}_{G \times}\mathbf{V} \end{cases} \quad (3.5)$$

Let us denote  $\mathbf{f} \in \mathbb{R}^3$  the coordinate vector expressed in  $\{\mathcal{A}\}$  of the total force acting on the body at a certain point, and  $\boldsymbol{\tau} \in \mathbb{R}^3$  the coordinate vector expressed in  $\{\mathcal{A}\}$  of the total torque acting around an axis through that point. Assume that the acted point is the CB, then one can neglect the rotational momentum terms due to eccentric forces. The dynamics of the rigid body is thus given by [46]:

$$\dot{\mathbf{P}} = \mathbf{P} \times \boldsymbol{\Omega} + \mathbf{F} \quad (3.6a)$$

$$\dot{\boldsymbol{\Pi}} = \boldsymbol{\Pi} \times \boldsymbol{\Omega} + \mathbf{P} \times \mathbf{V} + \boldsymbol{\Gamma} \quad (3.6b)$$

where  $\mathbf{F} = \mathbf{R}^\top \mathbf{f}$  and  $\mathbf{\Gamma} = \mathbf{R}^\top \boldsymbol{\tau}$  are the coordinate vectors expressed in  $\{\mathcal{B}\}$  of the total force and torque, respectively.

The kinetic energy of the rigid body including translational and rotational kinetic energies has the following form

$$E_B = \frac{1}{2} \mathbf{W}^\top \mathbf{M}_B \mathbf{W} \quad (3.7)$$

with the abstract rigid body mass matrix

$$\mathbf{M}_B \triangleq \begin{bmatrix} m\mathbf{I}_3 & -m\mathbf{r}_{G\times} \\ m\mathbf{r}_{G\times} & \mathbf{J}_B \end{bmatrix} \quad (3.8)$$

and  $\mathbf{W} \triangleq [\mathbf{V}^\top, \boldsymbol{\Omega}^\top]^\top \in \mathbb{R}^6$ .

### 3.3.2 Added mass

In 1828, after accounting for buoyancy effect F. Bessel observed that period of a pendulum submersed in a fluid relatively increase in comparison with in vacuum. He proposed the concept of added mass [77] to indicate that the surrounding fluid must be accelerated that increases the effective mass of accelerating submersed body.

According to Kirchhoff and Lamb theory [45], the liquid surrounding the body has the following kinetic energy

$$E_F = \frac{1}{2} \mathbf{W}^\top \mathbf{M}_A \mathbf{W} \quad (3.9)$$

where the added mass matrix is denoted as

$$\mathbf{M}_A \triangleq \begin{bmatrix} \mathbf{M}_A^{11} & \mathbf{M}_A^{12} \\ \mathbf{M}_A^{21} & \mathbf{M}_A^{22} \end{bmatrix} \in \mathbb{R}^{6 \times 6} \quad (3.10)$$

For a fully submerged body,  $\mathbf{M}_A$  is positive definite and all its diagonal components are positive. In [20] it is shown that  $\mathbf{M}_A = \mathbf{M}_A^\top$  is a good approximation, thereby resulting in  $\mathbf{M}_A^{21} = \mathbf{M}_A^{12^\top}$ . Identification experiments in testing pool only allow for estimating the diagonal terms – the most significant ones of the added mass matrix. Alternatively to this time-consuming and high-cost method, the identification can be numerically carried out using WAMIT<sup>1</sup>, a panel program designed to solve the boundary-value problem for the interaction of water-waves with submersed body. However, this costly commercial software is only affordable by a limited number of companies and institutions. In addition, the result of identification strongly depends on mesh generation.

In practice for low-speed maneuvering underwater vehicle with three planes of sym-

<sup>1</sup><https://www.wamit.com/>

### 3.3. Dynamics

---

metry, the effect of off-diagonal components of  $\mathbf{M}_A$  can be neglected [20]. This fact thus allows one to approximate  $\mathbf{M}_A$  by a diagonal matrix, which in turn leads to the approximation  $\mathbf{M}_A^{21} = \mathbf{M}_A^{12} \approx \mathbf{0}$ . In this thesis, due to the unavailability of testing pool and identification commercial program, the diagonal components of  $\mathbf{M}_A$  are identified based on empirical method. By approximating the AUV's main geometric components by corresponding symmetrical objects which have added mass expressed in analytical forms [61], these diagonal components can be roughly estimated.

#### 3.3.3 Body-fluid dynamics

The vehicle's dynamic equations are derived based on the translational and rotational momentums of the body-fluid system. The total kinetic energy of the body-fluid system is  $E_T = E_B + E_F$ . One thus deduces

$$E_T = \frac{1}{2} \mathbf{W}^\top \mathbf{M}_T \mathbf{W}, \text{ with } \mathbf{M}_T = \begin{bmatrix} \mathbf{M} & \boldsymbol{\Xi}^\top \\ \boldsymbol{\Xi} & \mathbf{J} \end{bmatrix} \quad (3.11)$$

where  $\mathbf{M} \triangleq m\mathbf{I}_3 + \mathbf{M}_A^{11}$ ,  $\mathbf{J} \triangleq \mathbf{J}_B + \mathbf{M}_A^{22}$ , and

$$\boldsymbol{\Xi} \triangleq m\mathbf{r}_{G\times} + \mathbf{M}_A^{21} \quad (3.12)$$

In the particular case where  $\mathbf{M}_A^{21} = \mathbf{M}_A^{12} \approx \mathbf{0}$ , one has  $\boldsymbol{\Xi}^\top = -\boldsymbol{\Xi} \approx -m\mathbf{r}_{G\times}$ .

The translational and rotational momentums are computed as

$$\begin{cases} \mathbf{P} = \frac{\partial E_T}{\partial \mathbf{V}} = \mathbf{M}\mathbf{V} - \boldsymbol{\Xi}\boldsymbol{\Omega} \\ \boldsymbol{\Pi} = \frac{\partial E_T}{\partial \boldsymbol{\Omega}} = \mathbf{J}\boldsymbol{\Omega} + \boldsymbol{\Xi}\mathbf{V} \end{cases} \quad (3.13)$$

In view of (3.6) and (3.13) and due to the fact that  $(\mathbf{r}_{G\times}\mathbf{V})_\times = \mathbf{r}_{G\times}\mathbf{V}_\times - \mathbf{V}_\times\mathbf{r}_{G\times}$ , the dynamics of the AUV can be expressed as follows

$$\mathbf{M}\dot{\mathbf{V}} - \boldsymbol{\Xi}\dot{\boldsymbol{\Omega}} = (\mathbf{M}\mathbf{V} - \boldsymbol{\Xi}\boldsymbol{\Omega}) \times \boldsymbol{\Omega} + \mathbf{F} \quad (3.14a)$$

$$\mathbf{J}\dot{\boldsymbol{\Omega}} + \boldsymbol{\Xi}\dot{\mathbf{V}} = (\mathbf{J}\boldsymbol{\Omega}) \times \boldsymbol{\Omega} + (\mathbf{M}\mathbf{V}) \times \mathbf{V} + \boldsymbol{\Xi}(\mathbf{V} \times \boldsymbol{\Omega}) + \boldsymbol{\Gamma} \quad (3.14b)$$

So far, the dynamics of the AUV is derived using an abstract form of the total force  $\mathbf{F}$  and total torque  $\boldsymbol{\Gamma}$  acting on the vehicle. In the next sections, details on  $\mathbf{F}$  and  $\boldsymbol{\Gamma}$  will be discussed.

## 3.4 External forces and torques

### 3.4.1 Restoring forces

Underwater vehicles are constrained by the gravity and buoyancy forces which are aligned with  $\vec{e}_3^g$ . While the former acts on the body at the CG, the acted point of the latter is at the CB, which is not usually coincident with the CG. The torque generated by the two forces statically stabilizes the vehicle to its orientation of equilibrium. These forces are thus called restoring forces in naval architecture.

The resulting restoring forces expressed in  $\{\mathcal{B}\}$  is defined as

$$\mathbf{F}_{gb} \triangleq \beta_{gb} \mathbf{R}^\top \mathbf{e}_3 \quad (3.15)$$

where  $\beta_{gb} \triangleq mg - F_b$  is the sum of the gravity and the buoyancy force  $F_b$  which is equal to the gravitational weight of the liquid displaced by the vehicle.

Since the CB is the origin of the frame  $\{\mathcal{B}\}$ , the restoring torque expressed in  $\{\mathcal{B}\}$  is the gravity torque which is defined as

$$\mathbf{\Gamma}_g \triangleq mg \mathbf{r}_{G \times} \mathbf{R}^\top \mathbf{e}_3 \quad (3.16)$$

In practice, marine vehicles are often intendedly designed as "heavy bottom" to benefit from restoring forces. To keep the vehicle safe from sinking,  $F_B$  is slightly larger than its weight. Additional masses (payloads or/and ballasts) and floats are employed for adjusting zero-pitch and zero-roll orientation.

### 3.4.2 Drag

A marine vehicle submersed in a fluid environment is constrained by drag (also called as fluid resistance). It is a force preventing the relative motion of the vehicle moving with respect to a surrounding fluid. In Section 3.3.2, the term of added mass is also proposed for explaining the interaction between the vehicle and the surrounding fluid. The drag and the added mass (or added inertia) thus must be carefully differentiate. Since the former describes the effect of the surrounding liquid on a body moving at certain relative speed, the latter is only applied in the context of acceleration.

For underwater vehicles, the wavemaking drag is ignored because of lacking of interaction between vehicles and the free water surface. Therefore, only three other kinds of drag are considered including potential, skin friction and vortex shedding. However, it is difficult to separate these terms in the total drag of underwater vehicles in real fluid.

In practice, it is often assumed that high order drag effects can be neglected, and different drag terms contribute to either linear or quadratic drag. The drag force and

### 3.4. External forces and torques

---

torque are thus modeled as the sum of linear and quadratic terms as follows

$$\begin{cases} \mathbf{F}_d(\mathbf{V}) = -(\mathbf{D}_{Vl} + |\mathbf{V}|\mathbf{D}_{Vq})\mathbf{V} \\ \mathbf{\Gamma}_d(\mathbf{\Omega}) = -(\mathbf{D}_{\Omega l} + |\mathbf{\Omega}|\mathbf{D}_{\Omega q})\mathbf{\Omega} \end{cases} \quad (3.17)$$

with positive damping matrices  $\mathbf{D}_{Vl}, \mathbf{D}_{Vq}, \mathbf{D}_{\Omega l}, \mathbf{D}_{\Omega q} \in \mathbb{R}^{3 \times 3}$ .

For some specific underwater vehicle like glider, additional control surfaces (i.e hydrofoils) are used for gliding forward while descending or climbing back up through the water. This phenomenon results in none zero off-diagonal components in the damping matrices  $\mathbf{D}_{Vl}, \mathbf{D}_{Vq}$ . However, this coupling effect is often considered in separate terms corresponding to control surfaces in the vehicle dynamics. The body of underwater vehicle is thus considered having "correct design" with all zero off-diagonal components.

In practice, the damping matrices  $\mathbf{D}_{Vl}, \mathbf{D}_{Vq}, \mathbf{D}_{\Omega l}, \mathbf{D}_{\Omega q}$  are identified using reduced scale model in towing tank. Or alternatively and less expensive, they are calculated by computational fluid dynamics (CFD) programs, for instance commercial ANSYS Fluent<sup>2</sup> or open-source Code\_Saturne<sup>3</sup>. However, the identification results depend strongly on choosing and setting parameters of the calculation modules, more importantly the form and size of computational grid.

For a certain number of basic two- or three- dimensional bodies like flat plate, sphere, half-sphere, cone, circular cylinder with different noses, etc. in a certain range of Reynolds number, the value of drag coefficients are almost constant [27]. Therefore, the values of damping matrices of underwater vehicles in this thesis are identified by empirical method. The vehicles are decomposed into basic bodies with defined drag coefficients. By superposition, the terms of damping matrices  $\mathbf{D}_{Vl}, \mathbf{D}_{Vq}$  of the whole vehicle can be calculated. The terms of rotational damping matrices  $\mathbf{D}_{\Omega l}, \mathbf{D}_{\Omega q}$  then are calculated by considering decomposed bodies rotating around the vehicle's principal axis. Also, the terms of damping matrices are verified by comparison with published data sets, for instance in [17].

#### 3.4.3 Propulsion system

The propulsion system gives underwater vehicle movement and maneuverability against water resistance. In view of dynamical model of the vehicle, it provides control force  $\mathbf{F}_c$  and torque  $\mathbf{\Gamma}_c$ . There exist different kinds of propulsion for underwater vehicles like variable-buoyancy propulsion system [74] for underwater gliders, hydraulic thrusters<sup>4</sup> typically for large work class ROVs, or wide range of thermal propulsion systems [38] for

<sup>2</sup><https://www.ansys.com/fr-fr/products/fluids/ansys-fluent>

<sup>3</sup><https://www.code-saturne.org/cms/>

<sup>4</sup><https://innerspacethrusters.com/products/hydraulic-thrusters/>

torpedoes. However, only electric thrusters employed in experimental platforms used in this work are considered.

For slender body vehicles traveling at high speed, the thrusters whose axes are perpendicular to the vehicle longitudinal axis can be ineffective. Therefore, control surfaces (i.e. elevator or ruder) are often employed for orientation control.

### 3.4.4 Current

For underwater vehicles, current is an external factor that effects the vehicle operation. It is thus must be taken into account in the modeling. For simplification, it is assumed that the current velocity  $\mathbf{v}_f$  expressed in inertial frame  $\mathcal{A}$  is constant and irrotational.

Let  $\mathbf{V}_f$  be the vector of coordinates of the current velocity expressed in  $\mathcal{B}$ . Then the CoB's velocity relative to the current expressed in  $\mathcal{B}$  is denoted as  $\mathbf{V}_h \triangleq \mathbf{V} - \mathbf{V}_f$ . Let us denote  $\mathbf{W}_h \triangleq [\mathbf{V}_h^\top, \boldsymbol{\Omega}^\top]^\top$ , then the total kinetic energy of the body-fluid system yields

$$E_T = \frac{1}{2} \mathbf{W}_h^\top \mathbf{M}_T \mathbf{W}_h \quad (3.18)$$

The translational and rotational momentums with current taken into account are computed as

$$\begin{cases} \mathbf{P}_h = \frac{\partial E_T}{\partial \mathbf{V}_h} = \mathbf{M} \mathbf{V}_h - \boldsymbol{\Xi} \boldsymbol{\Omega} \\ \boldsymbol{\Pi}_h = \frac{\partial E_T}{\partial \boldsymbol{\Omega}} = \mathbf{J} \boldsymbol{\Omega} + \boldsymbol{\Xi} \mathbf{V}_h \end{cases} \quad (3.19)$$

In view of (3.6) and (3.13), the dynamics of the AUV can be expressed as follows

$$\mathbf{M} \dot{\mathbf{V}}_h - \boldsymbol{\Xi} \dot{\boldsymbol{\Omega}} = (\mathbf{M} \mathbf{V}_h - \boldsymbol{\Xi} \boldsymbol{\Omega}) \times \boldsymbol{\Omega} + \mathbf{F} \quad (3.20a)$$

$$\mathbf{J} \dot{\boldsymbol{\Omega}} + \boldsymbol{\Xi} \dot{\mathbf{V}}_h = (\mathbf{J} \boldsymbol{\Omega}) \times \boldsymbol{\Omega} + (\mathbf{M} \mathbf{V}_h) \times \mathbf{V}_h + \boldsymbol{\Xi} (\mathbf{V}_h \times \boldsymbol{\Omega}) + \boldsymbol{\Gamma} \quad (3.20b)$$

Current also has effect on the drag of the vehicle. The first equation of (3.17) representing the drag force is thus written as follows

$$\mathbf{F}_d(\mathbf{V}_h) = -(\mathbf{D}_{Vl} + |\mathbf{V}_h| \mathbf{D}_{Vq}) \mathbf{V}_h \quad (3.21)$$

In control design, the terms relating to current are often considered as disturbances. With considering the fact that  $\dot{\mathbf{V}}_f = \mathbf{V}_f \times \boldsymbol{\Omega}$ , equations (3.20a) and (3.20b) are thus rewritten as

$$\mathbf{M} \dot{\mathbf{V}} - \boldsymbol{\Xi} \dot{\boldsymbol{\Omega}} = (\mathbf{M} \mathbf{V} - \boldsymbol{\Xi} \boldsymbol{\Omega}) \times \boldsymbol{\Omega} + \mathbf{F} + \boldsymbol{\Delta}_F \quad (3.22a)$$

$$\mathbf{J} \dot{\boldsymbol{\Omega}} + \boldsymbol{\Xi} \dot{\mathbf{V}} = (\mathbf{J} \boldsymbol{\Omega}) \times \boldsymbol{\Omega} + (\mathbf{M} \mathbf{V}) \times \mathbf{V} + \boldsymbol{\Xi} (\mathbf{V} \times \boldsymbol{\Omega}) + \boldsymbol{\Gamma} + \boldsymbol{\Delta}_\Gamma \quad (3.22b)$$

### 3.5. Complete nonlinear model

---

with the “disturbance” terms

$$\begin{aligned}\Delta_F &\triangleq -(\mathbf{M}\mathbf{V}_f)_{\times}\boldsymbol{\Omega} - \mathbf{M}\boldsymbol{\Omega}_{\times}\mathbf{V}_f \\ \Delta_{\Gamma} &\triangleq -(\mathbf{M}\mathbf{V})_{\times}\mathbf{V}_f - (\mathbf{M}\mathbf{V}_f)_{\times}(\mathbf{V} - \mathbf{V}_f)\end{aligned}$$

## 3.5 Complete nonlinear model

So far in this chapter, the mathematical modeling for AUV is briefly recalled. The model is foundation for identification, control design and simulation in the next chapters. In summary, the following mathematical model is considered:

$$\mathbf{M}\dot{\mathbf{V}} - \boldsymbol{\Xi}\dot{\boldsymbol{\Omega}} = (\mathbf{M}\mathbf{V} - \boldsymbol{\Xi}\boldsymbol{\Omega}) \times \boldsymbol{\Omega} + \mathbf{F}_c + \mathbf{F}_{gb} + \mathbf{F}_d \quad (3.23a)$$

$$\mathbf{J}\dot{\boldsymbol{\Omega}} + \boldsymbol{\Xi}\dot{\mathbf{V}} = (\mathbf{J}\boldsymbol{\Omega}) \times \boldsymbol{\Omega} + (\mathbf{M}\mathbf{V}) \times \mathbf{V} + \boldsymbol{\Xi}(\mathbf{V} \times \boldsymbol{\Omega}) + \boldsymbol{\Gamma}_c + \boldsymbol{\Gamma}_g + \boldsymbol{\Gamma}_d \quad (3.23b)$$

Depending on the quantity of thrusters and how they are distributed, underwater vehicles can be fully actuated or underactuated. The vehicles considered in Chapters 5 and 6 is fully actuated where  $\mathbf{F}_c$  together with  $\boldsymbol{\Gamma}_c$  provides full six control variables for controlling vehicle’s position and orientation. In contrast, the vehicles considered in Chapter 8 are underactuated. Since  $\mathbf{F}_c$  is fixed to be parallel to the  $\vec{e}_1^b$  longitudinal axis of the vehicle, there is only one variable for controlling the vehicle’s translation (i.e.  $\mathbf{F}_c = T\mathbf{e}_1$ ) whereas its rotational dynamics are fully actuated. In this work, for simplification, we assume that the available components of the control force  $\mathbf{F}_c$  and control torque  $\boldsymbol{\Gamma}_c$  are not bounded.

**Remark 1.** *If the vehicle shape is cubic or a spherical, then system model (3.23) can be more simplified. These particular shapes result in the approximations  $\mathbf{M}_A^{21} \approx \mathbf{M}_A^{12} \approx \mathbf{M}_A^{22} \approx \mathbf{0}$  and  $\mathbf{M}_A^{11} \approx m_A\mathbf{I}_3$ , where  $m_A = \alpha\rho l^3$  with  $\alpha \approx 0.7$  for a cube with length of edge  $l$  submerged in water with density  $\rho$ , or  $m_A = \frac{2}{3}\pi\rho r^3$  for a sphere with radius  $r$ . The term  $\mathbf{M}$  thus has the form  $\bar{m}\mathbf{I}_3$  with  $\bar{m} \triangleq m + m_A$ , and consequently the Munk moment term  $(\mathbf{M}\mathbf{V}) \times \mathbf{V}$  is null. The model of the vehicle can thus be more simplified as*

$$\begin{aligned}\bar{m}\dot{\mathbf{V}} - \boldsymbol{\Xi}\dot{\boldsymbol{\Omega}} &= (\bar{m}\mathbf{V} - \boldsymbol{\Xi}\boldsymbol{\Omega}) \times \boldsymbol{\Omega} + \mathbf{F}_c + \mathbf{F}_{gb} + \mathbf{F}_d \\ \mathbf{J}_B\dot{\boldsymbol{\Omega}} + \boldsymbol{\Xi}\dot{\mathbf{V}} &= (\mathbf{J}_B\boldsymbol{\Omega}) \times \boldsymbol{\Omega} + \boldsymbol{\Xi}(\mathbf{V} \times \boldsymbol{\Omega}) + \boldsymbol{\Gamma}_c + \boldsymbol{\Gamma}_g + \boldsymbol{\Gamma}_d\end{aligned}$$

## **Part II**

# **Dynamic Homography-Based Visual Servo (HBVS) control of fully-actuated AUVs without linear velocity measurements**



---

**S**APE and efficient navigation of AUVs in cluttered environments remains a challenging task. Scientific issues are particularly related to the fact that global acoustic positioning systems become unusable or insufficiently precise in such situations, leading to an obvious interest in developing advanced sensor-based control strategies for AUV applications in close proximity to a complex sea bottom or submarine structures. While acoustic systems have been widely used for sensing underwater environments, cameras offer an appealing alternative due to the rich information captured by images and their high update rate. By using vision sensors as a sensor modality for relative (scaled) position and orientation, the control problems can be cast into Position-Based Visual Servoing (PBVS) or Image-Based Visual Servoing (IBVS) [13]. Classical visual servo control techniques have been initially developed for robotic manipulators and mobile ground vehicles [36, 50] and then for aerial drones [24, 22, 68]. In underwater robotics, vision sensors have been used to perform station keeping or positioning [48, 78, 21, 15], docking [11, 54, 79, 49], and pipeline following [57, 73, 7, 6], etc.

Both stereo and monocular cameras have been exploited for stabilization and positioning of AUVs. When the vehicle's pose (i.e. position and orientation) can be estimated, existing PBVS controllers can be directly applied [66]. In contrast, the case of monocular vision without the assumption of planarity of the visual target and the prior knowledge of its geometry is more involved since full pose reconstruction from visual data is not possible. However, monocular vision can be sufficient to achieve stabilization of an AUV in front of a planar target [48, 78, 11]. Recently, an advanced kinematic IBVS control scheme was proposed in [8] by exploiting the so-called homography that is an invertible mapping relating two camera views of the same planar scene by encoding in a single matrix the camera pose, the distance between the camera and the scene, and the normal direction to the scene [26, 8]. A noteworthy feature of this approach is the non-requirement of homography decomposition which is often computationally expensive and sensitive to measurement noise (see e.g. [56]), as opposed to other homography-based visual servo (HBVS) controllers [55, 11]. More recently, this kinematic HBVS control approach has been extended in [44] in order to account for the full dynamics of fully-actuated AUVs and to obtain an enlarged provable domain of stability. The research work presented in this part is an extension of [44] to the case where linear velocity measurements are unavailable. One of the main motivations behind our efforts are related to the development of a low-cost but efficient solution for station keeping and positioning of AUVs without the need of a costly DVL velocity sensor. More precisely, the proposed solution makes use of a minimal and inexpensive sensor suite consisting of an IMU and an embedded video camera.

HBVS control can be applied to numerous AUV applications once a locally planar visual target is available. For instance, station keeping using a downward-looking camera

---

to observe the ocean floor is a classical application. One can also mention stabilization or positioning in front of a man-made subsea manifold for high-resolution imaging, monitoring, or inspection, or for manipulation like valve-turning, or for maintenance like cleaning, repairing, or changing underwater structures. Finally, docking on a planar docking station is also a relevant application for HBVS control.

This part is structured into four chapters. Homography definition, some feature-based homography estimation methods and a review of existing homography-based visual servo control techniques are provided in Chapter 4. In Chapter 5, a dynamic HBVS control approach for AUV equipped with a downward-looking camera observing a (near) horizontal target is proposed. Then, another dynamic HBVS control approach for AUV equipped with a forward-looking camera observing a (near) vertical target is developed in Chapter 6. The control designs for both cases have a cascade inner-outer loop control architecture. While the inner-loop designs are identical, the outer-loop designs for these cases are significantly different. All the proposed control approaches are first validated by simulation using Matlab/Simulink and then by experiment using an in-house platform named *I3S-UV*. In Chapter 7, practical issues relating to the development of the *I3S-UV* platform are presented.

# 4

## Preliminaries on homography estimation and homography-based control techniques

**P**ART II is dedicated to the control design for the stabilization or positioning problem of fully-actuated AUVs equipped with a monocular camera and an IMU as sensor modalities. By focussing on the case of a camera observing a textured (near) planar visual target such as a sea floor, it is natural to exploit the so-called homography as feedback information for control design. Robust and precise homography estimation is one of the essential requirements to guarantee a high performance of the designed homography-based visual servo (HBVS) controllers. Aiming to provide preliminary materials about homography, the organization of this chapter is thereby sequential. First, some basic notion of homography is recalled. Then we discuss about some relevant feature-based methods for homography estimation with a particular focus on a nonlinear homography observer on  $SL(3)$  that has been developed by the I3S-OSCAR team [34]. Note that the library **HomographyLab**<sup>1</sup> implementing this observer for real-time,

---

<sup>1</sup><http://homographylab.i3s.unice.fr>

highly robust and efficient homography estimation has been used for the experimental validations of our proposed HBVS controllers. Finally, we briefly recall and discuss about some state-of-the-art HBVS controllers that have inspired our works on this topic.

## 4.1 Homography definition

Originated from the field of Computer Vision, the so-called homography is an invertible mapping that relates two camera views of the same planar scene by encoding in a single matrix the camera pose, the distance between the camera and the scene, along with the normal direction to the scene (e.g., [26]). For further understanding, more details about the homography (by borrowing some elements of [34]) are developed next.

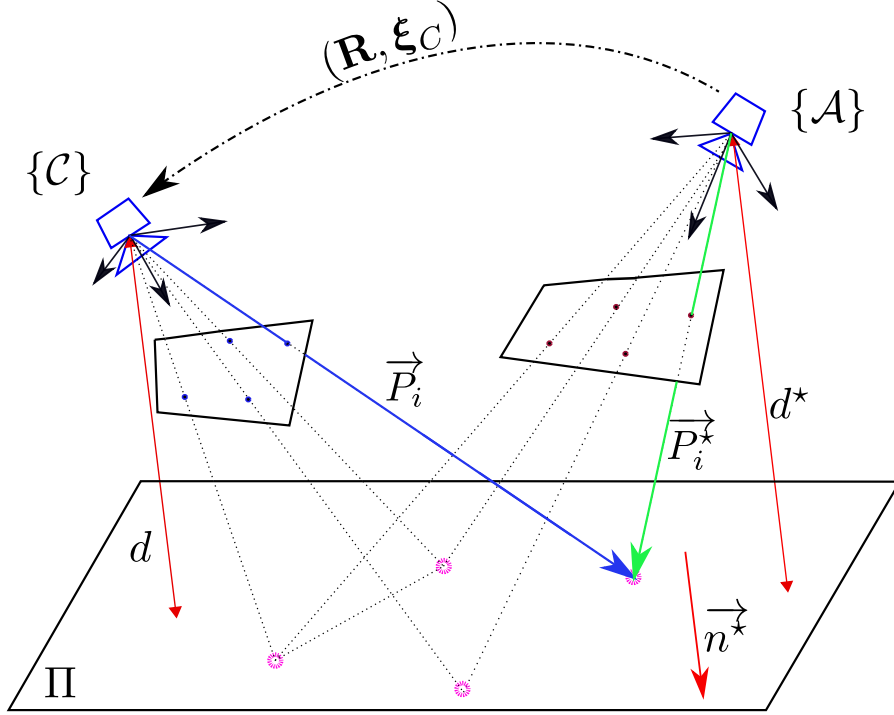


Figure 4.1: The pose of the camera  $(\mathbf{R}, \xi_C)$  determines a rigid body transformation from  $\{A\}$  to  $\{C\}$ . The Euclidean homography  $\mathbf{H} \cong \mathbf{R}^\top - (1/d^*)\mathbf{R}^\top \xi_C \mathbf{n}^{*\top}$  maps Euclidean coordinates of the scene's points from  $\{A\}$  to  $\{C\}$ . Arrow notation  $(\vec{\cdot})$  is used for Euclidean vectors.

Let  $\mathcal{A}$  (resp.  $\mathcal{C}$ ) denote projective coordinates for the image plane of a camera  $A$  (resp.  $C$ ), and let  $\{A\}$  (resp.  $\{C\}$ ) denote its reference (resp. current) frame. Let  $\xi_C \in \mathbb{R}^3$  denote the position of the origin of the frame  $\{C\}$  with respect to  $\{A\}$  expressed in  $\{A\}$ . The orientation of the frame  $\{C\}$  with respect to  $\{A\}$  is represented by a rotation matrix  $\mathbf{R} \in \text{SO}(3)$  (see Fig. 4.1).

Let  $d^*$  (resp.  $d$ ) and  $\mathbf{n}^*$  (resp.  $\mathbf{n}$ ) denote the distance from the origin of  $\{\mathcal{A}\}$  (resp.  $\{\mathcal{C}\}$ ) to the observed planar scene and the coordinate normal vector pointing towards the scene expressed in  $\{\mathcal{A}\}$  (resp.  $\{\mathcal{C}\}$ ), respectively. One easily verifies that

$$\begin{cases} \mathbf{n} = \mathbf{R}^\top \mathbf{n}^* \\ d = d^* - \mathbf{n}^{*\top} \boldsymbol{\xi}_C \end{cases} \quad (4.1)$$

The coordinate vectors  $\mathbf{P}^* \in \{\mathcal{A}\}$  and  $\mathbf{P} \in \{\mathcal{C}\}$  of the same point  $P$  on the scene are related by

$$\mathbf{P} = \mathbf{R}^\top (\mathbf{P}^* - \boldsymbol{\xi}_C) \quad (4.2)$$

Since the considered points belong to the observed planar scene

$$\Pi := \{\forall \mathbf{P} \in \mathbb{R}^3 : \mathbf{n}^\top \mathbf{P} - d = 0\} = \{\forall \mathbf{P}^* \in \mathbb{R}^3 : \mathbf{n}^{*\top} \mathbf{P}^* - d^* = 0\}$$

one derives from the plane constraint  $\frac{\mathbf{n}^{*\top} \mathbf{P}^*}{d^*} = 1$  and Eq. (4.2) that

$$\mathbf{P} = \mathbf{R}^\top \left( \mathbf{I} - \frac{\boldsymbol{\xi}_C \mathbf{n}^{*\top}}{d^*} \right) \mathbf{P}^* \quad (4.3)$$

Let  $\mathbf{p}_{img}^* \in \mathcal{A}$  (resp.  $\mathbf{p}_{img} \in \mathcal{C}$ ) denote the image of the considered point when the camera is aligned with the frame  $\{\mathcal{A}\}$  (resp. frame  $\{\mathcal{C}\}$ ). Note that  $\mathbf{p}_{img}^*$  and  $\mathbf{p}_{img}$  have the form  $(u, v, 1)^\top$  using the homogeneous coordinate representation and they are related to the 3D coordinates of that point by<sup>2</sup>:

$$\mathbf{p}_{img}^* \cong \mathbf{K} \mathbf{P}^*, \quad \mathbf{p}_{img} \cong \mathbf{K} \mathbf{P} \quad (4.4)$$

with  $\mathbf{K} \in \mathbb{R}^{3 \times 3}$  denoting the camera calibration matrix that contains the intrinsic parameters of the camera such as the focal length, the pixel aspect ratio, the principal point, etc [51]. If the camera is well calibrated (i.e.  $\mathbf{K}$  is known) then all quantities can be re-normalized onto the unit 2-sphere  $\mathbb{S}^2$  as

$$\mathbf{p}^* := \frac{\mathbf{P}^*}{|\mathbf{P}^*|} = \frac{\mathbf{K}^{-1} \mathbf{p}_{img}^*}{|\mathbf{K}^{-1} \mathbf{p}_{img}^*|}, \quad \mathbf{p} := \frac{\mathbf{P}}{|\mathbf{P}|} = \frac{\mathbf{K}^{-1} \mathbf{p}_{img}}{|\mathbf{K}^{-1} \mathbf{p}_{img}|} \quad (4.5)$$

Using Eqs. (4.3) and (4.5), the projected points satisfies

$$\mathbf{p} \cong \mathbf{R}^\top \left( \mathbf{I} - \frac{\boldsymbol{\xi}_C \mathbf{n}^{*\top}}{d^*} \right) \mathbf{p}^* \cong \mathbf{H} \mathbf{p}^* \quad (4.6)$$

<sup>2</sup>Unless otherwise stated, most statements in projective geometry involve equality up to a multiplicative constant denoted by  $\cong$ .

## 4.2. Existing feature-based homography estimation techniques

---

where the projective mapping

$$\mathbf{H} \cong \mathbf{R}^\top - \mathbf{R}^\top \frac{\boldsymbol{\xi}_{\mathcal{C}} \mathbf{n}^{\star\top}}{d^*} \quad (4.7)$$

is defined as the Euclidean homography that maps Euclidean coordinates of the scene's points from  $\{A\}$  to  $\{C\}$ . Using (4.1) one verifies that

$$\mathbf{H}^{-1} \cong \mathbf{R} + \frac{\boldsymbol{\xi}_{\mathcal{C}} \mathbf{n}^\top}{d} \quad (4.8)$$

Depending on literature, either  $\mathbf{H}$  given by (4.7) or  $\mathbf{H}^{-1}$  given by (4.8) is referred to as **Homography**. The first definition (i.e. (4.7)) is adopted in this thesis due to its direct use in our proposed HBVS control schemes.

Since a non-degenerate homography matrix  $\mathbf{H}$  (i.e.  $\det(\mathbf{H}) \neq 0$ ) is only defined up to a scale factor, it has 8 degrees of freedom while it has 9 entries. An additional constraint is thus required. Several possibilities have been proposed in literature. For instance, a simple constraint of fixing the third diagonal element of  $\mathbf{H}$  equal to 1 (i.e.  $h_{3,3} = 1$ ) is proposed in [26]. Another possibility consists in fixing the Frobenius norm of  $\mathbf{H}$  equal to 1 [26]. Finally, as any non-degenerate homography matrix is associated with a unique matrix  $\bar{\mathbf{H}} \in \text{SL}(3)$  by re-scaling  $\bar{\mathbf{H}} = \det(\mathbf{H})^{-\frac{1}{3}} \mathbf{H}$  such that  $\det(\bar{\mathbf{H}}) = 1$ , without loss of generality it can be assumed that  $\mathbf{H}$  is an element of  $\text{SL}(3)$  as originally proposed in [9].

Recall that the scale factor  $\gamma$  such that  $\mathbf{H} = \gamma \mathbf{R}^\top \left( \mathbf{I} - \frac{\boldsymbol{\xi}_{\mathcal{C}} \mathbf{n}^{\star\top}}{d^*} \right)$  is equal  $(d^*/d)^{\frac{1}{3}}$  and corresponds to the second singular value of  $\mathbf{H}$  [51].

The so-called ‘‘image’’ homography matrix  $\mathbf{H}_{img} \in \text{SL}(3)$  that maps pixel coordinates from  $\mathcal{A}$  to  $\mathcal{C}$  (i.e.  $\mathbf{p}_{img} \cong \mathbf{H}_{img} \mathbf{p}_{img}^*$ ) then satisfies  $\mathbf{H}_{img} = \mathbf{K} \mathbf{H} \mathbf{K}^{-1}$ .

Expression (4.6) provides the transformation by the homography  $\mathbf{H}$  of point-feature correspondences between two image frames. Analogously, one can find the transformation by  $\mathbf{H}$  of the correspondences of line features in [35] and conic features (i.e ellipses, hyperbolas) [30].

## 4.2 Existing feature-based homography estimation techniques

Classical algorithms for homography estimation taken from the computer vision community consist of computing the homography on a frame-by-frame basis by solving algebraic constraints related to correspondences of image features (points, lines, conics, contours, etc.) [26, 3, 37, 40, 14]. These algorithms only considered the homography as an incidental variable and were not focused on improving (or filtering) the homography over time. In recent years, advances have been made in homography estimation algorithms by exploiting the temporal correlation of data across a video sequence rather than

computing algebraically individual raw homography for each image. Powerful methodologies for nonlinear observer design on Lie groups (e.g. [53]) have been instrumental for the derivation of these algorithms.

A nonlinear observer was proposed in [52] based on the underlying structure of the Special Linear group  $SL(3)$ , which is isomorphic to the group of homographies [9]. Velocity information was exploited to interpolate across a sequence of images and improve the individual homography estimates. The observer, however, still requires individual image homographies (previously computed using an algebraic technique) as the feedback information. Thus, it needed both a classical homography algorithm and a temporal filter algorithm, and only functions if each pair of images provides sufficient features to algebraically compute a raw homography.

In order to overcome these drawbacks, the question of deriving an observer for a sequence of image homographies, which takes image point-feature correspondences directly as input has been considered [25, 34]. The previous observer is extended by also incorporating image line-feature correspondences (in addition to point-feature correspondences) directly as input in the design of observer innovation [33]. In line with this effort, conic-feature correspondences (i.e. non-degenerate second-order features such as ellipses and hyperbolas) are considered for the construction of observer innovation [30]. Without requiring any prior step for reconstruction of individual homographies for feeding the observer innovation, these algorithms are suitable for real-time applications using an embedded computer. In contrast with algebraic techniques, these observers are also well posed even when there is insufficient data for full reconstruction of a homography. In such situations, these algorithms continue to operate by incorporating available information and relying on propagation of prior estimates.

In this work, the experimental validations of homography-based visual servo control algorithms proposed in Chapters 5 and 6 have been performed using HomographyLab library<sup>3</sup> that implements in C++ the homography estimation observer proposed in [34]. This library allows for running in real time and sufficiently fast the homography estimation for control applications with a modest companion computer (for instance 10  $Hz$  with a Hardkernel XU-4 or 20  $Hz$  with an Nvidia Jetson Nano).

Thereafter, a classical algebraic algorithm and a state-of-the-art nonlinear observer on  $SL(3)$  for homography estimation that exploit the simplest feature correspondences – the point correspondences – are recalled for the purpose of understanding.

---

<sup>3</sup><http://homographylab.i3s.unice.fr/>

### 4.2.1 A classical algebraic algorithm of homography estimation

Homography estimation is a topic well developed and discussed in classical computer vision books [26, 69]. In this section, the so-called Direct Linear Transformation (DLT) method which employs point correspondences for homography estimation is briefly re-vised.

Given a set of four 2D to 2D point correspondences,  $\mathbf{p}_i \leftrightarrow \mathbf{p}_i^*$ , where  $\mathbf{p}_i^*$  (resp.  $\mathbf{p}_i^*$ ) is the re-normalized point of  $\mathbf{P}_i$  (resp.  $\mathbf{P}_i^*$ ), as shown in (4.5). Denote  $[u_i, v_i, w_i]^\top$  coordinates of  $\mathbf{p}_i$ . Equation (4.6) implies that  $\mathbf{p}_i \times (\mathbf{H}\mathbf{p}_i^*) = \mathbf{0}$  which in turn yields

$$\begin{bmatrix} \mathbf{0} & -w_i\mathbf{p}_i^{*\top} & v_i\mathbf{p}_i^{*\top} \\ w_i\mathbf{p}_i^{*\top} & \mathbf{0} & -u_i\mathbf{p}_i^{*\top} \\ -v_i\mathbf{p}_i^{*\top} & u_i\mathbf{p}_i^{*\top} & \mathbf{0} \end{bmatrix} \begin{bmatrix} \mathbf{h}_1 \\ \mathbf{h}_2 \\ \mathbf{h}_3 \end{bmatrix} = \mathbf{0} \quad (4.9)$$

with  $\mathbf{h}_j$  ( $j = 1, 2, 3$ ) the  $j^{\text{th}}$  column of  $\mathbf{H}$ . Equation (4.9) contains three equations, however only two of them are linearly independent. By omitting, for instance, the third equation, each point correspondence  $\mathbf{p}_i \leftrightarrow \mathbf{p}_i^*$  gives two equations in the entries of  $\mathbf{H}$  as

$$\begin{bmatrix} \mathbf{0} & -w_i\mathbf{p}_i^{*\top} & v_i\mathbf{p}_i^{*\top} \\ w_i\mathbf{p}_i^{*\top} & \mathbf{0} & -u_i\mathbf{p}_i^{*\top} \end{bmatrix} \begin{bmatrix} \mathbf{h}_1 \\ \mathbf{h}_2 \\ \mathbf{h}_3 \end{bmatrix} = \mathbf{0}$$

These equations have the form  $\mathbf{L}_i\mathbf{h} = \mathbf{0}$  where  $\mathbf{L}_i$  is a  $2 \times 9$  matrix and  $\mathbf{h} = [\mathbf{h}_1^\top \quad \mathbf{h}_2^\top \quad \mathbf{h}_3^\top]^\top$  the vector of 9 unknown entries of  $\mathbf{H}$ . From a set of four point correspondences on the observed plane, a set of 8 equations in form of  $\mathbf{L}\mathbf{h} = \mathbf{0}$  is obtained, where  $\mathbf{L}$  is the matrix of dimension  $8 \times 9$  obtained by stacking the rows of  $\mathbf{L}_i$  contributed from each correspondence. One observes that  $\mathbf{h} = \mathbf{0}$  is an obvious solution.

For a set of four consistent points (in the sense that all triplets of these four points are linearly independent),  $\mathbf{L}$  has rank 8, and thus with an additional constraint of the norm  $|\mathbf{h}| > 0$ , the obvious solution is avoided and  $\mathbf{h}$  is defined up to scale. For simplification, one can choose  $|\mathbf{h}| = 1$  which is equivalent to having the Frobenius norm of  $\mathbf{H}$  equal to 1.

Solving these algebraic equations on a frame-by-frame basis requires computation power. It can only be carried out if the number of point correspondence is not less than 4 and these point correspondences are consistent. Insufficient number of feature correspondence leads to calculation corruption. The above-presented algorithm is the basis of the `cv::findHomography` function of OpenCV<sup>4</sup>.

<sup>4</sup><https://docs.opencv.org/3.4.1/d9/dab/tutorial-homography.html>

## 4.2.2 A state-of-the-art nonlinear homography observer on $SL(3)$

The homography defined by (4.6) in this work maps Euclidean coordinates of the scene's points from  $\{\mathcal{A}\}$  to  $\{\mathcal{C}\}$ . In the reverse direction,  $\bar{\mathbf{H}} := \mathbf{H}^{-1}$  mapping Euclidean coordinates of the scene's points from  $\{\mathcal{C}\}$  to  $\{\mathcal{A}\}$  satisfies

$$\mathbf{p}_i^* \cong \bar{\mathbf{H}}\mathbf{p}_i \quad (4.10)$$

The re-normalized point  $\mathbf{p}_i$  is thus given by

$$\mathbf{p}_i = \frac{\bar{\mathbf{H}}^{-1}\mathbf{p}_i^*}{|\bar{\mathbf{H}}^{-1}\mathbf{p}_i^*|} \quad (4.11)$$

Since the determinant of  $\mathbf{H} \in SL(3)$  is equal to 1, the determinant of  $\bar{\mathbf{H}}$  is also equal to 1 and  $\bar{\mathbf{H}}$  thus also belongs to  $SL(3)$  – the set of all real valued  $3 \times 3$  matrices with unit determinant. The Lie-algebra  $\mathfrak{sl}(3)$  of  $SL(3)$  is the set of all real valued  $3 \times 3$  matrices with trace equal to zero. The adjoint operator is a mapping  $\text{Ad} : SL(3) \times \mathfrak{sl}(3) \rightarrow \mathfrak{sl}(3)$  defined by:

$$\text{Ad}_{\bar{\mathbf{H}}} \mathbf{X} := \bar{\mathbf{H}}\mathbf{X}\bar{\mathbf{H}}^{-1}, \quad \bar{\mathbf{H}} \in SL(3), \mathbf{X} \in \mathfrak{sl}(3).$$

In the sequel, basic ideas of observer design proposed in [34] for  $\bar{\mathbf{H}}$  on  $SL(3)$  based on direct point correspondence are recalled.

### 4.2.2.1 Observer on $SL(3)$ based on direct point correspondences

Consider the kinematics of  $SL(3)$  given by

$$\dot{\bar{\mathbf{H}}} = F(\bar{\mathbf{H}}, \mathbf{U}) := \bar{\mathbf{H}}\mathbf{U}, \quad \bar{\mathbf{H}}(0) \in SL(3) \quad (4.12)$$

with  $\mathbf{U} \in \mathfrak{sl}(3)$  the group velocity. To expose the underlying ideas of observer design, in this section we consider the simplified case where the group velocity  $\mathbf{U}$  is known. Assume that a set of  $n$  measurements  $\mathbf{p}_i = h(\bar{\mathbf{H}}, \mathbf{p}_i^*) \in \mathbb{P}^2, i = \{1 \dots n\}$  in form of (4.11) in the camera frame  $\{\mathcal{C}\}$  is available, where  $\mathbf{p}_i^* \in \mathbb{P}^2$  are constant and known.

In [34] it is verified that the kinematics (4.12) are right equivariant, the observer design framework proposed in [53] thus can be applied.

Assume that a set  $\mathcal{M}_n$  of  $n \geq 4$  vector directions  $\mathbf{p}_i^* \in \mathbb{P}^2$ , with  $i = \{1 \dots n\}$  contains a subset  $\mathcal{M}_4 \subset \mathcal{M}_n$  of 4 constant vector directions such that all vector triplets in  $\mathcal{M}_4$  are linearly independent. In this case,  $\mathcal{M}_n$  is called *consistent*.

Let  $\hat{\bar{\mathbf{H}}} \in SL(3)$  denote the estimate of  $\bar{\mathbf{H}}$ . Define the right group error  $\mathbf{E} := \hat{\bar{\mathbf{H}}}\bar{\mathbf{H}}^{-1} \in$

## 4.2. Existing feature-based homography estimation techniques

---

SL(3) and the output errors  $\mathbf{e}_i \in \mathbb{P}^2$ :

$$\mathbf{e}_i := \rho(\hat{\mathbf{H}}^{-1}, \mathbf{p}_i) = \frac{\hat{\mathbf{H}}\mathbf{p}_i}{|\hat{\mathbf{H}}\mathbf{p}_i|} = \frac{\mathbf{E}\mathbf{p}_i^*}{|\mathbf{E}\mathbf{p}_i^*|}.$$

The proposed observer takes the form

$$\dot{\hat{\mathbf{H}}} = \hat{\mathbf{H}}\mathbf{U} - \Delta(\hat{\mathbf{H}}, \mathbf{p})\hat{\mathbf{H}}, \quad \hat{\mathbf{H}}(0) \in \text{SL}(3) \quad (4.13)$$

where  $\Delta(\hat{\mathbf{H}}, \mathbf{p}) \in \mathfrak{sl}(3)$  is the innovation term designed as

$$\Delta(\hat{\mathbf{H}}, \mathbf{p}) = \left( \text{grad}_1 \mathcal{C}_{\hat{\mathbf{p}}}(\hat{\mathbf{H}}, \mathbf{p}) \right) \hat{\mathbf{H}}^{-1}$$

where  $\text{grad}_1$  is the gradient using a *right-invariant Riemannian metric* on SL(3) and the *right-invariant* cost function  $\mathcal{C}_{\hat{\mathbf{p}}}(\hat{\mathbf{H}}, \mathbf{p})$  exploiting the point correspondence is defined as

$$\mathcal{C}_{\hat{\mathbf{p}}}(\hat{\mathbf{H}}, \mathbf{p}) \triangleq \sum_{i=1}^n \frac{k_i}{2} \left| \frac{\hat{\mathbf{H}}\mathbf{p}_i}{|\hat{\mathbf{H}}\mathbf{p}_i|} - \mathbf{p}_i^* \right|^2$$

Straightforward computations then yield

$$\Delta(\hat{\mathbf{H}}, \mathbf{p}) = - \sum_{i=1}^n k_i \pi_{\mathbf{e}_i} \mathbf{p}_i^* \mathbf{e}_i^\top \quad (4.14)$$

with  $\pi_{\mathbf{x}} := (I - \mathbf{x}\mathbf{x}^\top)$ ,  $\forall \mathbf{x} \in \mathbb{S}^2$ .

It is verified that  $\Delta(\hat{\mathbf{H}}, \mathbf{p})$  is *right equivariant* and according to [53] the dynamics of the group error  $\mathbf{E}$  are autonomous and given by

$$\dot{\mathbf{E}} = -\Delta(\mathbf{E}, \mathbf{p}^*)\mathbf{E} \quad (4.15)$$

Furthermore, provided that the measurement set  $\mathcal{M}_n$  is consistent, the estimate  $\hat{\mathbf{H}}$  converges locally exponentially to  $\bar{\mathbf{H}}$  [34, Th. 1].

### 4.2.2.2 Observers with partially known group velocity

In previous section, it is assumed that the group velocity  $\mathbf{U}$  is known for the purpose of observer design. However, that assumption is not fully true in practice. The observer design with partial knowledge of the group velocity is thus recalled thereafter.

Consider a camera attached to the moving frame  $\{\mathcal{C}\}$  moving with kinematics

$$\begin{aligned}\dot{\mathbf{R}} &= \mathbf{R}\boldsymbol{\Omega}_\times \\ \dot{\boldsymbol{\xi}}_C &= \mathbf{R}\mathbf{V}_C\end{aligned}$$

viewing a stationary planar scene, where  $\boldsymbol{\Omega}$  and  $\mathbf{V}_C$  are the angular and linear velocities of  $\{\mathcal{C}\}$  with respect to  $\{\mathcal{A}\}$  expressed in  $\{\mathcal{C}\}$ , respectively. The group velocity  $\mathbf{U} \in \mathfrak{sl}(3)$  induced by the camera motion, and such that the dynamics of  $\hat{\mathbf{H}}$  are in the form (4.12), then satisfies [52, Lem. 5.3]

$$\mathbf{U} = \boldsymbol{\Omega}_\times + \frac{\mathbf{V}_C \mathbf{n}^\top}{d} - \frac{\mathbf{n}^\top \mathbf{V}_C}{3d} \mathbf{I}$$

Note that the group velocity  $\mathbf{U}$  induced by camera motion depends on the additional variables  $\mathbf{n}$  and  $d$  that define the scene geometry at time  $t$  as well as the scale factor  $\gamma$ . Since these variables are unmeasurable and cannot be extracted directly from the measurements, one rewrites

$$\mathbf{U} = \boldsymbol{\Omega}_\times + \boldsymbol{\Gamma} = \boldsymbol{\Omega}_\times + \boldsymbol{\Gamma}_1 - \frac{1}{3} \text{tr}(\boldsymbol{\Gamma}_1) \mathbf{I} \quad (4.16)$$

with  $\boldsymbol{\Gamma} \triangleq \frac{\mathbf{V}_C \mathbf{n}^\top}{d} - \frac{\mathbf{n}^\top \mathbf{V}_C}{3d} \mathbf{I}$  and  $\boldsymbol{\Gamma}_1 \triangleq \frac{\mathbf{V}_C \mathbf{n}^\top}{d}$ .

Since  $\{\mathcal{A}\}$  is stationary by assumption, the vector  $\boldsymbol{\Omega}$  can be directly obtained from the set of embedded gyroscopes. Assume that the unknown part  $\boldsymbol{\Gamma}$  (resp.  $\boldsymbol{\Gamma}_1$ ) is constant or slowly time varying. In practice, instead of the group velocity  $\mathbf{U}$ , only the angular velocity  $\boldsymbol{\Omega}$  is measured, then an additional observer for estimating the unknown part  $\boldsymbol{\Gamma}$  (resp.  $\boldsymbol{\Gamma}_1$ ) of the group velocity  $\mathbf{U}$  is employed.

The observer when  $\frac{\dot{\boldsymbol{\xi}}_C}{d}$  is constant (e.g., the situation in which the camera moves with a constant velocity parallel to the scene or converges exponentially towards it) is chosen as follows (compare to (4.13))

$$\begin{cases} \dot{\hat{\mathbf{H}}} &= \hat{\mathbf{H}}(\boldsymbol{\Omega}_\times + \hat{\boldsymbol{\Gamma}}) - \boldsymbol{\Delta}(\hat{\mathbf{H}}, \mathbf{p})\hat{\mathbf{H}} \\ \dot{\hat{\boldsymbol{\Gamma}}} &= \hat{\boldsymbol{\Gamma}}\boldsymbol{\Omega}_\times - \boldsymbol{\Omega}_\times \hat{\boldsymbol{\Gamma}} - k_I \text{Ad}_{\hat{\mathbf{H}}^\top} \boldsymbol{\Delta}(\hat{\mathbf{H}}, \mathbf{p}) \end{cases} \quad (4.17)$$

and the observer when  $\frac{\mathbf{V}}{d}$  is constant (e.g., the situation in which the camera follows a circular trajectory over the scene or performs an exponential convergence towards it) is defined as follows

$$\begin{cases} \dot{\hat{\mathbf{H}}} &= \hat{\mathbf{H}} \left( \boldsymbol{\Omega}_\times + \hat{\boldsymbol{\Gamma}}_1 - \frac{1}{3} \text{tr}(\hat{\boldsymbol{\Gamma}}_1) \mathbf{I} \right) - \boldsymbol{\Delta}(\hat{\mathbf{H}}, \mathbf{p})\hat{\mathbf{H}} \\ \dot{\hat{\boldsymbol{\Gamma}}}_1 &= \hat{\boldsymbol{\Gamma}}_1 \boldsymbol{\Omega}_\times - k_I \text{Ad}_{\hat{\mathbf{H}}^\top} \boldsymbol{\Delta}(\hat{\mathbf{H}}, \mathbf{p}) \end{cases} \quad (4.18)$$

### 4.3. Discussions on existing HBVS controllers

---

with some positive gain  $k_I$  and  $\Delta(\hat{\mathbf{H}}, \mathbf{p})$  given by (4.14).

The assumption of the consistency of  $\mathcal{M}_n$  with  $n \geq 4$  guarantees the convergence of the estimate  $\hat{\mathbf{H}}$  to  $\bar{\mathbf{H}}$ . This condition is equivalent to the geometric constraint that requires at least 4 point-correspondences to fully reconstruct the 8 degrees of freedom of the homography using algebraic techniques as discussed in Section 4.2.1.

The homography observers (4.15), (4.17) and (4.18) exploit directly point correspondences in the innovation term  $\Delta(\hat{\mathbf{H}}, \mathbf{p})$ , thereby depleting the need of reconstruction of individual image homographies. This mechanism thus may save considerable computational resources, making the proposed algorithm suitable for embedded systems with simple feature tracking software. Another practical advantage in comparison with classical algebraic techniques is that the proposed algorithm is well posed even when there is insufficient data (*i.e.* less than 4 point correspondences) for full reconstruction of homography. In such situations while algebraic algorithms stop working, the observers proposed in [34] continue to operate by incorporating available information and relying on propagation of prior estimates.

### 4.3 Discussions on existing HBVS controllers

With the assumption of planar visual target and by using monocular camera as sensor modality, one can estimate homography and use it for control design purposes.

#### 4.3.1 HBVS kinematic controllers based on homography decomposition

In this section we first briefly recall the well known  $2\frac{1}{2}D$  visual servoing technique proposed by Malis et al. [55].

- Assume that the planar stationary target is textured enough so that the “image” homography matrix  $\mathbf{H}_{img}$  can be estimated using either feature-based or dense-based algorithms. Assume also that the camera calibration matrix  $\mathbf{K}$  is precisely calibrated so that the Euclidean homography matrix can be determined as follows

$$\mathbf{H} (= \mathbf{R}^\top + \frac{\mathbf{R}^\top \bar{\boldsymbol{\xi}}_C \mathbf{n}^{*\top}}{d^*}) = \frac{\mathbf{K}^{-1} \mathbf{H}_{img} \mathbf{K}}{\gamma} \quad (4.19)$$

where the scale factor  $\gamma$  is equal to the second singular value of  $\mathbf{K}^{-1} \mathbf{H}_{img} \mathbf{K}$ .

- Using homography decomposition techniques [56],  $\mathbf{H}$  can be decomposed into the rotation matrix  $\mathbf{R}^\top$  and a matrix  $\bar{\boldsymbol{\xi}}_C \mathbf{n}^{*\top}$  with  $\bar{\boldsymbol{\xi}}_C = \frac{\mathbf{R}^\top \bar{\boldsymbol{\xi}}_C}{d^*}$  from which one may be able to further decompose into  $\bar{\boldsymbol{\xi}}_C$  and  $\mathbf{n}^*$ .
- Denote  $\mathbf{P} \triangleq [X \ Y \ Z]^\top$  and  $\mathbf{P}^* \triangleq [X^* \ Y^* \ Z^*]^\top$  the 3D coordinates expressed in

$\{\mathcal{C}\}$  and  $\{\mathcal{A}\}$ , respectively, of a reference point  $P$  in the visual target. Let  $\mathbf{m} \triangleq [x \ y \ 1]^\top = [\frac{X}{Z} \ \frac{Y}{Z} \ 1]^\top$  and  $\mathbf{m}^* \triangleq [\frac{X^*}{Z^*} \ \frac{Y^*}{Z^*} \ 1]^\top$  denote the normalized coordinates of the point  $P$  corresponding to  $\{\mathcal{C}\}$  and  $\{\mathcal{A}\}$ , respectively. It has been proved that

$$\frac{Z}{Z^*} = \rho \frac{\mathbf{n}^{*\top} \mathbf{m}^*}{\mathbf{n}^\top \mathbf{m}} \quad (4.20)$$

with  $\rho \triangleq \frac{d}{d^*} = \det(\mathbf{H})$ .

- By introducing an extended image coordinates  $\mathbf{m}_e$  that link  $[x \ y]$  and  $[X \ Y \ Z]$  as follows

$$\mathbf{m}_e \triangleq [x \ y \ z]^\top = \left[ \frac{X}{Z} \ \frac{Y}{Z} \ \ln(Z) \right]^\top \quad (4.21)$$

with  $z = \ln(Z)$  is a supplementary normalized coordinate, Malis et al. derived the following kinematic relation

$$\dot{\mathbf{m}}_e = \begin{bmatrix} \frac{1}{d^*} \mathbf{L}_v & \mathbf{L}_{v,w} \end{bmatrix} \begin{bmatrix} \mathbf{V}_C \\ \boldsymbol{\Omega} \end{bmatrix} \quad (4.22)$$

with

$$\mathbf{L}_v \triangleq \frac{1}{\rho_1} \begin{bmatrix} -1 & 0 & x \\ 0 & -1 & y \\ 0 & 0 & -1 \end{bmatrix}, \quad \mathbf{L}_{v,w} \triangleq \begin{bmatrix} xy & -(1+x^2) & y \\ 1+y^2 & -xy & -x \\ -y & x & 0 \end{bmatrix}, \quad \rho_1 \triangleq \frac{Z}{d^*}$$

Expression (4.22) represents the relation between the position of a chosen reference point w.r.t the camera velocities expressed in current frame  $\{\mathcal{C}\}$ . Since the image point  $P$  is fixed in  $\{\mathcal{A}\}$ , (4.22) is used to indirectly control the position of the camera w.r.t the target image.

- The control of the orientation of the camera w.r.t the target image is more trivial since the rotation matrix  $\mathbf{R}$  can be calculated by homography decomposition. Denote  $\mathbf{u}$  and  $\theta$  are rotation axis and rotation angle obtained from  $\mathbf{R}$ , respectively. It is proved that

$$\frac{d(\mathbf{u}\theta)}{dt} = \begin{bmatrix} \mathbf{0} & \mathbf{L}_w \end{bmatrix} \begin{bmatrix} \mathbf{V}_C \\ \boldsymbol{\Omega} \end{bmatrix} \quad (4.23)$$

with the Jacobian matrix  $\mathbf{L}_w$  defined by

$$\mathbf{L}_w \triangleq \mathbf{I}_3 - \frac{\theta}{2} \mathbf{u}_\times + \left( 1 - \frac{\text{sinc}(\theta)}{\text{sinc}^2(\frac{\theta}{2})} \right) (\mathbf{u}_\times)^2, \quad \text{with } \text{sinc}(\theta) \triangleq \frac{\sin(\theta)}{\theta} \quad (4.24)$$

- The positioning task is described as the regulation to zero of the task function

$$\mathbf{e} \triangleq \begin{bmatrix} \mathbf{m}_e - \mathbf{m}_e^* \\ \theta \mathbf{u} \end{bmatrix} \quad (4.25)$$

with the reference  $\mathbf{m}_e^* \triangleq [x^* \ y^* \ z^*]^\top = \left[ \frac{X^*}{Z^*} \ \frac{Y^*}{Z^*} \ \ln(Z^*) \right]^\top$  and

$$\mathbf{m}_e - \mathbf{m}_e^* = \left[ x - x^* \quad y - y^* \quad \ln\left(\frac{Z}{Z^*}\right) \right]^\top$$

The first two components of  $\mathbf{m}_e - \mathbf{m}_e^*$  are directly calculated from the current and reference images whereas the third one is estimated using (4.20).

In view of (4.22) and (4.23), the time derivative of the task function (4.25) is related to the camera velocities by

$$\dot{\mathbf{e}} = \mathbf{L} \begin{bmatrix} \mathbf{V}_C \\ \boldsymbol{\Omega} \end{bmatrix}, \quad \text{with } \mathbf{L} \triangleq \begin{bmatrix} \frac{1}{d^*} \mathbf{L}_v & \mathbf{L}_{v,w} \\ \mathbf{0} & \mathbf{L}_w \end{bmatrix} \quad (4.26)$$

- The kinematic control law for the objective of exponential stabilization of  $\mathbf{e}$  to zero has been proposed

$$\begin{bmatrix} \mathbf{V}_C \\ \boldsymbol{\Omega} \end{bmatrix} = -\lambda \hat{\mathbf{L}}^{-1} \mathbf{e} \quad (4.27)$$

where  $\hat{\mathbf{L}}^{-1}$  is an approximation of  $\mathbf{L}^{-1}$ ,  $\lambda$  is a positive number used for tuning the convergence rate. Denote  $\hat{d}^*$  the estimate of  $d^*$  and from the fact that  $\mathbf{L}_w^{-1} \mathbf{u} \theta = \mathbf{u} \theta$ , the control law (4.27) is finally given by

$$\begin{bmatrix} \mathbf{V}_C \\ \boldsymbol{\Omega} \end{bmatrix} = -\lambda \begin{bmatrix} \hat{d}^* \mathbf{L}_v^{-1} & -\hat{d}^* \mathbf{L}_v^{-1} \mathbf{L}_{u,w} \\ \mathbf{0} & \mathbf{I}_3 \end{bmatrix} \mathbf{e} \quad (4.28)$$

Some significant attributes of this  $2\frac{1}{2}D$  visual servoing technique are discussed next.

- The advantage of the extended image coordinates  $\mathbf{m}_e$  expressed in (4.21) is that it links the coordinates in the 3D space with the image space (2D), and because of this the visual servoing technique is called  $2\frac{1}{2}D$ .
- The rotational control is decoupled from translational one.
- The kinematic equation (4.26) when applying kinematic control law (4.28) and the

fact that  $\mathbf{L}_w^{-1}\mathbf{u}\theta = \mathbf{u}\theta$  (in view of (4.24)) results in

$$\dot{\mathbf{e}} = -\lambda \begin{bmatrix} \frac{\hat{d}^*}{d^*} & \left(1 - \frac{\hat{d}^*}{d^*}\right) \\ 0 & 1 \end{bmatrix} \mathbf{e} \quad (4.29)$$

The equilibrium  $\mathbf{e} = \mathbf{0}$  of System (4.29) is exponentially stable even when  $\hat{d}^*$  is poorly estimated, showing a certain robustness of this kinematic  $2\frac{1}{2}D$  visual servo controller.

- The estimation of  $\rho_1 (= \frac{\rho}{\mathbf{n}^\top \mathbf{m}})$  and  $\ln(\frac{Z}{Z^*}) = \ln(\rho \frac{\mathbf{n}^{*\top} \mathbf{m}^*}{\mathbf{n}^\top \mathbf{m}})$  can be carried out only if the knowledge of the normal vector  $\mathbf{n}$  and  $\mathbf{n}^*$  is available, for instance, from homography decomposition. However, precisely estimating  $\mathbf{n}$  and  $\mathbf{n}^*$  from homography decomposition is quite challenging in practice due to noise influence. For instance, in case of station keeping it is desirable that  $(\mathbf{R}, \boldsymbol{\xi}_C)$  is stabilized about  $(\mathbf{I}, \mathbf{0})$ . However, when the camera approaches the desired position, the normal vector  $\mathbf{n}^*$  (and  $\mathbf{n}$ ) from homography decomposition can be poorly estimated due to measurement noise and is degenerate when  $\boldsymbol{\xi}_C = \mathbf{0}$ . The dependence of the Jacobian matrix  $\mathbf{L}_v$  and the visual error  $\ln(\frac{Z}{Z^*})$  on the normal vector estimates thus renders this kinematic  $2\frac{1}{2}D$  visual servo controller extremely sensitive to measurement noise especially in a close neighborhood of the desired position. This drawback yields an evident interest of developing HBVS controllers without relying on homography decomposition as initially led by Malis and his former student [8].

The  $2\frac{1}{2}D$  technique of Malis et al. [55] is a milestone in the history of visual servo control. Hereafter, several control works for underwater vehicles based on that technique are briefly recalled and discussed.

In [47], Lots et al. applied this kinematic control to perform station-keeping task where the validation experiments were carried out in a test tank using a Cartesian robot emulating two d.o.f of the ROV ANGUS 003. The bottom of the test tank emulates the seabed and is considered as unmarked target. By using a sparse feature tracker, some points on the target are tracked for homography estimation. The camera is rigidly mounted at the *CG* of the vehicle and pointing downwards such that the vehicle's body  $\vec{e}_3^b$  axis and the camera's optical axis coincide. Since the target plane is horizontal and the vehicle's  $\vec{e}_3^b$ -axis is always parallel with the inertial  $\vec{e}_3^a$ -axis, relation (4.20) can be simplified as  $\frac{Z}{Z^*} = \rho = \det(\mathbf{H})$  and the rotation axis  $\mathbf{u}$  is equal to  $[0 \ 0 \ 1]^\top$ . The last component of visual error  $(\mathbf{m}_e - \mathbf{m}_e^*)$  in (4.3.1) is thus equal to  $\ln(\det(\mathbf{H}))$ . Since the vehicle having 4 controllable d.o.f namely surge, sway, heave and heading (*i.e* yaw), the authors proposed a modified control scheme by discarding roll and pitch control inputs,

### 4.3. Discussions on existing HBVS controllers

---

resulting in a modified version of the Jacobian matrix  $\mathbf{L}$

$$\dot{\mathbf{e}} = \mathbf{L} \begin{bmatrix} \mathbf{V}_C \\ \Omega_3 \end{bmatrix}, \text{ where } \mathbf{L} \triangleq \begin{bmatrix} -\frac{1}{Z} & 0 & \frac{x}{Z} & y \\ 0 & -\frac{1}{Z} & \frac{y}{Z} & -x \\ 0 & 0 & -\frac{1}{Z} & 0 \\ 0 & 0 & 0 & 0 \\ 0 & 0 & 0 & 0 \\ 0 & 0 & 0 & 1 \end{bmatrix}_{6 \times 4} \quad (4.30)$$

In order to render the scheme robust to disturbances, Lots et al. replaced the original error variable by a composition of proportional, derivative and integral terms, resulting in the following kinematic control law

$$\begin{bmatrix} \mathbf{V}_C \\ \Omega_3 \end{bmatrix} = -\mathbf{\Lambda} \hat{\mathbf{L}}^+ \left( \mathbf{K}_p \mathbf{e} + \mathbf{K}_d \dot{\mathbf{e}} + \mathbf{K}_i \int_0^t \mathbf{e} dt \right) \quad (4.31)$$

with  $\mathbf{\Lambda} \in \mathbb{R}^{4 \times 4}$ ,  $\mathbf{K}_p, \mathbf{K}_d, \mathbf{K}_i \in \mathbb{R}^{6 \times 6}$  positive diagonal matrices and  $\hat{\mathbf{L}}^+ \in \mathbb{R}^{4 \times 6}$  the pseudo-inverse of the estimated Jacobian  $\hat{\mathbf{L}}$  which requires the knowledge of the initial depth  $Z^*$ . However, the authors did not provide any stability analysis for that control law.

In the later work [48] also with the assumption that the target plane is horizontal and the vehicle's  $\vec{e}_3^b$ -axis is always parallel with the inertial  $\vec{e}_3^a$ -axis, Lots et al. proposed a more simplified control solution. In more detail, the depth  $Z$  is estimated as  $Z = \det(\mathbf{H})Z^*$  with the initial depth  $Z^*$  assumed to be known. However, the depth control is not explicitly explained and presented. While discarding roll and pitch control, and considering that the heading (*i.e* yaw) can be independently and directly controlled in view of (4.30), the authors argue that the control problem can be restricted to two degrees of freedom, equivalently to a 2D visual servoing. By denoting  $\bar{\mathbf{e}}$  a simplified visual error vector containing only the first two components of  $\mathbf{e}$  defined in (4.25), it is verified that

$$\dot{\bar{\mathbf{e}}} = \begin{bmatrix} -\frac{1}{Z} & 0 \\ 0 & -\frac{1}{Z} \end{bmatrix} \begin{bmatrix} V_{C1} \\ V_{C2} \end{bmatrix} \quad (4.32)$$

The authors consider the simplified dynamics of the vehicle on the horizontal plane

$$M_{11} \dot{V}_{C1} = B_{11}(V_{C1} - V_{f1})(|V_{C1} - V_{f1}| + D_1) + \alpha_1 \beta + \alpha_2 |\beta| \quad (4.33a)$$

$$M_{22} \dot{V}_{C2} = B_{22}(V_{C2} - V_{f2})(|V_{C2} - V_{f2}| + D_2) + \alpha_3 \gamma \quad (4.33b)$$

with  $M_{ii}$  ( $i = 1, 2$ ) the mass matrix coefficients;  $B_{ii}$  ( $i = 1, 2$ ),  $D_1$  and  $D_2$  the hydro-

dynamic drag coefficients;  $V_{f1}$  and  $V_{f2}$  the components of sea current expressed in the body-fixed frame. The normalized control input of the two back thrusters is  $\beta \in [-1, 1]$ ; the normalized control input of the sway thrusters is  $\gamma \in [-1, 1]$ ;  $\alpha_i$  ( $i = 1, 2$ ) are the thrusters' efficient coefficients. Using the decoupled dynamics (4.33), the authors then propose the following PID control law

$$\begin{bmatrix} \beta \\ \gamma \end{bmatrix} = \begin{bmatrix} -Z & 0 \\ 0 & -Z \end{bmatrix} \left( \mathbf{K}_p \bar{\mathbf{e}} + \mathbf{K}_d \dot{\bar{\mathbf{e}}} + \mathbf{K}_i \int_0^t \bar{\mathbf{e}} dt \right) \quad (4.34)$$

with  $\mathbf{K}_p, \mathbf{K}_d, \mathbf{K}_i \in \mathbb{R}^{2 \times 2}$  positive diagonal matrices. Although the authors exploit the vehicle dynamics, and actually the proposed control forces (4.34) are calculated based on visual error  $\bar{\mathbf{e}}$ , no stability analysis is provided when incorporating the kinematic relation (4.32) with vehicle dynamics (4.33). The experiments were again carried out in a test tank and on a Cartesian robot emulating two d.o.f of the ROV ANGUS 003 using unmarked natural target and is reported as successful under artificial disturbances.

Besides the lack of rigorous stability analysis in [47, 48], it worth noting that either the derivative term  $\dot{\mathbf{e}}$  involved in (4.31) or  $\dot{\bar{\mathbf{e}}}$  involved in (4.34) requires numerical derivative of  $\mathbf{e}$  or  $\bar{\mathbf{e}}$  and may be very noisy due to high noise level and low frequency of homography measurements. It is noted that the experiment setup only allows for visual servoing at 5 Hz.

Similarly to the previously cited work [48], Van der Zwaan et al. [78] proposed a decoupled control scheme between station keeping in the horizontal plane and depth control. While the former task is almost identical to 2D visual servoing in [48], the later one is explicitly introduced. The depth controller is designed based on the partial information obtained from homography matrix. In fact the depth scale factor  $\rho$  ( $= d/d^*$ ) satisfies

$$\rho = \det \begin{bmatrix} h_{11} & h_{12} \\ h_{21} & h_{22} \end{bmatrix} \quad (4.35)$$

By using  $\rho$  as feedback information for depth control (in fact, the authors have used  $s = \sqrt{\rho}$  maybe by error), the desired vertical velocity in form of PID terms is given analogously to (4.31). In addition, the authors propose a method to enhance tracker system by using optical flow information in prediction phase. The experiments were performed with positive results, first on an unmanned blimp in laboratory environment and then on a hover-capable ROV in the open sea.

In [11], Brignone et al. proposed a fully autonomous docking technique for an underwater vehicle [1]. The task includes two phases. In the first one, a passive acoustic marker and sonar are used for identifying the docking station on the seabed from dis-

### 4.3. Discussions on existing HBVS controllers

---

tance up to 50  $m$ . In the second one when the vehicle approaches the docking station at a visual range (about 2  $m$  to 3  $m$ ), a controller based directly on  $2\frac{1}{2}D$  visual servoing technique [55] is employed. A downward-looking camera with optical axis parallel to vehicle's body  $\vec{e}_3^b$ -axis is used for that purpose. Even the thrusters' configuration is not explicitly presented, it can be guessed that the vehicle is fully actuated. For guiding the vehicle to vertically align with the docking structure, the simplified visual error  $\bar{\mathbf{e}}$  that contains only the first two components of  $\mathbf{e}$  (defined in (4.25)) is used. The expression (4.26) can be simplified as

$$\dot{\bar{\mathbf{e}}} = \mathbf{L} \begin{bmatrix} \mathbf{V}_C \\ \boldsymbol{\Omega} \end{bmatrix}, \text{ with } \mathbf{L}(x, y, Z) \triangleq \begin{bmatrix} -\frac{1}{Z} & 0 & \frac{x}{Z} & xy & -(1+x^2) & y \\ 0 & -\frac{1}{Z} & \frac{y}{Z} & 1+y^2 & -xy & -x \end{bmatrix}$$

The kinematic control law for the objective of exponential stabilization of  $\bar{\mathbf{e}}$  to zero was propose as follows

$$\begin{bmatrix} \mathbf{V}_C \\ \boldsymbol{\Omega} \end{bmatrix} = -\lambda \mathbf{L}^+(x^*, y^*, Z^*) \bar{\mathbf{e}} \quad (4.36)$$

Here, instead of choosing the pseudo-inverse of the Jacobian  $\mathbf{L}$  for  $(x, y, Z)$  (i.e.  $\mathbf{L}^+(x, y, Z)$ ), a simplified choice  $\mathbf{L}^+(x^*, y^*, Z^*)$  is adopted in (4.36). The authors argue that even though this convenient simplification may have implications, the stability of the equilibrium  $\bar{\mathbf{e}} = \mathbf{0}$  can still be successfully achieved because of the slow dynamic response of the hovering vehicle. The controller has been tested in a pool with checkerboards placed in the bottom. The overall visual servoing algorithm was performed on a embedded computer at 12  $Hz$ .

**Remark 2.** *The  $2\frac{1}{2}D$  visual servoing technique in [55] that is proposed for a general case of a visual target requires the estimates of the normal vector (i.e.  $\mathbf{n}^*$  and  $\mathbf{n}$ ) for establishing the Jacobian matrix term  $\mathbf{L}_v$  and the visual error  $\ln(\frac{Z}{Z^*})$ . As discussed above, this can be problematic for station keeping task since  $\mathbf{n}^*$  (and  $\mathbf{n}$ ) calculated from homography decomposition can be strongly effected by noise or even degenerate. However, in underwater works [47, 48, 78, 11], only a particular case is considered when the textured target plane is horizontal, the vehicle's body  $\vec{e}_3^b$ -axis, the camera's optical axis and the inertial  $\vec{e}_3^a$ -axis are parallel. This configuration results in trivial relations  $\mathbf{n} = \mathbf{n}^* = [0 \ 0 \ 1]^T$  and consequently  $Z = d$ ,  $Z^* = d^*$ ,  $\frac{Z}{Z^*} = \det(\mathbf{H})$ . The estimate of  $Z$  and consequently  $\mathbf{L}_v$  depends only on the estimate of  $d^*$ . The main drawback of  $2\frac{1}{2}D$  visual servoing technique thus can be avoided. However, it can be seen from this scenario that the proposed technique has considerable limitation in practical application. Above all, the requirement of the visual target to be horizontal seems restrictive in reality.*

### 4.3.2 HBVS kinematic controllers without homography decomposition

All the aforementioned works [55, 47, 48, 78, 11] in the previous section are based on homography decomposition that often requires much computational resource and is sensitive to measurement noise [56]. For avoiding these practical issues, an advanced HBVS approach without relying on homography decomposition has been proposed by Benhmane and Malis in [8]. This *kinematic* control approach consists in using  $(\mathbf{V}_C, \boldsymbol{\Omega})$  as control inputs to stabilize the visual errors  $\mathbf{e}_p, \mathbf{e}_\Theta \in \mathbb{R}^3$  to zero, where these errors are directly computed from the homography matrix  $\mathbf{H} = \mathbf{R}^\top + \frac{\mathbf{R}^\top \boldsymbol{\xi}_C \mathbf{n}^{\star\top}}{d^*}$  as follows

$$\mathbf{e}_p \triangleq (\mathbf{I}_3 - \mathbf{H})\mathbf{m}^*, \quad \mathbf{e}_\Theta \triangleq \text{vex}(\mathbf{H}^\top - \mathbf{H}), \quad (4.37)$$

with  $\mathbf{m}^* \in \mathbb{S}^2$  an arbitrary unit vector satisfying  $\mathbf{n}^{\star\top} \mathbf{m}^* > 0$ . Denote  $\mathbf{V}_C$  the vector of coordinates (expressed in  $\{\mathcal{C}\}$ ) of the linear velocity of the camera  $C$ . The derivatives of  $\mathbf{H}$  satisfies

$$\dot{\mathbf{H}} = -\boldsymbol{\Omega} \times \mathbf{H} - \frac{1}{d^*} \mathbf{V}_C \mathbf{n}^{\star\top} \quad (4.38)$$

It is shown in [8] that the following kinematic controller

$$\mathbf{V}_C = -k_p \mathbf{e}_p, \quad \boldsymbol{\Omega} = -k_\Theta \mathbf{e}_\Theta \quad (4.39)$$

with positive gains  $k_p$  and  $k_\Theta$  ensures the local exponential stability of the equilibrium  $(\mathbf{R}, \boldsymbol{\xi}_C) = (\mathbf{I}_3, \mathbf{0})$ , i.e.  $\mathbf{H} = \mathbf{I}_3$ .

### 4.3.3 HBVS dynamical controllers without homography decomposition

The presented controllers in Section 4.3.1 and 4.3.2 (except for [48]) are kinematic based. However, for mechanical systems such as AUVs, dynamical model should be taken into account while forces and torques should be used as control inputs instead of the linear and angular velocities. In this section we recall a prior work on this topic of the I3S-OSCAR team [44]. For discussion purposes, the following simplified dynamical system is considered

$$\begin{cases} \dot{\mathbf{V}}_C = \mathbf{F}_c \\ \dot{\boldsymbol{\Gamma}} = \boldsymbol{\Gamma}_c \end{cases} \quad (4.40)$$

with  $\mathbf{F}_c, \boldsymbol{\Gamma}_c \in \mathbb{R}^3$  control variables. This dynamical system can be controlled to stabilize  $\mathbf{V}_C$  and  $\boldsymbol{\Omega}$  at any smooth reference values  $\mathbf{V}_{Cr}$  and  $\boldsymbol{\Omega}_r$  as long as the derivatives  $\dot{\mathbf{V}}_{Cr}$  and  $\dot{\boldsymbol{\Omega}}_r$  are at our disposal, by the following proportional controller

$$\begin{cases} \mathbf{F}_c = -k_V(\mathbf{V}_C - \mathbf{V}_{Cr}) + \dot{\mathbf{V}}_{Cr} \\ \boldsymbol{\Gamma}_c = -k_\Omega(\boldsymbol{\Omega} - \boldsymbol{\Omega}_r) + \dot{\boldsymbol{\Omega}}_r \end{cases} \quad (4.41)$$

### 4.3. Discussions on existing HBVS controllers

---

with positive gains  $k_V$  and  $k_\Omega$ . It is not difficult to verify that the equilibrium  $(\mathbf{V}_C, \boldsymbol{\Omega}) = (\mathbf{V}_{C_r}, \boldsymbol{\Omega}_r)$  of the controlled system is globally exponential stable.

Continuing to exploit the visual errors  $\mathbf{e}_p, \mathbf{e}_\Theta$  defined in (4.37), in view of (4.39), it is logical to define the reference velocities as

$$\begin{cases} \mathbf{V}_{C_r} = -k_p \mathbf{e}_p \\ \boldsymbol{\Omega}_r = -k_\Theta \mathbf{e}_\Theta \end{cases} \quad (4.42)$$

and apply controller (4.41) to System (4.38)+(4.41) in order to ensure the stability of the equilibrium  $(\mathbf{H}, \mathbf{V}_C, \boldsymbol{\Omega}) = (\mathbf{I}, \mathbf{0}, \mathbf{0})$ . However, since the derivative of  $\mathbf{e}_p$  and  $\mathbf{e}_\Theta$  are not computable by the controller due to the unknown quantities  $\mathbf{n}^*$  and  $d^*$ , it is impossible to compute the feed-forward terms  $\dot{\mathbf{V}}_{C_r}$  and  $\dot{\boldsymbol{\Omega}}_r$  involved in (4.41). A popular and practical solution to this issue consists in neglecting the uncomputable terms  $\dot{\mathbf{V}}_{C_r}$  and  $\dot{\boldsymbol{\Omega}}_r$  in (4.41), i.e. setting  $\dot{\mathbf{V}}_{C_r} = \dot{\boldsymbol{\Omega}}_r = \mathbf{0}$ . In [44] the stability analysis for System (4.38)+(4.41) with the ‘‘hierarchical’’ PD(proportional- derivative)-controller is developed. The proposed hierarchical PD-controller

$$\mathbf{F}_c = -k_V(\mathbf{V}_C - \mathbf{V}_{C_r}), \quad \boldsymbol{\Gamma}_c = -k_\Omega(\boldsymbol{\Omega} - \boldsymbol{\Omega}_r) \quad (4.43)$$

with  $\mathbf{V}_{C_r}$  and  $\boldsymbol{\Omega}_r$  defined by (4.42) and positive gains  $k_p, k_\Theta, k_V, k_\Omega$  ensures the local exponential stability (LES) of the equilibrium  $(\mathbf{H}, \mathbf{V}_C, \boldsymbol{\Omega}) = (\mathbf{I}, \mathbf{0}, \mathbf{0})$  of the controlled system.

The control design and associated stability analysis of the hierarchical PD-controller (4.43) are carried out on a local basis. It is thus difficult to characterize its domain of attraction. For underwater vehicles whose translational and rotational dynamics are nonlinear and strongly coupled due to added mass effects (see Chapter 3), this controller may not guarantee an acceptable performance.

In order to overcome such local stability property, in [44] the authors proposed a HBVS dynamical control approach relying on the classical inner-outer loop strategy, such that the inner loop stabilizes the linear and angular velocities  $\mathbf{V}_C, \boldsymbol{\Omega}$  to any smooth reference values  $\mathbf{V}_{C_r}, \boldsymbol{\Omega}_r$ , provided that  $\dot{\mathbf{V}}_{C_r}, \dot{\boldsymbol{\Omega}}_r$  are computable, while the outer loop makes use of  $\mathbf{V}_{C_r}, \boldsymbol{\Omega}_r$  as intermediate control variables to stabilize  $\mathbf{H}$  about  $\mathbf{I}_3$  (or equivalently, stabilize  $(\mathbf{e}_p, \mathbf{e}_\Theta)$  about zero) to fulfill the visual servoing control objective. Since the vehicle dynamics is fully actuated, the inner loop control objective can be achieved without too much difficulty. The interested readers are recommended to read the details of inner-loop control design in [44]. The design of the outer loop which is more important for our discussion will thus be recalled thereafter.

First, the design of reference linear velocity  $\mathbf{V}_{C_r}$  is presented. It is verified that the

derivative of visual error  $\mathbf{e}_p$  satisfies

$$\dot{\mathbf{e}}_p = -\boldsymbol{\Omega} \times (\mathbf{e}_p - \mathbf{m}^*) + a^* \mathbf{V}_C \quad (4.44)$$

with  $a^* \triangleq \frac{(\mathbf{n}^{*\top} \mathbf{e}_3)}{d^*}$  an unknown number. However, we know that it is positive using the condition  $\mathbf{n}^{*\top} \mathbf{m}^* > 0$ . For the purpose of  $\mathbf{V}_{Cr}$  design, the authors introduce the adaptive scalar dynamics

$$\dot{z}_p = \mathbf{e}_p^\top (\boldsymbol{\Omega} \times \mathbf{m}^*), \quad z_p(0) \in \mathbb{R} \quad (4.45)$$

and the following augmented dynamics

$$\dot{\hat{\mathbf{e}}}_p = -\boldsymbol{\Omega} \times \hat{\mathbf{e}}_p - k_{p2}(\hat{\mathbf{e}}_p - \mathbf{e}_p), \quad \hat{\mathbf{e}}_p(0) \in \mathbb{R}^3, \quad k_{p2} > 0 \quad (4.46)$$

It is assumed that the reference angular velocity  $\boldsymbol{\Omega}_r$  and its derivative are bounded and computable by the inner loop controller, and the inner loop controller ensures the global asymptotical stability and local exponential stability of the equilibrium  $(\mathbf{V}_C, \boldsymbol{\Omega}) = (\mathbf{V}_{Cr}, \boldsymbol{\Omega}_r)$ . Then, by considering visual error dynamics (4.44), employing the augmented system (4.45)+(4.46), and introducing the following reference linear velocity used by the inner loop controller:

$$\mathbf{V}_{Cr} = -k_p \hat{\mathbf{e}}_p - z_p \boldsymbol{\Omega}_r \times \mathbf{m}^* \quad (4.47)$$

it is shown that there exists a positive number  $\kappa_p$  such that if  $\frac{k_{p2}}{k_{p1}} > \kappa_p$  so that  $\mathbf{e}_p$  is globally stabilized about zero [44, Propo. 1].

**Remark 3.** *In the particular case where  $\mathbf{m}^*$  is chosen parallel to  $\mathbf{u}$  (for example in the case where  $\mathbf{u} = \mathbf{e}_3$  (gravity direction) and  $\mathbf{m}^* = \mathbf{e}_3$  (downward-looking camera observing a seafloor)), the adaptive term  $z_p$  given in (4.45) can be neglected in the outer-loop controller  $\mathbf{V}_{Cr}$  defined by (4.47) so that the latter can be simplified to*

$$\mathbf{V}_{Cr} = -k_{p1} \hat{\mathbf{e}}_p, \quad k_{p1} > 0$$

and  $\hat{\mathbf{e}}_p$  is the solution of the following equation (instead of (4.46))

$$\dot{\hat{\mathbf{e}}}_p = -\omega_r \mathbf{u} \times \hat{\mathbf{e}}_p - k_{p2}(\hat{\mathbf{e}}_p - \mathbf{e}_p), \quad k_{p2} > 0$$

It can be proved that the global asymptotic stability of  $\mathbf{e}_p = \mathbf{0}$  no longer requires any condition on  $k_{p1}$  and  $k_{p2}$  [44, Rem. 7].

Second, the design of reference angular velocity  $\boldsymbol{\Omega}_r$  to ensure the convergence of  $\mathbf{e}_\Theta$  is recalled. By exploiting visual error  $\mathbf{e}_\Theta$  while introducing the following dynamics

$$\dot{\boldsymbol{\Omega}}_r = -k_{\Theta 2} \boldsymbol{\Omega}_r - k_{\Theta 1} \text{sat}^{\Delta\omega}(\mathbf{e}_\Theta), \quad \boldsymbol{\Omega}_r(0) \in \mathbb{R}^3, \quad (4.48)$$

### 4.3. Discussions on existing HBVS controllers

---

with positive numbers  $k_{\Theta 1}, k_{\Theta 2}$  and  $\Delta_\omega$ , it is stated that the equilibrium  $(\mathbf{H}, \mathbf{V}_C, \boldsymbol{\Omega}) = (\mathbf{I}_3, \mathbf{0}, \mathbf{0})$  of the controlled system is locally asymptotically stable (LAS). Furthermore, there exists a positive number  $\underline{k}_{\Theta 1}$  such that if  $k_{\Theta 1} \leq \underline{k}_{\Theta 1}$  then the equilibrium  $(\mathbf{H}, \mathbf{V}_C, \boldsymbol{\Omega}) = (\mathbf{I}_3, \mathbf{0}, \mathbf{0})$  is LES [44, Propo. 2].

Although convergence of the visual error  $\mathbf{e}_p$  to zero is global, the visual error variable  $\mathbf{e}_\Theta$  is only locally stabilized about zero. For obtaining a stronger stability result, the authors [44] proposed an enhanced design of the reference angular velocity (instead of (4.48))

$$\boldsymbol{\Omega}_r \triangleq k_u \mathbf{u} \times \mathbf{R}^\top \mathbf{u} + \omega_r \mathbf{u} \quad (4.49)$$

where  $\mathbf{u} \in \mathbb{S}^2$  a known inertial unit vector, which is assumed to be measured in the vehicle body-fixed frame  $\{\mathcal{B}\}$ , is employed for control design. In practice,  $\mathbf{u}$  can be the gravity direction that can be obtained from accelerometer measurements. The inner-loop control is thus re-designed correspondingly to ensure not only the convergence of  $(\mathbf{V}_C, \boldsymbol{\Omega})$  to  $(\mathbf{V}_{Cr}, \boldsymbol{\Omega}_r)$  but also the convergence of  $\mathbf{R}^\top \mathbf{u}$  to  $\mathbf{u}$ .

It is verified that for any  $\mathbf{u} \in \mathbb{S}^2$ , there exists a well-defined rotation matrix  $\mathbf{R}_u \in \text{SO}(3)$  such that  $\mathbf{R}_u \mathbf{u} = \mathbf{e}_3$ . Define a matrix  $\bar{\mathbf{H}} \triangleq \mathbf{R}_u \mathbf{H} \mathbf{R}_u^\top$  and  $\bar{h}_{12}$  the element at the intersection of the first row and second column of  $\bar{\mathbf{H}}$ . The information embedded in  $\bar{h}_{12}$  then is used for design  $\omega_r$  term included in (4.49) as follows

$$\dot{\omega}_r = -k_{\Theta 2} \omega_r - k_{\Theta 1} \text{sat}^{\Delta_\omega}(\bar{h}_{12}), \quad \omega_r(0) \in \mathbb{R}. \quad (4.50)$$

Assuming that inner loop controller ensures the almost global asymptotical stability and local exponential stability of the equilibrium  $(\mathbf{V}_C, \boldsymbol{\Omega}, \mathbf{R}^\top \mathbf{u}) = (\mathbf{V}_{Cr}, \boldsymbol{\Omega}_r, \mathbf{u})$ , it is proved that by applying the reference translational velocity  $\mathbf{V}_{Cr}$  (4.47) and the reference rotational velocity  $\boldsymbol{\Omega}_r$  (4.49) where  $\omega_r$  is defined by (4.50), there exist some positive numbers  $\bar{k}_\Theta$  and  $\bar{\Delta}_\omega$  such that for all positive numbers  $k_{\Theta 1}, k_{\Theta 2}, \Delta_\omega$  satisfying  $k_{\Theta 2}/\sqrt{k_{\Theta 1}}$  and  $\Delta_\omega > \bar{\Delta}_\omega$  the homography matrix  $\mathbf{H}$  is stabilized about  $\mathbf{I}_3$  for almost all initial conditions [44, Theo. 1].

So far, [44] establishes a dynamical control approach in the form of inner-outer loop control scheme for fully-actuated AUVs. In the outer loop level, visual errors  $\mathbf{e}_p, \mathbf{e}_\Theta$  computed directly from homography matrix without the need of homography decomposition are employed to stabilize  $\mathbf{H}$  about  $\mathbf{I}_3$ . In the inner loop level, the vehicle nonlinear dynamics are taken into account. In addition to the estimated homography, implementing these controllers requires measurements of the linear and angular velocities which can be obtained from a DVL and an IMU, respectively. In practice, while IMUs are relatively inexpensive, the cost of the cheapest DVL exceeds €15,000 per item. DVLs are thus unaffordable for underwater vehicle projects with a limited budget. Their large dimensions and high weight also limit the possibility of mounting them into small size

underwater vehicles, for instance man-portable ones. Moreover, many applications such as intervention and high-resolution imaging for inspection require the vehicle to operate in close proximity to man-made structure. However, at a close distance less than 1 *m* DVL measurements are very imprecise. For these reasons, there is an obvious need of advanced vision-based control techniques without relying on linear velocity measurements. This constitutes the main motivation of our works presented in Chapters 5 and 6.

### 4.3. Discussions on existing HBVS controllers

---

# 5

## **Dynamic HBVS control of fully-actuated AUVs without linear velocity measurements: the case of downward-looking camera**

**T**HIS chapter establishes a novel inertial-aided homography-based dynamic control approach of fully-actuated AUVs without relying on linear velocity measurements. A particular application of the proposed approach concerns the capability of maintaining the AUV at a desired pose during a long period (i.e. station-keeping).

This chapter is structured into seven sections. Problem formulation of HBVS control of fully-actuated AUVs is provided in Section 5.1. Section 5.2 presents a simplified control model. Basic ideas of control design are explained in Section 5.3. In Section 5.4 the novel dynamic HBVS control approach is proposed. Comparative simulation results conducted on a realistic AUV model are reported in Section 5.5 illustrating the performance and robustness of the proposed approach. Section 5.6 first describes the experimental setup and then reports extensive experimental validation results in a real

## 5.1. Problem formulation

environment. Three video links are also provided showing these experimental results. Section ?? presents prospective extensions of the proposed control approach.

### 5.1 Problem formulation

Assume that the AUV, equipped with a downward-looking monocular camera, operates sufficiently close to a (near) planar textured seafloor. To perform the station-keeping task, a reference image of the seafloor is first taken at a desired pose. Then, the visual servoing controller must stabilize the AUV about the desired pose by exploiting information encoded in both the current and reference images.

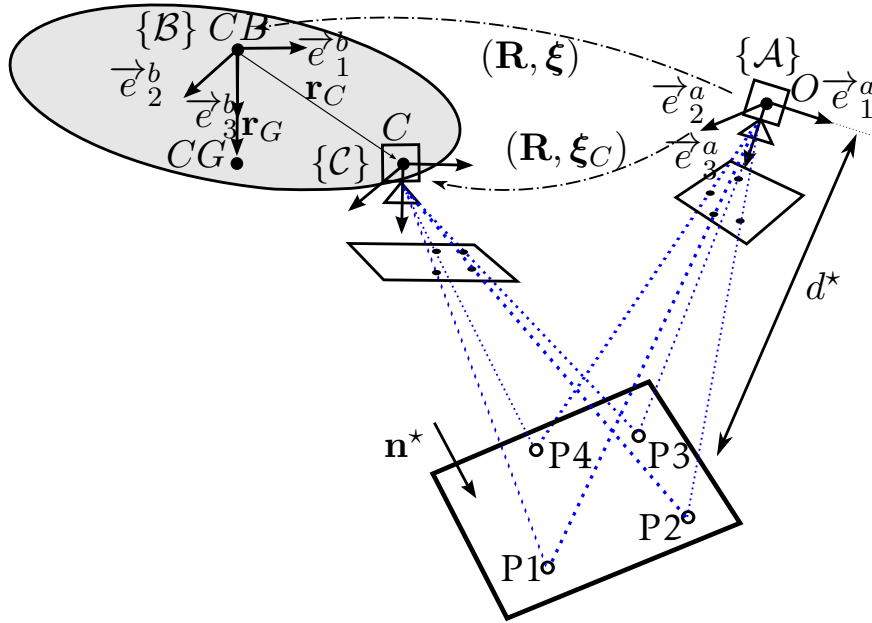


Figure 5.1: An AUV with a downward-looking camera and notation

Let us define the inertial frame  $\{A\}$  attached to the camera's desired pose as depicted in Fig. 5.1. Assume that the estimation of the homography  $\mathbf{H} = \mathbf{R}^\top + \frac{\mathbf{R}^\top \xi_C \mathbf{n}^{*\top}}{d^*} \in \mathbb{R}^{3 \times 3}$  between the current image and the reference image is available for control design. Such a homography matrix contains coupled information about the rotation and translation between the current camera frame  $\{C\}$  and the inertial  $\{A\}$ . Recall that the derivative of  $\mathbf{H}$  satisfies (4.38).

In addition to the estimate of  $\mathbf{H}$ , (approximate) measurements of the angular velocity  $\Omega$  and of the gravity direction  $\mathbf{R}^\top \mathbf{e}_3$  provided by an IMU are also available for control design.

The considered control objective consists in asymptotically stabilizing  $\mathbf{H}$  about  $\mathbf{I}_3$ , which is equivalent to the stabilization of  $(\mathbf{R}, \xi_C)$  about  $(\mathbf{I}_3, \mathbf{0})$ . Main difficulties for con-

trol design are related to the unknown quantities  $d^*$  and  $\mathbf{n}^*$  involved in the expression (4.7) of the homography  $\mathbf{H}$ , the coupled rotation and translation transformations encoded in  $\mathbf{H}$ , and last but not least the unavailability of linear velocity measurements (i.e. DVL is not used). For future use, let us denote

$$\begin{bmatrix} h_{11} & h_{12} & h_{13} \\ h_{21} & h_{22} & h_{23} \\ h_{31} & h_{32} & h_{33} \end{bmatrix} \triangleq \mathbf{H} \quad (5.1)$$

and  $\mathbf{R}_\psi$  the rotation matrix around AUV's axis  $\vec{e}_3^b$  as

$$\mathbf{R}_\psi \triangleq \begin{bmatrix} \cos \psi & -\sin \psi & 0 \\ \sin \psi & \cos \psi & 0 \\ 0 & 0 & 1 \end{bmatrix} \quad (5.2)$$

## 5.2 Simplified model for control design

The translational and rotational dynamics (3.23a)-(3.23b) are tightly coupled due to the coupling matrix  $\Xi$  involved in the definition (3.5) of the momentum terms. These complex dynamic couplings are often neglected in the literature by neglecting all terms involving  $\Xi$  using the fact that the considered AUV is compact and the distance between the CB and CG is relatively small. Moreover, since the linear velocity is not measured, the ‘‘Munk moment’’  $(\mathbf{M}\mathbf{V}_h) \times \mathbf{V}_h$  is here considered as a disturbance. Finally, all terms involving unknown current velocity  $\mathbf{V}_f$ , together with the damping force and torque, are also considered as disturbances. These considerations result in the following simpler dynamic equations that decouple the translational and rotational dynamics:

$$\mathbf{M}\dot{\mathbf{V}} = (\mathbf{M}\mathbf{V}) \times \boldsymbol{\Omega} + \mathbf{F}_c + \mathbf{F}_{gb} + \boldsymbol{\Delta}_F \quad (5.3a)$$

$$\mathbf{J}\dot{\boldsymbol{\Omega}} = (\mathbf{J}\boldsymbol{\Omega}) \times \boldsymbol{\Omega} + \boldsymbol{\Gamma}_c + \boldsymbol{\Gamma}_g + \boldsymbol{\Delta}_\Gamma \quad (5.3b)$$

with the ‘‘disturbance’’ terms

$$\begin{aligned} \boldsymbol{\Delta}_F &\triangleq -(\mathbf{M}\mathbf{V}_f) \times \boldsymbol{\Omega} - \mathbf{M}\boldsymbol{\Omega} \times \mathbf{V}_f + (\Xi^\top \boldsymbol{\Omega}) \times \boldsymbol{\Omega} - \Xi^\top \dot{\boldsymbol{\Omega}} + \mathbf{F}_d \\ \boldsymbol{\Delta}_\Gamma &\triangleq (\Xi \mathbf{V}_h) \times \boldsymbol{\Omega} + \mathbf{P}_h \times \mathbf{V}_h - \Xi \dot{\mathbf{V}}_h + \boldsymbol{\Gamma}_d \end{aligned}$$

In the case of station keeping,  $\boldsymbol{\Delta}_F$  and  $\boldsymbol{\Delta}_\Gamma$  would eventually converge to constant vectors. In the sequel, these terms will be first neglected in the derivation of a basic controller, which later on will be robustified via both integral correction actions and a high-gain observer of  $\boldsymbol{\Delta}_\Gamma$ .

**Remark 4.** *Assumption that  $\boldsymbol{\Delta}_F$  and  $\boldsymbol{\Delta}_\Gamma$  are constant seems to be restrictive but we have demonstrated via simulation and experimental results that such an assumption is reasonably*

acceptable.

### 5.3 Basic ideas of control design

For illustrating the main idea of control design, let us consider the following simple system:

$$\begin{cases} \dot{\mathbf{e}}_p = a^* \mathbf{V} \\ \dot{\mathbf{V}} = \mathbf{u} \end{cases} \quad (5.4)$$

with  $\mathbf{e}_p \in \mathbb{R}^3$  available for control design,  $a^*$  a positive **unknown** constant, and  $\mathbf{u} \in \mathbb{R}^3$  control input.

Let us first assume that  $\mathbf{V}$  is available for control design. Since  $a^*$  is positive, the following controller

$$\mathbf{u} = -k_1 \mathbf{e}_p - k_2 \mathbf{V}; \quad k_1, k_2 > 0$$

results in a stable closed-loop system  $\ddot{\mathbf{e}}_p + k_2 \dot{\mathbf{e}}_p + a^* k_1 \mathbf{e}_p = 0$ .

Another possible solution is reminiscent of the one discussed in Remark 3 in Chapter 4. Since System (5.4) is in cascade form, the control design can be carried out with an inner-outer loop control architecture.

- The inner-loop controller, governing the dynamics  $\dot{\mathbf{V}} = \mathbf{u}$ , is given by  $\mathbf{u} = -k_3(\mathbf{V} - \mathbf{V}_r) + \dot{\mathbf{V}}_r$  with  $k_3 > 0$  provided that  $\dot{\mathbf{V}}_r$  is computable. Global exponential stability of  $\mathbf{V}$  about any smooth reference velocity  $\mathbf{V}_r$  is ensured in view of the resulting closed-loop system  $\dot{\mathbf{V}} - \dot{\mathbf{V}}_r = -k_3(\mathbf{V} - \mathbf{V}_r)$ .
- The outer-loop controller, governing the kinematic  $\dot{\mathbf{e}}_p = a^* \mathbf{V}$ , defines the reference velocity  $\mathbf{V}_r = -k_2 \hat{\mathbf{e}}_p$  with  $k_2 > 0$  and an augmented system

$$\dot{\hat{\mathbf{e}}}_p = -k_1(\hat{\mathbf{e}}_p - \mathbf{e}_p); \quad \hat{\mathbf{e}}_p(0) \in \mathbb{R}^3; \quad k_1 > 0 \quad (5.5)$$

The resulting outer-loop system can be written as

$$\begin{cases} \dot{\mathbf{e}}_p = -a^* k_2 \hat{\mathbf{e}}_p + \varepsilon(t) \\ \dot{\hat{\mathbf{e}}}_p = k_1 \mathbf{e}_p - k_1 \hat{\mathbf{e}}_p \end{cases} \quad (5.6)$$

with  $\varepsilon(t) \triangleq a^*(\mathbf{V} - \mathbf{V}_r)$  an exponentially vanishing term as a result of the inner-loop controller. System (5.6) can be rewritten in the following particular time-varying cascaded interconnection studied by Panteley and Loria [67]:

$$\dot{\mathbf{x}}_1 = \mathbf{f}_1(t, \mathbf{x}_1) + \mathbf{G}\mathbf{x}_2 \quad (5.7)$$

where  $\mathbf{x}_1 = [\mathbf{e}_p^\top, \hat{\mathbf{e}}_p^\top]^\top$ ,  $\mathbf{x}_2 = \varepsilon$ , the function  $\mathbf{f}_1(t, \mathbf{x}_1)$  can be easily deduced, and

$\mathbf{G}$  is a constant matrix composed of 0 and 1 in our case. System (5.7) can be seen as a nominal system  $\dot{\mathbf{x}}_1 = \mathbf{f}_1(t, \mathbf{x}_1)$  perturbed by the output  $\mathbf{x}_2$  of an exponentially stable system. In view of [67, Theorem 3] corresponding to the case where the function  $\mathbf{f}_1(t, \mathbf{x}_1)$  grows faster than  $\mathbf{G}$ , it suffices to prove that the nominal system  $\dot{\mathbf{x}}_1 = \mathbf{f}_1(t, \mathbf{x}_1)$  (i.e. setting  $\varepsilon(t) \equiv 0$  in (5.6)) is uniformly globally asymptotically stable. This system is clearly uniformly globally asymptotically stable by studying its characteristic polynomial given by  $P(\lambda) = (\lambda^2 + k_1\lambda + a^*k_1k_2)^3$ .

However, in the case when  $\mathbf{V}$  is unavailable for control design, the aforementioned inner-outer loop control architecture is not applicable. In order to overcome this issue, let us keep using the augmented variable  $\hat{\mathbf{e}}_p$  specified in (5.5) and propose the following controller

$$\mathbf{u} = k_2(\hat{\mathbf{e}}_p - \mathbf{e}_p) - k_3\mathbf{e}_p, \quad k_2, k_3 > 0 \quad (5.8)$$

The global asymptotical stability of the equilibrium  $(\hat{\mathbf{e}}_p, \mathbf{e}_p, \mathbf{V}) = (\mathbf{0}, \mathbf{0}, \mathbf{0})$  of System (5.4)+(5.5) can be pointed out by examining the following Lyapunov function

$$\mathcal{L} = \frac{1}{2}|\hat{\mathbf{e}}_p - \mathbf{e}_p|^2 + \frac{k_3}{2k_2}|\mathbf{e}_p|^2 + \frac{a^*}{2k_2}|\mathbf{V}|^2$$

whose derivative satisfies

$$\dot{\mathcal{L}} = -k_1|\hat{\mathbf{e}}_p - \mathbf{e}_p|^2 \leq 0$$

It is interesting that even though  $a^*$  is an unknown constant and the measurement of  $\mathbf{V}$  is not available, one can still stabilize  $\mathbf{e}_p$  about zero by employing the augmented variable  $\hat{\mathbf{e}}_p$  (5.5) and the controller (5.8).

In the following section, the control design for performing station keeping of underwater vehicle equipped with a downward-looking camera observing (nearly) planar textured seabed will be presented. The outer-loop controller for the stabilization of the visual error  $\mathbf{e}_p$  about zero will be established based on the above-presented basic idea.

## 5.4 Control design

By analogy to the cascade inner-outer loop control architecture proposed in [44], the following modified version (illustrated by Fig. 5.2) handling the unavailability of linear velocity measurements is adopted:

- An inner-loop controller, governing the rotation dynamics (3.2) and (5.3b), defines the torque control vector  $\mathbf{\Gamma}_c$  to ensure the asymptotic stabilization of  $(\mathbf{\Omega}, \mathbf{R}^\top \mathbf{e}_3)$  about  $(\mathbf{\Omega}_r, \mathbf{e}_3)$ , where the reference angular velocity  $\mathbf{\Omega}_r$  is defined by

$$\mathbf{\Omega}_r \triangleq k_g \mathbf{e}_3 \times \mathbf{R}^\top \mathbf{e}_3 + \omega_{3r} \mathbf{e}_3 \quad (5.9)$$

## 5.4. Control design

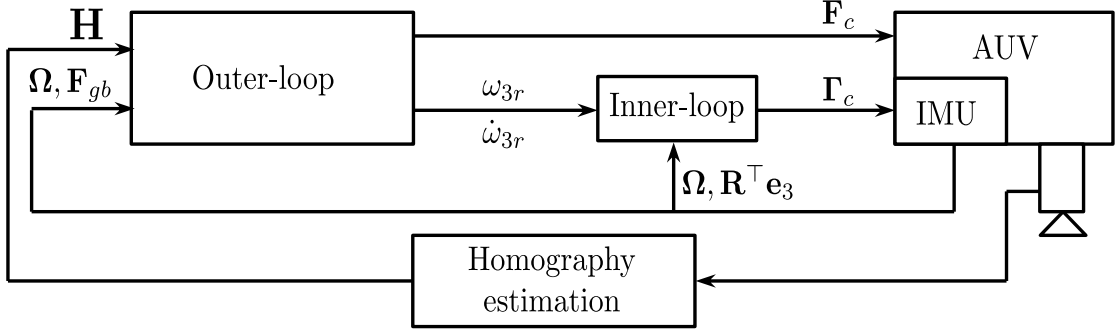


Figure 5.2: Control architecture of the proposed HBVS

with  $k_g > 0$  positive gain and  $\omega_{3r} \in \mathbb{R}$  the reference yaw angular velocity to be specified by the outer-loop controller. Note that  $\dot{\omega}_{3r}$  must be computable so that the feedforward term  $\dot{\Omega}_r$  is also computable by the torque controller.

- An outer-loop controller defines the force control vector  $\mathbf{F}_c$  together with the reference yaw angular velocity  $\omega_{3r}$  (for the inner-loop controller) to fulfill the main objective of stabilizing  $\mathbf{H}$  about  $\mathbf{I}_3$ , provided that the inner-loop controller ensures the almost global asymptotic stability (almost-GAS) and local exponential stability (LES) of the equilibrium  $(\boldsymbol{\Omega}, \mathbf{R}^\top \mathbf{e}_3) = (\boldsymbol{\Omega}_r, \mathbf{e}_3)$ .

The inner-loop control design is less involved and is postponed after the outer-loop control design, which is the main contribution of this thesis.

### 5.4.1 Outer-loop control design

#### 5.4.1.1 Force control design

Analogously to the control approach proposed in [44], the control design for stabilizing the visual error  $\mathbf{e}_p$  defined in (4.37) about zero is first carried out, but here without linear velocity measurements.

The angle between the target plane's normal vector and the camera axis at the desired pose should be smaller than  $90^\circ$ , which implies that  $\mathbf{n}^{*\top} \mathbf{e}_3 > 0$ . It follows that the simple choice  $\mathbf{m}^* = \mathbf{e}_3$  ensures the validity of the condition  $\mathbf{n}^{*\top} \mathbf{m}^* > 0$  without any prior knowledge of  $\mathbf{n}^*$ .

In view of (4.38) and (4.37) and using the choice  $\mathbf{m}^* = \mathbf{e}_3$ , the dynamics of  $\mathbf{e}_p$  satisfy

$$\dot{\mathbf{e}}_p = -\boldsymbol{\Omega} \times (\mathbf{e}_p - \mathbf{e}_3) + a^* \mathbf{V}_C \quad (5.10)$$

with  $a^* \triangleq \frac{(\mathbf{n}^{*\top} \mathbf{e}_3)}{d^*}$  an unknown number. However, we know that it is positive using the condition  $\mathbf{n}^{*\top} \mathbf{e}_3 > 0$ .

In order to handle the case with an arbitrary position of the camera w.r.t the CB in the control design, instead of  $\mathbf{V}$ , a modified velocity variable is employed:

$$\bar{\mathbf{V}} \triangleq \mathbf{V} + \omega_{3r} \mathbf{e}_3 \times \mathbf{r}_C \quad (5.11)$$

As a result of the inner-loop controller (to be designed thereafter) that ensures the exponential convergence of  $(\boldsymbol{\Omega}, \mathbf{R}^\top \mathbf{e}_3)$  to  $(\boldsymbol{\Omega}_r, \mathbf{e}_3)$ , one ensures that  $\boldsymbol{\Omega}$  converges to  $\omega_{3r} \mathbf{e}_3$ , which in turn implies that  $\mathbf{V}_C$  converges to  $\bar{\mathbf{V}}$  and  $\boldsymbol{\Omega} \times \mathbf{e}_3$  converges to zero. Therefore, (5.10) can be rewritten as

$$\dot{\mathbf{e}}_p = -\boldsymbol{\Omega} \times \mathbf{e}_p + a^* \bar{\mathbf{V}} + \boldsymbol{\varepsilon}(t) \quad (5.12)$$

with exponentially vanishing term  $\boldsymbol{\varepsilon}(t) \triangleq \boldsymbol{\Omega} \times \mathbf{m}^* + a^*(\mathbf{V}_C - \bar{\mathbf{V}})$ . On the other hand, using (5.3a) the dynamics of  $\bar{\mathbf{V}}$  verify

$$\begin{aligned} \mathbf{M} \dot{\bar{\mathbf{V}}} &= (\mathbf{M} \bar{\mathbf{V}}) \times \boldsymbol{\Omega} + \mathbf{F}_c + \mathbf{F}_{gb} + \boldsymbol{\Delta}_F \\ &\quad + \dot{\omega}_{3r} \mathbf{M}(\mathbf{e}_3 \times \mathbf{r}_C) - \omega_{3r} (\mathbf{M}(\mathbf{e}_3 \times \mathbf{r}_C)) \times \boldsymbol{\Omega} \\ &= (\mathbf{M} \bar{\mathbf{V}}) \times \boldsymbol{\Omega} + \bar{\mathbf{F}}_c + \mathbf{F}_{gb} + \boldsymbol{\Delta}_F + \boldsymbol{\varepsilon}_1(t) \end{aligned} \quad (5.13)$$

with new control force variable

$$\begin{aligned} \bar{\mathbf{F}}_c &\triangleq \mathbf{F}_c + \dot{\omega}_{3r} \mathbf{M}(\mathbf{e}_3 \times \mathbf{r}_C) - \omega_{3r}^2 (\mathbf{M}(\mathbf{e}_3 \times \mathbf{r}_C)) \times \mathbf{e}_3 \\ &= \mathbf{F}_c + (\dot{\omega}_{3r} \mathbf{I}_3 + \omega_{3r}^2 [\mathbf{e}_3]_\times) \mathbf{M}(\mathbf{e}_3 \times \mathbf{r}_C) \end{aligned} \quad (5.14)$$

and exponentially vanishing term

$$\boldsymbol{\varepsilon}_1(t) \triangleq -\omega_{3r} (\mathbf{M}(\mathbf{e}_3 \times \mathbf{r}_C)) \times (\boldsymbol{\Omega} - \omega_{3r} \mathbf{e}_3)$$

To expose the main ideas of control design, the outer-loop control design will be first carried out for the case where the disturbance term  $\boldsymbol{\Delta}_F$  involved in (5.13) is considered null, i.e.  $\boldsymbol{\Delta}_F \equiv \mathbf{0}$ . Then, we will show later on how to cope with external disturbances and model uncertainties via integral correction actions.

**Proposition 1.** *Consider system including the dynamics (5.12) of  $\mathbf{e}_p$  and translation dynamics given by (5.13) with  $\boldsymbol{\Delta}_F \equiv \mathbf{0}$ . Assume that the disturbance terms  $\boldsymbol{\varepsilon}(t)$  and  $\boldsymbol{\varepsilon}_1(t)$  remain bounded for all time and converge exponentially to zero. Introduce the augmented system*

$$\dot{\hat{\mathbf{e}}}_p = -\boldsymbol{\Omega} \times \hat{\mathbf{e}}_p - \mathbf{K}_1 \hat{\mathbf{e}}_p + \mathbf{K}_1 \mathbf{e}_p, \quad \hat{\mathbf{e}}_p(0) = \mathbf{e}_p(0) \quad (5.15)$$

with  $\mathbf{K}_1 \in \mathbb{R}^{3 \times 3}$  positive gain matrix. Assume that  $\boldsymbol{\Omega}$  remains bounded for all time. Apply the control force

$$\bar{\mathbf{F}}_c = \bar{m} \mathbf{M}^{-1} (\text{sat}^{\eta_1}(k_2 \tilde{\mathbf{e}}_p) - \text{sat}^{\eta_2}(k_3 \mathbf{e}_p)) - \mathbf{F}_{gb} \quad (5.16)$$

#### 5.4. Control design

with  $\bar{m}, k_2, k_3, \eta_1, \eta_2$  positive numbers, and  $\tilde{\mathbf{e}}_p \triangleq \hat{\mathbf{e}}_p - \mathbf{e}_p$ . Then, the equilibrium  $(\hat{\mathbf{e}}_p, \mathbf{e}_p, \bar{\mathbf{V}}) = (\mathbf{0}, \mathbf{0}, \mathbf{0})$  is globally asymptotically stable (GAS). Moreover,  $\bar{\mathbf{F}}_c$  remains bounded by

$$|\bar{\mathbf{F}}_c| \leq \bar{m} \lambda_{\mathbf{M}}^{-1} (\eta_1 + \eta_2) + |mg - F_b| \quad (5.17)$$

with  $\lambda_{\mathbf{M}}$  the smallest eigenvalue of  $\mathbf{M}$ .

**Proof.** The closed-loop system of system (5.12)+(5.13)+(5.15) can be rewritten in the following particular time-varying cascaded interconnection studied by Panteley and Loria [67]:

$$\dot{\mathbf{x}}_1 = \mathbf{f}_1(t, \mathbf{x}_1) + \mathbf{G}\mathbf{x}_2 \quad (5.18)$$

where  $\mathbf{x}_1 = [\hat{\mathbf{e}}_p^\top, \mathbf{e}_p^\top, \bar{\mathbf{V}}^\top]^\top$ ,  $\mathbf{x}_2 = [\varepsilon^\top, \varepsilon_1^\top]^\top$ , the function  $\mathbf{f}_1(t, \mathbf{x}_1)$  can be easily deduced, and  $\mathbf{G}$  is a constant matrix composed of 0 and 1 in our case. System (5.18) can be seen as a nominal system  $\dot{\mathbf{x}}_1 = \mathbf{f}_1(t, \mathbf{x}_1)$  perturbed by the output  $\mathbf{x}_2$  of a exponentially stable system. In view of [67, Theorem 3] corresponding to the case where the function  $\mathbf{f}_1(t, \mathbf{x}_1)$  grows faster than  $\mathbf{G}$ , it suffices to prove that the nominal system  $\dot{\mathbf{x}}_1 = \mathbf{f}_1(t, \mathbf{x}_1)$  (i.e. setting  $\varepsilon(t) \equiv 0$  in (5.12) and  $\varepsilon_1(t) \equiv 0$  in (5.13)) is uniformly globally asymptotically stable. This allows us to avoid using input-to-state stability (ISS) argument and, subsequently, the need of constructing of a strict Lyapunov function for the nominal system.

From (5.15) and (5.12) (with  $\varepsilon(t) \equiv \mathbf{0}$ ) one obtains

$$\dot{\tilde{\mathbf{e}}}_p = -\boldsymbol{\Omega} \times \tilde{\mathbf{e}}_p - \mathbf{K}_1 \tilde{\mathbf{e}}_p - a^* \bar{\mathbf{V}} \quad (5.19)$$

Consider the following Lyapunov function candidate

$$\mathcal{L} \triangleq \int_0^{|\tilde{\mathbf{e}}_p|} \text{sat}^{\eta_1}(k_2 s) ds + \int_0^{|\mathbf{e}_p|} \text{sat}^{\eta_2}(k_3 s) ds + \frac{a^*}{2\bar{m}} |\mathbf{M}\bar{\mathbf{V}}|^2 \quad (5.20)$$

One verifies that the time-derivative of  $\mathcal{L}$  along any solution to the controlled unperturbed system is

$$\begin{aligned} \dot{\mathcal{L}} &= -\text{sat}^{\eta_1}(k_2 \tilde{\mathbf{e}}_p)^\top \mathbf{K}_1 \tilde{\mathbf{e}}_p \\ &\quad - a^* \text{sat}^{\eta_1}(k_2 \tilde{\mathbf{e}}_p)^\top \bar{\mathbf{V}} + a^* \text{sat}^{\eta_2}(k_3 \mathbf{e}_p)^\top \bar{\mathbf{V}} \\ &\quad + a^* \bar{m}^{-1} (\mathbf{M}\bar{\mathbf{V}})^\top (\bar{\mathbf{F}}_c + \mathbf{F}_{gb}) \\ &= -\text{sat}^{\eta_1}(k_2 \tilde{\mathbf{e}}_p)^\top \mathbf{K}_1 \tilde{\mathbf{e}}_p \end{aligned} \quad (5.21)$$

From (5.21) one deduces that  $\dot{\mathcal{L}}$  is semi-negative definite and, thus,  $\tilde{\mathbf{e}}_p$ ,  $\mathbf{e}_p$ , and  $\bar{\mathbf{V}}$  remain bounded by initial conditions. One then easily verifies that  $\dot{\tilde{\mathbf{e}}}_p$  and  $\ddot{\tilde{\mathbf{e}}}_p$  also

remain bounded, implying the uniform continuity of  $\dot{\mathcal{L}}$ . Then, application of Barbalat's lemma [42] ensures the convergence of  $\dot{\mathcal{L}}$  and, thus, of  $\tilde{e}_p$  to zero. Then, from (5.19) and by application of the extended Barbalat's lemma [58] one also ensures the convergence of  $\dot{\tilde{e}}_p$  to zero, which in turn implies that  $\bar{\mathbf{V}}$  converges to zero. Similar arguments can be used to show the convergence of  $\dot{\bar{\mathbf{V}}}$  to zero. In view of (5.13) (with  $\Delta_F \equiv \mathbf{0}$ ),  $\varepsilon_1(t) \equiv \mathbf{0}$  and  $\bar{\mathbf{F}}_c$  given by (5.16), one ensures that  $\mathbf{e}_p$  converges to zero. The stability of the equilibrium  $(\mathbf{e}_p, \hat{\mathbf{e}}_p, \bar{\mathbf{V}}) = (\mathbf{0}, \mathbf{0}, \mathbf{0})$  is a direct consequence of (5.20) and (5.21). Finally, the bound of the force control vector  $\bar{\mathbf{F}}_c$  given by (5.17) is directly deduced from (5.16).  $\square$

**Remark 5.** In first order approximations, the force control  $\bar{\mathbf{F}}_c$  given by (5.16) is given by

$$\bar{\mathbf{F}}_c = k_2 \bar{m} \mathbf{M}^{-1} \hat{\mathbf{e}}_p - (k_2 + k_3) \bar{m} \mathbf{M}^{-1} \mathbf{e}_p - \mathbf{F}_{gb} \quad (5.22)$$

The proof of global asymptotic stability of the equilibrium  $(\hat{\mathbf{e}}_p, \mathbf{e}_p, \bar{\mathbf{V}}) = (\mathbf{0}, \mathbf{0}, \mathbf{0})$ , with  $\bar{\mathbf{F}}_c$  given by (5.22), proceeds analogously to the proof of Proposition 1. The linear approximation (5.22) of  $\bar{\mathbf{F}}_c$  is useful for gain tuning using, for instance, pole placement technique, while its nonlinear expression (5.16) that involves saturation functions allows us to define explicitly the bound of the force control input  $\bar{\mathbf{F}}_c$  as given by (5.17). The latter property is of particular importance in practice since it is often desirable to take explicitly actuation limitations into account. For instance, (5.17) implies that the desired bound of  $|\bar{\mathbf{F}}_c|$  can be set to any value  $\mu (> |mg - F_b|)$  if

$$\eta_1 + \eta_2 \leq \bar{m}^{-1} \underline{\lambda}_{\mathbf{M}} (\mu - |mg - F_b|)$$

Note that Proposition 1 applies to the case where the perturbation term  $\Delta_F$  is negligible. While this basic controller would be able to handle small currents, in practice it is often desirable to enhance control robustness by incorporating integral correction actions. However, in our case the system considered in Proposition 1 (i.e. (5.15)+(5.12)+(5.13)) is already a third-order time-varying system. Thus, adding an integrator would lead to a fourth-order time-varying system. Too high order system, together with the presence of an unknown multiplicative factor  $a^*$  in (5.12) and the unavailability of linear velocity measurements, excludes the possibility of establishing global (or semi-global) stability results similar to Proposition 1. However, it is still possible to state local exponential stability. For simplicity, let us consider the case where  $\mathbf{M}$  can be roughly approximated by a positive diagonal matrix, i.e.  $\mathbf{M} \approx \text{diag}(m_{1,1}, m_{2,2}, m_{3,3})$ .

**Proposition 2.** Consider system including dynamics of  $\mathbf{e}_p$  given by (5.12) and translation dynamics given by (5.13) with constant disturbance  $\Delta_F$  and diagonal total mass matrix  $\mathbf{M} = \text{diag}(m_{1,1}, m_{2,2}, m_{3,3})$ . Assume that the disturbance terms  $\varepsilon(t)$  and  $\varepsilon_1(t)$  remaining bounded

#### 5.4. Control design

for all time and converging exponentially to zero. Introduce the following integrator

$$\dot{\mathbf{z}} = -\boldsymbol{\Omega} \times \mathbf{z} + \mathbf{e}_p, \quad \mathbf{z}(0) \in \mathbb{R}^3 \quad (5.23)$$

and the following augmented system

$$\dot{\hat{\mathbf{e}}}_p = -\boldsymbol{\Omega} \times \hat{\mathbf{e}}_p - \mathbf{K}_1 \hat{\mathbf{e}}_p + \mathbf{K}_1 \bar{\mathbf{e}}_p, \quad \hat{\mathbf{e}}_p(0) = \mathbf{e}_p(0) \quad (5.24)$$

with positive diagonal matrix  $\mathbf{K}_1 \in \mathbb{R}^{3 \times 3}$  and  $\bar{\mathbf{e}}_p \triangleq \mathbf{e}_p + k_I \mathbf{z}$  with positive integral gain  $k_I$ . Apply the control force

$$\bar{\mathbf{F}}_c = \bar{m} \mathbf{M}^{-1} (\text{sat}^{\eta_1}(k_2 \tilde{\mathbf{e}}_p) - \text{sat}^{\eta_2}(k_3 \bar{\mathbf{e}}_p)) - \mathbf{F}_{gb} \quad (5.25)$$

with positive numbers  $\bar{m}$ ,  $k_2$ ,  $k_3$ ,  $\eta_1$ ,  $\eta_2$ , and  $\tilde{\mathbf{e}}_p \triangleq \hat{\mathbf{e}}_p - \bar{\mathbf{e}}_p$ . Choose  $\eta_2$  high enough such that

$$\eta_2 > \bar{m}^{-1} |\mathbf{M} \boldsymbol{\Delta}_F| \quad (5.26)$$

and choose  $k_I$  satisfying

$$k_I < \frac{k_2 \lambda_{\mathbf{K}_1}}{k_2 + k_3} \quad (5.27)$$

with  $\lambda_{\mathbf{K}_1}$  the smallest diagonal component of  $\mathbf{K}_1$ . Assume that the outer-loop control  $\omega_{3r}$  together with the inner-loop control  $\boldsymbol{\Gamma}_c$  ensures that  $\boldsymbol{\Omega}$  can be considered as a first order term in first order approximations. Then, the equilibrium  $(\hat{\mathbf{e}}_p, \mathbf{e}_p, \bar{\mathbf{V}}, \mathbf{z}) = (k_I \mathbf{z}^*, \mathbf{0}, \mathbf{0}, \mathbf{z}^*)$ , with  $\mathbf{z}^* \triangleq (\bar{m} k_3 k_I)^{-1} \mathbf{M} \boldsymbol{\Delta}_F$ , of the controlled system is locally exponentially stable (LES).

**Proof.** One verifies that the linearized system of Eqs. (5.12), (5.3a), (5.24) augmented with integrator (5.23) around the equilibrium  $(\hat{\mathbf{e}}_p, \mathbf{e}_p, \bar{\mathbf{V}}, \mathbf{z}) = (k_I \mathbf{z}^*, \mathbf{0}, \mathbf{0}, \mathbf{z}^*)$  is  $\dot{\mathbf{X}} = \mathbf{A} \mathbf{X}$  with  $\mathbf{X} \in \mathbb{R}^{12}$  and  $\mathbf{A} \in \mathbb{R}^{12 \times 12}$  given by

$$\mathbf{A} \triangleq \begin{bmatrix} -\mathbf{K}_1 & \mathbf{K}_1 & \mathbf{0} & k_I \mathbf{K}_1 \\ \mathbf{0} & \mathbf{0} & a^* \mathbf{M}^{-1} & \mathbf{0} \\ k_2 \bar{m} \mathbf{M}^{-1} & -(k_2 + k_3) \bar{m} \mathbf{M}^{-1} & \mathbf{0} & -k_I (k_2 + k_3) \bar{m} \mathbf{M}^{-1} \\ \mathbf{0} & \mathbf{I}_3 & \mathbf{0} & \mathbf{0} \end{bmatrix}$$

$$\mathbf{X} \triangleq [\hat{\mathbf{e}}_p^\top \quad \mathbf{e}_p^\top \quad (\mathbf{M} \bar{\mathbf{V}})^\top \quad \mathbf{z}^\top]^\top$$

One verifies from (5.3a) and (5.25) that at equilibrium configuration  $\mathbf{z}^* \triangleq (\bar{m} k_3 k_I)^{-1} \mathbf{M} \boldsymbol{\Delta}_F$ . Also from these equations, when  $\tilde{\mathbf{e}}_p = 0$ , if  $|k_2 \bar{\mathbf{e}}_p| \geq \eta_2$ , one deduces that  $\eta_2 = \bar{m}^{-1} |\mathbf{M} \boldsymbol{\Delta}_F|$ . Therefore, condition (5.26) is necessary so that the integral action can compensate for the disturbance  $\boldsymbol{\Delta}_F$ .

The 12th-order characteristic polynomial of the linearized system is  $Q(\lambda) = Q_1(\lambda) Q_2(\lambda) Q_3(\lambda)$ , with

$$Q_i(\lambda) = \lambda^4 + k_{1i}\lambda^3 + (k_2 + k_3)a^* \frac{\bar{m}}{m_{i,i}^2} \lambda^2 + (k_{1i}k_3 + (k_2 + k_3)k_I)a^* \frac{\bar{m}}{m_{i,i}^2} \lambda + k_{1i}k_3k_I a^* \frac{\bar{m}}{m_{i,i}^2}$$

with  $k_I$  satisfying (5.27). Application of Routh-Hurwitz criterion ensures the exponential stability of the linearized system.  $\square$

#### 5.4.1.2 Control design of the reference yaw angular velocity

The previous part of outer-loop control design ensures the convergence of  $\mathbf{e}_p$  to zero. From there, the design of  $\omega_{3r}$  can proceed identically to our prior work [44] and is, thus, recalled here for the sake of completeness.

Let  $\psi$  denote the AUV's yaw angle and  $\mathbf{R}_\psi$  the corresponding rotation matrix around AUV's axis  $\vec{e}_3^b$ . In view of (5.9), the designed angular velocity  $\boldsymbol{\Omega}_r$  includes two components. The first one (i.e.  $k_g \mathbf{e}_3 \times \mathbf{R}^\top \mathbf{e}_3$ ) is used for the convergence of  $\mathbf{R}^\top \mathbf{e}_3$  about  $\mathbf{e}_3$ , or equivalently roll and pitch angles about zero, in the inner-loop. Consequently, the designed control force  $\mathbf{F}_c$  in form of (5.16) or (5.25) stabilizes  $\mathbf{e}_p$  to zero or equivalently  $\boldsymbol{\xi}_C$  to zero, in the outer-loop. In view of the definition of homography matrix  $\mathbf{H}$  in (4.7),  $\mathbf{H}$  converges to  $\mathbf{R}^\top$ , which in turn converges to  $\mathbf{R}_\psi^\top$  as a consequence of the inner-loop controller. In view of (5.1) and (5.2), the component  $h_{12}$  of  $\mathbf{H}$  converges to  $\sin \psi$ . The second component (i.e.  $\omega_{3r} \mathbf{e}_3$ ) with  $\omega_{3r}$  is thus designed for guiding the yaw angle to zero using the information embedded in  $h_{12}$  as follows:

**Proposition 3.** (see [44] for proof) Assume that the inner-loop torque controller  $\Gamma_c$  ensures the almost-GAS and LES of the equilibrium  $(\boldsymbol{\Omega}, \mathbf{R}^\top \mathbf{e}_3) = (\boldsymbol{\Omega}_r, \mathbf{e}_3)$ , with  $\boldsymbol{\Omega}_r$  defined by (5.9) combined with  $\omega_{3r}$  (involved in (5.9)) solution to the following system

$$\dot{\omega}_{3r} = -k_{\Theta 2} \omega_{3r} - k_{\Theta 1} \text{sat}^{\Delta_\Theta}(h_{12}), \quad \omega_{3r}(0) \in \mathbb{R} \quad (5.28)$$

with  $k_{\Theta 1}, k_{\Theta 2}, \Delta_\Theta$  positive numbers and  $h_{1,2}$  the element at the first row and second column of  $\mathbf{H}$ . Apply the outer-loop force controller  $\mathbf{F}_c$  given either by Proposition 1 (when  $\Delta_F \equiv \mathbf{0}$ ) or Proposition 2 (when  $\Delta_F$  is constant). Then, the equilibrium  $\mathbf{H} = \mathbf{I}_3$  is LES. Moreover, this equilibrium is almost-GAS in the case where  $\bar{\mathbf{F}}_c$  is given by Proposition 1 and  $\Delta_F \equiv \mathbf{0}$ .

#### 5.4.2 Inner-loop control design

The more involved part concerning the outer-loop control design has been presented. It remains to design an effective inner-loop torque controller that ensures the stability of the equilibrium  $(\boldsymbol{\Omega}, \mathbf{R}^\top \mathbf{e}_3) = (\boldsymbol{\Omega}_r, \mathbf{e}_3)$ , with  $\boldsymbol{\Omega}_r$  defined by (5.9) combined with (5.28).

In view of the rotation dynamics (i.e. (3.2) and (5.3b)), it is not too difficult to carry

#### 5.4. Control design

---

out the above-mentioned objective since the sub-system under consideration is fully-actuated and the measurements of both  $\Omega$  and  $\mathbf{R}^\top \mathbf{e}_3$  are at our disposal. However, the troublesome term  $\Delta_\Gamma$  involved in (5.3b) should be carefully addressed, especially when the vehicle is subjected to strong currents that excite the Munk moment effects. Since the angular velocity can be measured at high frequency and with good precision, we propose to estimate  $\Delta_\Gamma$  using a high-gain observer similarly to the idea proposed in [28, Proposition 8].

**Lemma 1.** *Consider the following observer of  $\Delta_\Gamma$ :*

$$\begin{cases} \mathbf{J}\dot{\hat{\Omega}} = (\mathbf{J}\hat{\Omega}) \times \hat{\Omega} + \Gamma_c + \Gamma_g + \hat{\Delta}_\Gamma + k_0 \mathbf{J}(\Omega - \hat{\Omega}) \\ \dot{\hat{\Delta}}_\Gamma = a_0^2 k_0^2 \mathbf{J}(\Omega - \hat{\Omega}) \end{cases} \quad (5.29)$$

with  $\hat{\Omega}$  and  $\hat{\Delta}_\Gamma$  the estimates of  $\Omega$  and  $\Delta_\Gamma$ , respectively;  $\hat{\Omega}(0) \in \mathbb{R}^3$ ,  $\hat{\Delta}_\Gamma(0) \in \mathbb{R}^3$ ;  $a_0, k_0$  some positive gains. Assume that  $\dot{\Delta}_\Gamma$  is uniformly ultimately bounded (u.u.b.). Then for any  $a_0 \in (1 - \sqrt{2}/2, 1 + \sqrt{2}/2)$ ,

1. The errors  $\hat{\Omega} - \Omega$  and  $\hat{\Delta}_\Gamma - \Delta_\Gamma$  are u.u.b. by a positive constant  $\varepsilon(k_0)$  that tends to zero when  $k_0$  tends to  $+\infty$ . Moreover, these terms converge exponentially to zero for any  $k_0 > 0$  if  $\Delta_\Gamma$  is constant.
2.  $\dot{\hat{\Delta}}_\Gamma$  is u.u.b. by a constant independent of  $k_0$ .

The proof proceeds identically to the proof of [28, Proposition 8]. Now, we can use the estimate  $\hat{\Delta}_\Gamma$  as a feedforward term for the inner-loop torque control design.

Define the angular velocity error variable  $\tilde{\Omega} \triangleq \Omega - \Omega_r$ . From (5.3b), one obtains the following error equation

$$\mathbf{J}\dot{\tilde{\Omega}} = (\mathbf{J}\tilde{\Omega}) \times \tilde{\Omega} + \Gamma_c + \Gamma_g + \Gamma + \hat{\Delta}_\Gamma + \bar{\Delta}_\Gamma \quad (5.30)$$

with  $\Gamma \triangleq (\mathbf{J}\Omega) \times \Omega_r - \mathbf{J}\dot{\Omega}_r$  and  $\bar{\Delta}_\Gamma \triangleq \Delta_\Gamma - \hat{\Delta}_\Gamma$ .

**Proposition 4.** *Consider error equation given by (5.30). Assume that the unknown perturbation term  $\bar{\Delta}_\Gamma$  is constant and bounded by a known value  $\bar{\epsilon}$ . Define an anti-windup integrator  $\mathbf{I}_\Omega$  solution to the following differential equation*

$$\dot{\mathbf{I}}_\Omega = -k\mathbf{I}_\Omega + \text{sat}^{\Delta_1}(k\mathbf{I}_\Omega + \text{sat}^{\Delta_2}(\mathbf{Q}\tilde{\Omega})), \quad \mathbf{I}_\Omega(0) \in \mathbb{R}^3 \quad (5.31)$$

with  $k$  a positive gain,  $\Delta_1, \Delta_2$  some positive constants, and  $\mathbf{Q} \in \mathbb{R}^{3 \times 3}$  satisfying  $\mathbf{Q}^\top \mathbf{Q} = \mathbf{J}$ .

Apply the control torque

$$\begin{aligned} \Gamma_c = & -\text{sat}^{\eta_3}(\mathbf{K}_\Omega \tilde{\Omega}) - k_{i\Omega} \mathbf{Q}^\top \mathbf{I}_\Omega \\ & + \max\left(0, \frac{|\mathbf{Q}\tilde{\Omega}|}{\Delta_2} - 1\right) \Gamma_g - \Gamma - \hat{\Delta}_\Gamma \end{aligned} \quad (5.32)$$

with  $\mathbf{K}_\Omega \in \mathbb{R}^{3 \times 3}$  positive diagonal gain matrix,  $k_{i\Omega}$  positive gain,  $\eta_3$  a positive number, and  $\Omega_r$  defined by (5.9) combined with (5.28). If

$$\frac{k}{k_{i\Omega}} \|\mathbf{Q}^{-\top}\| \bar{\epsilon} + \Delta_2 \leq \Delta_1 \quad (5.33)$$

then, the following properties hold.

1. The error state  $(\tilde{\Omega}, \mathbf{I}_\Omega, \mathbf{R}^\top \mathbf{e}_3)$  converges either to  $(\mathbf{0}, \mathbf{I}_\Omega^*, \mathbf{e}_3)$  or  $(\mathbf{0}, \mathbf{I}_\Omega^*, -\mathbf{e}_3)$  for all initial conditions, with  $\mathbf{I}_\Omega^* \triangleq k_{i\Omega}^{-1} \mathbf{Q}^{-\top} \bar{\Delta}_\Gamma$ .
2. The “desired” equilibrium  $(\tilde{\Omega}, \mathbf{I}_\Omega, \mathbf{R}^\top \mathbf{e}_3) = (\mathbf{0}, \mathbf{I}_\Omega^*, \mathbf{e}_3)$  is almost-GAS and LES. The “undesired” equilibrium  $(\tilde{\Omega}, \mathbf{I}_\Omega, \mathbf{R}^\top \mathbf{e}_3) = (\mathbf{0}, \mathbf{I}_\Omega^*, -\mathbf{e}_3)$  is unstable.

**Proof.** Consider the positive storage function

$$\mathcal{V} \triangleq \begin{cases} \frac{1}{2} |\mathbf{Q}\tilde{\Omega}|^2 & \text{if } |\mathbf{Q}\tilde{\Omega}| \leq \Delta_2 \\ \frac{1}{2} (2|\mathbf{Q}\tilde{\Omega}| - \Delta_2) \Delta_2 & \text{otherwise} \end{cases}$$

Using the fact that  $\mathbf{J} = \mathbf{Q}^\top \mathbf{Q}$  one verifies that

$$\dot{\mathcal{V}} = \min\left(1, \frac{\Delta_2}{|\mathbf{Q}\tilde{\Omega}|}\right) \tilde{\Omega}^\top \mathbf{J} \dot{\tilde{\Omega}} \quad (5.34)$$

From (5.30), (5.32) and the definition of  $\tilde{\Omega}$  one obtains

$$\begin{aligned} \mathbf{J} \dot{\tilde{\Omega}} = & (\mathbf{J}\Omega)_\times \tilde{\Omega} - \text{sat}^{\eta_3}(\mathbf{K}_\Omega \tilde{\Omega}) + \max\left(1, \frac{|\mathbf{Q}\tilde{\Omega}|}{\Delta_2}\right) \Gamma_g \\ & - k_{i\Omega} \mathbf{Q}^\top \mathbf{I}_\Omega + \bar{\Delta}_\Gamma \end{aligned} \quad (5.35)$$

Consider the Lyapunov function candidate

$$\mathcal{L}_1 \triangleq \mathcal{V} + mgl(1 - \mathbf{e}_3^\top \mathbf{R}^\top \mathbf{e}_3) + \frac{1}{2} \mathbf{k}_{i\Omega} |\tilde{\mathbf{I}}_\Omega|^2 \quad (5.36)$$

with  $\tilde{\mathbf{I}}_\Omega \triangleq \mathbf{I}_\Omega - \mathbf{I}_\Omega^*$ . Calculating the time-derivative of  $\mathcal{L}_1$  using the expression (5.34) of  $\dot{\mathcal{V}}$ , equation (5.30), the torque control expression (5.32), the definition (5.9) of  $\Omega_r$ ,

#### 5.4. Control design

the expression (5.31) of  $\dot{\mathbf{I}}_\Omega$  and the fact that  $\text{sat}^{\Delta_2}(\mathbf{Q}\tilde{\Omega}) = \min(1, \frac{\Delta_2}{|\mathbf{Q}\tilde{\Omega}|})\mathbf{Q}\tilde{\Omega}$ , one deduces

$$\begin{aligned}
\dot{\mathcal{L}}_1 &= -\min(1, \frac{\Delta_2}{|\mathbf{Q}\tilde{\Omega}|})\tilde{\Omega}^\top \text{sat}^{\eta_3}(\mathbf{K}_\Omega \tilde{\Omega}) - \mathbf{k}_{i\Omega} \tilde{\mathbf{I}}_\Omega^\top \text{sat}^{\Delta_2}(\mathbf{Q}\tilde{\Omega}) \\
&\quad - mgl\Omega_r^\top \mathbf{e}_3 \times \mathbf{R}^\top \mathbf{e}_3 + \mathbf{k}_{i\Omega} \tilde{\mathbf{I}}_\Omega^\top \dot{\mathbf{I}}_\Omega \\
&= -\min(1, \frac{\Delta_2}{|\mathbf{Q}\tilde{\Omega}|})\tilde{\Omega}^\top \text{sat}^{\eta_3}(\mathbf{K}_\Omega \tilde{\Omega}) - mglk_g |\mathbf{e}_3 \times \mathbf{R}^\top \mathbf{e}_3|^2 \\
&\quad - kk_{i\Omega} |\tilde{\mathbf{I}}_\Omega|^2 + k_{i\Omega} \tilde{\mathbf{I}}_\Omega^\top (-k\mathbf{I}_{i\Omega}^* - \text{sat}^{\Delta_2}(\mathbf{Q}\tilde{\Omega})) \\
&\quad + \text{sat}^{\Delta_1}(k\tilde{\mathbf{I}}_\Omega + k\mathbf{I}_\Omega^* + \text{sat}^{\Delta_2}(\mathbf{Q}\tilde{\Omega})) \\
&\leq -\min(1, \frac{\Delta_2}{|\mathbf{Q}\tilde{\Omega}|})\tilde{\Omega}^\top \text{sat}^{\eta_3}(\mathbf{K}_\Omega \tilde{\Omega}) - mglk_g |\mathbf{e}_3 \times \mathbf{R}^\top \mathbf{e}_3|^2
\end{aligned} \tag{5.37}$$

where the last inequality is obtained using condition (5.33) and the fact that  $\forall a, b \in \mathbb{R}^3, \Delta \in \mathbb{R}^+$  one has  $|-a + \text{sat}^\Delta(b+a)| \leq |b|$  if  $|a| \leq \Delta$  (see [28] for the proof). Clearly  $\dot{\mathcal{L}}_1$  is negative semi-definite. Remark that system (5.35) and (5.31) is not autonomous due to the time-varying term  $\Omega$  and consequently La Salle's principle does not apply. However,  $\tilde{\Omega}$  and  $\mathbf{I}_\Omega$  are bounded with respect to initial conditions. Since  $\Omega_r$  and its derivative are bounded thanks to the expressions (5.9) and (5.28), one deduces from (5.35) that  $\dot{\tilde{\Omega}}$  is also bounded. Then it is straightforward to verify that  $\ddot{\mathcal{L}}$  is also bounded, implying the uniform continuity of  $\dot{\mathcal{L}}$ . Then, application of Barbalat's lemma ensures that  $\dot{\mathcal{L}}$  and, thus,  $\tilde{\Omega}$  and  $\mathbf{e}_3 \times \mathbf{R}^\top \mathbf{e}_3$  converge to zero. Next, using Barbalat-like arguments it can be shown that  $\dot{\tilde{\Omega}}$  also converges to zero, implying the convergence of  $\mathbf{I}_\Omega$  to  $\mathbf{I}_\Omega^*$ . The convergence of  $\mathbf{e}_3 \times \mathbf{R}^\top \mathbf{e}_3$  to zero implies that  $\mathbf{R}\mathbf{e}_3$  converges to either  $\mathbf{e}_3$  or  $-\mathbf{e}_3$ . So far we have proved that  $(\tilde{\Omega}, \mathbf{I}_\Omega, \mathbf{R}\mathbf{e}_3)$  converges either to  $(\mathbf{0}, \mathbf{I}_\Omega^*, \mathbf{e}_3)$  or  $(\mathbf{0}, \mathbf{I}_\Omega^*, -\mathbf{e}_3)$ .

It remains to show that the "desired" equilibrium  $(\tilde{\Omega}, \mathbf{I}_\Omega, \mathbf{R}\mathbf{e}_3) = (\mathbf{0}, \mathbf{I}_\Omega^*, \mathbf{e}_3)$  is LES and the "undesired" equilibrium  $(\tilde{\Omega}, \mathbf{z}_\Omega, \mathbf{R}\mathbf{e}_3) = (\mathbf{0}, \mathbf{I}_\Omega^*, -\mathbf{e}_3)$  is unstable. Note that the almost-GAS of the "desired" equilibrium then directly follows. In the first-order approximations, one has  $\mathbf{R} \approx \mathbf{I} + \Theta_\times$  with  $\Theta = [\phi, \theta, \psi]^\top$  and, subsequently,  $\mathbf{e}_3 \times \mathbf{R}^\top \mathbf{e}_3 \approx [-\phi, -\theta, 0]^\top$ . Denoting  $[\tilde{\omega}_1, \tilde{\omega}_2, \tilde{\omega}_3]^\top \triangleq \tilde{\Omega}$  and using the approximation  $\dot{\Theta} \approx \Omega$ , one obtains the following linearized system of (5.30) and (5.31)

$$\begin{cases} \dot{\phi} \approx \tilde{\omega}_1 - k_g \phi \\ \dot{\theta} \approx \tilde{\omega}_2 - k_g \theta \\ \dot{\tilde{\Omega}} \approx -\mathbf{J}^{-1} \mathbf{K}_\Omega \tilde{\Omega} - \mathbf{J}^{-1} k_{i\Omega} \mathbf{Q}^\top \tilde{\mathbf{I}}_\Omega + mgl\mathbf{J}^{-1} [-\phi, -\theta, 0]^\top \\ \dot{\mathbf{I}}_\Omega = \mathbf{Q}\tilde{\Omega} \end{cases} \tag{5.38}$$

Consider the following Lyapunov function candidate

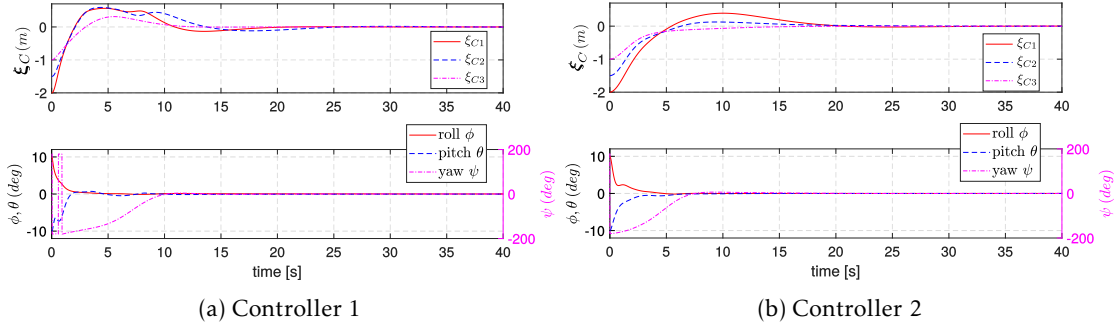


Figure 5.3: AUV's position and attitude (Euler angles) vs. time

$$\mathcal{L}_\Omega = \frac{1}{2} \tilde{\Omega}^\top \mathbf{J} \tilde{\Omega} + \frac{1}{2} \mathbf{k}_{i\Omega} |\tilde{\mathbf{I}}_\Omega|^2 + \frac{1}{2} mgl(\phi^2 + \theta^2) \quad (5.39)$$

One verifies that

$$\dot{\mathcal{L}}_\Omega = -\tilde{\Omega}^\top \mathbf{K}_\Omega \tilde{\Omega} - k_g mgl(\phi^2 + \theta^2) \leq 0 \quad (5.40)$$

From here, LaSalle's principle ensures that  $\tilde{\Omega}$ ,  $\phi$  and  $\theta$  and, thus,  $\dot{\tilde{\Omega}}$  converge to zero, which implies the convergence of  $\mathbf{z}_\Omega$  to zero. The convergence of  $\phi$  and  $\theta$  to zero is equivalent to the convergence of  $\mathbf{R}^\top \mathbf{e}_3$  to  $\mathbf{e}_3$ . Since the equilibrium  $(\tilde{\Omega}, \mathbf{z}_\Omega, \mathbf{R}^\top \mathbf{e}_3) = (\mathbf{0}, \mathbf{0}, \mathbf{e}_3)$  of the linearized system (5.38) is asymptotically stable, it is also exponentially stable.

Now, the Chetaev's theorem is used to prove the instability of the equilibrium  $(\tilde{\Omega}, \mathbf{z}_\Omega, \mathbf{R}^\top \mathbf{e}_3) = (\mathbf{0}, \mathbf{0}, -\mathbf{e}_3)$ . Define  $\mathbf{y} = \mathbf{e}_3 + \mathbf{R}^\top \mathbf{e}_3$ . Consider the positive function  $\mathcal{S}_1(\mathbf{y}) \triangleq \mathbf{y}^\top \mathbf{e}_3 = 1 + \mathbf{e}_3^\top \mathbf{R}^\top \mathbf{e}_3$ , satisfying  $\mathcal{S}_1(\mathbf{0}) = 0$ . Define  $U_r \triangleq \{\mathbf{y} | \mathcal{S}_1(\mathbf{y}) > 0, |\mathbf{y}| < r\}$  for some number  $0 < r < 1$ . Note that  $U_r$  is non-empty. By neglecting all high-order terms, one verifies that

$$\dot{\mathcal{S}}_1 \approx \mathbf{e}_3^\top \mathbf{R} \Omega_{r \times 3} \mathbf{e}_3 = k_g |\mathbf{e}_{3 \times 3} \mathbf{R}^\top \mathbf{e}_3|^2 = k_g |\mathbf{e}_{3 \times 3} \mathbf{y}|^2$$

For all  $\mathbf{y} \in U_r$ , the fact that  $\mathbf{y}^\top \mathbf{e}_3 > 0$  is equivalent to  $|\mathbf{e}_{3 \times 3} \mathbf{y}|^2 > 0$ , which implies that  $\dot{\mathcal{S}}_1 > 0$ . Since all conditions of Chetaev's theorem are now united [42], the origin of the linearized system about the undesired equilibrium (so that  $\mathbf{y} = \mathbf{0}$ ) is unstable.  $\square$

## 5.5 Comparative simulation results

The proposed control approach applied to station keeping of fully-actuated AUVs without the need of linear velocity measurements is, in fact, inspired by the one proposed in [44, Remark 7] which corresponds to the particular case of using a downward-looking camera and which makes use of linear velocity measurements. Although the novel approach already has a practical advantage by depleting the need of a costly DVL, it is even

## 5.5. Comparative simulation results

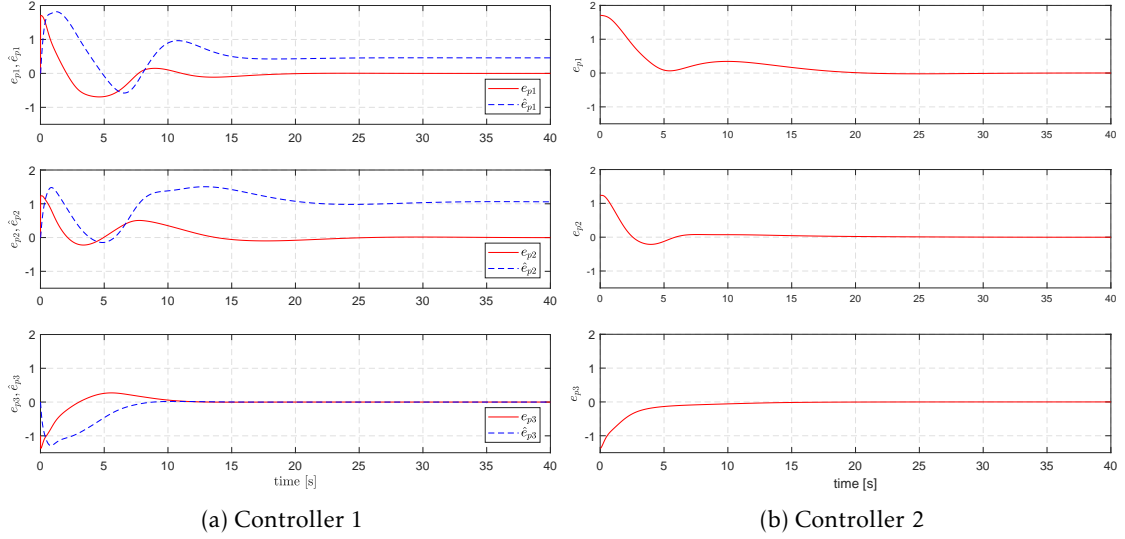


Figure 5.4:  $e_p$  (and  $\hat{e}_p$ ) vs. time

more desirable if its performance is also comparable to the previous approach. Therefore, comparative simulation results of the two approaches using a realistic model of a fully-actuated AUV and in presence of a constant horizontal current  $\mathbf{v}_f = [\frac{1}{2\sqrt{2}}, \frac{1}{2\sqrt{2}}, 0]^\top$  [m/s] will be reported thereafter. For convenience, let us call the proposed controller and the one proposed in [44] as **Controller 1** and **Controller 2**, respectively.

The simulated vehicle is the BlueROV<sup>1</sup>. Its physical parameters are provided in Tab. 5.1, where the added-mass, added-inertia and damping coefficients are roughly identified from the given shape. To test the robustness of the controllers with respect to model uncertainties, the following “erroneous” estimates of  $\mathbf{M}$  and  $\mathbf{J}$  are used:

$$\begin{cases} \hat{\mathbf{M}} = m\mathbf{I}_3 + \hat{\mathbf{M}}_A^{11} = \text{diag}(8.712, 12.712, 10.816) [kg] \\ \hat{\mathbf{J}} = \hat{\mathbf{J}}_0 + \hat{\mathbf{M}}_A^{22} = \text{diag}(0.1642, 0.5643, 0.5116) [kg.m^2] \end{cases}$$

One notes that these estimated parameters are quite different from the corresponding “real” ones.

The homography  $\mathbf{H}$  is directly computed using (5.1) with  $d^* = 1$  [m] and  $\mathbf{n}^* = \mathbf{R}_{\{\frac{\pi}{18}, \frac{\pi}{6}, 0\}} \mathbf{e}_3 = [0.4924, -0.1736, 0.8529]^\top$ . The initial conditions are  $\mathbf{p}_C(0) = [-2, -1.5, -1]^\top$  [m],  $\mathbf{R}(0) = \mathbf{R}_{\{\frac{\pi}{18}, -\frac{\pi}{18}, \pi\}}$ ,  $\mathbf{V}(0) = \mathbf{\Omega}(0) = \mathbf{0}$ . The initial roll and pitch errors are chosen small to guarantee that the target scene stays in the field of view of the downward-looking camera. In contrast, a very large initial yaw error is chosen (i.e.  $\psi = \pi$ ) to verify the large stability domain of the control algorithms.

• **Simulation with Controller 1 (i.e proposed approach):** The proposed control approach including the outer-loop controller given in Propositions 2–3 and the inner-

<sup>1</sup><http://bluerobotics.com/store/retired/bluerov-r1/>

Specification	Numerical value
$m$ [kg]	7.6
$F_b$ [N]	1.01mg
$l$ [m]	0.025
$\mathbf{r}_C$ [m]	[0 0 0.15]
$\mathbf{J}_0$ [kg.m <sup>2</sup> ]	$\begin{bmatrix} 0.0842 & 0.004 & 0.005 \\ 0.004 & 0.2643 & 0.007 \\ 0.005 & 0.007 & 0.3116 \end{bmatrix}$
$\mathbf{M}_A^{22}$ [kg.m <sup>2</sup> ]	$\begin{bmatrix} 0.1 & 0.005 & 0.006 \\ 0.005 & 0.25 & 0.008 \\ 0.006 & 0.008 & 0.3 \end{bmatrix}$
$\mathbf{M}_A^{11}$ [kg]	$\begin{bmatrix} 1.39 & 0.10 & 0.12 \\ 0.10 & 4.26 & 0.13 \\ 0.12 & 0.13 & 4.02 \end{bmatrix}$
$\mathbf{M}_A^{21} = \mathbf{M}_A^{12}$	$\begin{bmatrix} 0.002 & 0.02 & 0.01 \\ 0.02 & 0.003 & 0.018 \\ 0.01 & 0.018 & 0.003 \end{bmatrix}$
$\mathbf{D}_{Vl}$ [kg.s <sup>-1</sup> ]	diag(5.85, 9.21, 11.03)
$\mathbf{D}_{Vq}$ [kg.m <sup>-1</sup> ]	diag(36.57, 57.58, 68.97)
$\mathbf{D}_{\Omega l}$ [kg.m <sup>2</sup> .s <sup>-1</sup> ]	diag(0.01126, 0.01855, 0.01701)
$\mathbf{D}_{\Omega q}$ [N.m]	diag(0.0053, 0.0130, 0.0118)

Table 5.1: Specifications of the simulated AUV

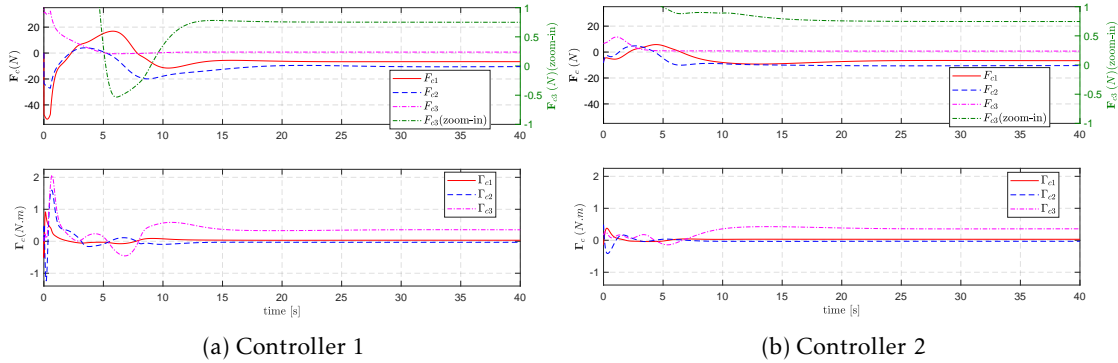


Figure 5.5: Control force  $\mathbf{F}_c$  and torque  $\mathbf{\Gamma}_c$  vs. time

loop controller given in Proposition 4 is simulated, with gains and parameters given in Tab. 5.2. The control gains has been obtained based on the classical pole placement technique using a coarse estimation of  $a^*$  equal to 1. Due to the current velocity of significant magnitude (i.e. 0.5 [m/s]), the drag force and Munk moment are not negligible. This shows the need of control robustification using, for instance, the integrator and high-gain observer techniques proposed in this paper. As observed from the sim-

## 5.5. Comparative simulation results

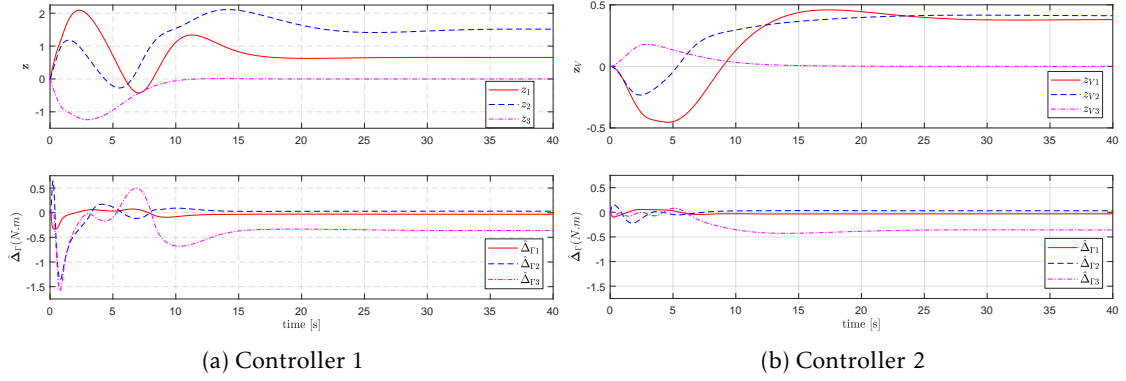


Figure 5.6:  $\mathbf{z}$  (left),  $\mathbf{z}_V$  (right), and  $\hat{\Delta}_\Gamma$  vs. time

ulation results reported in Figs. 5.3a–5.6a, the estimate  $\hat{\Delta}_\Gamma$  and the integrators in both inner- and outer-loop controllers successfully counteract for these above-mentioned disturbances as well as the imprecise estimated system parameters. Fig. 5.3a shows the convergence of the AUV’s position and orientation to zero without large overshoots. The sea current on horizontal plane has a clear impact on the integral variable  $\mathbf{z}$ , the estimate terms  $\hat{\mathbf{e}}_p$  and  $\hat{\Delta}_\Gamma$ , as well as the control force and torque. More precisely,  $z_1$ ,  $z_2$ ,  $\hat{e}_{p1}$ ,  $\hat{e}_{p2}$ ,  $\hat{\Delta}_{\Gamma 3}$ ,  $F_{c1}$ ,  $F_{c2}$  and  $\Gamma_{c3}$  converge to non-null values as shown in Figs. 5.4a–5.6a. On the other hand, the vertical component of  $F_{c3}$  converges to a positive value since the vehicle is positively buoyant.

Controller	Gains and other parameters
Outer-loop	$\mathbf{K}_1 = \text{diag}(3s, 3s, 3s)$ $k_2 = \frac{8}{3} \frac{s^2}{a^*}$ , $k_3 = \frac{1}{3} \frac{s^2}{a^*}$ , $s = \sqrt{2}$ $k_I = 0.7$ , $\eta_1 = 1.8$ , $\eta_2 = 2.3$ $k_g = 1$ , $k_{\Theta 1} = 1$ , $k_{\Theta 2} = \sqrt{2}$ , $\Delta_\Theta = 1$
Inner-loop	$\mathbf{K}_\Omega = \text{diag}(3, 3, 3)$ , $k_{i\Omega} = 2$ $k = 10$ , $\Delta_1 = 6.25$ , $\Delta_2 = 2$ $a_0 = 0.5$ , $k_0 = 20$ , $\eta_3 = 8$

Table 5.2: Control gains and parameters of Controller 1

• **Simulation with Controller 2 (i.e. approach proposed in [44]):** To make a fair comparison, the inner-loop controller of [44] has been revised by also incorporating a high-gain observer of the perturbation torque induced by sea current, similarly to the one proposed in Lemma 1. Control parameters and gains of the controller are given in Tab. 5.3. They have been chosen so that the time evolution of the AUV’s position has almost the same settling time as in the previous simulation. Simulation results are reported in Figs 5.3b–5.6b. In overall, the time evolutions of the vehicle’s pose and of the

Controller	Gains and other parameters
Outer-loop	$k_{p1} = 0.4145, k_{p2} = \sqrt{2}$ $k_u = 1, k_{\Theta 1} = 1, k_{\Theta 2} = \sqrt{2}, \Delta_{\Theta} = 1$
Inner-loop	$\mathbf{K}_V = \text{diag}(5, 5, 5), \mathbf{K}_{iV} = 0.4\mathbf{K}_V$ $\mathbf{K}_{\Omega} = \text{diag}(3, 3, 3), k_{i\Omega} = 2$ $k = 10, \Delta_1 = 6.25, \Delta_2 = 2$ $a_0 = 0.5, k_0 = 20, \eta_3 = 8$

Table 5.3: Control gains and parameters of Controller 2

visual error  $\mathbf{e}_p$  are quite reminiscent of the corresponding ones resulted by Controller 1. This implies that the performance of the proposed controller is comparable to our prior control approach [44] that in contrast relies on a costly DVL for linear velocity measurements.

## 5.6 Experimental validations

### 5.6.1 Experimental setup

The implementation of the proposed algorithm with real-time homography estimation has been performed on an in-house AUV experimental platform (see Fig. 5.7). At the moment when the experiment was performed, a Hardkernel Odroid XU-4 played a role of the companion computer in the I3S-UV control architecture (c.f. Fig. 5.8).

For performing the real-time homography estimation, the AUV is equipped with a myAHRS+ IMU sensor providing measurement output at  $100 [Hz]$  and an oCam downward-looking monocular camera providing color images of  $640 [px] \times 480 [px]$  at  $20 [Hz]$ . The homography estimation algorithm [34] has been implemented in C++, combined with OpenCV for image processing, on the ground station laptop with an Intel Core i7-7700HQ octa-core CPU running at  $2.8 GHz$ . The transmission of the data from the camera and the IMU to the ground station is carried out through the high speed Ethernet cable. The laptop has a Linux-based operating system and is responsible for the following tasks: 1) interfacing with the camera and IMU hardwares and acquisition of images and IMU data 2) real-time estimation of the homography at  $10 [Hz]$  3) perform outer control loop at  $10 [Hz]$ , and 4) interfacing with the joystick and Pixhawk via Odroid to remotely control the vehicle.

For the homography estimation, an image captured by the camera is chosen as the reference image. The *FAST Feature Detector* and *ORB Descriptor Extractor* algorithms available in the OpenCV library are employed for carrying out feature detection and descriptor extraction in images.

## 5.6. Experimental validations

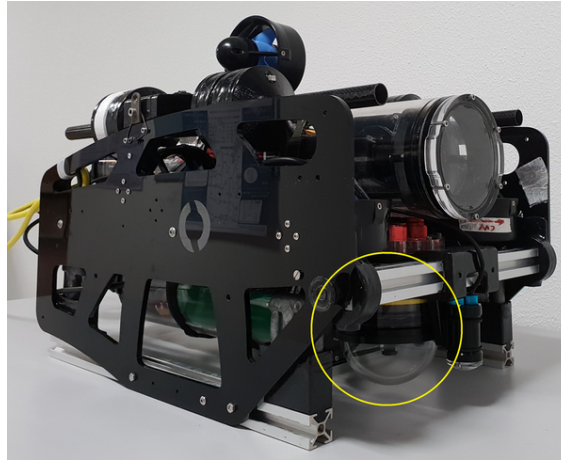


Figure 5.7: AUV with downward-looking camera (inside yellow circle)

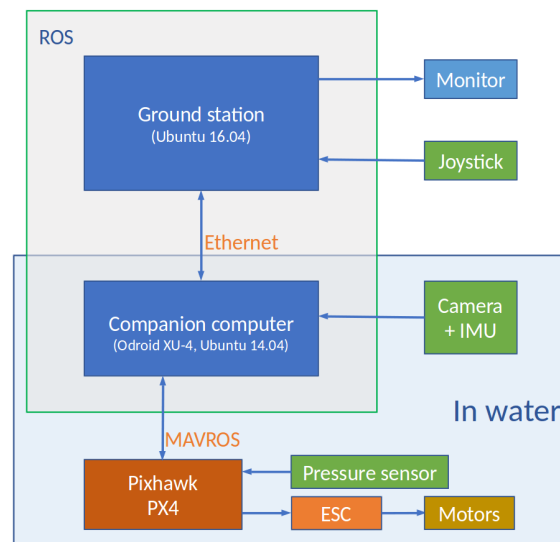


Figure 5.8: AUV's architecture

To perform the station-keeping task, the UAV is initially in the teleoperation mode and is manually positioned at a certain depth above the lakebed so that the latter is visible by the camera ensuring a sufficient number of detected features for good homography estimation. Such unknown depth thus varies according to lighting conditions and water turbidity. In the reported experiment, the vehicle was positioned at about  $0.5[m]$  above the lakebed.

The parameters and control gains involved in the computation of the control inputs are given in Tab. 5.4 and Tab. 5.5.

### 5.6.2 Experimental results

Experimental results carried out in lake Saint-Cassien (France) are reported next (see Fig. 5.9). Due to space limitation, only brief but most representative parts of total results

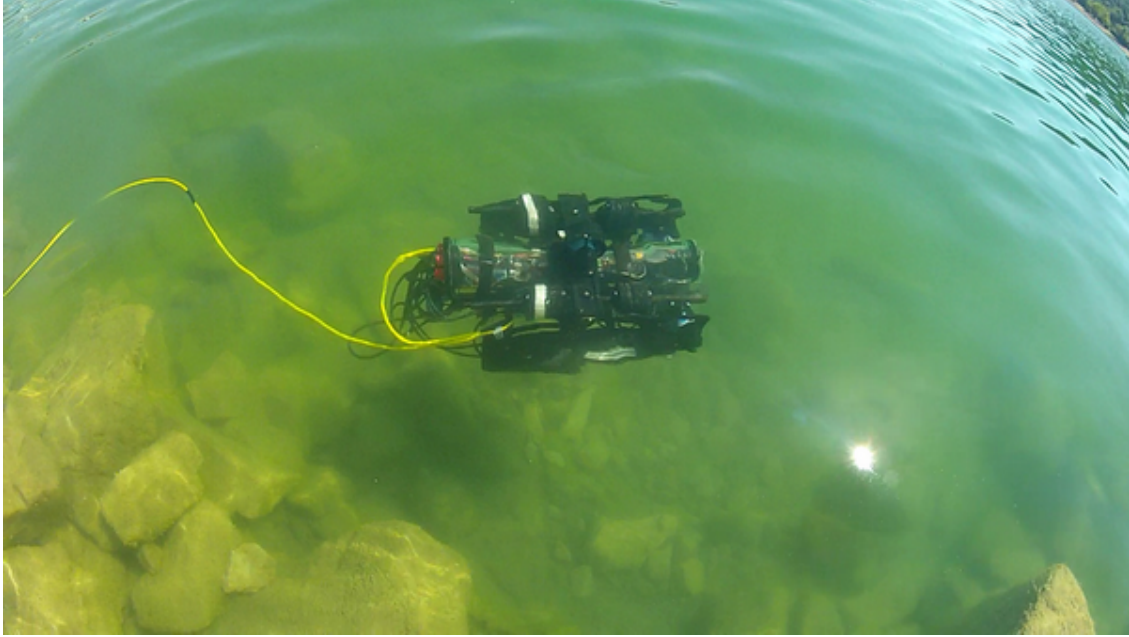


Figure 5.9: Experimental validations in lake Saint-Cassien

Specification	Numerical value
$m$ [kg]	16
$F_b$ [N]	1.01mg
$l$ [m]	0.025
$\mathbf{r}_C$ [m]	[0.2 0 0.15]
$\hat{\mathbf{M}} = m\mathbf{I}_3 + \hat{\mathbf{M}}_A^{11}$ [kg]	$diag(17.868, 23.868, 21.024)$
$\hat{\mathbf{J}} = \mathbf{J}_0 + \hat{\mathbf{M}}_A^{22}$ [kg.m <sup>2</sup> ]	$diag(0.3105, 0.8486, 1.0)$
$\hat{\mathbf{D}} = m\mathbf{l}\mathbf{e}_{3 \times 3}$ [kg.m]	$0.4\mathbf{e}_{3 \times 3}$

Table 5.4: Specifications of the experimental AUV

are presented in the video [https://youtu.be/p\\_oiISP0tgw](https://youtu.be/p_oiISP0tgw). However, the reader can also view two other videos showing the capability of long-term station keeping (more than 30 minutes) as well as other trials carried out during our research process with different water turbidity conditions and target images:

- <https://youtu.be/mkAAjX3mgVk>
- <https://youtu.be/KjAfYu1jG18>

## 5.6. Experimental validations

Controller	Gains and other parameters
Proposition 2	$\mathbf{K}_1 = \text{diag}(3s, 3s, 3s)$ $k_2 = \frac{8 s^2}{3 a^*}, k_3 = \frac{1 s^2}{3 a^*}, s = 0.9$ $k_I = 0.1, \eta_1 = 1.8, \eta_2 = 2.3$
Proposition 3	$k_g = 1, k_{\Theta 1} = 1/2, k_{\Theta 2} = \sqrt{2}, \Delta_{\Theta} = 2\sqrt{2}$
Proposition 4 Lemma 1	$\mathbf{K}_{\Omega} = \text{diag}(1.863, 5.0916, 5.0), K_{i\Omega} = 0.1$ $a_0 = 0.5, k_0 = 20, \eta_3 = 6$

Table 5.5: Control gains and parameters in experiment

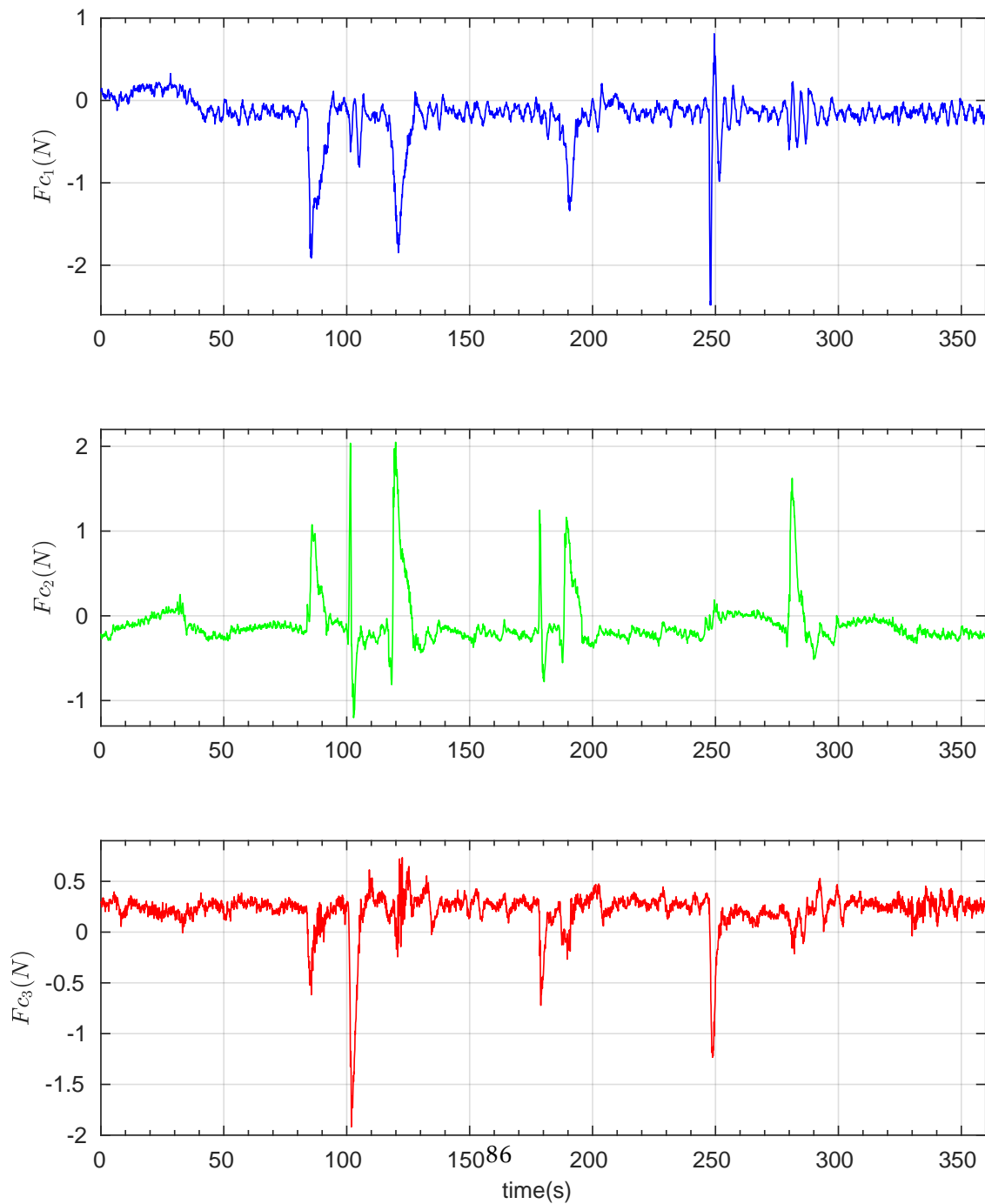


Figure 5.10: Control force  $\mathbf{F}_c$  vs. time

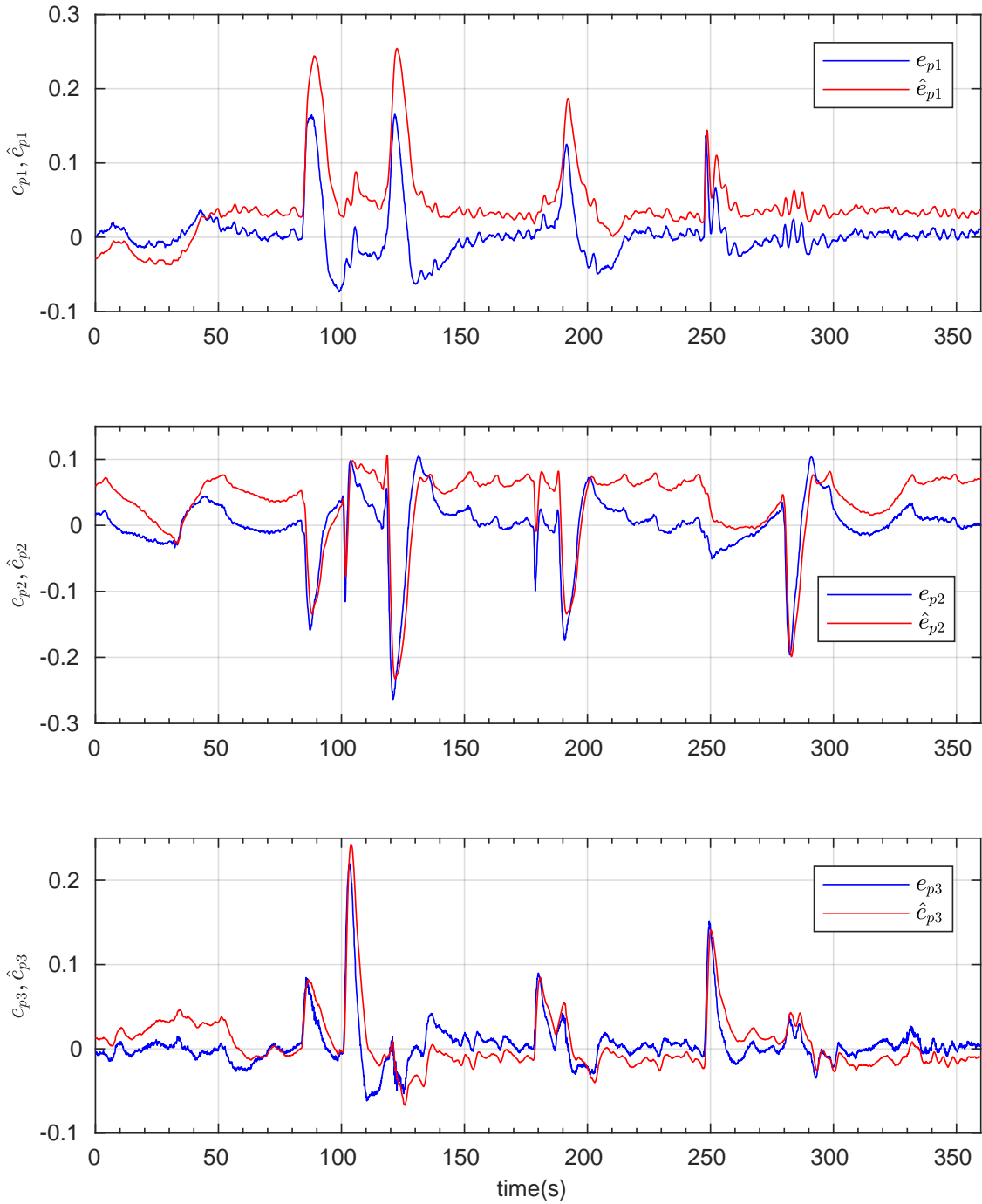


Figure 5.11:  $e_p$  and  $\hat{e}_p$  vs. time

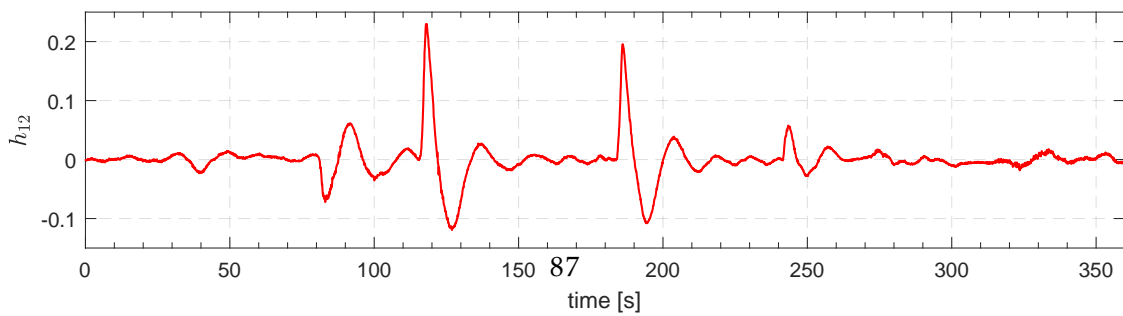


Figure 5.12:  $h_{12}$  vs. time

## 5.6. Experimental validations

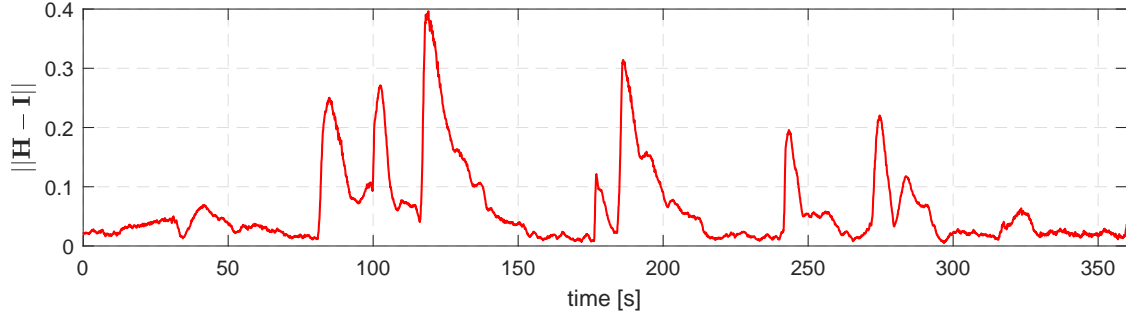


Figure 5.13: Frobenius norm  $\|\mathbf{H} - \mathbf{I}\|$  vs. time. The AUV has been pushed by a stick at time instants 85 [s], 100 [s], 120 [s], 180 [s], 245 [s] and 280 [s]. One observes the practical convergence of  $\|\mathbf{H} - \mathbf{I}\|$  to zero after these instants.

Regarding the reported video, experimental results including the time evolution of the control force  $\mathbf{F}_c$ , the visual error  $\mathbf{e}_p$  and its estimate  $\hat{\mathbf{e}}_p$ , the homography component  $h_{12}$ , and the Frobenius norm of  $\mathbf{H} - \mathbf{I}$  are shown in Figs. 5.10–5.13, respectively.

To excite the external force response, the AUV has been manually moved by a stick at time instants 85 [s], 100 [s], 120 [s], 180 [s], 245 [s] and 280 [s]. In Fig. 5.11 one observes that right after finishing the interaction, the AUV went back to its stabilized pose with relatively small overshoot. The control force generated for pushing the AUV back to the reference position is shown in Fig. 5.10. The settling time is about 30 seconds. The transient response also shows the efficiency of the integrator in eliminating the static error caused by the current.

In general, one can clearly observe the practical convergence of the AUV's pose to the desired one as illustrated by the practical convergence of the Frobenius norm  $\|\mathbf{H} - \mathbf{I}\|$  to zero (see Fig. 5.13). In particular, the convergence of the AUV's position is attested by the convergence of visual error  $\mathbf{e}_p$  to zero (Fig. 5.11) whereas the component  $h_{12}$  converges near to zero (Fig. 5.12) showing the practical convergence of the AUV's yaw angle to the desired one.

The effectiveness of the integrator correction in dealing with unknown currents and model uncertainties can be appreciated from Figs. 5.10 and 5.11. In steady state, the horizontal components of the control force  $F_{c1}$  and  $F_{c2}$  (Fig. 5.10) converge to non-zero values required to compensate for the horizontal current. The vertical component  $F_{c3}$  ultimately remains far from zero since the AUV is positively buoyant. In Fig. 5.11 it can be seen that  $\mathbf{e}_p$  converges near to zero and that the offsets between the corresponding components of  $\mathbf{e}_p$  and  $\hat{\mathbf{e}}_p$  are almost constant in steady state.

As can be observed from the reported video, the experiment has been carried out on a sunny day and the waves generate moving bright spots in the lakebed that periodically alter local brightness of the images captured. However, very good and robust quality of homography estimation can be appreciated despite the changes in light illumination as

well as large occlusions due to a panel fixed to the stick in between 310 [s] and 360 [s]. It is also worth noting that, theoretically, the homography estimation uses a planar target. In the experiment, this assumption does not hold true since the lakebed is covered by 3D reliefs such as sand rocks, and additionally the camera is relatively close to the lakebed. However, the proposed controller along with real-time homography estimation keeps working efficiently, showing the robustness of the control approach.

One can observe some small oscillations during the convergence. This is essentially due to the fact that the outer-loop control runs at a low frequency (10 [Hz]) and also due to the imperfect thrust generated by the thrusters inside its dead-band. This phenomenon becomes more prominent when the outer-loop poles are large. Hence, smaller pole values have been chosen while tuning the gains in the actual experiment as compared to the ones used in the reported simulation.

In conclusion, the experimental results for the overall control approach (i.e inner and outer-loop controls) are quite convincing even though some vehicle's physical parameters (e.g. added mass and added moment of inertia) are only roughly estimated and the AUV was subjected to various challenging conditions (e.g. significant unknown currents, water turbidity, lighting variation, target occlusion, etc.).

## 5.7 Conclusion

In this chapter a dynamic HBVS control approach of fully-actuated underwater vehicles is proposed. An advanced feature with respect to existing works on the topic is the non-requirement of a costly DVL used for linear velocity measurements. A potential application to station keeping has been demonstrated in a real environment with very encouraging results despite challenging conditions such as important disturbances induced by currents, water turbidity, lighting variation, target occlusion, etc. The proposed approach will undoubtedly enlarge the working envelop of low-cost (ROVs) as a costly DVL is not required. Even for industrial or professional ROVs and AUVs equipped with DVLs, the approach also allows for overcoming the common problem of measurement imprecision of DVLs caused by threshold violation when operating close to underwater structures or a sea bottom. The proposed control approach together with its extensions allow pilots to perform surveillance/intervention tasks in a more comfortable manner, which can reduce workload and thus increase work efficiency.

## 5.7. Conclusion

---

# 6

## Dynamic HBVS control of fully-actuated AUVs without linear velocity measurements: the case of forward-looking camera

**A** more challenging case of a fully-actuated AUV equipped with a forward-looking camera observing a (near) vertical visual target is considered in this chapter. A similar problem concerning underactuated aerial drones has been addressed in [16] which is in line with our effort in dealing with the system's dynamics and in depleting the need of a linear velocity sensor. However, that approach relies on the assumption that the *visual velocity* is available for control design, for instance, via the use of a high-gain observer, but a complete stability analysis including such high-gain observer is missing.

This chapter is part of our continuing efforts in developing low-cost but efficient visual servoing solutions for AUVs by depleting the need of a costly DVL. Potential applications encompass, for instance, docking on a planar docking station, stabilization or

## 6.1. Problem formulation

positioning in front of a man-made subsea manifold for performing common tasks in off-shore industry such as high-resolution imaging, monitoring, inspection, valve-turning, cleaning, repairing, or changing underwater structures, etc.

In this chapter, some basic notions used in system modeling in Chapter 3 are reused. However, some notions concerning outer-loop control design are redefined and used for other purposes (i.e. different from Chapter 5).

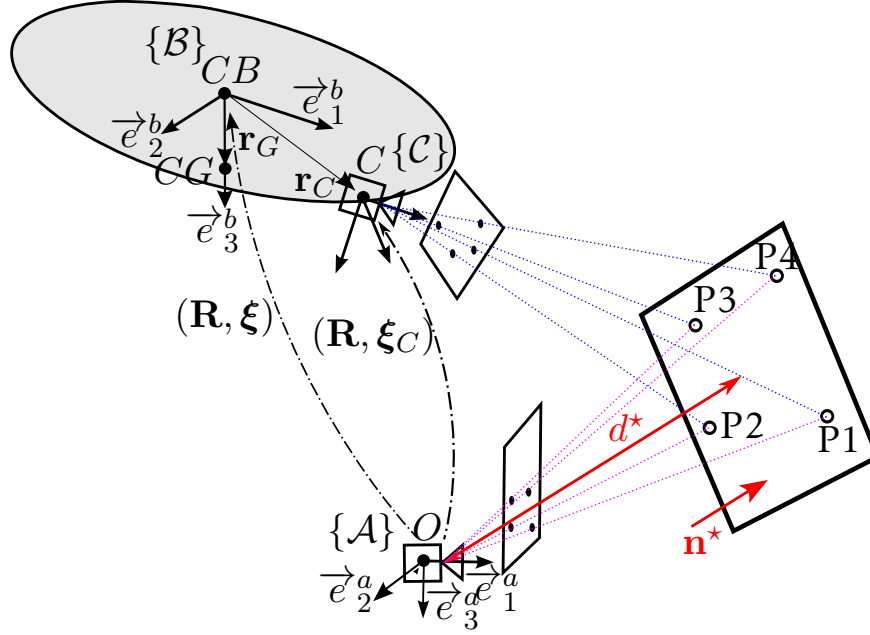


Figure 6.1: An AUV with a forward-looking camera and notation

## 6.1 Problem formulation

Based on a reference image, taken at some desired pose using a forward-looking monocular camera, and the current images, the control design objective consists in stabilizing the camera's pose to the reference one. Let us choose the inertial frame  $\{\mathcal{A}\}$  attached to the camera's desired pose (see Fig. 6.1). Assume that a good estimate of the homography matrix  $\mathbf{H}$  is available for control design. This latter encodes geometric information about the rotation and translation between the current camera frame  $\{\mathcal{C}\}$  and the reference frame  $\{\mathcal{A}\}$  [8]

$$\begin{bmatrix} h_{11} & h_{12} & h_{13} \\ h_{21} & h_{22} & h_{23} \\ h_{31} & h_{32} & h_{33} \end{bmatrix} \triangleq \mathbf{H} = \mathbf{R}^\top \left( \mathbf{I}_3 - \frac{1}{d^*} \boldsymbol{\xi}_C \mathbf{n}^{*\top} \right) \quad (6.1)$$

with  $d^*$  the distance between the camera optical center and the target plane and  $\mathbf{n}^* \in \mathbb{S}^2$  the unit vector normal pointing towards the target plane expressed in  $\{\mathcal{A}\}$  (see Fig. 6.1).

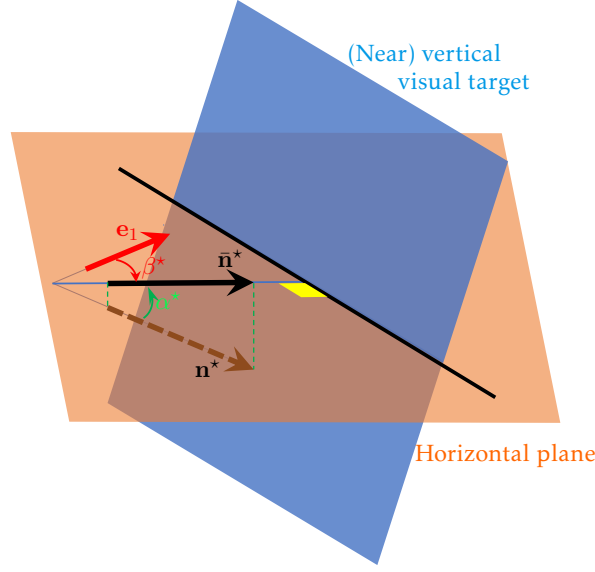


Figure 6.2: Illustration of angles  $\alpha^*$  and  $\beta^*$ . The projection vector  $\bar{\mathbf{n}}^*$  and  $\mathbf{e}_1$  lie on the horizontal plane and  $\bar{\mathbf{n}}^*$  is perpendicular to the intersection line of the two planes.

Denote  $\bar{\mathbf{n}}^*$  the projection vector of  $\mathbf{n}^*$  on the horizontal plane;  $\beta^*$  the angle between  $\bar{\mathbf{n}}^*$  and camera optical axis when taking the reference image; and  $\alpha^*$  the angle between  $\mathbf{n}^*$  and the horizontal plane (see Fig. 6.2). One verifies that

$$\mathbf{n} = [n_1 \ n_2 \ n_3]^\top \triangleq \frac{\mathbf{n}^*}{d^*} = \frac{1}{d^*} \begin{bmatrix} c_{\alpha^*} c_{\beta^*} & c_{\alpha^*} s_{\beta^*} & s_{\alpha^*} \end{bmatrix}^\top \quad (6.2)$$

Since the visual target is within the camera's field of view (FOV) when taking the reference image, one should have  $|\alpha^*|, |\beta^*| < \frac{\pi}{2}$ , which in turn imply that  $n_1 > 0$ .

In addition to the estimation of  $\mathbf{H}$ , it is assumed that an IMU is available to provide measurements of the angular velocity  $\boldsymbol{\Omega}$  together with an approximate of the gravity direction  $\mathbf{R}^\top \mathbf{e}_3$ .

The control objective consists in stabilizing  $\mathbf{H}$  about  $\mathbf{I}_3$  (or equivalently stabilizing  $(\mathbf{R}, \boldsymbol{\xi}_C)$  about  $(\mathbf{I}_3, \mathbf{0})$ ) using only  $(\mathbf{H}, \boldsymbol{\Omega}, \mathbf{R}^\top \mathbf{e}_3)$  as available information. In addition to the lack of the linear velocity measurement, the main issues of control design are related to the unknown terms  $d^*$  and  $\mathbf{n}^*$  involved in the expression (6.1) of  $\mathbf{H}$ . More importantly, we here exploit directly  $\mathbf{H}$  without extracting the usual components  $(\mathbf{R}, \frac{\boldsymbol{\xi}_C}{d^*}, \mathbf{n}^*)$  via a complex and computationally expensive decomposition [56].

## 6.2 Control design

A cascade inner-outer loop control architecture as depicted in Fig. 6.3 is proposed.

- The inner-loop controller (developed in Subsection 6.2.2) governs the rotation dy-

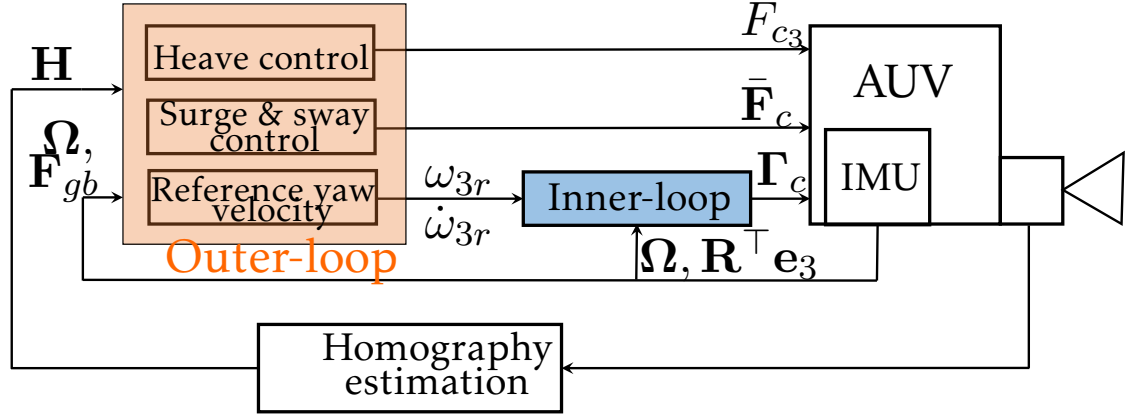


Figure 6.3: Control architecture of the proposed HBVS

namics (3.2) and (5.3b) by defining the torque control vector  $\Gamma_c$  to ensure the almost global asymptotic stability (almost-GAS) of the equilibrium  $(\Omega, \mathbf{R}^\top \mathbf{e}_3) = (\Omega_r, \mathbf{e}_3)$ , where the reference angular velocity  $\Omega_r$  is defined by

$$\Omega_r \triangleq k_g \mathbf{e}_3 \times \mathbf{R}^\top \mathbf{e}_3 + \omega_{3r} \mathbf{e}_3 \quad (6.3)$$

with  $k_g > 0$  positive gain and  $\omega_{3r} \in \mathbb{R}$  the reference yaw angular velocity to be specified by the outer-loop controller. Assume that  $\omega_{3r}$  is bounded by design. Note that  $\dot{\omega}_{3r}$  must be computable so that the feedforward term  $\dot{\Omega}_r$  is also computable by the torque controller.

- The outer-loop controller (developed in Subsection 6.2.1) defines the force control vector  $\mathbf{F}_c$  and the reference yaw angular velocity  $\omega_{3r}$  (used by the inner-loop controller) to fulfill the main objective of stabilizing  $(\mathbf{R}, \xi_C)$  about  $(\mathbf{I}_3, \mathbf{0})$ .

In the sequel we first present the outer-loop control design, which constitutes the main contribution of this thesis. The design for the inner-loop is identical to the case of horizontal visual target which is presented in Section 5.4.2.

### 6.2.1 Outer-loop control design

Let  $\psi$  denote the AUV's yaw angle and  $\mathbf{R}_\psi$  the rotation matrix around AUV's axis  $\vec{e}_3^b$ . Denote

$$\Delta_R = \begin{bmatrix} \Delta_{11} & \Delta_{12} & \Delta_{13} \\ \Delta_{21} & \Delta_{22} & \Delta_{23} \\ \Delta_{31} & \Delta_{32} & \Delta_{33} \end{bmatrix} \triangleq \mathbf{R}^\top - \mathbf{R}_\psi^\top$$

Since  $\mathbf{R}^\top \mathbf{e}_3$  converge to  $\mathbf{e}_3$  as a result of the inner-loop controller, one verifies that  $\Delta_R$  converges to zero. The convergence of  $\mathbf{R}^\top \mathbf{e}_3$  about  $\mathbf{e}_3$  implies that  $\omega_1$  and  $\omega_2$  converge to zero. One then deduces that  $\dot{\Delta}_R$  remains bounded and converges to zero.

Define the following visual errors

$$\boldsymbol{\sigma} \triangleq \begin{bmatrix} -h_{11} + h_{22} \\ -h_{12} - h_{21} \end{bmatrix}, \quad \varrho \triangleq -h_{31}$$

Using (6.1) one deduces

$$\begin{bmatrix} \boldsymbol{\sigma} \\ \varrho \end{bmatrix} = \begin{bmatrix} \mathbf{N} & 0 \\ 0 & n_1 \end{bmatrix} \mathbf{R}^\top \boldsymbol{\xi}_C + \begin{bmatrix} -\Delta_{11} + \Delta_{22} \\ -\Delta_{12} - \Delta_{21} \\ -\Delta_{31} \end{bmatrix} \quad (6.4)$$

with  $\mathbf{N} \triangleq n_1 \mathbf{I}_2 + n_2 \mathbf{S}$ ,  $\mathbf{S} \triangleq \begin{bmatrix} 0 & -1 \\ 1 & 0 \end{bmatrix}$ . This in turn yields

$$\mathbf{R}^\top \boldsymbol{\xi}_C = \begin{bmatrix} \mathbf{N}^{-1} & 0 \\ 0 & \frac{1}{n_1} \end{bmatrix} \begin{bmatrix} \boldsymbol{\sigma} \\ \varrho \end{bmatrix} - \begin{bmatrix} \mathbf{N}^{-1} & 0 \\ 0 & \frac{1}{n_1} \end{bmatrix} \begin{bmatrix} -\Delta_{11} + \Delta_{22} \\ -\Delta_{12} - \Delta_{21} \\ -\Delta_{31} \end{bmatrix} \quad (6.5)$$

Using (6.4) and (6.5) one verifies that

$$\begin{aligned} \dot{\boldsymbol{\sigma}} &= -\omega_3 \mathbf{S} \boldsymbol{\sigma} + \mathbf{N} \bar{\mathbf{V}}_C - \frac{\varrho}{n_1} \mathbf{N} \boldsymbol{\omega}_{12} - \frac{\Delta_{31}}{n_1} \mathbf{N} \boldsymbol{\omega}_{12} \\ &\quad + \omega_3 \mathbf{S} \begin{bmatrix} -\Delta_{11} + \Delta_{22} \\ -\Delta_{12} - \Delta_{21} \end{bmatrix} + \begin{bmatrix} -\dot{\Delta}_{11} + \dot{\Delta}_{22} \\ -\dot{\Delta}_{12} - \dot{\Delta}_{21} \end{bmatrix} \end{aligned} \quad (6.6)$$

$$\begin{aligned} \dot{\varrho} &= n_1 V_3 + n_1 \boldsymbol{\omega}_{12}^\top \mathbf{N}^{-1} \boldsymbol{\sigma} \\ &\quad - n_1 \boldsymbol{\omega}_{12}^\top \mathbf{N}^{-1} \begin{bmatrix} -\Delta_{11} + \Delta_{22} \\ -\Delta_{12} - \Delta_{21} \end{bmatrix} - \dot{\Delta}_{31} \end{aligned} \quad (6.7)$$

with  $\boldsymbol{\omega}_{12} \triangleq [\omega_2 \quad -\omega_1]^\top$ . By denoting  $\bar{\mathbf{P}} \triangleq [P_1 \ P_2]^\top$  (respectively  $\bar{\mathbf{F}}_c \triangleq [F_{c1} \ F_{c2}]^\top$ ), the vector of the two first components of  $\mathbf{P}$  (respectively  $\mathbf{F}_c$ ), and rewriting  $\mathbf{F}_{gb} = F_{gb} [\Delta_{13} \ \Delta_{23} \ 1 + \Delta_{33}]^\top$ , one can write (5.3a) as two interconnected dynamics (surge-and-sway and heave) as follows

$$\dot{\bar{\mathbf{P}}} = -\omega_3 \mathbf{S} \bar{\mathbf{P}} + \bar{\mathbf{F}}_c - \boldsymbol{\omega}_{12} P_3 + F_{gb} \begin{bmatrix} \Delta_{13} \\ \Delta_{23} \end{bmatrix} \quad (6.8a)$$

$$\dot{P}_3 = F_{c3} + F_{gb} + \boldsymbol{\omega}_{12}^\top \bar{\mathbf{P}} + F_{gb} \Delta_{33} \quad (6.8b)$$

with  $P_3$  the third component of  $\mathbf{P}$ . Introduce a new velocity variable<sup>1</sup>

<sup>1</sup> $\bar{\mathbf{V}}$  is used for handling the case with an arbitrary position of the camera w.r.t the CB. The convergence of  $\omega_{3r}$  to zero then results in  $\bar{\mathbf{V}} \rightarrow \bar{\bar{\mathbf{V}}}$ .

## 6.2. Control design

$$\bar{\bar{\mathbf{V}}} \triangleq \bar{\mathbf{V}} + \omega_{3r} \mathbf{S} \bar{\mathbf{r}}_C \quad (6.9)$$

One verifies that

$$\bar{\mathbf{V}}_C = \bar{\bar{\mathbf{V}}} + (\omega_3 - \omega_{3r}) \mathbf{S} \bar{\mathbf{r}}_C + r_{C3} \omega_{12} \quad (6.10)$$

Define the following new control force

$$\bar{\bar{\mathbf{F}}}_c \triangleq \bar{\mathbf{F}}_c + (\dot{\omega}_{3r} \mathbf{I}_2 + \omega_{3r}^2 \mathbf{S}) \bar{\mathbf{M}} \mathbf{S} \bar{\mathbf{r}}_C \quad (6.11)$$

Denoting  $\bar{\bar{\mathbf{P}}} \triangleq \bar{\mathbf{M}} \bar{\bar{\mathbf{V}}}$  and using (6.9), (6.10), (6.11), Subsystem (6.6)+ (6.8a) and Subsystem (6.7)+(6.8b) can be rewritten as

$$\begin{cases} \dot{\boldsymbol{\sigma}} = -\omega_3 \mathbf{S} \boldsymbol{\sigma} + \mathbf{N} \bar{\mathbf{M}}^{-1} \bar{\bar{\mathbf{P}}} - \frac{\varrho}{n_1} \mathbf{N} \boldsymbol{\omega}_{12} + \boldsymbol{\varepsilon}_1 \\ \dot{\bar{\bar{\mathbf{P}}}} = -\omega_3 \mathbf{S} \bar{\bar{\mathbf{P}}} + \bar{\bar{\mathbf{F}}}_c - P_3 \boldsymbol{\omega}_{12} + \boldsymbol{\varepsilon}_2 \end{cases} \quad (6.12)$$

$$\begin{cases} \dot{\varrho} = \frac{n_1}{m_3} P_3 + n_1 \boldsymbol{\omega}_{12}^\top \mathbf{N}^{-1} \boldsymbol{\sigma} + \varepsilon_3 \\ \dot{P}_3 = F_{c3} + F_{gb} + \boldsymbol{\omega}_{12}^\top \bar{\bar{\mathbf{P}}} + \varepsilon_4 \end{cases} \quad (6.13)$$

with bounded vanishing terms

$$\begin{cases} \boldsymbol{\varepsilon}_1 \triangleq (\omega_3 - \omega_{3r}) \mathbf{N} \mathbf{S} \bar{\mathbf{r}}_C + r_{C3} \mathbf{N} \boldsymbol{\omega}_{12} - \frac{\Delta_{31}}{n_1} \mathbf{N} \boldsymbol{\omega}_{12} \\ \quad + \omega_3 \mathbf{S} \begin{bmatrix} -\Delta_{11} + \Delta_{22} \\ -\Delta_{12} - \Delta_{21} \end{bmatrix} + \begin{bmatrix} -\dot{\Delta}_{11} + \dot{\Delta}_{22} \\ -\dot{\Delta}_{12} - \dot{\Delta}_{21} \end{bmatrix} \\ \boldsymbol{\varepsilon}_2 \triangleq F_{gb} \begin{bmatrix} \Delta_{13} \\ \Delta_{23} \end{bmatrix} \\ \boldsymbol{\varepsilon}_3 \triangleq -\dot{\Delta}_{31} - n_1 \boldsymbol{\omega}_{12}^\top \mathbf{N}^{-1} \begin{bmatrix} -\Delta_{11} + \Delta_{22} \\ -\Delta_{12} - \Delta_{21} \end{bmatrix} \\ \boldsymbol{\varepsilon}_4 \triangleq -\omega_{3r} \boldsymbol{\omega}_{12}^\top \bar{\mathbf{M}} \mathbf{S} \bar{\mathbf{r}}_C + F_{gb} \Delta_{33} \end{cases}$$

One observes that systems (6.12) and (6.13) are interconnected (see Fig. 6.4). In the sequel we first neglect all coupling terms in the outer-loop control design. This is intuitively guided by the fact that these terms are multiplicative terms by vanishing variables  $\omega_1$  and  $\omega_2$ . Then, a more complete stability analysis for this interconnected system will be carried out thereafter.

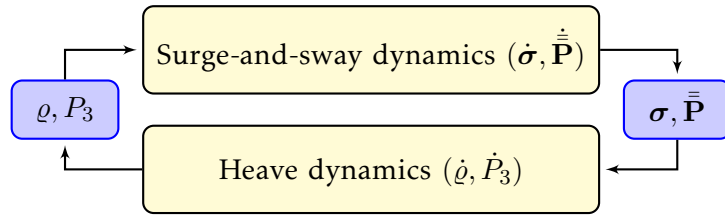


Figure 6.4: Interconnected translational dynamics

### 6.2.1.1 Heave control design

Similarly to the approach proposed in [62], the altitude (heave) control can be designed independently from surge-and-sway and yaw control design.

**Proposition 5.** *Consider System (6.13) where the coupling terms involving  $\sigma$  and  $\bar{\mathbf{P}}$  are neglected. Introduce the augmented system*

$$\dot{\hat{\varrho}} = -k_{13}(\hat{\varrho} - \varrho), \quad \hat{\varrho}(0) = \varrho(0)$$

with  $k_{13} > 0$ . Apply the control force

$$F_{c3} = m_3 k_{23} \hat{\varrho} - m_3 k_{33} \varrho - (mg - F_b)$$

with  $k_{33} > k_{23} > 0$ . Then, the equilibrium  $(\hat{\varrho}, \varrho, P_3) = (0, 0, 0)$  of the controlled system is globally asymptotically stable (GAS) with exponential convergence rate after some time instant  $T > 0$ .

**Proof.** The considered system can be rewritten as

$$\dot{\mathbf{x}} = \bar{\mathbf{A}}\mathbf{x} + \boldsymbol{\varepsilon}_{34} \tag{6.14}$$

with

$$\mathbf{x} \triangleq \begin{bmatrix} \hat{\varrho} \\ \varrho \\ P_3 \end{bmatrix}, \quad \bar{\mathbf{A}} \triangleq \begin{bmatrix} -k_{13} & k_{13} & 0 \\ 0 & 0 & \frac{n_1}{m_3} \\ m_3 k_{23} & -m_3 k_{33} & 0 \end{bmatrix}, \quad \boldsymbol{\varepsilon}_{34} \triangleq \begin{bmatrix} 0 \\ \varepsilon_3 \\ \varepsilon_4 \end{bmatrix} \tag{6.15}$$

From there, the proof is straightforward since the nominal system  $\dot{\mathbf{x}} = \bar{\mathbf{A}}\mathbf{x}$  is Hurwitz (using  $k_{33} > k_{23} > 0$ ) while the perturbation terms  $\varepsilon_3$  and  $\varepsilon_4$  converge to zero.  $\square$

### 6.2.1.2 Surge-and-sway control design

Consider System (6.12) and neglect all coupling terms involving  $\varrho$  and  $P_3$ . Introduce the following augmented system

$$\dot{\hat{\boldsymbol{\sigma}}} = -\omega_3 \mathbf{S} \hat{\boldsymbol{\sigma}} - k_1 \hat{\boldsymbol{\sigma}} + k_1 \boldsymbol{\sigma}, \quad \hat{\boldsymbol{\sigma}}(0) = \boldsymbol{\sigma}(0) \tag{6.16}$$

with  $k_1 > 0$ . Apply the control force

$$\bar{\mathbf{F}}_c = k_2 \bar{\mathbf{M}} \hat{\boldsymbol{\sigma}} - k_3 \bar{\mathbf{M}} \boldsymbol{\sigma} \tag{6.17}$$

## 6.2. Control design

with  $k_2, k_3 > 0$ . Then, the controlled surge-and-sway subsystem is given by

$$\begin{cases} \dot{\hat{\sigma}} = -\omega_3 \mathbf{S} \hat{\sigma} - k_1 \hat{\sigma} + k_1 \sigma \\ \dot{\sigma} = -\omega_3 \mathbf{S} \sigma + \mathbf{N} \bar{\mathbf{M}}^{-1} \bar{\mathbf{P}} + \varepsilon_1 \\ \dot{\bar{\mathbf{P}}} = -\omega_3 \mathbf{S} \bar{\mathbf{P}} + k_2 \bar{\mathbf{M}} \hat{\sigma} - k_3 \bar{\mathbf{M}} \sigma + \varepsilon_2 \end{cases} \quad (6.18)$$

Denote

$$\begin{aligned} \mathbf{X}_1 &= \begin{bmatrix} x_{11} \\ x_{12} \end{bmatrix} \triangleq \hat{\sigma}, \quad \mathbf{X}_2 = \begin{bmatrix} x_{21} \\ x_{22} \end{bmatrix} \triangleq \sigma, \quad \mathbf{X}_3 = \begin{bmatrix} x_{31} \\ x_{32} \end{bmatrix} \triangleq \bar{\mathbf{P}} \\ \mathbf{X} &\triangleq \begin{bmatrix} \mathbf{X}_1 \\ \mathbf{X}_2 \\ \mathbf{X}_3 \end{bmatrix}, \quad \varepsilon_{12} \triangleq \begin{bmatrix} \varepsilon_1 \\ \varepsilon_2 \end{bmatrix}, \quad \bar{\mathbf{S}} \triangleq \begin{bmatrix} \mathbf{S} & 0 & 0 \\ 0 & \mathbf{S} & 0 \\ 0 & 0 & \mathbf{S} \end{bmatrix} \end{aligned} \quad (6.19)$$

$$\mathbf{A} \triangleq \begin{bmatrix} -k_1 \mathbf{I}_2 & k_1 \mathbf{I}_2 & 0 \\ 0 & 0 & n_1 \bar{\mathbf{M}}^{-1} \\ k_2 \bar{\mathbf{M}} & -k_3 \bar{\mathbf{M}} & 0 \end{bmatrix}, \quad \mathbf{B} \triangleq \begin{bmatrix} 0 & 0 & 0 \\ 0 & 0 & n_2 \bar{\mathbf{S}} \bar{\mathbf{M}}^{-1} \\ 0 & 0 & 0 \end{bmatrix} \quad (6.20)$$

System (6.18) can be rewritten as

$$\dot{\mathbf{X}} = -\omega_{3r} \bar{\mathbf{S}} \mathbf{X} + \mathbf{A} \mathbf{X} + \mathbf{B} \mathbf{X} - \tilde{\omega}_3 \bar{\mathbf{S}} \mathbf{X} + \varepsilon_{12} \quad (6.21)$$

with  $\tilde{\omega}_3 \triangleq \omega_3 - \omega_{3r}$ . In the sequel we will specify a sufficient condition ensuring that the origin of System (6.21) is GAS.

**Lemma 2.** Consider system

$$\dot{\mathbf{X}} = \mathbf{A} \mathbf{X} + \mathbf{B} \mathbf{X} \quad (6.22)$$

with  $\mathbf{A}$  and  $\mathbf{B}$  defined in (6.20). Assume that the reference image is captured with a reference heading angle satisfying

$$|\beta^*| < \beta_{max}^* \triangleq \arctan\left(\frac{1}{\sqrt{1+\sqrt{2}}}\right) \approx 32.8^\circ \quad (6.23)$$

Then, there exist  $\bar{k}_1 > 0$  large and  $\epsilon > 0$  small enough, with  $\bar{k}_1$  and  $\epsilon$  depending on  $(\beta_{max}^*, |\beta^*|)$ , such that system (6.22) is globally exponentially stable (GES) provided that  $k_1 > \bar{k}_1$ ,  $1 < k_3/k_2 < 1 + \epsilon$ .

The proof is given in Section 6.2.3.1.

**Proposition 6.** Consider System (6.21). Assume that all assumptions of Lemma 2 hold. Assume that the inner-loop controller ensures the uniform boundedness and convergence to zero of  $\varepsilon_{12}$  and  $\tilde{\omega}_3$ . Then, there exists a positive number  $\varpi$  such that if  $\sup |\omega_{3r}| < \varpi$  then the equilibrium  $\mathbf{X} = \mathbf{0}$  is GAS with exponential convergence rate after some time instant  $T > 0$ .

The proof is given in Section 6.2.3.2.

So far the outer-loop control design and associated stability analysis have been carried out for systems (6.12) and (6.13) by neglecting all coupling terms. Next, stability analysis for the full interconnected system will be developed. The interconnected system (6.12)–(6.13) can be rewritten as

$$\begin{cases} \dot{\mathbf{X}} = -\omega_3(t)\bar{\mathbf{S}}\mathbf{X} + \mathbf{A}\mathbf{X} + \mathbf{B}\mathbf{X} + \mathbf{E}_1\mathbf{x} + \boldsymbol{\varepsilon}_{12} \\ \dot{\mathbf{x}} = \bar{\mathbf{A}}\mathbf{x} + \mathbf{E}_2\mathbf{X} + \boldsymbol{\varepsilon}_{34} \end{cases} \quad (6.24)$$

with vanishing matrices

$$\mathbf{E}_1 \triangleq \begin{bmatrix} \mathbf{0} & \mathbf{0} & \mathbf{0} \\ \mathbf{0} & -\frac{\mathbf{N}}{n_1}\boldsymbol{\omega}_{12} & \mathbf{0} \\ \mathbf{0} & \mathbf{0} & -\boldsymbol{\omega}_{12} \end{bmatrix}, \quad \mathbf{E}_2 \triangleq \begin{bmatrix} \mathbf{0} & \mathbf{0} & \mathbf{0} \\ \mathbf{0} & n_1\boldsymbol{\omega}_{12}^\top\mathbf{N}^{-1} & \mathbf{0} \\ \mathbf{0} & \mathbf{0} & \boldsymbol{\omega}_{12}^\top \end{bmatrix} \quad (6.25)$$

**Theorem 1.** *Consider the interconnected system (6.24). Assume that all assumptions in Propositions 5 and 6 hold. Assume that all outer-loop control gains and  $\omega_{3r}$  are chosen as in Propositions 5 and 6. Assume that the inner-loop controller ensures the uniform boundedness and convergence to zero of  $\boldsymbol{\varepsilon}_{12}$ ,  $\boldsymbol{\varepsilon}_{34}$  and  $\tilde{\omega}_3$ . Then, the equilibrium  $(\mathbf{X}, \mathbf{x}) = (\mathbf{0}, \mathbf{0})$  is GAS with exponential convergence rate after some time instant.*

**Proof.** As a result of Propositions 5 and 6, there exists a time instant  $T_1 > 0$  and some positive numbers  $\alpha_1, \alpha_2, \beta_1, \beta_2$  such that  $\forall t \geq T_1$  one has

$$\begin{aligned} \frac{d}{dt}(\mathbf{X}^\top \mathbf{D}\mathbf{X}) &\leq -\alpha_1|\mathbf{X}|^2 + \beta_1\|\mathbf{E}_1\|\|\mathbf{X}\|\|\mathbf{x}\| \\ \frac{d}{dt}(\mathbf{x}^\top \bar{\mathbf{D}}\mathbf{x}) &\leq -\alpha_2\|\mathbf{x}\|^2 + \beta_2\|\mathbf{E}_2\|\|\mathbf{X}\|\|\mathbf{x}\| \end{aligned}$$

with  $\mathbf{D}$  given in the proof of Lemma 2 and  $\bar{\mathbf{D}}$  the symmetric positive matrix solution to the Lyapunov equation  $\bar{\mathbf{D}}\bar{\mathbf{A}} + \bar{\mathbf{A}}^\top\bar{\mathbf{D}} = -\mathbf{I}_3$ . Subsequently, the time-derivative of the aggregate Lyapunov function  $\mathcal{L} \triangleq \mathbf{X}^\top \mathbf{D}\mathbf{X} + \mathbf{x}^\top \bar{\mathbf{D}}\mathbf{x}$  satisfies

$$\dot{\mathcal{L}}(t \geq T_1) \leq -\alpha_1|\mathbf{X}|^2 - \alpha_2\|\mathbf{x}\|^2 + (\beta_1\|\mathbf{E}_1\| + \beta_2\|\mathbf{E}_2\|)\|\mathbf{X}\|\|\mathbf{x}\|$$

Since  $\mathbf{E}_1$  and  $\mathbf{E}_2$  converge uniformly to zero, there exists another time instant  $T_2 > T_1$  such that  $\forall t \geq T_2$  the cross term is dominated by the quadratic terms. Thus, there exists a positive number  $\nu$  such that  $\dot{\mathcal{L}}(t \geq T_2) \leq -\nu\mathcal{L}(t \geq T_2)$ , implying the exponential convergence of  $(\mathbf{X}, \mathbf{x})$  to zero.  $\square$

### 6.2.1.3 Control design of the reference yaw angular velocity

The previous parts of outer-loop control design ensure the convergence of  $\xi_C$  to zero. In view of the definition (6.1) of the homography,  $\mathbf{H}$  converges to  $\mathbf{R}^\top$ , which in turn converges to  $\mathbf{R}_\psi^\top$  as a consequence of the inner-loop controller. Therefore, the component  $h_{12}$  of  $\mathbf{H}$  converges to  $\sin \psi$ . It, thus, can be exploited for the design of  $\omega_{3r}$  for ensuring the convergence of  $\mathbf{R}$  to  $\mathbf{I}$ . Note that the whole control design process in the previous subsections is based on the assumption about the boundedness of  $\omega_{3r}$  (see Proposition 6). The design of  $\omega_{3r}$  and associated stability analysis (omitted due to space limitation) proceeds identically to [29].

**Proposition 7.** *Assume that the inner-loop torque control  $\Gamma_c$  ensures the almost-GAS of the equilibrium  $(\Omega, \mathbf{R}^\top \mathbf{e}_3) = (\Omega_r, \mathbf{e}_3)$ , with  $\Omega_r$  defined by (6.3) combined with  $\omega_{3r}$  (involved in (6.3)) solution to the following system*

$$\dot{\omega}_{3r} = -k_{\Theta 2}\omega_{3r} - k_{\Theta 1}\text{sat}^{\Delta_\Theta}(h_{12}), \quad \omega_{3r}(0) \in \mathbb{R} \quad (6.26)$$

with positive numbers  $k_{\Theta 1}, k_{\Theta 2}, \Delta_\Theta$  satisfying  $\frac{k_{\Theta 1}}{k_{\Theta 2}}\Delta_\Theta < \varpi$  where  $\varpi$  is defined from Proposition 6. Apply the outer-loop force control  $\mathbf{F}_c = \left[ \bar{\mathbf{F}}_c^\top \ F_{c3} \right]^\top$  where  $\bar{\mathbf{F}}_c$  is given by (6.11)+(6.17) with control gains  $k_2, k_3$  specified in Lemma 2 and  $F_{c3}$  is defined in Proposition 5. Then, the equilibrium  $(\mathbf{R}, \xi_C) = (\mathbf{I}_3, \mathbf{0})$  is almost-GAS.

## 6.2.2 Inner-loop control design

The more involved part concerning the outer-loop control design has been presented. The design of an effective inner-loop torque controller that ensures the stability of the equilibrium  $(\Omega, \mathbf{R}^\top \mathbf{e}_3) = (\Omega_r, \mathbf{e}_3)$ , with  $\Omega_r$  defined by (6.3) combined with (6.26) proceeds identically the Section 5.4.2 for the case of downward-looking camera.

## 6.2.3 Analyses for Chapter 6

### 6.2.3.1 Proof of Lemma 2

One verifies that  $\mathbf{A}$  is Hurwitz if  $k_3 > k_2 > 0$  by applying Routh-Hurwitz criterion on its characteristic polynomial  $P_{\mathbf{A}}(\lambda) = (\lambda^3 + k_1\lambda^2 + n_1k_3\lambda + n_1(k_3 - k_2)k_1)^2$ .

Consider the following positive diagonal matrix

$$\mathbf{Q} = \begin{bmatrix} q\mathbf{I}_2 & 0 & 0 \\ 0 & q\mathbf{I}_2 & 0 \\ 0 & 0 & \bar{\mathbf{M}}^{-2} \end{bmatrix}, \quad q > 0$$

According to the Lyapunov theorem [42], there exists a unique  $\mathbf{D} = \mathbf{D}^\top > 0$  such that

$\mathbf{DA} + \mathbf{A}^\top \mathbf{D} = -\mathbf{Q}$ . Straightforward computations result in

$$\mathbf{D} = \frac{1}{2} \begin{bmatrix} d_{11} \mathbf{I}_2 & d_{12} \mathbf{I}_2 & d_{13} \bar{\mathbf{M}}^{-1} \\ d_{12} \mathbf{I}_2 & d_{22} \mathbf{I}_2 & d_{23} \bar{\mathbf{M}}^{-1} \\ d_{13} \bar{\mathbf{M}}^{-1} & d_{23} \bar{\mathbf{M}}^{-1} & d_{33} \bar{\mathbf{M}}^{-2} \end{bmatrix} \quad (6.27)$$

with

$$\begin{aligned} d_{11} &\triangleq \frac{1}{k_1} \left( \frac{k_2}{n_1} + \frac{k_3+k_2}{k_3-k_2} q \right) \\ d_{12} &\triangleq -\frac{1}{k_1} \left( \frac{k_3}{n_1} + q \right) \\ d_{13} &\triangleq \frac{1}{n_1} + \frac{2q}{k_3-k_2} \\ d_{22} &\triangleq \frac{k_1}{n_1} \left( \frac{k_3}{k_2} - 1 \right) \left( \frac{1}{n_1} + \frac{2q}{k_3-k_2} \right) + \frac{k_3}{k_1 k_2} \left( \frac{k_3}{n_1} + q \right) \\ d_{23} &\triangleq -\frac{1}{n_1} \\ d_{33} &\triangleq \frac{n_1}{k_1 k_2} \left( \frac{k_3}{n_1} + q \right) + \frac{k_1}{k_2} \left( \frac{1}{n_1} + \frac{2q}{k_3-k_2} \right) \end{aligned} \quad (6.28)$$

Consider the Lyapunov function  $\mathcal{L}_1 \triangleq \mathbf{X}^\top \mathbf{D} \mathbf{X}$ , with  $\mathbf{D}$  given by (6.27)–(6.28). After some straightforward computations, one deduces

$$\begin{aligned} \dot{\mathcal{L}}_1 &= \mathbf{X}^\top (\mathbf{DA} + \mathbf{A}^\top \mathbf{D}) \mathbf{X} + \mathbf{X}^\top (\mathbf{DB} + \mathbf{B}^\top \mathbf{D}) \mathbf{X} \\ &= -\left( \frac{x_{31}^2}{m_1^2} + \frac{x_{32}^2}{m_2^2} \right) \left[ 1 - \frac{n_2^2}{4q} (d_{12}^2 + d_{22}^2) \right] \\ &\quad - \left( \sqrt{q} x_{11} + \frac{d_{12} n_2}{2\sqrt{q} m_2} x_{32} \right)^2 - \left( \sqrt{q} x_{12} - \frac{d_{12} n_2}{2\sqrt{q} m_1} x_{31} \right)^2 \\ &\quad - \left( \sqrt{q} x_{21} + \frac{d_{22} n_2}{2\sqrt{q} m_2} x_{32} \right)^2 - \left( \sqrt{q} x_{22} - \frac{d_{22} n_2}{2\sqrt{q} m_1} x_{31} \right)^2 \end{aligned} \quad (6.29)$$

Now the task consists in finding sufficient conditions for  $(k_1, k_2, k_3, q)$  so that

$$1 > \frac{n_2^2}{4q} (d_{12}^2 + d_{22}^2) \quad (6.30)$$

which ensures that  $\dot{\mathcal{L}}$  is negative definite and, thus, the origin of System (6.22) is GAS. Note that  $d_{12}$  and  $d_{22}$  are functions of  $(k_1, k_2, k_3, q)$  as defined in (6.28).

From (6.2) and (6.23), one verifies that  $\frac{n_1^2}{n_2^2} > 1 + \sqrt{2}$ . Define  $\delta \triangleq \frac{n_1^2}{n_2^2} - (1 + \sqrt{2}) > 0$ . One verifies that  $\delta = \frac{1}{\arctan^2 \beta^*} - \frac{1}{\arctan^2 \beta_{max}^*}$ . Rewrite  $k_3 = \gamma k_2$  (with  $\gamma > 1$ ) and  $k_1 = \alpha k_2$  (with  $\alpha > 0$ ). Denote

$$\zeta_1 \triangleq \frac{\alpha(\gamma-1)k_2}{n_1^2} \frac{\alpha n_1}{\gamma^2}, \quad \zeta_2 \triangleq \frac{n_1 \gamma}{\alpha^2 k_2}, \quad \bar{\zeta} \triangleq \zeta_2 (1 - \zeta_1 \zeta_2)$$

After some computations, one verifies that inequality (6.30) is equivalent to

$$\begin{aligned} &\alpha^2 \left[ \bar{\zeta}^2 + (2 + \zeta_2)^2 \right] q^2 + \frac{1}{\alpha^2} \left[ \frac{1}{(1-\zeta_1 \zeta_2)^2} + \frac{(\zeta_1+1)^2}{(1-\zeta_1 \zeta_2)^4} \right] \\ &+ 2 \left[ \zeta_2 + \frac{(\zeta_1+1)(\zeta_2+2)}{(1-\zeta_1 \zeta_2)^2} - 2 - 2\sqrt{2} - 2\delta \right] q < 0 \end{aligned} \quad (6.31)$$

Denote

## 6.2. Control design

$$\zeta \triangleq \begin{bmatrix} \zeta_1 & \zeta_2 \end{bmatrix}^\top, \quad g_1(\zeta) \triangleq \zeta_2 + \frac{(\zeta_1+1)(\zeta_2+2)}{(1-\zeta_1\zeta_2)^2}$$

$$g_2(\zeta) \triangleq \left[ \zeta_2^2 + \frac{(2+\zeta_2)^2}{(1-\zeta_1\zeta_2)^2} \right] \left[ 1 + \frac{(\zeta_1+1)^2}{(1-\zeta_1\zeta_2)^2} \right]$$

The condition for inequality (6.31) having solution  $q > 0$  is

$$\begin{cases} \Delta' = (g_1(\zeta) - 2 - 2\sqrt{2} - 2\delta)^2 - g_2(\zeta) > 0 \\ -(g_1(\zeta) - 2 - 2\sqrt{2} - 2\delta) > 0 \end{cases}$$

or equivalently

$$\delta > g(\zeta) \triangleq \frac{g_1(\zeta)-2}{2} + \frac{\sqrt{g_2(\zeta)-2\sqrt{2}}}{2} \quad (6.32)$$

We will show that we can always choose positive control gains  $k_1, k_2, k_3$  (i.e.  $\zeta_1, \zeta_2$ ) such that condition (6.32) holds. One verifies that  $g_1(\zeta) > 2$ ,  $g_2(\zeta) > 8$ ,  $g(\zeta) > 0$ , with  $\zeta_1, \zeta_2 > 0$ . One also has

$$\lim_{\zeta_1, \zeta_2 \rightarrow 0^+} g_1(\zeta) = 2, \quad \lim_{\zeta_1, \zeta_2 \rightarrow 0^+} g_2(\zeta) = 8$$

and consequently

$$\lim_{\zeta_1, \zeta_2 \rightarrow 0^+} g(\zeta) = 0 \quad (6.33)$$

From (6.33), with  $g(\zeta)$  defined in (6.32), one deduces that  $\forall \delta > 0$  there exists  $\zeta^* > 0$  such that  $g(\zeta) < \delta$  whenever  $|\zeta| < \zeta^*$ . This implies that there always exist  $\zeta_1 = \frac{n_1 k_3}{k_1^2}$  and  $\zeta_2 = \left(1 - \frac{k_2}{k_3}\right) \frac{1}{\zeta_1}$  small enough such that  $\sqrt{\zeta_1^2 + \zeta_2^2} < \zeta^*$  and, consequently, (6.30) is satisfied. Therefore, there exist  $\bar{k}_1 > 0$  large and  $\epsilon > 0$  small enough such that inequality (6.30) has solution  $q > 0$  provided that  $k_1 > \bar{k}_1$ ,  $1 < \frac{k_3}{k_2} < 1 + \epsilon$ .

### 6.2.3.2 Proof of Proposition 6

The system (6.21) can be rewritten in the following particular time-varying cascaded interconnection studied by Panteley and Loria [67]:

$$\dot{\mathbf{x}}_1 = \mathbf{f}_1(t, \mathbf{x}_1) + \mathbf{G}\mathbf{x}_2 \quad (6.34)$$

where  $\mathbf{x}_1 = \mathbf{X}$ ,  $\mathbf{x}_2 = [\mathbf{0}, \boldsymbol{\varepsilon}_1^\top, \boldsymbol{\varepsilon}_2^\top]^\top$ ,  $\mathbf{G}$  is an identity matrix in our case, and the function  $\mathbf{f}_1(t, \mathbf{x}_1)$  can be easily deduced as follows:

$$\mathbf{f}_1(t, \mathbf{x}_1) = \dot{\mathbf{X}} = -\omega_{3r}(t)\bar{\mathbf{S}}\mathbf{X} + \mathbf{A}\mathbf{X} + \mathbf{B}\mathbf{X} - \tilde{\omega}_3\bar{\mathbf{S}}\mathbf{X} \quad (6.35)$$

System (6.34) can be seen as a nominal system  $\dot{\mathbf{x}}_1 = \mathbf{f}_1(t, \mathbf{x}_1)$  perturbed by the output  $\mathbf{x}_2$  of an exponentially stable system. In view of [67, Theorem 3] corresponding to the case where the function  $\mathbf{f}_1(t, \mathbf{x}_1)$  grows faster than  $\mathbf{G}$ , it suffices to prove that the nominal system  $\dot{\mathbf{x}}_1 = \mathbf{f}_1(t, \mathbf{x}_1)$  (i.e. setting  $\boldsymbol{\varepsilon}_1(t) \equiv 0$  and  $\boldsymbol{\varepsilon}_2(t) \equiv 0$  in (6.21)) is uniformly globally asymptotically stable. This allows us to avoid using input-to-state stability (ISS) argu-

ment and, subsequently, the need of constructing of a strict Lyapunov function for the nominal system.

As a consequence of Lemma 2, there exists  $\nu > 0$  such that

$$\mathbf{X}^\top(\mathbf{A}^\top\mathbf{D}+\mathbf{D}\mathbf{A}+\mathbf{B}^\top\mathbf{D}+\mathbf{D}\mathbf{B})\mathbf{X} \leq -\nu|\mathbf{X}|^2$$

Since  $\tilde{\omega}_3$  converges to zero, for any  $0 < \varepsilon_\omega < 1$  there exists  $T > 0$  such that  $\forall \tau \geq T$ ,  $|\tilde{\omega}_3(\tau)| \leq \frac{\varepsilon_\omega \nu}{2\|\mathbf{D}\|}$  and, subsequently,

$$\dot{\mathcal{L}}_1(\tau \geq T) \leq -(1 - \varepsilon_\omega)\nu|\mathbf{X}|^2 + 2(\sup|\omega_{3r}|)\|\mathbf{D}\|\|\mathbf{X}\|^2$$

If  $\sup|\omega_{3r}| < \varpi \triangleq \frac{1-\varepsilon_\omega}{2\|\mathbf{D}\|}\nu$ , there exists  $\nu_1 > 0$  such that  $\dot{\mathcal{L}}_1(\tau \geq T) \leq -\nu_1\mathcal{L}_1(\tau \geq T)$ , implying the exponential convergence of  $\mathbf{X}$  to zero.

### 6.3 Simulation results

The proposed control approach has been tested in simulation using a realistic model where the physical parameters are given in Tab. 6.1.

The robustness of the proposed controller with respect to model uncertainties are tested by using the ‘‘erroneous’’ estimated parameters  $\hat{\mathbf{J}}, \hat{\mathbf{M}}$  given by

$$\begin{cases} \hat{\mathbf{M}} = m\mathbf{I}_3 + \hat{\mathbf{M}}_a = \text{diag}(17.868, 23.868, 21.024) [kg] \\ \hat{\mathbf{J}} = \hat{\mathbf{J}}_0 + \hat{\mathbf{J}}_a = \text{diag}(0.3105, 0.8486, 1.0) [kg.m^2] \end{cases}$$

The homography  $\mathbf{H}$  is directly computed using (6.1) with  $d^* = 1 [m]$  and  $\mathbf{n}^* = [0.8259, 0.5364, -0.1736]^\top$  corresponding to  $(\alpha^*, \beta^*) = (10^\circ, 33^\circ)$ . The initial conditions are chosen as follows:  $\boldsymbol{\xi}_C(0) = [-1, -0.5, -0.5]^\top [m]$ ,  $\mathbf{R}(0) = \mathbf{R}_{\{\text{roll}=10^\circ, \text{pitch}=-10^\circ, \text{yaw}=45^\circ\}}$ ,  $\mathbf{V}(0) = \boldsymbol{\Omega}(0) = \mathbf{0}$ . The initial yaw and camera’s position are chosen rather large to verify the large stability domain of the proposed controller. Control parameters and gains<sup>2</sup> are summarized in Table 6.2.

The performance of proposed controller is illustrated by Figs. 6.5–6.8. One observes from Fig. 6.5 a smooth convergence to zero of the position and orientation errors. Fig. 6.6 shows the fast convergence to zero of the visual error  $(\boldsymbol{\sigma}, \varrho)$  and their augmented variables  $(\hat{\boldsymbol{\sigma}}, \hat{\varrho})$ . The time evolutions of the control force and torque are shown in Fig. 6.7. All components of the control force and torque converge to zero except the third component of the control force that allows for compensating for  $\mathbf{F}_{gb}$ . The convergence of the angular velocity  $\boldsymbol{\Omega}$  to the reference value  $\boldsymbol{\Omega}_r$  as depicted in Fig. 6.8 shows the effectiveness of the inner-loop controller.

---

<sup>2</sup>Tuned by applying the classical pole placement technique when considering  $\mathbf{n} \equiv \mathbf{e}_1$ .

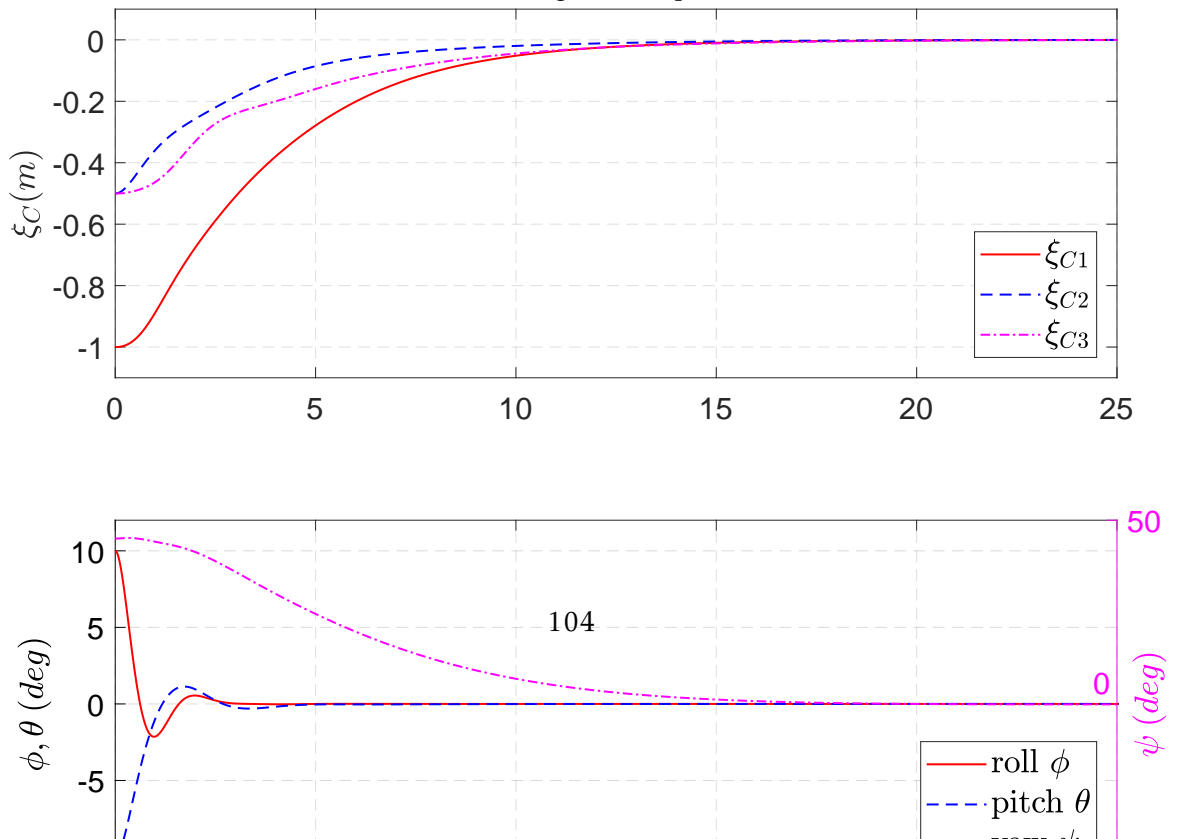
### 6.3. Simulation results

Specification	Numerical value
$m$ [kg]	16
$F_b$ [N]	$1.01mg$
$l$ [m]	0.025
$\mathbf{r}_C$ [m]	[0.2 0 0.1]
$\mathbf{J}_0$ [kg.m <sup>2</sup> ]	$\begin{bmatrix} 0.0842 & 0.004 & 0.005 \\ 0.004 & 0.2643 & 0.007 \\ 0.005 & 0.007 & 0.3116 \end{bmatrix}$
$\mathbf{J}_a$ [kg.m <sup>2</sup> ]	$\begin{bmatrix} 0.1 & 0.005 & 0.006 \\ 0.005 & 0.25 & 0.008 \\ 0.006 & 0.008 & 0.3 \end{bmatrix}$
$\mathbf{M}_a$ [kg]	$\begin{bmatrix} 1.39 & 0.10 & 0.12 \\ 0.10 & 4.26 & 0.13 \\ 0.12 & 0.13 & 4.02 \end{bmatrix}$
$\Xi = m\mathbf{l}\mathbf{e}_{3\times}$ [kg.m]	$0.4\mathbf{e}_{3\times}$
$\mathbf{D}_{Vl}$ [kg.s <sup>-1</sup> ]	$\text{diag}(5.85, 9.21, 11.03)$
$\mathbf{D}_{Vq}$ [kg.m <sup>-1</sup> ]	$\text{diag}(36.57, 57.58, 68.97)$
$\mathbf{D}_{\Omega l}$ [kg.m <sup>2</sup> .s <sup>-1</sup> ]	$\text{diag}(0.01126, 0.01855, 0.01701)$
$\mathbf{D}_{\Omega q}$ [N.m]	$\text{diag}(0.0053, 0.0130, 0.0118)$

Table 6.1: Specifications of the simulated AUV

Controller	Gains and other parameters
Proposition 5	$k_{13} = 3s_1, k_{23} = \frac{8}{3}\frac{s_1^2}{n_1}, k_{33} = 3\frac{s_1^2}{n_1}, s_1 = 1$
Proposition 6	$k_1 = 3s_2, k_2 = \frac{8}{3}\frac{s_2^2}{n_1}, k_3 = 3\frac{s_2^2}{n_1}, s_2 = 1.1$
Proposition 7	$k_g = 1, k_{\Theta 1} = 0.0625, k_{\Theta 2} = 0.5, \Delta_{\Theta} = 1$
Proposition 4	$\mathbf{K}_{\Omega} = 3\hat{\mathbf{J}}, K_{i\Omega} = 0$
Lemma 1	$a_0 = 0.5, k_0 = 20, \eta_3 = 8$

Table 6.2: Control gains and parameters



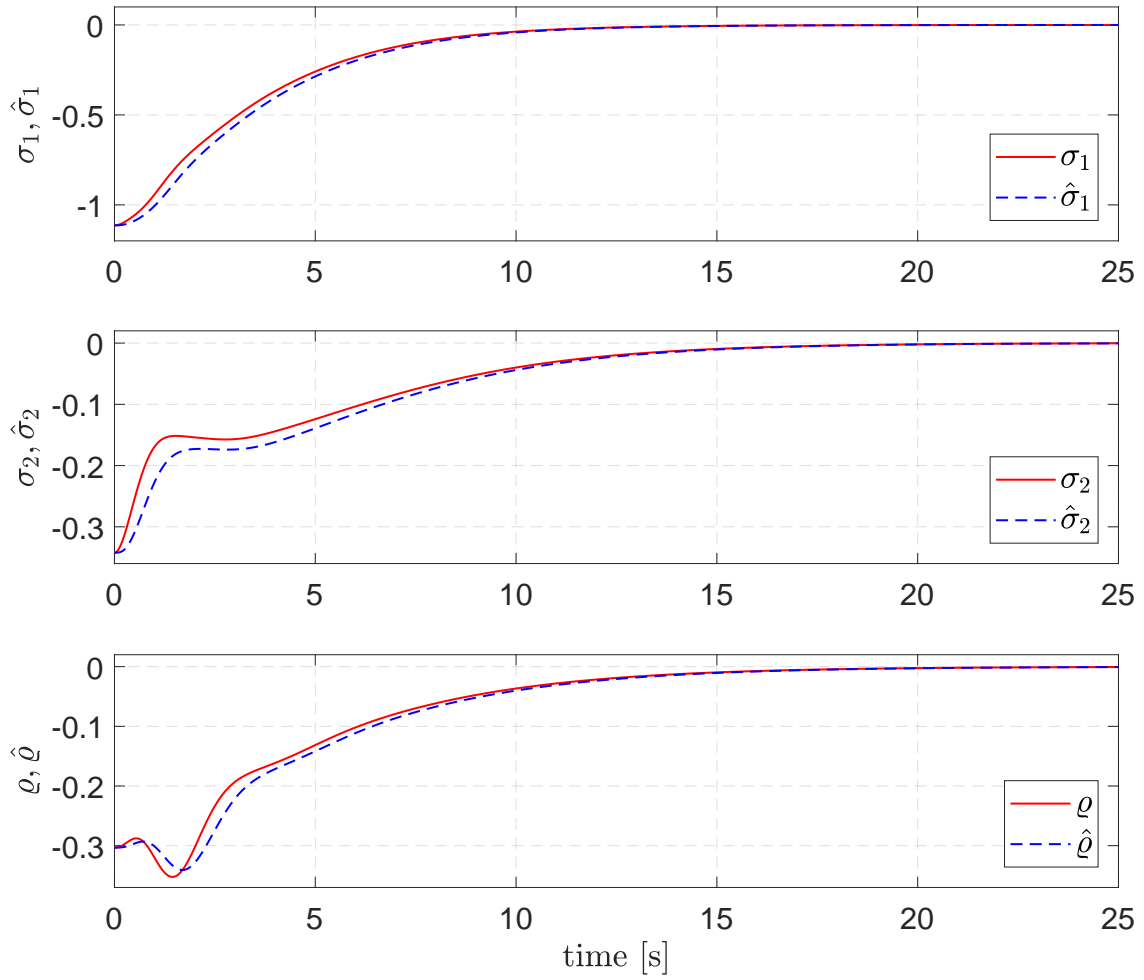


Figure 6.6: Visual errors vs. time

## 6.4. Experimental validations

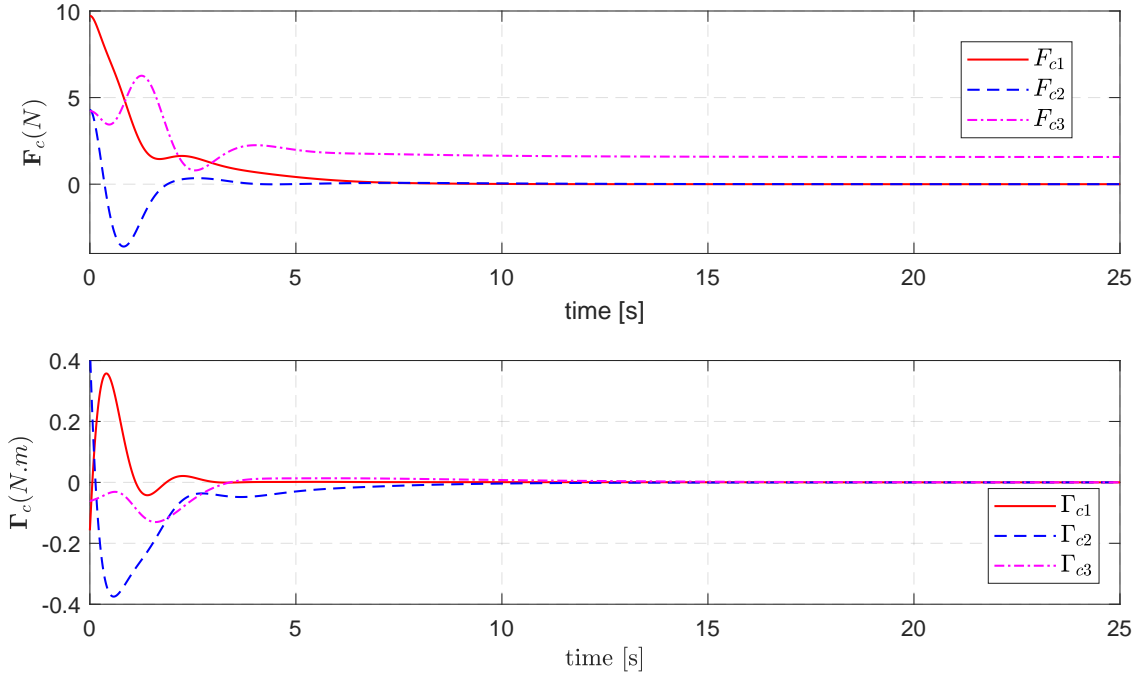


Figure 6.7: Control force  $\mathbf{F}_c$  and moment  $\Gamma_c$  vs. time

## 6.4 Experimental validations

### 6.4.1 Experimental setup

The implementation of the proposed algorithm with real-time homography estimation has been performed on the I3S-UV experimental platform (see Fig. 6.9). At the moment when the experiment was performed, a Hardkernel Odroid XU-4 played a role of the companion computer in the I3S-UV control architecture (c.f. Fig. 5.8).

For performing the real-time homography estimation, the AUV is equipped with a myAHRS+ IMU sensor providing measurement output at  $100 [Hz]$  and an oCam downward-looking monocular camera providing color images of  $640 [px] \times 480 [px]$  at  $30 [Hz]$ . The homography estimation algorithm [34] has been implemented in C++, combined with OpenCV for image processing, on the ground station laptop with an Intel Xeon(R) E-2176M CPU of 12 cores running at  $2.7 GHz$ , 32GB of RAM and Quadro P3200/PCIe/SSE2 graphic card allowing to run homography estimation with CUDA. The laptop has a Linux-based operating system and is responsible for the following tasks: 1) interfacing with the camera and IMU hardwares and acquisition of images and IMU data 2) real-time estimation of the homography at  $29.4 [Hz]$  3) perform outer control loop at  $100 [Hz]$ , and 4) interfacing with the joystick and Pixhawk via Odroid to remotely control the vehicle.

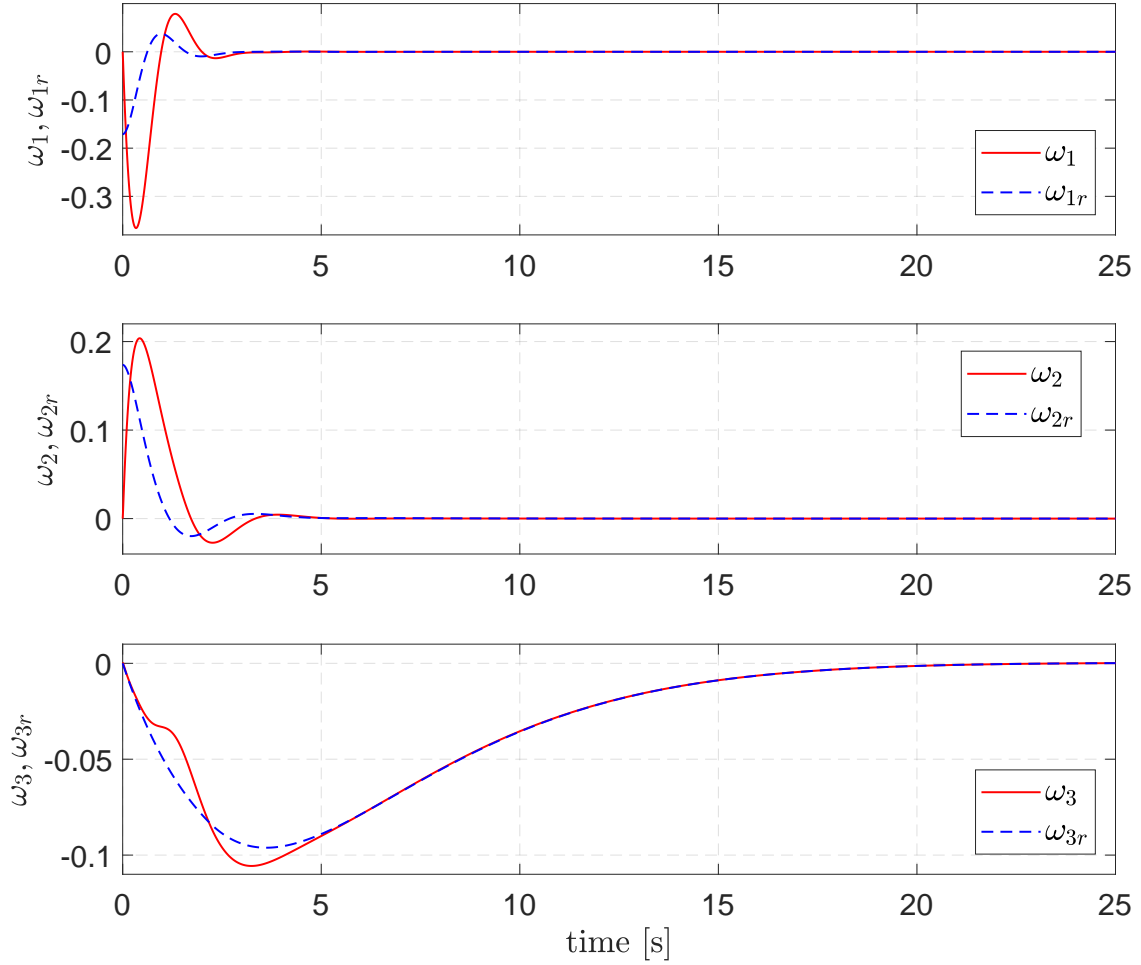


Figure 6.8:  $\Omega$  and  $\Omega_r$  vs. time

To perform the station-keeping task, the UAV is initially in the teleoperation mode and is manually positioned at a certain distance w.r.t. the artificial visual target so that the latter is visible by the camera ensuring a sufficient number of detected features for good homography estimation. In the reported experiment, the vehicle was positioned at about  $0.3[m]$  far from the target <sup>3</sup>.

Note that here, the heave control is different from Proposition 5 in Section 6.2.1.1 since it is enhanced by integral effect to eliminate static errors. In fact, by introducing a new variable:

$$\bar{\varrho} = \varrho + k_{Ih} z_\varrho; \quad k_{Ih} > 0$$

where  $z_\varrho$  is an anti-windup integrator, which is defined as:

$$\dot{z}_\varrho = -k_z z_\varrho + k_z \text{sat}^{\delta_z} \left( z_\varrho + \frac{\varrho}{k_z} \right); \quad z_\varrho(0) \in \mathbb{R}; \quad k_z, \delta_z > 0$$

<sup>3</sup>Due to limitation of dimensions of the water tank, we could not test for much farther distance.

## 6.4. Experimental validations

---



Figure 6.9: AUV with downward-looking camera

Then, control design can be carried out analogically to the one presented in Section 6.2.1.1, when replacing  $\varrho$  by the new variable  $\bar{\varrho}$ , as follows:

$$\dot{\hat{\varrho}} = -k_{13}(\hat{\varrho} - \bar{\varrho}), \quad \hat{\varrho}(0) = \varrho(0)$$

$$F_{c3} = m_3 \text{sat}^{\eta_{31}}(k_{23}(\hat{\varrho} - \bar{\varrho})) - m_3 \text{sat}^{\eta_{32}}(k_{33}\bar{\varrho}) - (mg - F_b) \quad (6.36)$$

The saturation functions in (6.36) are employed for dealing with thrusters' limitation. For heave control in this experiment, the parameters are chosen as:  $k_{Ih} = 0.1$ ,  $k_z = 10$ ,  $\delta_z = 10$ ,  $\eta_{31} = 1.8$ ,  $\eta_{32} = 2.3$  and  $k_{13} = 3s_1$ ,  $k_{23} = \frac{8}{3} \frac{s_1^2}{n_1}$ ,  $k_{33} = 3 \frac{s_1^2}{n_1}$ ,  $s_1 = 1$ ,  $n_1 = \frac{1}{0.3}$ .

The other parameters and control gains involved in the computation of the control inputs are given in Tab. 6.3 and Tab. 6.4.

Specification	Numerical value
$m$ [kg]	16
$F_b$ [N]	$1.01mg$
$l$ [m]	0.025
$\mathbf{r}_C$ [m]	[0.2 0 0.1]
$\hat{\mathbf{M}} = m\mathbf{I}_3 + \hat{\mathbf{M}}_A^{11}$ [kg]	$\text{diag}(17.868, 23.868, 21.024)$
$\hat{\mathbf{J}} = \mathbf{J}_0 + \hat{\mathbf{M}}_A^{22}$ [kg.m <sup>2</sup> ]	$\text{diag}(0.3105, 0.8486, 1.0)$
$\hat{\mathbf{D}} = m\mathbf{l}\mathbf{e}_{3 \times}$ [kg.m]	$0.4\mathbf{e}_{3 \times}$

Table 6.3: Specifications of the experimental AUV

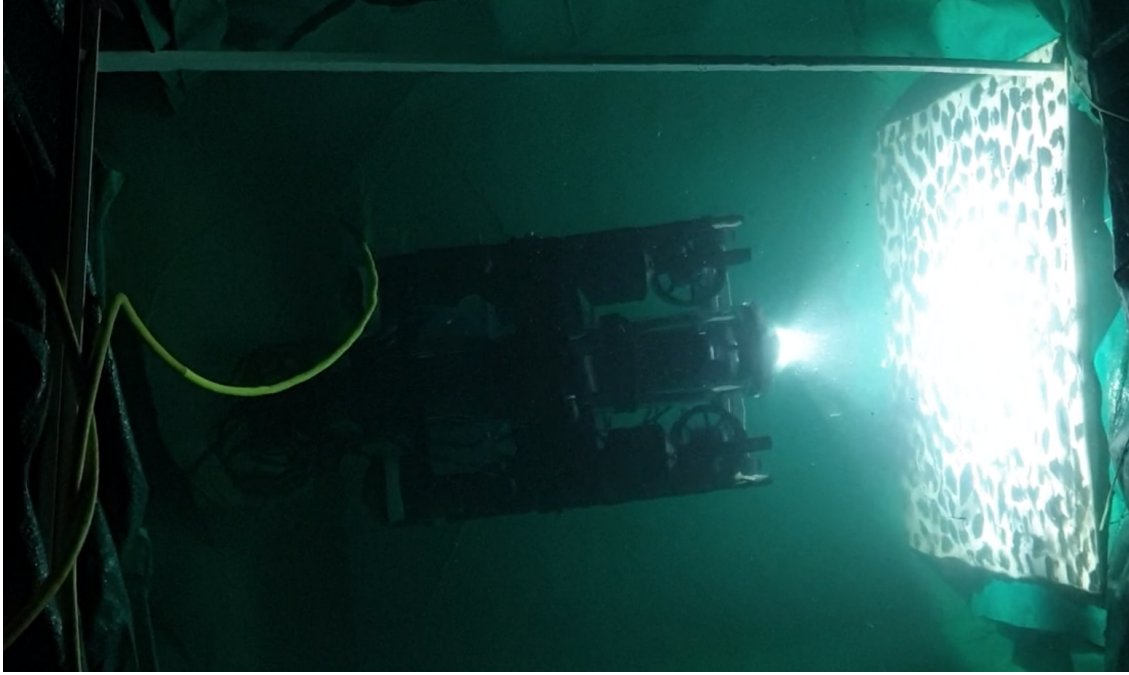


Figure 6.10: Experimental validation in a water tank

Controller	Gains and other parameters
Proposition 6	$k_1 = 3s_2, k_2 = \frac{8}{3} \frac{s_2^2}{n_1}, k_3 = 3 \frac{s_2^2}{n_1}, s_2 = \sqrt{2}$
Proposition 7	$k_g = 0.7, k_{\Theta 1} = 0.0625, k_{\Theta 2} = 0.5, \Delta_{\Theta} = 1$
Proposition 4	$\mathbf{K}_{\Omega} = 3\hat{\mathbf{J}}, K_{i\Omega} = 0.1$
Lemma 1	$a_0 = 0.5, k_0 = 20, \eta_3 = 8$

Table 6.4: Control gains and parameters

### 6.4.2 Preliminary experimental results

The preliminary experimental results carried out in a water tank of dimensions 1.2 m (L) x 0.8 m (W) x 1.5 m (H) are reported next (see Fig. 6.10). The reader can view the video showing station keeping capability of our in-house I3S-UV (employing a forward-looking camera) observing an (nearly) vertical artificial visual target at <https://youtu.be/CmAsWkz-9AQ>.

Experimental results including the time evolution of the orientation (Euler angles), the control force  $\mathbf{F}_c$ , the control torque  $\mathbf{\Gamma}_c$ , the visual errors  $(\boldsymbol{\sigma}, \varrho)$  and their corresponding estimations  $(\hat{\boldsymbol{\sigma}}, \hat{\varrho})$ , the homography component  $h_{12}$ , and the Frobenius norm of  $(\mathbf{H} - \mathbf{I})$  are shown in Figs. 6.11–6.16, respectively.

In fact, the I3S-UV platform was not well calibrated since the line connecting the

## 6.4. Experimental validations

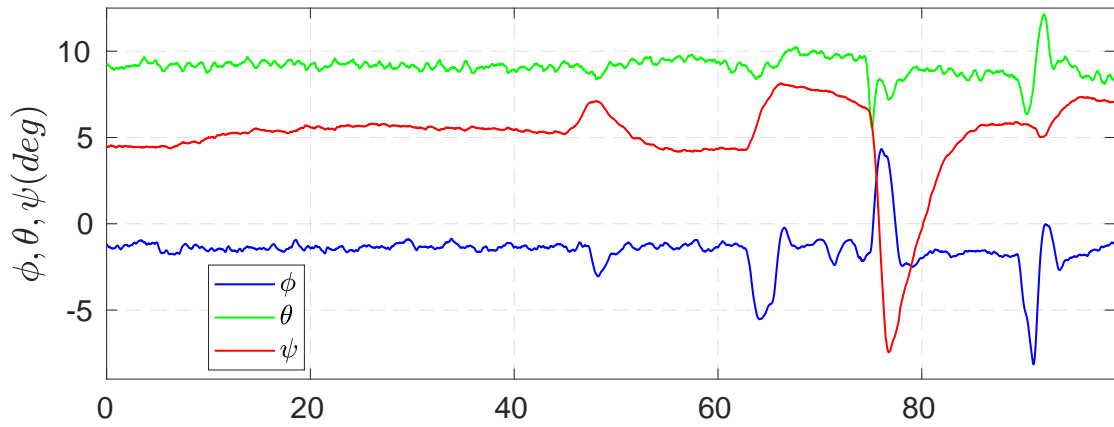


Figure 6.11: Attitude: roll  $\phi$ , pitch  $\theta$ , yaw  $\psi$  vs. time

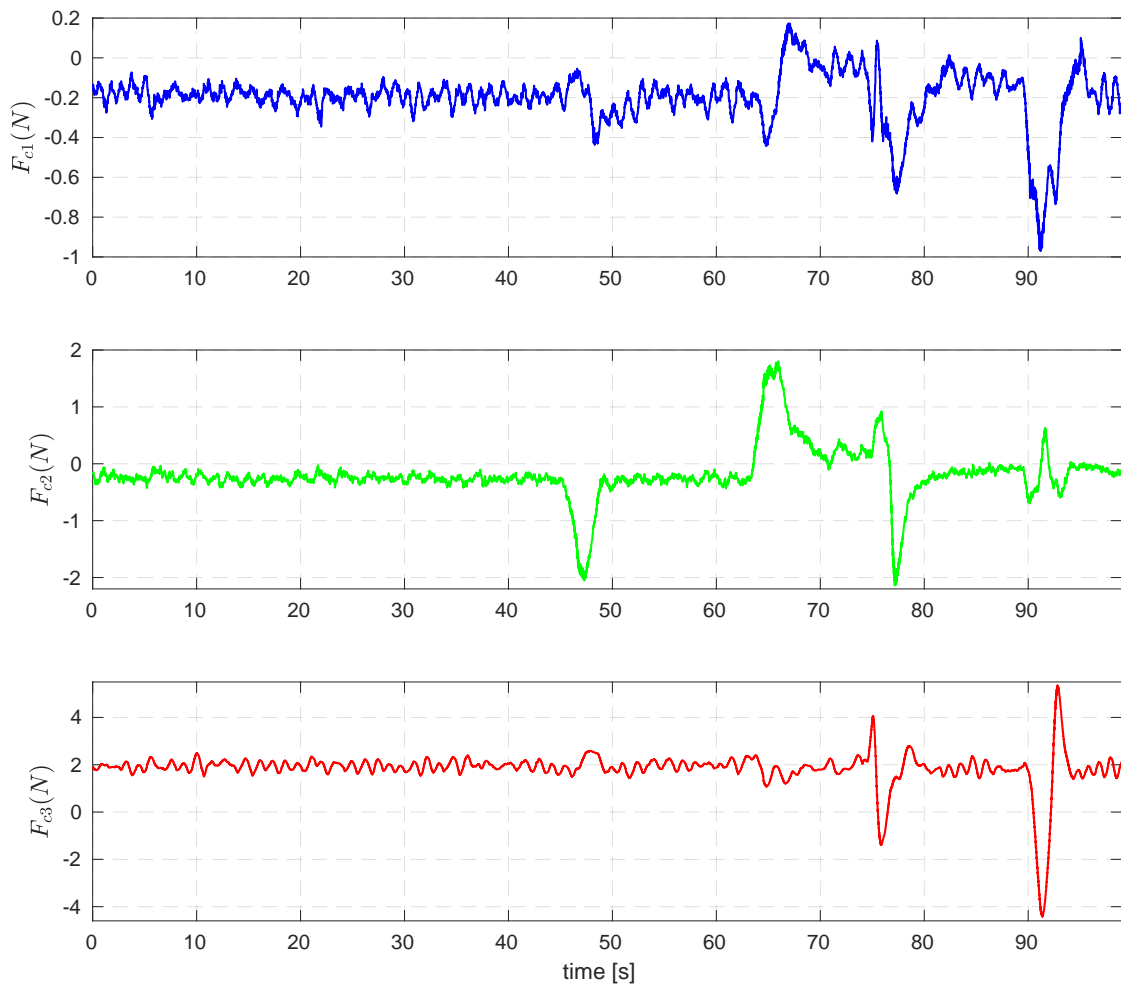


Figure 6.12: Control force  $\mathbf{F}_c$  vs. time

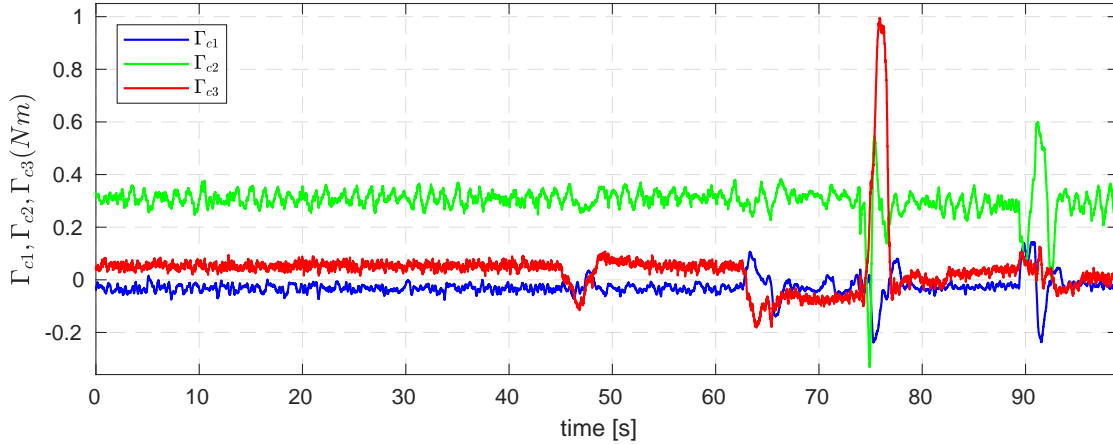


Figure 6.13: Control torque  $\Gamma_c$  vs. time

CG and the CB is not parallel with  $\vec{e}_3^b$ . This issue results in an inclination angle of the plane ( $\vec{e}_1^b, \vec{e}_2^b$ ) of the platform with the horizontal plane. Since the platform is designed as positive buoyant, the restoring forces play the role of external forces acting on it in the convergence state. Because of the inclination, projections of the restoring forces on axes  $\vec{e}_1^b$  and  $\vec{e}_2^b$  of  $\{\mathcal{B}\}$  are not null. As can be seen in Fig. 6.11, roll and pitch angles are approximately equal to  $1.5^\circ$  and  $9^\circ$ , respectively, in the convergence state. Non zero control force components  $F_{c1}$ ,  $F_{c2}$  and  $F_{c3}$  are thus required to maintain the platform at the stabilized position, as illustrated in Fig. 6.12. Also from this figure, the positive component  $F_{c3}$  affirms that the I3S-UV vehicle is positive buoyant.

It is noteworthy to mention that theoretically, the stabilization of  $\mathbf{e}_3$  to  $\mathbf{R}^\top \mathbf{e}_3$  is carried out by means of the inner-loop controller enhanced with bounded integrator defined in Proposition 4. The inclination of the plane ( $\vec{e}_1^b, \vec{e}_2^b$ ) with the horizontal plane can be explained by the fact that parameters of the bounded inner-loop integrator of the inner-loop controller were not well tuned. As can be seen in Fig. 6.13, this results in the ineffectiveness of the integrator since  $\Gamma_{c1}$  and  $\Gamma_{c2}$  in steady state are not sufficient for compensating for static error caused by the issue relating to position of CG<sup>4</sup>.

To excite the external force response, the AUV has been manually moved by a stick at time instants 46 [s], 63 [s], 74 [s], and 90 [s]. In Fig. 6.14 one observes that right after finishing the interaction, the AUV went back to its stabilized position and orientation without overshoots in surge and sway directions which correspond to the components of the visual error  $\sigma$ . On the contrary, the overshoot can be clearly observed in heave direction (corresponding to the visual error  $\varrho$ ).

<sup>4</sup>We believe that this issue is not too difficult to address by a more proper tuning of the control gains and parameters for future validations. Due to time constraint we have to be content to report these experimental results.

## 6.4. Experimental validations

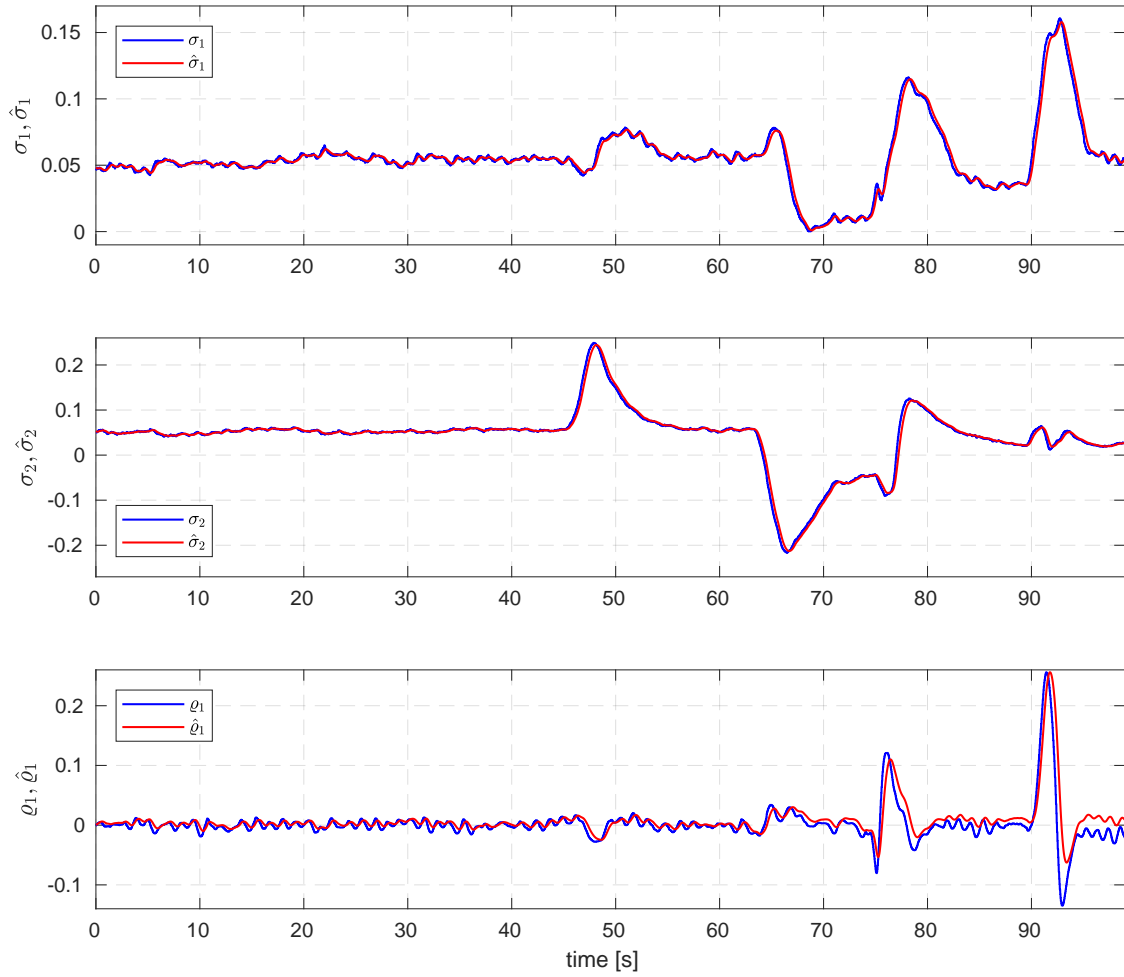


Figure 6.14: Visual errors ( $\sigma$ ,  $\rho$ ) vs. time

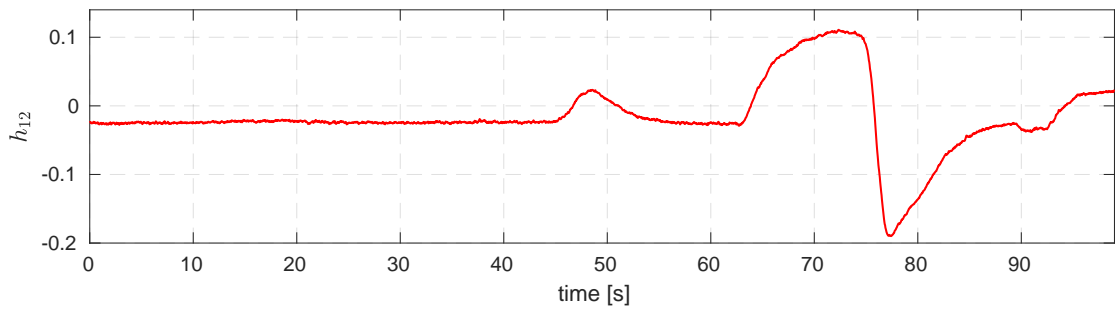


Figure 6.15:  $h_{12}$  vs. time

It can be observed from Fig. 6.14 that  $\rho$  (in blue) converges to zero while its estimate  $\hat{\rho}$  (in red) converge to non zero value. This fact shows the effectiveness of the integrator in eliminating static uncertainties. Indeed, buoyant blocks added for calibration purpose are not completely waterproof. They absorbed water and consequently the mass of the

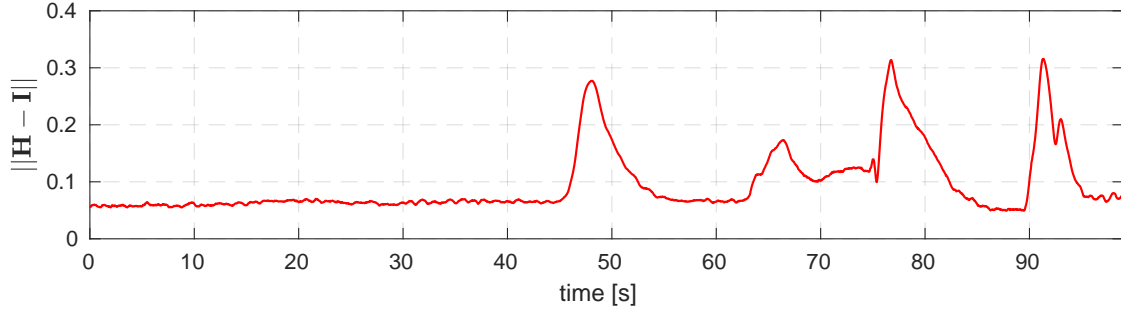


Figure 6.16: Frobenius norm  $\|\mathbf{H} - \mathbf{I}\|$  vs. time. The AUV has been pushed by a stick at time instants 46 [s], 63 [s], 74 [s] and 90 [s]. One observes that  $\|\mathbf{H} - \mathbf{I}\|$  converges to none zero value due to static errors.

I3S-UV platform was increased slightly over time. This results in a slight decrease of  $F_{c3}$  over time, as shown in Fig. 6.12. For surge-and-sway control, the components of visual error  $\sigma$  do not converge to zero due to the absence of integrator correction actions. The effect of static errors can also be clearly seen in Figs. 6.15 and 6.16 since the component  $h_{12}$  and the Frobenius norm  $\|\mathbf{H} - \mathbf{I}\|$  converge to nonzero constant values.

## 6.5 Conclusion

In this chapter a homography-based dynamic control approach of fully-actuated underwater vehicles equipped with a forward-looking camera observing a (near) vertical visual target is proposed. Improving the robustness of the outer-loop control in terms of surge-and-sway motion to external perturbations (e.g. current) is a topic for our future work. Then additional tests with a better tuning of gains and parameters will follow to validate the proposed approach, especially in challenging sea trials.

## 6.5. Conclusion

---

# 7

## Development of the I3S-UV platform

**I**N order to experimentally validate the control algorithms proposed in Chapters 5 and 6, a platform that we name I3S-UV has been developed at the I3S laboratory in the scope of this thesis project. The reasons for building such an in-house vehicle are the following.

- First, it is not easy for us to buy or hire an underwater vehicle fitting our limited budget and extension requirements. In fact, most ROVs available in the market are closed systems in the sense of mechanical structure and firmware/software. It is thus difficult to upgrade them to perform new functionalities. Although there exist few vehicles with possibilities of modifying their software and configuration in the market, they are often considerably heavy and voluminous, and/or excessively expensive in terms of price and operation cost. One can name VORTEX [1] with weight of  $220\text{ kg}$  and dimensions of  $1.3\text{ m} \times 1.1\text{ m} \times 1\text{ m}$  as an example.

In this PhD project, control algorithms have been developed for UVs in different shapes. A compact shape vehicle should be used for testing the HBVS control algorithms proposed in Chapters 5 and 6 whereas a slender axisymmetric one is needed for validating the trajectory tracking control algorithm proposed in Chapter 8. It is hard to buy all these vehicles or hire someone to construct all of them or upgrade new functionalities since our budget is rather bounded.

## 7.1. 3D design of I3S-UV

---

- Nowadays, several crucial components needed for building an UV from scratch can be easily found in the market. One can name Bluerobotics<sup>1</sup> on the top of the list of providers. Besides, many electronic parts can be purchased from Hobbyking<sup>2</sup> and other commercial websites.
- Finally, the I3S-OSCAR team possesses rich experience in building UAV systems in terms of hardware and software for the related research projects. Such know-how and experience are crucial for building a new UV system. Moreover, a large community of DIY with open resources is greatly helpful for this task.

In summary, the main reason for building the I3S-UV is our need to possess an open platform but with a limited budget. An important benefit of this practical work is that the I3S-OSCAR team can now be proactive in developing or upgrading any (new) UV system for future demands. Indeed, an underwater platform with slender body shape is planned to be built in a much faster manner than the already developed I3S-UV. It is because of the fact that its firmware (i.e. autopilot software) which has taken most of the development time can be reused with minor adaptations. Besides, since our vehicle belongs to the class of man-portable UVs, less support facilities are required for preliminary tests.

## 7.1 3D design of I3S-UV

In the beginning of this PhD project (since July 2015), there are a certain number of providers of micro/mini ROV systems including ROVs, firmware and human machine interface softwares. The price of the overall systems can be up to more than ten thousand US dollars. In comparison with the ones of working class in industry, this is relatively inexpensive. However, this is still a large amount of money in comparison with our limited budget. In addition, they are often closed systems preventing possible modifications in order to add other components (sensors, cameras, etc.) for performing new functionalities.

However, there exist crucial components for building a ROV from scratch such as thrusters, mechanical components resistant to high pressure, pressure sensors, lamps, etc. at more reasonable prices<sup>3</sup>. These components can resist to water pressure at a depth of at least 100 *m*, which is largely sufficient for all of our experimental validations. For reducing efforts and development time, we have purchased a not-full-option version of BlueROV1<sup>4</sup> (c.f. Fig. 7.1). The purchased developer kit goes with very basic components

---

<sup>1</sup><https://bluerobotics.com/>

<sup>2</sup><https://hobbyking.com/>

<sup>3</sup><https://bluerobotics.com/store/>

<sup>4</sup><http://bluerobotics.com/store/retired/bluerov-r1/>

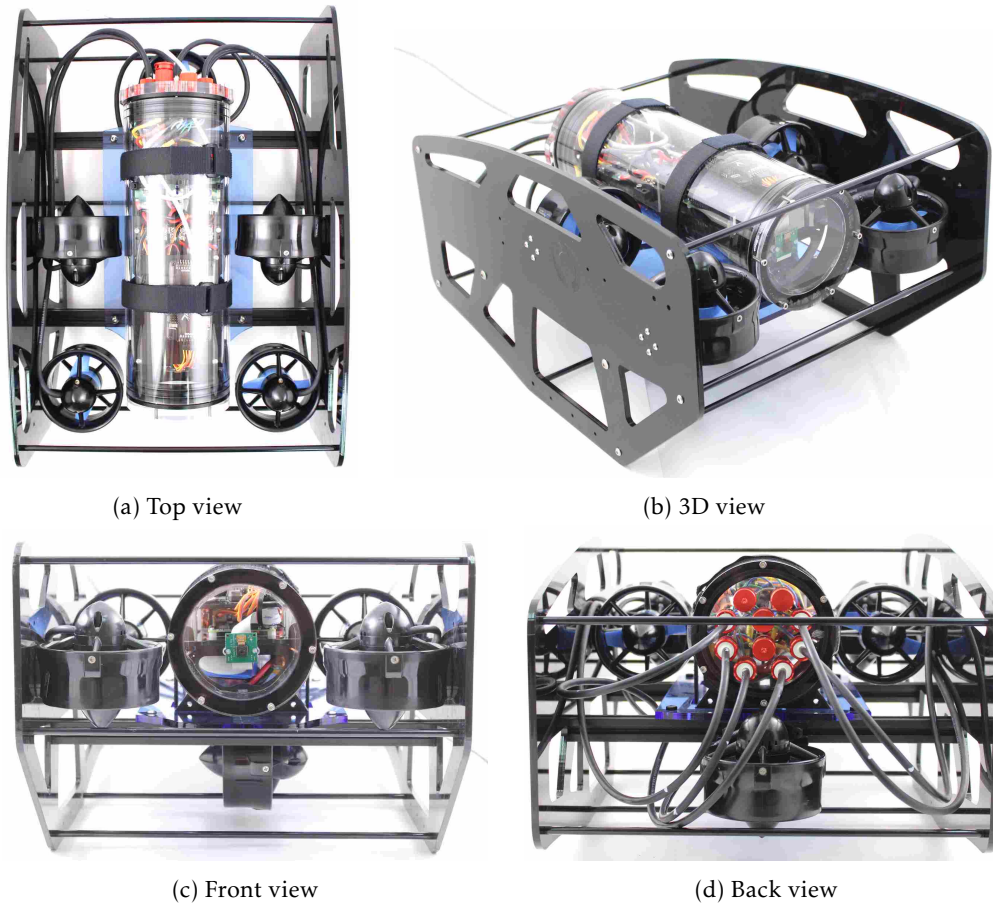


Figure 7.1: Different views of BlueROV1 (Source:www.bluerobotics.com)

including 6 thrusters, 6 ESCs, a pressure sensor, an underwater lamp and a tether system (of 50 m) whereas the control parts (flight controller and companion computer) are not included.

Based on the original BlueROV1, the structure is modified to add a longer watertight tube to accommodate the main electronic components (i.e. electronic tray) as illustrated in Fig. 7.2. The original tube of BlueROV1 (in olive color) is implanted right below for containing separately a bigger battery. In addition, a shorter tube with spherical dome end cap is dedicated for a camera. This camera tube together with a lamp (in black color) can be rotated and fixed in either downward-looking (c.f. Fig. 7.2a) or forward-looking (c.f. Fig. 7.2b) configuration. New components of structure are designed and printed by using a 3D printer with plastic filament (c.f. Fig. 7.3). For enhancing the resistance to external forces and moments, some components are designed with empty spaces in form of cylinder holes, which are then filled by carbon fiber composite rods or tubes. It is demonstrated via our practical trials in water that with appropriate choices

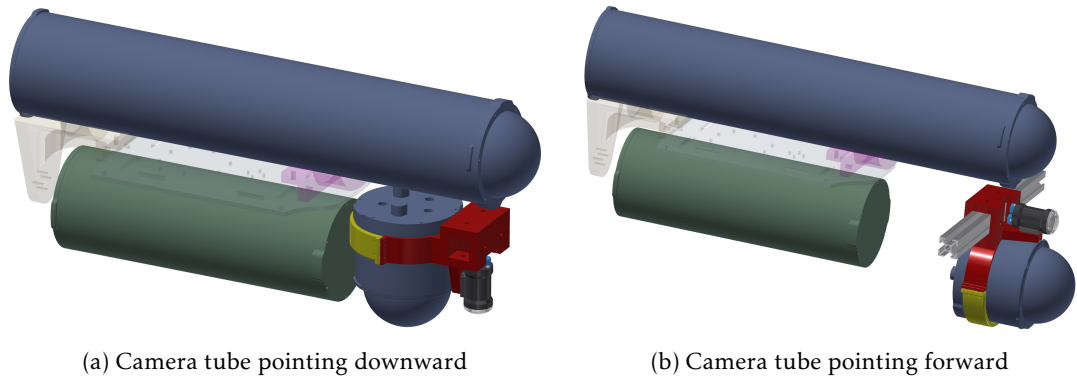


Figure 7.2: Water tight tubes of I3S-UV



Figure 7.3: 3D printed plastic components

of printing fulfillment density, material of filament, and coating to protect the surface of printed objects, the printed components can resist well to experimental conditions. The application of 3D printing technology indeed saves us a lot of development time and financial resources.

After incorporating all tubes and support components, the total volume of I3S-UV (c.f. Fig. 7.4) is almost double to its original design. Consequently, the buoyancy force

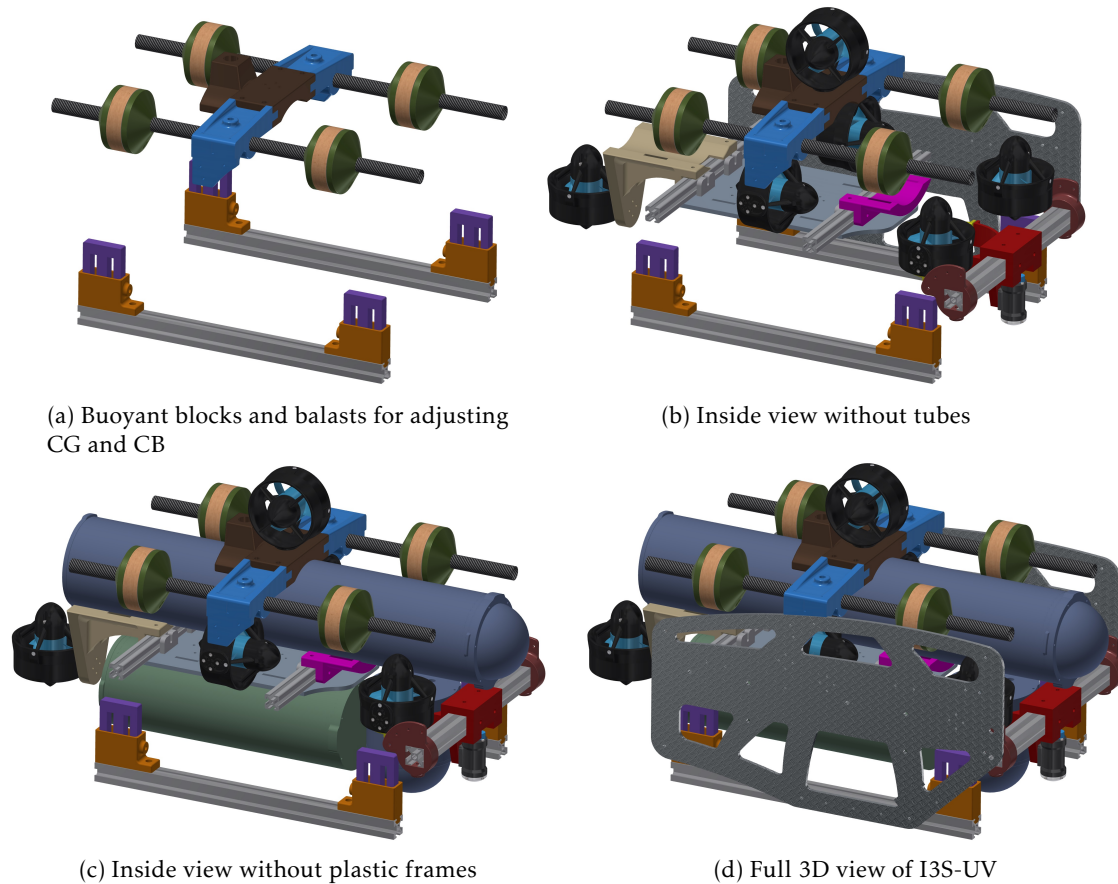


Figure 7.4: I3S-UV 3D design

is significantly increased. To overcome this issue and to have the capability of adjusting  $CG$  and  $CB$  such that the line connecting them is parallel with the direction of the downward-looking camera, additional ballast weights and buoyant blocks are attached to the vehicle (c.f. Fig. 7.4a). These include four lead ballasts of  $0.5\text{ kg}$  per item (in violet color) and two T-slotted aluminum extrusion bars. The position of the lead ballasts (resp. buoyant blocks in yellow color) can be adjusted by sliding them along the two aluminum bars (resp. cylinder carbon tubes). All the aluminum bars and carbon tubes are parallel. The flexible distribution of the ballast weights and the buoyant blocks allows us to easily calibrate the vehicle in practice. The resulting total weight of I3S-UV is approximately  $16\text{ kg}$  in air whereas the original value of BlueROV1 is only  $7.6\text{ kg}$ . The overall dimensions of I3S-UV are  $0.39\text{ m} \times 0.33\text{ m} \times 0.65\text{ m}$  in height, width and length. The vehicle is fully actuated in the sense that it is equipped with three vertical thrusters for heave, pitch and roll actuations, two horizontal thrusters for yaw and surge actuations, and one lateral thruster for sway actuation (c.f. Fig. 7.4b). In fact, the distribution and orientation of thrusters are kept almost unchanged in the I3S-UV except their mounting

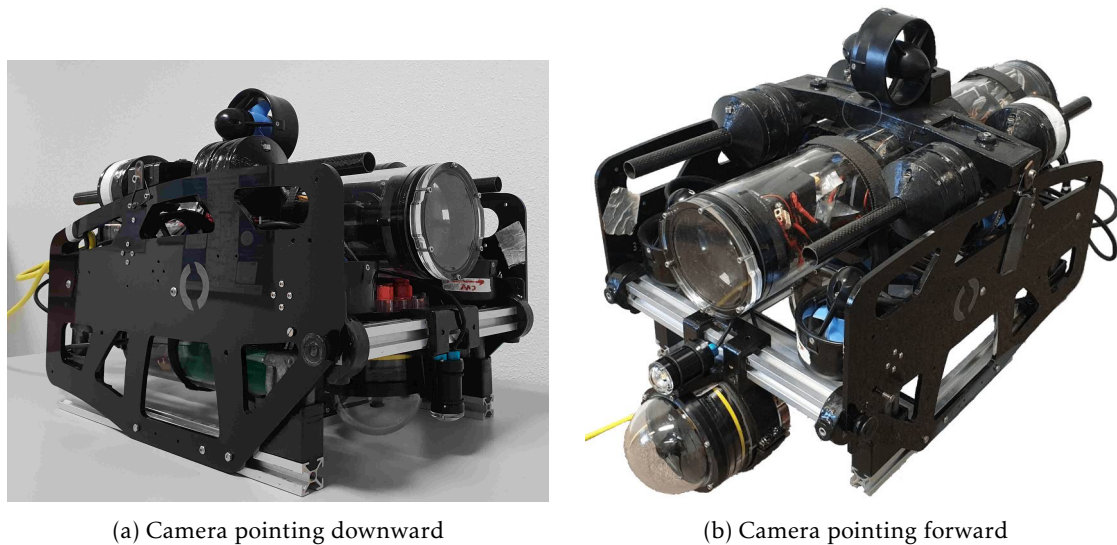


Figure 7.5: I3S-UV in reality

positions. The lateral thruster is mounted on the top of I3S-UV whereas in BlueROV1, it is fixed under the water tight tube. The real view of the I3S-UV is shown in Fig. 7.5.

In summary, parts of the developer kit BlueROV1 are completely reused in I3S-UV. New components are included in order to accommodate a bigger electronic tray, a bigger battery and a camera. The compact configuration of I3S-UV has been proved to be highly effective in our practical experiments.

## 7.2 Software system

In fact, the control system of the I3S-UV in the sense of hardware and software has been developed in parallel with vehicle's 3D design and fabrication right in the beginning. Because of that reason, the BlueROV1 developer kit which is ready to mount control hardware is tremendously important for us. It indeed saves us development time since some basic controls in manual mode can be tested without too much efforts.

The I3S-UV software system has been created for implementing control architecture (c.f. Fig. 7.6) including high- and low-level controls. In the high level, the proposed advanced control algorithms (in Chapters 5 and 6) are implemented in form of a ROS package in C++ and run in the companion computer which uses ROS as middleware. The low-level control which is mainly in charge of allocation control is run in Pixhawk. The source code of the low level is adapted from the open-source autopilot PX4 which is based on Mavlink communication. The MAVROS package in ROS which provides communication between Mavlink and ROS is thus employed to link two control levels. In reality, Pixhawk and the companion computer are wired by serial connection. A low-cost

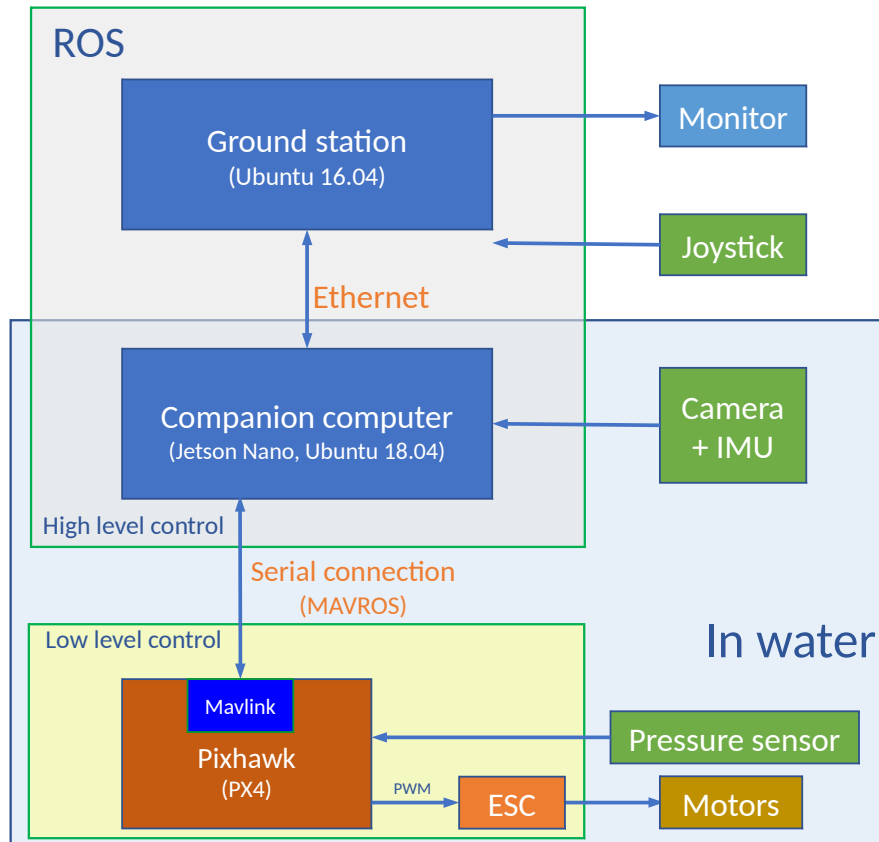


Figure 7.6: I3S-UV control architecture

and compact SBC is used as companion computer for running high-level control, image acquisition (and possible homography estimation by employing HomographyLab and communication over Ethernet with the ground station computer. It was a Hardkernel XU4 which has been recently upgraded to an Nvidia Jetson Nano in May 2019. The high level control is set to run at a frequency of  $100\text{ Hz}$  even though the rate of homography estimation (in station keeping mode) is much lower. The low level control rate is  $100\text{ Hz}$ .

In the experimental process, the I3S-UV always starts in manual control mode. The station keeping mode is fully autonomous. There is a mechanism to control the switching between these two modes depending on the quality of homography estimation. The whole software system of the I3S-UV is thus developed for performing the following functionalities:

1. Control forward/backward movement and heading (i.e yaw angle or turn left-/right) of the vehicle in manual control mode.
2. Control the vehicle depth, auto-depth stabilization in manual control mode.
3. Control the  $e_3$  direction of the vehicle in manual control mode for having different FOV of the camera since the latter is rigidly fixed to the vehicle.

4. Switching between manual control and station keeping modes
5. Station keeping mode

Besides, additional packages available in ROS such as online graphical analysis of data, image view, etc. can be run on the ground station computer for directly debugging while performing the experiments. Sensor data, images and values of control inputs can be recorded in files in the form of *rosvbag*, which are then useful for post-experiment data analysis and conducting emulation experiments (i.e offline) in ROS.

In this software system, ROS with its decentralized architecture plays a crucial role. It allows all processes (nodes) to run independently while messages between them are exchanged through topics. A ROS master node control the registering of nodes and enables individual ROS nodes to locate one another and then communicate with each other peer-to-peer. The decentralized architecture also allows nodes to run either in the companion computer or the ground station computer. The homography estimation node thus can be run in different computers for comparing the performance.

### 7.2.1 Homography estimation

Let us explain how homography estimation works in practice as illustrated in Fig. 7.7. Note that all nodes are in oval with colored background while topics are in rectangular.

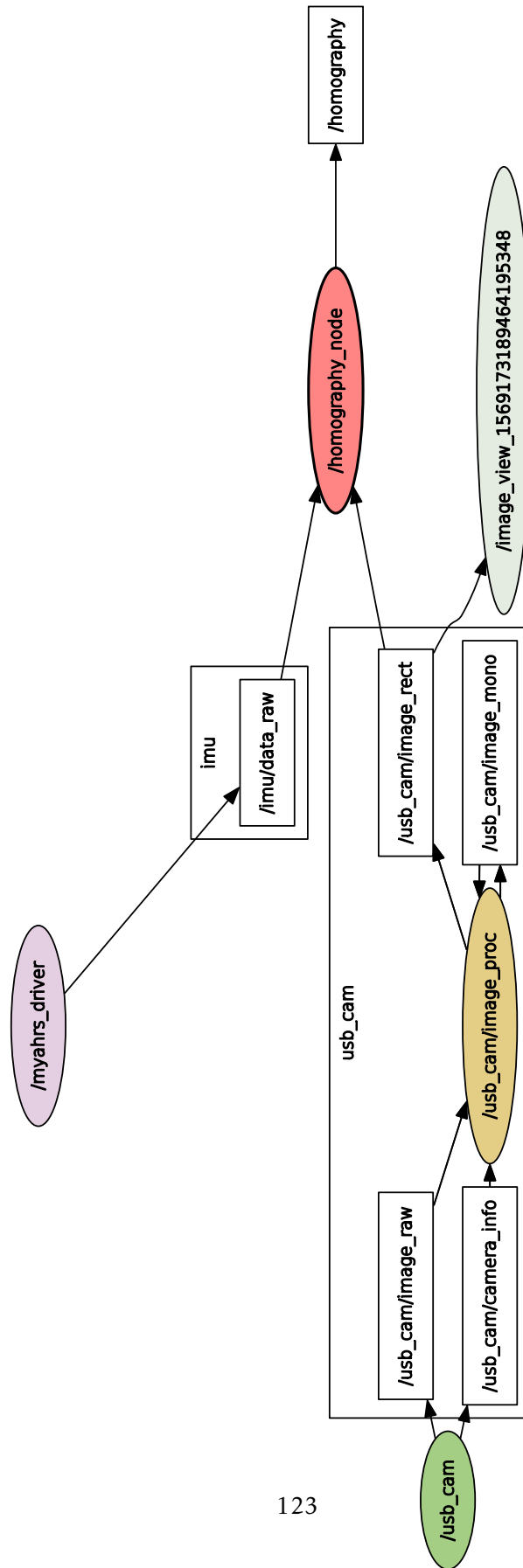


Figure 7.7: ROS nodes and topics in homography estimation

## 7.2. Software system

The images acquired from the camera connected to the companion computer are processed by `/usb_cam` node and published to a topic named `usb_cam/image_raw`. Then they are processed to eliminate distortion (i.e calibrated) by using camera calibration matrix by `/usb_cam/image_proc` node and published to a topic namely `/usb_cam/image_rect`. The `/homography_node` node (i.e. HomographyLab) subscribes to this topic and to `/imu/data_raw` to obtain rectified images and measured angular velocity, respectively. The estimated homography is published to `/homography` topic.

In reality, a myAHRS+ IMU sensor provides measurement output at  $100 [Hz]$  and an oCam downward-looking monocular camera provides color images of  $640 [px] \times 480 [px]$ . They are connected with the companion computer over USB serial ports. The companion and ground station computers are linked by high speed Ethernet connection. The performance of HomographyLab software running in different computers is presented in Tab. 7.1.

Computer	Configuration	Image acquisition rate $[Hz]$	Homography estimation rate $[Hz]$
XU4	CPU: Exynos5422 Cortex-A15 2Ghzx4 Cortex-A7x4 RAM: 2GB LPDDR3	20	10
Jetson Nano	GPU:128-core Maxwell CPU: Quad-core ARM A57 RAM: 4 GB 64-bit LPDDR4	30	20
Dell 7530	CPU: Intel Xeon E-2176M 2.7GHzx12 Mem- ory: 32GB Graphic card: Quadro P3200	50	48

Table 7.1: Performance of homography estimation in different computer configurations

### 7.2.2 High level control

The high level control is illustrated in Fig. 7.8. The operator uses a joystick to provide control references including:

- selected mode (manual or station keeping),
- desired depth, orientation and movement,
- desired lamp intensity,
- and emergency stop signal.

These references are indeed processed by `/joy_node` node and published to `/joy`. A main program (i.e `/control_in_ros_node`) subscribes to `/homography` and `/joy` topics to obtain homography estimation and control references, respectively. In `/control_in_ros_node`

node, control force  $\mathbf{F}_c$  and control torque  $\mathbf{\Gamma}_c$  are calculated (either in manual or station keeping mode), then are sent to */mavros* node through custom messages (i.e topics) */i3s\_auv\_custom\_2\_topx4\_nh* and */i3s\_auv\_custom\_3\_topx4\_nh*, respectively. The information of switching between two control modes, emergency stop signal, pwm of lamp (for turning on/off or adjusting light intensity) are sent to */mavros* node over */i3s\_auv\_custom\_1\_topx4\_nh*. The three custom message topics are in red rectangular in Fig. 7.8. The vehicle's attitude and angular velocity required for control algorithms are estimated/measured in Pixhawk and transformed into Mavlink messages. They are sent to */mavros* node and then to */control\_in\_ros\_node* over */mavros/imu/data\_raw* and */mavros/imu/data* topics.

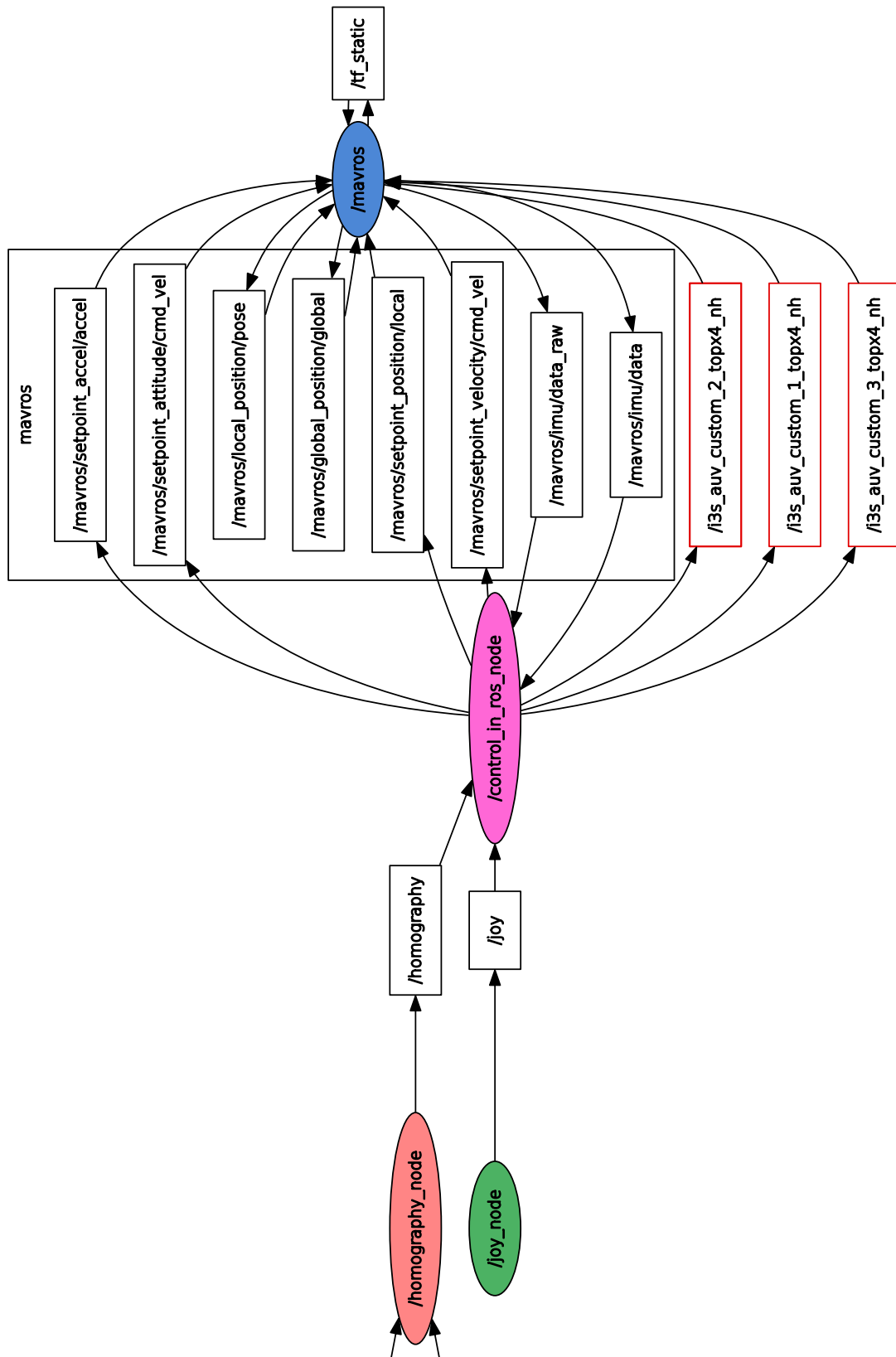


Figure 7.8: ROS nodes and topics in high level control

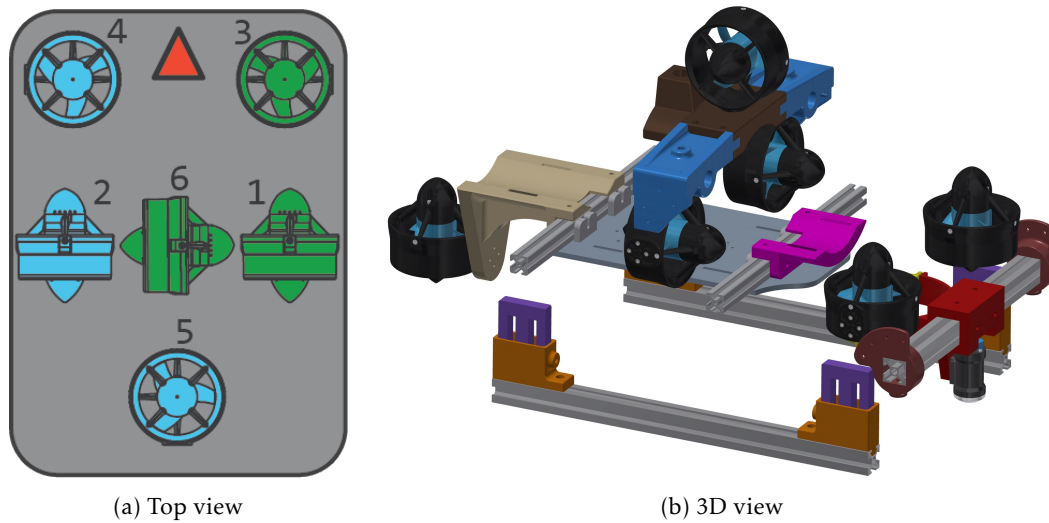


Figure 7.9: Configuration of 6 thrusters.

### 7.2.3 Low level control

In the beginning of this PhD project, there was not any opensource autopilot exclusively dedicated to UV<sup>5</sup>. For aerial, surface or ground vehicles, there exist mainly two widely used autopilots and their corresponding communities: ArduPilot and PX4. In this project, PX4 is chosen since our I3S-OSCAR team has a rich experience in exploiting this flight controller. We have performed some modifications in PX4 for performing low-level control of the I3S-UV and measuring submerged depth. The compiled PX4 firmware runs in a 3DR Pixhawk v2 flight controller.

#### 7.2.3.1 Control allocation

As seen from Fig. 7.9, the positions of the 6 thrusters of I3S-UV expressed in the body-fixed frame are given by:<sup>6</sup>

<sup>5</sup>The ArduSub developed by Blue Robotics based on ArduPilot has been officially announced in April 11th 2016, and merged with ArduPilot project in February 22nd 2017.

<sup>6</sup> $L, W, H$  stand for Length, Width, Height respectively.

$$\left\{ \begin{array}{l} \mathbf{P}_1 = \begin{bmatrix} L_1 \\ W_1 \\ H_1 \end{bmatrix}, \quad \mathbf{P}_2 = \begin{bmatrix} L_1 \\ -W_1 \\ H_1 \end{bmatrix}, \\ \mathbf{P}_3 = \begin{bmatrix} L_3 \\ W_3 \\ H_3 \end{bmatrix}, \quad \mathbf{P}_4 = \begin{bmatrix} L_3 \\ -W_3 \\ H_3 \end{bmatrix}, \\ \mathbf{P}_5 = \begin{bmatrix} -L_5 \\ 0 \\ H_5 \end{bmatrix}, \quad \mathbf{P}_6 = \begin{bmatrix} L_6 \\ 0 \\ -H_6 \end{bmatrix} \end{array} \right.$$

Force vectors are given by

$$\left\{ \begin{array}{l} \mathbf{F}_1 = T_1 \mathbf{e}_1, \quad \mathbf{F}_2 = T_2 \mathbf{e}_1, \\ \mathbf{F}_3 = -T_3 \mathbf{e}_3, \quad \mathbf{F}_4 = -T_4 \mathbf{e}_3, \\ \mathbf{F}_5 = -T_5 \mathbf{e}_3, \quad \mathbf{F}_6 = T_6 \mathbf{e}_2 \end{array} \right.$$

One thus has  $\mathbf{\Gamma}_i = \mathbf{P}_i \times \mathbf{F}_i$ , yielding

$$\left\{ \begin{array}{l} \mathbf{\Gamma}_1 = -W_1 T_1 \mathbf{e}_3 + H_1 T_1 \mathbf{e}_2 \\ \mathbf{\Gamma}_2 = W_1 T_2 \mathbf{e}_3 + H_1 T_2 \mathbf{e}_2 \\ \mathbf{\Gamma}_3 = L_3 T_3 \mathbf{e}_2 - W_3 T_3 \mathbf{e}_1 \\ \mathbf{\Gamma}_4 = L_3 T_4 \mathbf{e}_2 + W_3 T_4 \mathbf{e}_1 \\ \mathbf{\Gamma}_5 = -L_5 T_5 \mathbf{e}_2 \\ \mathbf{\Gamma}_6 = -L_6 T_6 \mathbf{e}_3 + H_6 T_6 \mathbf{e}_1 \end{array} \right.$$

One then deduces the total control force and torque vector

$$\begin{bmatrix} \mathbf{F}_c \\ \mathbf{\Gamma}_c \end{bmatrix} = \mathbf{A} \mathbf{T} \quad \text{where} \quad \mathbf{F}_c = \sum_{i=1}^6 \mathbf{F}_i, \quad \mathbf{\Gamma}_c = \sum_{i=1}^6 \mathbf{\Gamma}_i, \quad i = \overline{1,6}$$

with the control allocation matrix

$$\mathbf{A} \triangleq \begin{bmatrix} 1 & 1 & 0 & 0 & 0 & 0 \\ 0 & 0 & 0 & 0 & 0 & 1 \\ 0 & 0 & -1 & -1 & -1 & 0 \\ 0 & 0 & -W_3 & W_3 & 0 & H_6 \\ H_1 & H_1 & L_3 & L_3 & -L_5 & 0 \\ -W_1 & W_1 & 0 & 0 & 0 & -L_6 \end{bmatrix}$$

and  $\mathbf{T} \triangleq [T_1 \ T_2 \ T_3 \ T_4 \ T_5 \ T_6]^\top$  a vector of desired thrust values of all six motors.

Note that the values of  $L_1$ ,  $H_3$  and  $H_5$  do not have any influence on the resulting torques. Ideally one should have  $H_1 = 0$  and  $L_6 = 0$  so that  $T_1$  and  $T_2$  do not generate pitch torque (i.e. generate only yaw torque) and  $T_6$  does not generate yaw torque (i.e. generate only roll torque). For the I3S-UV, we consider this case. This consideration results in the following simplified control allocation matrix:

$$\mathbf{A} \triangleq \begin{bmatrix} 1 & 1 & 0 & 0 & 0 & 0 \\ 0 & 0 & 0 & 0 & 0 & 1 \\ 0 & 0 & -1 & -1 & -1 & 0 \\ 0 & 0 & -W_3 & W_3 & 0 & H_6 \\ 0 & 0 & L_3 & L_3 & -L_5 & 0 \\ -W_1 & W_1 & 0 & 0 & 0 & 0 \end{bmatrix}$$

It is assumed that there is no constraint on  $T_i$ , by rearranging the output vector one obtains

$$\begin{aligned} \begin{bmatrix} F_{c1} \\ \Gamma_{c3} \end{bmatrix} &= \begin{bmatrix} 1 & 1 \\ -W_1 & W_1 \end{bmatrix} \begin{bmatrix} T_1 \\ T_2 \end{bmatrix} \\ \Rightarrow \begin{bmatrix} T_1 \\ T_2 \end{bmatrix} &= \begin{bmatrix} \frac{1}{2} & -\frac{1}{2W_1} \\ \frac{1}{2} & \frac{1}{2W_1} \end{bmatrix} \begin{bmatrix} F_{c1} \\ \Gamma_{c3} \end{bmatrix} \end{aligned} \quad (7.1)$$

and

$$\begin{aligned} \begin{bmatrix} F_{cy} \\ F_{cz} \\ \Gamma_{cx} \\ \Gamma_{cy} \end{bmatrix} &= \begin{bmatrix} 0 & 0 & 0 & 1 \\ -1 & -1 & -1 & 0 \\ -W_3 & W_3 & 0 & H_6 \\ L_3 & L_3 & -L_5 & 0 \end{bmatrix} \begin{bmatrix} T_3 \\ T_4 \\ T_5 \\ T_6 \end{bmatrix} \\ \Rightarrow \begin{bmatrix} T_3 \\ T_4 \\ T_5 \\ T_6 \end{bmatrix} &= \begin{bmatrix} \frac{H_6}{2W_3} & -\frac{L_5}{2(L_3+L_5)} & -\frac{1}{2W_3} & \frac{1}{2(L_3+L_5)} \\ -\frac{H_6}{2W_3} & -\frac{L_5}{2(L_3+L_5)} & \frac{1}{2W_3} & \frac{1}{2(L_3+L_5)} \\ 0 & -\frac{L_3}{L_3+L_5} & 0 & -\frac{1}{L_3+L_5} \\ 1 & 0 & 0 & 0 \end{bmatrix} \begin{bmatrix} F_{cy} \\ F_{cz} \\ \Gamma_{cx} \\ \Gamma_{cy} \end{bmatrix} \end{aligned} \quad (7.2)$$

In PX4 expressions (7.1) and (7.2) are used to calculate the required thrust generated by thrusters. The configuration of I3S-UV thrusters is given by

$$\begin{aligned} L_3 &= 0.21 \text{ m}; & L_5 &= 0.23 \text{ m}; & L_6 &= 0 \text{ m} \\ W_1 &= 0.11 \text{ m}; & W_3 &= 0.11 \text{ m} \\ H_1 &= 0 \text{ m}; & H_6 &= 0.15 \text{ m} \end{aligned}$$

## 7.2. Software system

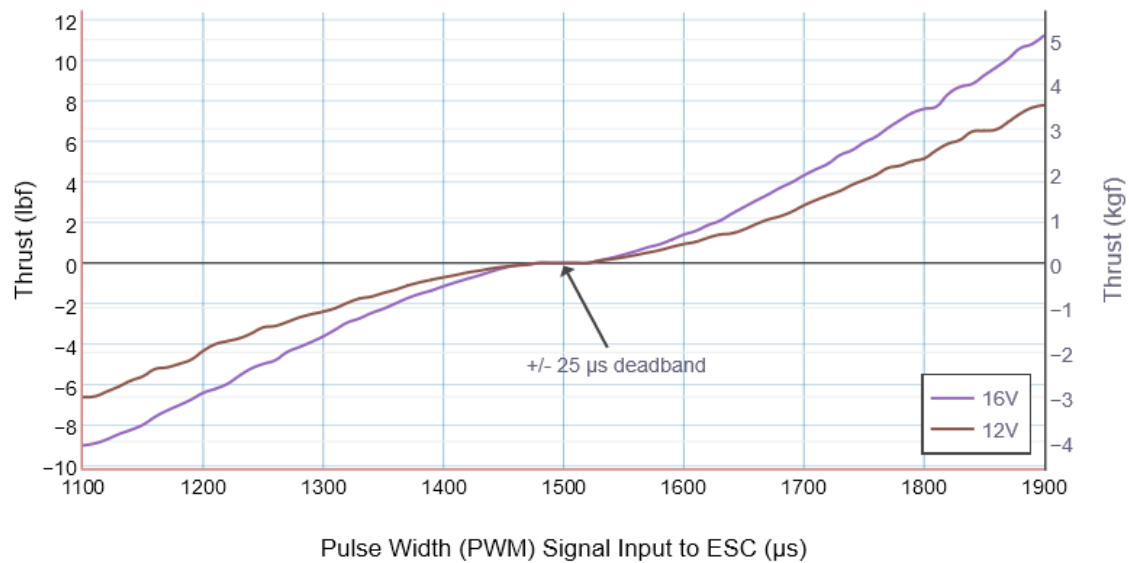


Figure 7.10: T200 Thruster: Thrust vs. PWM input to ESC, (source: [www.bluerobotics.com](http://www.bluerobotics.com))

### 7.2.3.2 PWM lookup table

Since the desired value of each thruster is calculated from control allocation in the previous section, one now needs to find the corresponding PWM value in order to send to the ESC for controlling the motor's speed.

For a T200 thruster with two different applied voltages, the corresponding thrust values (in *kgf* unit) generated at each PWM input signal are given in a table whose graphic representations are illustrated in Fig. 7.10. For the 15 *VDC* nominal applied voltage, the corresponding thrust value then can be interpolated. The PWM value of each thruster corresponding to a desired thrust ( $T$  in *kgf*, by dividing to 9.8065) at 15 *VDC* is thus inversely calculated in PX4 by using the following functions:

$$\left\{ \begin{array}{l}
 PWM = 0.8874T^2 + 86.1898T + 1425.6971, \text{ if } -3.8124 < T < -1.1317 \\
 PWM = 32.0868T^2 + 159.8091T + 1468.9169, \text{ if } -1.1317 \leq T < -0.0555 \\
 PWM = -4294.6327T^2 + 9.5768T + 1473.8331, \text{ if } -0.0555 \leq T < -0.01 \\
 PWM = 1500, \text{ if } -0.01 \leq T \leq 0.01 \\
 PWM = 502.3376T^2 + 94.9766T + 1523.0, \text{ if } 0.01 < T \leq 0.0566 \\
 PWM = 18.3647T^3 - 75.3368T^2 + 176.4630T + 1520.9868, \text{ if } 0.0566 < T \leq 1.7916 \\
 PWM = -2.1030T^2 + 82.5754T + 1558.4906, \text{ if } 1.7916 < T \leq 4.7037
 \end{array} \right.$$

Note that the calculated PWM value then needs to be rounded up to get the closest integer before sending to the ESC.

### 7.2.3.3 Depth measurement for depth control

For the purpose of depth measurement, the Bluerobotics Bar30 pressure sensor is connected directly to Pixhawk over I<sup>2</sup>C connection in the I3S-UV. The core of this sensor is MS5837. In fact, there exists a driver for barometer MS 5611 in PX4. By exploiting this driver and performing the necessary modifications, we successfully developed a driver for the Bar30 sensor. The sensor then is used to automatically stabilize the vehicle at a desired depth specified by the operator. The value of the measured pressure is sent from Pixhawk to the companion computer (i.e. `/control_in_ros_node`) by employing available (i.e. unused) message, for instance optical flow topic `/mavros/optical_flow` which is corresponding to `optical_flow` uORB message in PX4.

## 7.3 I3S-UV Product data sheet

The I3S-UV is a hybrid underwater vehicle of I3S-OSCAR team. It is employed with a very basic sensor suite including low-cost cameras and IMU. In manual control mode, it can be remotely controlled without or with auto-depth and auto-heading. Featured with advanced HomographyLab<sup>©</sup> and the state-of-the-art nonlinear control algorithm, the vehicle performs automatically dynamic positioning without a high-cost DVL. It

### 7.3. I3S-UV Product data sheet

---

can be upgraded to accept positioning systems for trajectory tracking. With additional side-scan sonar, it can be used for detecting debris items on the seabed or for fisheries research.

System Information	
Depth rating	100 m
Tether	50 m (can be upgraded to 300 m), neutral buoyancy
Submersible	
Dry weight	16 kg
Height	39 cm
Width	33 cm
Length	65 cm
Battery	LiPo, swappable with 2 hours endurance
Propulsion	
Configuration	6 thrusters (2 horizontal longitudinal/ 3 vertical/ 1 horizontal lateral)
Motor Type	Brushless
Thrust	10 kgf
Lighting	
Type	Cree XLamp MK-R LED
Number of Sources	one (can be added more if demanded)
Lumens	1500 lumens per light
Camera	
Sensor	OnSemi AR0135 CMOS Image Sensor
Orientation	Pointing forward/downward
View angle	92.8 ° Horizontal / 110 ° Diagonal
Integrated sensors	
IMU	System voltage
Leak indicator	Internal temperature
Depth sensor	Water temperature
Upgradable accessories	
Sonar	Navigation and Positioning Systems
Manipulators	Auxiliary Cameras
Auxiliary Lamps	

Table 7.2: I3S-UV product data sheet

### 7.3. I3S-UV Product data sheet

---

## **Part III**

# **Control of underactuated underwater vehicles**



# 8

## Trajectory tracking of slender-body axisymmetric underactuated underwater vehicles

**I**NTRODUCED by Bessel in 1828, the concept of added mass has become widely accepted nowadays. Mostly neglected in modeling and control design of heavier-than-air aircraft, added mass in contrast has always been at the heart of preoccupations of the Underwater Robotics and Automatic Control community [19, 46]. For underwater vehicles, added-mass effects often result in strongly nonlinear dynamics as the total mass matrix can no longer be considered as proportional to identity, except for spherical bodies [19]. These effects are all the more pronounced for underwater vehicles with a slender body shape conceived for reducing hydrodynamic drag along a nominal axis. However, added mass is not the unique source of complexity for control design. The complexity of hydrodynamic effects often impedes obtaining a precise dynamic model, valid in a large operating domain [45]. The vehicles are often subjected to strong perturbations (due to currents) whose magnitude can be commensurable with the available actuation power. Therefore, robust nonlinear control design for underwater vehicles is highly recommended.

---

Control design for underactuated AUVs has received increasing interest during the last three decades [19, 5, 72, 71]. When the control objective concerns the tracking of a reference position trajectory, whose velocity does not vanish for all time, various classical control design methodologies have been applied to provide solutions. For instance, various standard linear and nonlinear control methods have been applied on the basis of linear approximations of the two subsystems “depth-pitch” and “plane-yaw” about nominal operating points (see [19] and the reference therein). The main limitation of these approaches is the local nature of the control design and analysis. Moreover, stability and performance can suffer significantly when strong sea currents or aggressive manoeuvres excite the complex hydrodynamic and added-mass effects. Nonlinear Lyapunov-based control designs have been recently investigated to overcome some of these limitations. Most of them, however, only address the trajectory tracking problem in a horizontal plane, using a simplified and reduced “plane-yaw” 3-d.o.f model [5, 72]. Few works address this problem in the 3-dimensional space [4, 71]. A nonlinear high-gain backstepping-based controller proposed in [4] allows for exponential convergence of the position error to a small neighborhood of the origin, which means that asymptotic stabilization to zero is not fulfilled. Moreover, the attitude is not explicitly controlled but guided by the closed-loop system’s zero dynamics, thus possibly resulting in undesirable attitude dynamics. High-gain controllers are also known to be sensitive to measurement noise and time-delays of control inputs. Refnes et al. [71] have addressed the trajectory tracking for a slender-body underactuated AUV, with a model-based control approach. However, this approach heavily relies on the precision of the model parameters. Control performance can be drastically degraded when model errors are important (see, e.g., [76]). Nonlinear robust control design for underactuated AUVs thus remains an active research topic.

This chapter addresses the trajectory tracking control design for slender-body underactuated AUVs, whose body shape is symmetric with respect to the longitudinal axis, using a full 6-d.o.f model. The proposed control design methodology makes use of simple models of added mass and of dissipative hydrodynamic force acting on the vehicle. These models are both representative of the physics and sufficiently simple for control design and analysis. By considering an axisymmetric body, added-mass effects and dissipative hydrodynamic force are carefully accounted for via various adaptations, resulting in a modified apparent force independent of the vehicle’s orientation and subsequently a nonlinear system with a triangular control structure. The proposed controller is also complemented with bounded integral correction actions to compensate for unavoidable model uncertainties and external disturbances. Compared to [4], here almost global asymptotical stability is achieved and the attitude is explicitly controlled. The proposed control approach endowed with a cascade inner-outer loop architecture can be seen as

an extension of the thrust direction control paradigm that has been exploited for aerial vehicles [31, 70, 39], making a step towards a unified control approach for both aerial and underwater vehicles.

This chapter is organized as follows. System modeling is revised for axisymmetric underactuated underwater vehicles in Section 8.1. Then in the same section, a more simplified model for control design is derived. Control design supported by rigorous stability analysis is presented in Section 8.2. In section 8.3, comparative simulation results using a realistic model of a quasi-axisymmetric underwater vehicle illustrate the performance and robustness of the proposed control approach. Finally, a concluding section follows.

## 8.1 Modeling

### 8.1.1 System modeling

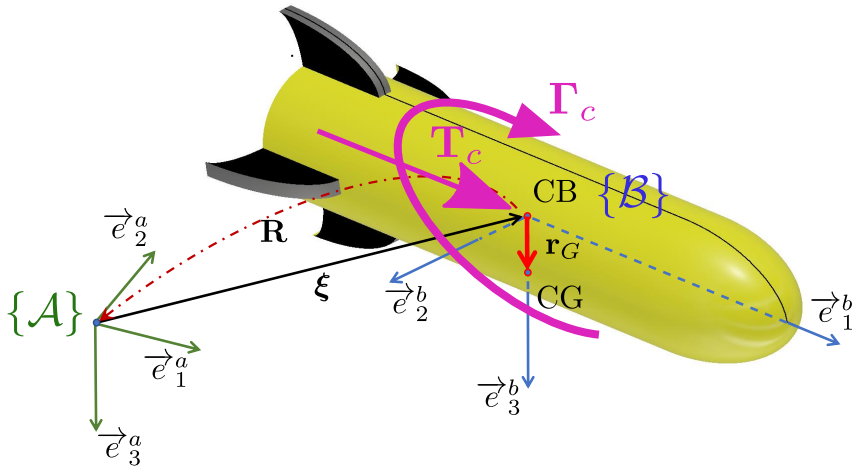


Figure 8.1: Slender-body underactuated vehicle

We consider a slender-body underactuated underwater vehicle with a body shape symmetric with respect to the longitudinal axis (e.g. the popular class of torpedo-shaped AUVs, c.f. Fig. 8.1). The vehicle is endowed with four control inputs, namely a thrust force intensity  $T_c \in \mathbb{R}$  of a control force vector  $\mathbf{T}_c$  acting along the vehicle's longitudinal axis (i.e.  $\mathbf{T}_c = T_c \mathbf{e}_1$ ) and three independent torque inputs  $\Gamma_c \in \mathbb{R}^3$  w.r.t. the CB to control the vehicle's orientation. The thrust force is assumed to apply at a point lying on the  $\{B; \vec{i}\}$ -axis so that it does not create any torque at the CB.

With the mentioned notions of control inputs, the vehicle dynamics with including

## 8.1. Modeling

---

current (3.20) can be written as

$$\begin{cases} \dot{\mathbf{P}}_h = \mathbf{P}_h \times \boldsymbol{\Omega} + \mathbf{F}_{gb} + \mathbf{F}_d + T_c \mathbf{e}_1 \\ \dot{\boldsymbol{\Pi}}_h = \boldsymbol{\Pi}_h \times \boldsymbol{\Omega} + \mathbf{P}_h \times \mathbf{V}_h + \boldsymbol{\Gamma}_g + \boldsymbol{\Gamma}_d + \boldsymbol{\Gamma}_c \end{cases} \quad (8.1)$$

The following classical model of  $\mathbf{F}_d$  is used:

$$\mathbf{F}_d(\mathbf{V}_h) = \underbrace{-\mathbf{K}_{dl} \mathbf{V}_h}_{\triangleq \mathbf{F}_{dl}(\mathbf{V}_h)} - \underbrace{|\mathbf{V}_h| \mathbf{K}_{dq} \mathbf{V}_h}_{\triangleq \mathbf{F}_{dq}(\mathbf{V}_h)}$$

with the damping diagonal matrices

$$\begin{aligned} \mathbf{K}_{dl} &= \text{diag}(k_{dl1}, k_{dl2}, k_{dl2}) \\ \mathbf{K}_{dq} &= \text{diag}(k_{dq1}, k_{dq2}, k_{dq2}) \end{aligned}$$

The second and third diagonal components of  $\mathbf{K}_{dl}$  and  $\mathbf{K}_{dq}$  are equal due to the body symmetry about the longitudinal axis. Similarly, the added-mass matrix can also be modeled as a diagonal matrix with the same second and third diagonal components, i.e.  $\mathbf{M}_a = \text{diag}(m_{a1}, m_{a2}, m_{a2})$ , with  $m_{a1} \ll m_{a2}$ . Thus, the summed mass matrix  $\mathbf{M}$  has the form  $\mathbf{M} = \text{diag}(m_1, m_2, m_2)$  with  $m_1 \triangleq m + m_{a1}$ ,  $m_2 \triangleq m + m_{a2}$ .

### 8.1.2 Model for control design

Due to the coupling matrix  $\boldsymbol{\Xi}$  involved in the definition (3.19) of the momentum terms and their dynamics (8.1), the translational and rotational dynamics are tightly coupled. These complex dynamic couplings are often neglected in the literature by neglecting all terms involving the matrix  $\boldsymbol{\Xi}$  using the fact that the distance between the CB and CG is small enough. This results in the following simpler control model that decouples the translational and rotational dynamics [4, 72, 71]:

$$\mathbf{M}\dot{\mathbf{V}} = (\mathbf{M}\mathbf{V}) \times \boldsymbol{\Omega} + \mathbf{F}_{gb} + \mathbf{F}_d(\mathbf{V}) + T_c \mathbf{e}_1 + \boldsymbol{\Delta}_F \quad (8.2a)$$

$$\mathbf{J}\dot{\boldsymbol{\Omega}} = (\mathbf{J}\boldsymbol{\Omega}) \times \boldsymbol{\Omega} + (\mathbf{M}\mathbf{V}) \times \mathbf{V} + \boldsymbol{\Gamma}_g + \boldsymbol{\Gamma}_d + \boldsymbol{\Gamma}_c + \boldsymbol{\Delta}_\Gamma \quad (8.2b)$$

with the “disturbance” terms

$$\begin{aligned} \boldsymbol{\Delta}_F &\triangleq -(\mathbf{M}\mathbf{V}_f) \times \boldsymbol{\Omega} - \mathbf{M}\boldsymbol{\Omega} \times \mathbf{V}_f + \mathbf{F}_d(\mathbf{V}_h) - \mathbf{F}_d(\mathbf{V}) \\ \boldsymbol{\Delta}_\Gamma &\triangleq (\mathbf{M}\mathbf{V}_h) \times \mathbf{V}_h - (\mathbf{M}\mathbf{V}) \times \mathbf{V} \end{aligned}$$

which are null if the current velocity is null. For the sake of simplicity, the disturbance term  $\boldsymbol{\Delta}_F$  will not be considered for control design (i.e.  $\boldsymbol{\Delta}_F \equiv \mathbf{0}$ ). However, integral corrections will be added so as to enhance control robustness w.r.t. unavoidable model errors and additive disturbances (i.e. current).

In the sequel, the simplified dynamics (8.2) (with  $\mathbf{\Delta}_F \equiv \mathbf{0}$ ) will be used for control design, whereas the dynamic equations (8.1) are still of use to simulate the vehicle's dynamics in the simulation section 8.3. Discrepancies between the two models represent an opportunity to test the robustness of the proposed controller.

Denote  $\mathbf{P} \triangleq \mathbf{M}\mathbf{V}$  and  $\mathbf{p} \triangleq \mathbf{R}\mathbf{P} = \mathbf{R}\mathbf{M}\mathbf{V}$  as the ‘‘simplified’’ translational momentums expressed in the body-fixed frame and the inertial frame, respectively. One easily verifies from (8.2a) that the dynamics of  $\mathbf{p}$  (i.e.  $\dot{\mathbf{p}}$ ) does not depend on  $\mathbf{\Omega}$ .

According to the basic control methodology for thrust-propelled underactuated vehicles presented in [31], control solution may become implicit (or even ill-posed) if the external force expressed in the inertial frame  $\mathbf{f}_e \triangleq \mathbf{R}(\mathbf{F}_{gb} + \mathbf{F}_d(\mathbf{V})) = \beta_{gb}\mathbf{e}_3 + \mathbf{R}\mathbf{F}_d(\mathbf{V})$  depends strongly on the vehicle's orientation  $\mathbf{R}$  but is not properly taken into account. The solution here proposed (similarly to the one developed in [70] for the control of axisymmetric aerial underactuated vehicles) consists in decomposing  $\mathbf{F}_d(\mathbf{V})$  into two parts with the first one acting along  $\mathbf{P}$  and the second one acting along  $\mathbf{e}_1$ . More precisely, one rewrites

$$\begin{aligned}\mathbf{F}_{dl}(\mathbf{V}) &= -\frac{k_{dl2}}{m_2}\mathbf{P} - \left(k_{dl1} - \frac{m_1k_{dl2}}{m_2}\right)V_1\mathbf{e}_1 \\ \mathbf{F}_{dq}(\mathbf{V}) &= -\frac{k_{dq2}}{m_2}|\mathbf{V}|\mathbf{P} - \left(k_{dq1} - \frac{m_1k_{dq2}}{m_2}\right)|\mathbf{V}|V_1\mathbf{e}_1\end{aligned}$$

so that Eq. (8.2a) can be rewritten as

$$\dot{\mathbf{P}} = \mathbf{P} \times \mathbf{\Omega} + \mathbf{F}_{gb} + \bar{\mathbf{F}}_{dl} + \bar{\mathbf{F}}_{dq} + \bar{T}\mathbf{e}_1 \quad (8.3)$$

with

$$\begin{cases} \bar{\mathbf{F}}_{dl} \triangleq -\beta_{dl}\mathbf{P}, \text{ with } \beta_{dl} \triangleq \frac{k_{dl2}}{m_2} \\ \bar{\mathbf{F}}_{dq} \triangleq -\beta_{dq}|\mathbf{V}|\mathbf{P}, \text{ with } \beta_{dq} \triangleq \frac{k_{dq2}}{m_2} \\ \bar{T} \triangleq T_c - \left(k_{dl1} - \frac{m_1k_{dl2}}{m_2}\right)V_1 - \left(k_{dq1} - \frac{m_1k_{dq2}}{m_2}\right)|\mathbf{V}|V_1 \end{cases}$$

Note that the quadratic drag force  $\mathbf{R}\bar{\mathbf{F}}_{dq}$ , expressed in the inertial frame  $\{\mathcal{I}\}$ , is not simply a function of  $\mathbf{p}$  but also depends on the norm of  $\mathbf{V}$  ( $= \mathbf{M}^{-1}\mathbf{R}^\top\mathbf{p}$ ) and thus on the attitude  $\mathbf{R}$ . This in turn implies that the time derivative of  $\mathbf{R}\bar{\mathbf{F}}_{dq}$  ( $= -\beta_{dq}|\mathbf{M}^{-1}\mathbf{R}^\top\mathbf{p}|$ ) involves the angular velocity  $\mathbf{\Omega}$ , making the control design more delicate.

## 8.2 Trajectory tracking control design

### 8.2.1 Basic developments

Let  $\boldsymbol{\xi}_r \in \mathbb{R}^3$  denote a smooth differentiable reference position trajectory (c.f. Fig. 8.2). Define  $\mathbf{v}_r \triangleq \dot{\boldsymbol{\xi}}_r \in \mathbb{R}^3$  as the reference velocity expressed in the inertial frame  $\{\mathcal{I}\}$ . Assume that  $|\mathbf{v}_r(t)| \geq c_v > 0$  and also that  $\mathbf{v}_r(t)$  and  $\dot{\mathbf{v}}_r(t)$  remain bounded for all time

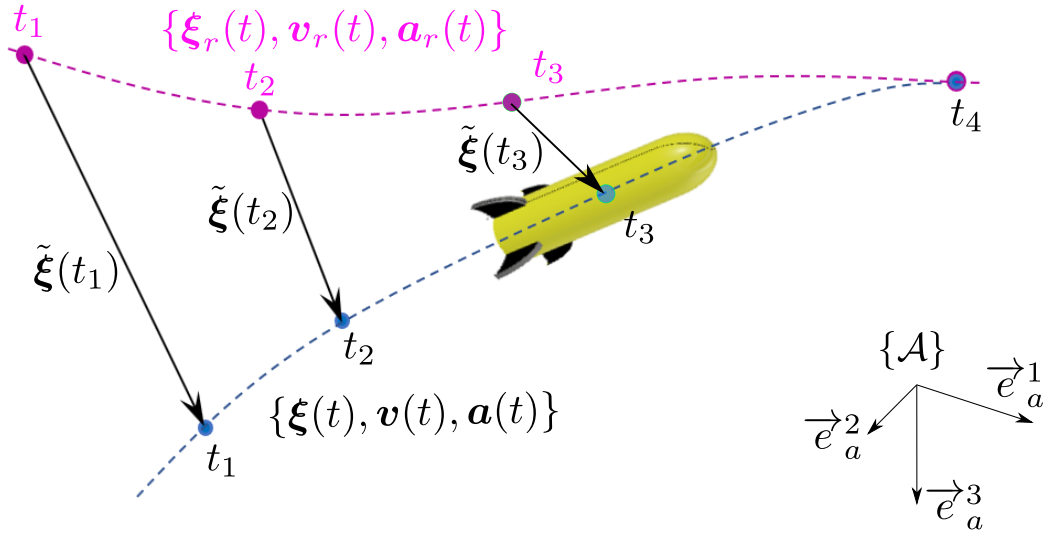


Figure 8.2: Trajectory tracking control problem

$t > 0$ .

The position and velocity errors are defined as

$$\begin{cases} \tilde{\xi} \triangleq \xi - \xi_r \\ \tilde{v} \triangleq v - v_r \end{cases} \quad (8.4)$$

whereas the velocity error and the translational momentum error, both expressed in the body-fixed frame, are defined as

$$\begin{cases} \tilde{V} \triangleq V - R^T v_r = R^T \tilde{v} \\ \tilde{P} \triangleq M \tilde{V} \end{cases} \quad (8.5)$$

Then, the control objective consists in stabilizing  $(\tilde{\xi}, \tilde{v})$  or, equivalently,  $(\tilde{\xi}, \tilde{P})$  about zero.

One easily verifies that

$$\dot{\tilde{\xi}} = R \tilde{V} = R M^{-1} \tilde{P} \quad (8.6)$$

On the other hand, using the decomposition

$$M = m_2 I_3 + m_{12} e_1 e_1^T$$

with  $m_{12} \triangleq m_1 - m_2 = m_{a1} - m_{a2} < 0$ , one deduces from (8.3) and (8.5) that

$$\begin{aligned}
 \dot{\tilde{\mathbf{P}}} &= -\mathbf{\Omega} \times \mathbf{P} + \mathbf{F}_{gb} + \bar{\mathbf{F}}_{dl} + \bar{\mathbf{F}}_{dq} + \bar{T} \mathbf{e}_1 \\
 &\quad + \mathbf{M} \mathbf{\Omega} \times \mathbf{R}^\top \mathbf{v}_r - \mathbf{M} \mathbf{R}^\top \dot{\mathbf{v}}_r \\
 &= -\mathbf{\Omega} \times \tilde{\mathbf{P}} - \mathbf{\Omega} \times \mathbf{M} \mathbf{R}^\top \mathbf{v}_r + \mathbf{M} \mathbf{\Omega} \times \mathbf{R}^\top \mathbf{v}_r \\
 &\quad + \mathbf{F}_{gb} + \bar{\mathbf{F}}_{dl} + \bar{\mathbf{F}}_{dq} - m_2 \mathbf{R}^\top \dot{\mathbf{v}}_r \\
 &\quad + (\bar{T} - m_{12} \mathbf{e}_1^\top \mathbf{R}^\top \dot{\mathbf{v}}_r) \mathbf{e}_1 \\
 &= -\mathbf{\Omega} \times \tilde{\mathbf{P}} - \beta_{dq} (|\mathbf{V}| - |\mathbf{v}_r|) \mathbf{P} + \alpha_r \mathbf{e}_1 \times \mathbf{\Omega} \\
 &\quad + \mathbf{R}^\top (\beta_{gb} \mathbf{e}_3 - \beta_{dl} \mathbf{p} - \beta_{dq} |\mathbf{v}_r| \mathbf{p} - m_2 \dot{\mathbf{v}}_r) + (\bar{T} - \dot{\alpha}_r) \mathbf{e}_1
 \end{aligned} \tag{8.7}$$

with

$$\alpha_r \triangleq m_{12} \mathbf{e}_1^\top \mathbf{R}^\top \mathbf{v}_r \tag{8.8}$$

The term  $-\beta_{dq} (|\mathbf{V}| - |\mathbf{v}_r|) \mathbf{P}$  involved in the last equality of (8.7) requires further developments. Using the decomposition

$$\tilde{\mathbf{P}} = \mathbf{P} - m_2 \mathbf{R}^\top \mathbf{v}_r - \alpha_r \mathbf{e}_1$$

one deduces

$$\begin{aligned}
 &(|\mathbf{V}| - |\mathbf{v}_r|) \mathbf{P} \\
 &= -(|\mathbf{V}| - |\mathbf{v}_r|) \alpha_r \mathbf{e}_1 + (|\mathbf{V}| - |\mathbf{v}_r|) (\tilde{\mathbf{P}} + m_2 \mathbf{R}^\top \mathbf{v}_r) \\
 &= -(|\mathbf{V}| - |\mathbf{v}_r|) \alpha_r \mathbf{e}_1 + \frac{|\tilde{\mathbf{V}} + \mathbf{R}^\top \mathbf{v}_r|^2 - |\mathbf{v}_r|^2}{|\mathbf{V}| + |\mathbf{v}_r|} (\tilde{\mathbf{P}} + m_2 \mathbf{R}^\top \mathbf{v}_r) \\
 &= -(|\mathbf{V}| - |\mathbf{v}_r|) \alpha_r \mathbf{e}_1 + \frac{|\tilde{\mathbf{V}}|^2 + 2\tilde{\mathbf{V}}^\top \mathbf{R}^\top \mathbf{v}_r}{|\mathbf{V}| + |\mathbf{v}_r|} (\tilde{\mathbf{P}} + m_2 \mathbf{R}^\top \mathbf{v}_r)
 \end{aligned} \tag{8.9}$$

From (8.7) and (8.9) one obtains

$$\begin{aligned}
 \dot{\tilde{\mathbf{P}}} &= -\mathbf{\Omega} \times \tilde{\mathbf{P}} - \beta_{dq} \frac{|\tilde{\mathbf{V}}|^2 + 2\tilde{\mathbf{V}}^\top \mathbf{R}^\top \mathbf{v}_r}{|\mathbf{V}| + |\mathbf{v}_r|} (\tilde{\mathbf{P}} + m_2 \mathbf{R}^\top \mathbf{v}_r) \\
 &\quad + \alpha_r \mathbf{e}_1 \times \mathbf{\Omega} + \mathbf{R}^\top \mathbf{f}_p + T_p \mathbf{e}_1
 \end{aligned} \tag{8.10}$$

with

$$\begin{cases} \mathbf{f}_p \triangleq \beta_{gb} \mathbf{e}_3 - \beta_{dl} \mathbf{p} - \beta_{dq} |\mathbf{v}_r| \mathbf{p} - m_2 \dot{\mathbf{v}}_r \\ T_p \triangleq \bar{T} - \dot{\alpha}_r + \beta_{dq} (|\mathbf{V}| - |\mathbf{v}_r|) \alpha_r \end{cases} \tag{8.11}$$

Let us call  $\mathbf{f}_p$  the ‘‘apparent’’ force (expressed in the inertial frame). Note that its time derivative is independent of the angular velocity  $\mathbf{\Omega}$  (i.e.  $\dot{\mathbf{f}}_p \approx \mathbf{\Omega}$ ), which is an important property for control design.

The proposed controller will be derived from Eqs. (8.6), (8.10) and (8.2b), which are in cascade form. In fact, the rotational dynamics given by (8.2b) are fully-actuated with a 3-dimensional control torque vector  $\mathbf{\Gamma}_c$  monitoring 3 degrees of freedom of rotation.

## 8.2. Trajectory tracking control design

It is thus straightforward to design an “inner-loop” controller that asymptotically stabilizes  $\Omega$  about any bounded smooth desired angular velocity  $\Omega_d$ , provided that the time derivative of the latter is available as feedforward. For instance, assuming that  $\Delta_\Gamma$  is constant, the following torque controller

$$\begin{aligned} \Gamma_c = & -\mathbf{K}_1 \tilde{\Omega} - \mathbf{K}_2 \mathbf{I}_{\tilde{\Omega}} + \mathbf{J} \dot{\Omega}_d \\ & - (\mathbf{J}\Omega) \times \Omega_d - (\mathbf{M}\mathbf{V}) \times \mathbf{V} - \Gamma_g - \Gamma_d \end{aligned} \quad (8.12)$$

with  $\tilde{\Omega} \triangleq \Omega - \Omega_d$ ,  $\mathbf{I}_{\tilde{\Omega}}$  an integrator of  $\tilde{\Omega}$ , and  $\mathbf{K}_{1,2} \in \mathbb{R}^{3 \times 3}$  positive diagonal gain matrices, results in a closed-loop stable sub-system. Hence, the underlying idea for “outer-loop” control design consists in using  $\Omega$  as an intermediate control variable for the translational dynamics (i.e. Eq. (8.10)).

### 8.2.2 Outer-loop control design

Let  $\mathbf{y} \triangleq \mathbf{K}_\xi \tilde{\xi}$  denote the position error scaled by a diagonal positive gain matrix  $\mathbf{K}_\xi \in \mathbb{R}^{3 \times 3}$ . By introducing feedback terms (i.e. functions of  $\tilde{\mathbf{P}}$  and  $\tilde{\xi}$ ), the translational error dynamics (8.10) can be rewritten as

$$\begin{aligned} \dot{\tilde{\mathbf{P}}} = & -\Omega \times \tilde{\mathbf{P}} - \underbrace{\mathbf{K}_P \tilde{\mathbf{P}} - \mathbf{M}^{-1} \mathbf{R}^\top \mathbf{K}_\xi (h(|\mathbf{y}|^2) \mathbf{y})}_{\text{feedback terms}} \\ & - \beta_{dq} \frac{|\tilde{\mathbf{V}}|^2 + 2\tilde{\mathbf{V}}^\top \mathbf{R}^\top \mathbf{v}_r}{|\mathbf{V}| + |\mathbf{v}_r|} (\tilde{\mathbf{P}} + m_2 \mathbf{R}^\top \mathbf{v}_r) \\ & + \alpha_r \mathbf{e}_{1 \times} \Omega + \mathbf{R}^\top \bar{\mathbf{f}}_p + \bar{T}_p \mathbf{e}_1 \end{aligned} \quad (8.13)$$

with  $\mathbf{K}_P \triangleq \text{diag}(k_{p1} + k_{p2}, k_{p1}, k_{p1})$ ,  $k_{p1}, k_{p2} > 0$ ,  $h(\cdot)$  denoting a smooth bounded strictly positive function defined on  $[0, +\infty)$  such that for some positive numbers  $\eta, \beta$

$$\begin{cases} \forall s \in \mathbb{R}, h(s^2)s < \eta \\ \forall s \in \mathbb{R}, \frac{\partial}{\partial s}(h(s^2)s) < \beta \end{cases}$$

and

$$\begin{cases} \bar{\mathbf{f}}_p \triangleq \mathbf{f}_p + k_{p1}(\mathbf{p} - m_2 \mathbf{v}_r) + \frac{1}{m_2} \mathbf{K}_\xi (h(|\mathbf{y}|^2) \mathbf{y}) \\ \bar{T}_p \triangleq T_p - k_{p1} \alpha_r + k_{p2} \tilde{P}_1 - \frac{m_{12}}{m_1 m_2} \mathbf{e}_1^\top \mathbf{R}^\top \mathbf{K}_\xi (h(|\mathbf{y}|^2) \mathbf{y}) \end{cases} \quad (8.14)$$

Note that the augmented apparent force  $\bar{\mathbf{f}}_p$  does not depend on the vehicle’s attitude  $\mathbf{R}$  nor on  $\Omega$ . Thus, its time derivative does not depend on the angular velocity  $\Omega$ .

If the outer-loop controller asymptotically stabilizes

$$\varepsilon_P \triangleq \alpha_r \mathbf{e}_{1 \times} \Omega + \mathbf{R}^\top \bar{\mathbf{f}}_p + \bar{T}_p \mathbf{e}_1 \quad (8.15)$$

about zero, then the resulting zero dynamics of (8.13) are

$$\begin{aligned} \dot{\tilde{\mathbf{P}}} &= -\boldsymbol{\Omega}_\times \tilde{\mathbf{P}} - \mathbf{K}_P \tilde{\mathbf{P}} - \mathbf{M}^{-1} \mathbf{R}^\top \mathbf{K}_\xi (h(|\mathbf{y}|^2) \mathbf{y}) \\ &\quad - \beta_{dq} \frac{|\tilde{\mathbf{V}}|^2 + 2\tilde{\mathbf{V}}^\top \mathbf{R}^\top \mathbf{v}_r}{|\mathbf{V}| + |\mathbf{v}_r|} (\tilde{\mathbf{P}} + m_2 \mathbf{R}^\top \mathbf{v}_r) \end{aligned} \quad (8.16)$$

We show next that appropriate choices of gains  $k_{p1}$  and  $k_{p2}$  (i.e.  $\mathbf{K}_P$ ) will render the origin of the zero-dynamic time-varying system (8.6)+(8.16) globally asymptotically stable

**Lemma 3.** Choose  $k_{p1}$  and  $k_{p2}$  such that

$$\begin{cases} k_{p1} > \left(1 + \frac{m_2}{2m_1}\right)^2 \beta_{dq} \sup(|\mathbf{v}_r|) \\ k_{p2} > \left(1 - \frac{m_2}{m_1}\right)^2 \beta_{dq} \sup(|\mathbf{v}_r|) \end{cases} \quad (8.17)$$

then the equilibrium  $(\tilde{\boldsymbol{\xi}}, \tilde{\mathbf{P}}) = (\mathbf{0}, \mathbf{0})$  of the zero-dynamic system (8.6)+(8.16) is globally asymptotically stable.

**Proof.** The time derivative of the Lyapunov function candidate

$$\mathcal{L} \triangleq \frac{1}{2} |\tilde{\mathbf{P}}|^2 + \int_0^{|\mathbf{y}|} h(s^2) s \, ds$$

satisfies

$$\begin{aligned} \dot{\mathcal{L}} &= -k_{p1} |\tilde{\mathbf{P}}|^2 - k_{p2} |\tilde{P}_1|^2 \\ &\quad - \beta_{dq} \frac{|\tilde{\mathbf{V}}|^2 + 2\tilde{\mathbf{V}}^\top \mathbf{R}^\top \mathbf{v}_r}{|\mathbf{V}| + |\mathbf{v}_r|} (|\tilde{\mathbf{P}}|^2 + m_2 \tilde{\mathbf{P}}^\top \mathbf{R}^\top \mathbf{v}_r) \\ &\leq -k_{p1} |\tilde{\mathbf{P}}|^2 - \frac{\beta_{dq}}{|\mathbf{V}| + |\mathbf{v}_r|} |\tilde{\mathbf{V}}|^2 |\tilde{\mathbf{P}}|^2 \\ &\quad + \frac{2\beta_{dq} |\mathbf{v}_r|}{|\mathbf{V}| + |\mathbf{v}_r|} |\tilde{\mathbf{V}}| |\tilde{\mathbf{P}}|^2 + \frac{\beta_{dq} m_2 |\mathbf{v}_r|}{|\mathbf{V}| + |\mathbf{v}_r|} |\tilde{\mathbf{V}}|^2 |\tilde{\mathbf{P}}| \\ &\quad - k_{p2} |\tilde{P}_1|^2 - \frac{2\beta_{dq} m_2^2}{|\mathbf{V}| + |\mathbf{v}_r|} (\tilde{\mathbf{V}}^\top \mathbf{R}^\top \mathbf{v}_r)^2 \\ &\quad + \frac{2\beta_{dq} m_2 |m_{12}| |\mathbf{v}_r|}{m_1 (|\mathbf{V}| + |\mathbf{v}_r|)} |\tilde{P}_1| |\tilde{\mathbf{V}}^\top \mathbf{R}^\top \mathbf{v}_r| \end{aligned}$$

Using the relation  $|\tilde{\mathbf{V}}| \leq \frac{1}{m_1} |\tilde{\mathbf{P}}|$  one then deduces

$$\begin{aligned} \dot{\mathcal{L}} &\leq -k_{p1} |\tilde{\mathbf{P}}|^2 - \frac{\beta_{dq}}{|\mathbf{V}| + |\mathbf{v}_r|} |\tilde{\mathbf{V}}|^2 |\tilde{\mathbf{P}}|^2 + \frac{(2 + \frac{m_2}{m_1}) \beta_{dq} |\mathbf{v}_r|}{|\mathbf{V}| + |\mathbf{v}_r|} |\tilde{\mathbf{V}}| |\tilde{\mathbf{P}}|^2 \\ &\quad - k_{p2} |\tilde{P}_1|^2 - \frac{2\beta_{dq} m_2^2}{|\mathbf{V}| + |\mathbf{v}_r|} (\tilde{\mathbf{V}}^\top \mathbf{R}^\top \mathbf{v}_r)^2 \\ &\quad + \frac{2\beta_{dq} m_2 |m_{12}| |\mathbf{v}_r|}{m_1 (|\mathbf{V}| + |\mathbf{v}_r|)} |\tilde{P}_1| |\tilde{\mathbf{V}}^\top \mathbf{R}^\top \mathbf{v}_r| \end{aligned}$$

The gain condition (8.17) then ensures that all the negative quadratic terms domi-

## 8.2. Trajectory tracking control design

nate the cross terms, i.e.

$$k_{p1}|\tilde{\mathbf{P}}|^2 + \frac{\beta_{dq}}{|\mathbf{V}|+|\mathbf{v}_r|}|\tilde{\mathbf{V}}|^2|\tilde{\mathbf{P}}|^2 > \frac{(2+\frac{m_2}{m_1})\beta_{dq}|\mathbf{v}_r|}{|\mathbf{V}|+|\mathbf{v}_r|}|\tilde{\mathbf{V}}||\tilde{\mathbf{P}}|^2$$

$$k_{p2}|\tilde{P}_1|^2 + \frac{2\beta_{dq}m_2^2}{|\mathbf{V}|+|\mathbf{v}_r|}(\tilde{\mathbf{V}}^\top \mathbf{R}^\top \mathbf{v}_r)^2 > \frac{2\beta_{dq}m_2|m_{12}||\mathbf{v}_r|}{m_1(|\mathbf{V}|+|\mathbf{v}_r|)}|\tilde{P}_1||\tilde{\mathbf{V}}^\top \mathbf{R}^\top \mathbf{v}_r|$$

This in turn implies the existence of a positive number  $c$  such that  $\dot{\mathcal{L}} \leq -c|\tilde{\mathbf{P}}|^2$ . From there one can easily verify the boundedness of  $\dot{\mathcal{L}}$  (i.e. the uniform continuity of  $\dot{\mathcal{L}}$ ) so that direct application of Barbalat's lemma then ensures the convergence of  $\dot{\mathcal{L}}$  and, thus, of  $\tilde{\mathbf{P}}$  to zero. From (8.16) and the convergence of  $\tilde{\mathbf{P}}$  to zero, one deduces by application of the extended Barbalat's lemma [58] that  $\dot{\tilde{\mathbf{P}}}$  also converges to zero, which in turn implies the convergence of  $\mathbf{y}$  (i.e.  $\tilde{\boldsymbol{\xi}}$ ) to zero. The remainder of the proof then follows.  $\square$

Now the remaining task consists in designing the desired value  $\boldsymbol{\Omega}_d$  for  $\boldsymbol{\Omega}$  and the thrust intensity  $\bar{T}_p$  (or equivalently  $T$ ) to stabilize

$$\alpha_r \mathbf{e}_{1 \times} \boldsymbol{\Omega}_d + \mathbf{R}^\top \bar{\mathbf{f}}_p + \bar{T}_p \mathbf{e}_1 \rightarrow \mathbf{0} \quad (8.18)$$

which is also equivalent to the stabilization of  $\varepsilon_P$  defined by (8.15) about zero as a consequence of the inner-loop controller that asymptotically stabilizes  $\boldsymbol{\Omega}$  about  $\boldsymbol{\Omega}_d$ .

**Remark 6.** By assumption  $\mathbf{v}_r$  does not vanish for all time and  $m_{12} = m_{a1} - m_{a2} \neq 0$  due to the slender-body form of the vehicle, one may expect that  $\alpha_r$  defined by (8.8) does not vanish for all time either. Assuming that  $\alpha_r(t) \neq 0 \forall t$ , in view of (8.18) one may define the outer-loop controller as follows:

$$\begin{cases} \bar{T}_p &= -\mathbf{e}_1^\top \mathbf{R}^\top \bar{\mathbf{f}}_p \\ \Omega_{d,2} &= -\frac{1}{\alpha_r} \mathbf{e}_3^\top \mathbf{R}^\top \bar{\mathbf{f}}_p \\ \Omega_{d,3} &= \frac{1}{\alpha_r} \mathbf{e}_2^\top \mathbf{R}^\top \bar{\mathbf{f}}_p \end{cases} \quad (8.19)$$

However, the outer-loop controller (8.19) leaves the attitude uncontrolled and ultimately guided by the system's zero dynamics, which may be excessively oscillating.

The outer-loop control solution proposed in this paper, by contrast, defines a desired direction  $\mathbf{u} \in S^2$  for  $\mathbf{R}^\top \boldsymbol{\gamma}$  with  $\boldsymbol{\gamma} \triangleq \bar{\mathbf{f}}_p / |\bar{\mathbf{f}}_p| \in S^2$  representing the direction of  $\bar{\mathbf{f}}_p$ , where  $\mathbf{u}$  is obtained by integration of the following differential equation

$$\dot{\mathbf{u}} = \mathbf{u} \times \boldsymbol{\Omega}_u, \quad \mathbf{u}(0) = -\mathbf{e}_1 \quad (8.20)$$

with  $\boldsymbol{\Omega}_u$  an augmented control input to be designed thereafter. For instance, assuming that  $\bar{\mathbf{f}}_p$  does not vanish for all time, one then verifies that

$$\dot{\gamma} = \gamma \times \Omega_\gamma \quad (8.21)$$

with  $\Omega_\gamma \triangleq -\frac{\bar{\mathbf{f}}_p \times \dot{\bar{\mathbf{f}}}_p}{|\bar{\mathbf{f}}_p|^2}$ , which does not depend on  $\Omega$ . In view of the expression of  $\bar{\mathbf{f}}_p$  in (8.14), one ensures that  $\Omega_\gamma$  does not depend on the angular velocity  $\Omega$ .

**Lemma 4.** *Assume that initially  $(\mathbf{R}^\top \gamma)(0) \neq -\mathbf{u}(0)$  and that the inner-loop controller ensures the convergence of  $\tilde{\Omega}$  about zero and also its boundedness. Then, by setting the following constraint*

$$\pi_{\mathbf{u}}(\Omega_d - \Omega_u) = -\pi_{\mathbf{u}}(\mathbf{R}^\top \Omega_\gamma) - \frac{k_u(\mathbf{R}^\top \gamma \times \mathbf{u})}{1 + \mathbf{u}^\top \mathbf{R}^\top \gamma} \quad (8.22)$$

with  $k_u > 0$ , one ensures that  $\mathbf{R}^\top \gamma$  converges asymptotically to  $\mathbf{u}$ .

**Proof.** Using (8.20), (8.21) and (8.22), the time derivative of the positive function  $\mathcal{L}_1 \triangleq 1 - \mathbf{u}^\top \mathbf{R}^\top \gamma$  verifies

$$\begin{aligned} \dot{\mathcal{L}}_1 &= (\Omega - \Omega_u + \mathbf{R}^\top \Omega_\gamma)^\top (\mathbf{R}^\top \gamma \times \mathbf{u}) \\ &= \tilde{\Omega}^\top (\mathbf{R}^\top \gamma \times \mathbf{u}) + (\Omega_d - \Omega_u + \mathbf{R}^\top \Omega_\gamma)^\top (\mathbf{R}^\top \gamma \times \mathbf{u}) \\ &= \tilde{\Omega}^\top (\mathbf{R}^\top \gamma \times \mathbf{u}) - k_u \frac{|\mathbf{R}^\top \gamma \times \mathbf{u}|^2}{1 + \mathbf{u}^\top \mathbf{R}^\top \gamma} \end{aligned}$$

where the first term  $\tilde{\Omega}^\top (\mathbf{R}^\top \gamma \times \mathbf{u})$  is bounded thanks to the boundedness of  $\tilde{\Omega}$ , whereas the division by  $1 + \mathbf{u}^\top \mathbf{R}^\top \gamma$  in the second term prevents  $\mathbf{R}^\top \gamma$  from tending close to  $-\mathbf{u}$  since  $\dot{\mathcal{L}}_1$  tends to  $-\infty$  in this case.

Using the relation  $|\mathbf{R}^\top \gamma \times \mathbf{u}|^2 + (\mathbf{u}^\top \mathbf{R}^\top \gamma)^2 = 1$ , one then deduces that

$$\dot{\mathcal{L}}_1 = \tilde{\Omega}^\top (\mathbf{R}^\top \gamma \times \mathbf{u}) - k_u \mathcal{L}_1$$

Since  $\tilde{\Omega}$  converges to zero, the application of the singular perturbation theory then ensures the convergence of  $\mathcal{L}_1$  to zero or equivalently of  $\mathbf{R}^\top \gamma$  to  $\mathbf{u}$ .  $\square$

Now the main result of this section can be stated.

**Proposition 8.** *Let  $\bar{T}_p$  and  $\bar{\mathbf{f}}_p$  be defined by (8.14)+(8.11) and  $\alpha_r$  be defined by (8.8). Apply the outer-loop controller*

$$\begin{cases} \bar{T}_p &= -\mathbf{e}_1^\top \mathbf{R}^\top \bar{\mathbf{f}}_p \\ \Omega_d &= \frac{|\bar{\mathbf{f}}_p|}{\alpha_r} \mathbf{e}_1 \times \mathbf{u} - \frac{k_u(\mathbf{R}^\top \gamma \times \mathbf{u})}{1 + \mathbf{u}^\top \mathbf{R}^\top \gamma} + \lambda \mathbf{e}_1 \end{cases} \quad (8.23)$$

where  $\mathbf{u}$  is obtained by integration of (8.20) with the augmented control input  $\Omega_u$  given by

$$\Omega_u = \frac{|\bar{\mathbf{f}}_p|}{\alpha_r} \mathbf{e}_1 \times \mathbf{u} + \pi_{\mathbf{u}}(\mathbf{R}^\top \Omega_\gamma) + \lambda \pi_{\mathbf{u}} \mathbf{e}_1 \quad (8.24)$$

## 8.2. Trajectory tracking control design

---

and  $\lambda(\cdot)$  is a function that can be independently assigned for other control objective related to the roll motion. Assume that  $\alpha_r \neq 0$  and  $|\bar{\mathbf{f}}_p| > 0$  for all time. Assume that all conditions and assumptions in Lemmas 3 and 4 hold. Then, the equilibrium  $(\boldsymbol{\xi}, \mathbf{v}, \mathbf{R}^\top \boldsymbol{\gamma}) = (\boldsymbol{\xi}_r, \mathbf{v}_r, \mathbf{u})$  is almost globally asymptotically stable.

The proof of this proposition is a direct result of Lemmas 3 and 4.

**Remark 7.** In the case  $m_{12} < 0$ ,  $\alpha_r$  is nominally negative. So if  $\boldsymbol{\Omega}_\gamma$  is not too large, the term  $\frac{|\bar{\mathbf{f}}_p|}{\alpha_r} \mathbf{e}_1 \times \mathbf{u}$  involved in (8.24) allows  $\mathbf{u}$  not to depart too far from  $-\mathbf{e}_1$ . This can be justified by examining the derivative of  $1 + \mathbf{e}_1^\top \mathbf{u}$ :

$$\frac{d}{dt}(1 + \mathbf{e}_1^\top \mathbf{u}) = \underbrace{\frac{|\bar{\mathbf{f}}_p|}{\alpha_r} |\mathbf{e}_1 \times \mathbf{u}|^2}_{\leq 0} + (\mathbf{e}_1 \times \mathbf{u})^\top (\mathbf{R}^\top \boldsymbol{\Omega}_\gamma)$$

**Remark 8.** Since  $\alpha_r$  may evolve near zero during a transient phase, to avoid the division by zero we suggest to replace the expressions of  $\boldsymbol{\Omega}_d$  and  $\boldsymbol{\Omega}_u$  given in (8.23) and (8.24) by

$$\begin{cases} \boldsymbol{\Omega}_d = \frac{|\bar{\mathbf{f}}_p|}{\sigma(\alpha_r)} \mathbf{e}_1 \times \mathbf{u} - \frac{k_u (\mathbf{R}^\top \boldsymbol{\gamma} \times \mathbf{u})}{1 + \mathbf{u}^\top \mathbf{R}^\top \boldsymbol{\gamma}} + \lambda \mathbf{e}_1 \\ \boldsymbol{\Omega}_u = \frac{|\bar{\mathbf{f}}_p|}{\sigma(\alpha_r)} \mathbf{e}_1 \times \mathbf{u} + \pi_{\mathbf{u}} (\mathbf{R}^\top \boldsymbol{\Omega}_\gamma) + \lambda \pi_{\mathbf{u}} \mathbf{e}_1 \end{cases} \quad (8.25)$$

with  $\sigma(\cdot)$  given by

$$\sigma(x) = \begin{cases} x & \text{if } |x| > \varepsilon \\ \varepsilon & \text{if } 0 < x \leq \varepsilon \\ -\varepsilon & \text{if } 0 \geq x \geq -\varepsilon \end{cases} \quad (8.26)$$

with  $\varepsilon$  a small positive number. With this modification, relation (8.22) is always satisfied and, thus, the convergence of  $\mathbf{R}^\top \boldsymbol{\gamma}$  about  $\mathbf{u}$  is still ensured.

### 8.2.3 Outer-loop control design with integral term

In practice it is often desirable to complement the control action with a position error integral correction term in order to compensate for model uncertainties and external disturbances. Bearing in mind that classical integrator of  $\tilde{\boldsymbol{\xi}}$  is often prone to the well-known phenomenon of integrator windup that may cause large overshoots of the position tracking error, we make use of the following bounded nonlinear second-order integrator of  $\tilde{\boldsymbol{\xi}}$  (initially proposed in [32]):

$$\ddot{\mathbf{I}}_{\tilde{\boldsymbol{\xi}}} = -2k_{vI} \dot{\mathbf{I}}_{\tilde{\boldsymbol{\xi}}} + \text{sat}_{\ddot{\mathbf{I}}_{max}/2}(k_{pI}(-\mathbf{I}_{\tilde{\boldsymbol{\xi}}} + \text{sat}_{\delta_I}(\mathbf{I}_{\tilde{\boldsymbol{\xi}}} + \tilde{\boldsymbol{\xi}}))) \quad (8.27)$$

with  $\ddot{\mathbf{I}}_{max}$ ,  $\delta_I$ ,  $k_{pI}$ ,  $k_{vI}$  denoting positive constants and with initial conditions satisfying  $|\mathbf{I}_{\tilde{\boldsymbol{\xi}}}(0)| < \delta_I + \ddot{\mathbf{I}}_{max}/(2k_{vI}^2)$  and  $|\dot{\mathbf{I}}_{\tilde{\boldsymbol{\xi}}}(0)| < \ddot{\mathbf{I}}_{max}/(2k_{vI})$ . As specified in [32], the ultimate

upper-bounds of  $|\mathbf{I}_{\tilde{\xi}}|$ ,  $|\dot{\mathbf{I}}_{\tilde{\xi}}|$ , and  $|\ddot{\mathbf{I}}_{\tilde{\xi}}|$  are  $\delta_I + \ddot{I}_{max}/(2k_{vI}^2)$ ,  $\dot{I}_{max}/(2k_{vI})$ , and  $\ddot{I}_{max}$ , respectively.

Define the augmented reference variables

$$\begin{cases} \bar{\boldsymbol{\xi}}_r \triangleq \boldsymbol{\xi}_r - \mathbf{K}_I \mathbf{I}_{\tilde{\xi}} \\ \bar{\mathbf{v}}_r \triangleq \mathbf{v}_r - \mathbf{K}_I \dot{\mathbf{I}}_{\tilde{\xi}} \end{cases} \quad (8.28)$$

with  $\mathbf{K}_I \in \mathbb{R}^{3 \times 3}$  a diagonal positive integral gain matrix. Define also the augmented error terms (compared to (8.4)–(8.5))

$$\begin{cases} \tilde{\boldsymbol{\xi}} \triangleq \boldsymbol{\xi} - \bar{\boldsymbol{\xi}}_r & = \tilde{\boldsymbol{\xi}} + \mathbf{K}_I \mathbf{I}_{\tilde{\xi}} \\ \tilde{\mathbf{v}} \triangleq \mathbf{v} - \bar{\mathbf{v}}_r & = \tilde{\mathbf{v}} + \mathbf{K}_I \dot{\mathbf{I}}_{\tilde{\xi}} \\ \tilde{\mathbf{V}} \triangleq \mathbf{V} - \mathbf{R}^\top \bar{\mathbf{v}}_r & = \mathbf{R}^\top \tilde{\mathbf{v}} \\ \tilde{\mathbf{P}} \triangleq \mathbf{M} \tilde{\mathbf{V}} & = \mathbf{P} - \mathbf{M} \mathbf{R}^\top \bar{\mathbf{v}}_r \end{cases} \quad (8.29)$$

One verifies that

$$\dot{\tilde{\boldsymbol{\xi}}} = \mathbf{R} \mathbf{M}^{-1} \dot{\tilde{\mathbf{P}}} \quad (8.30)$$

On the other hand, analogously to the developments carried out in (8.7)–(8.11) one deduces

$$\begin{aligned} \dot{\tilde{\mathbf{P}}} &= -\boldsymbol{\Omega}_\times \tilde{\mathbf{P}} \\ &\quad - \beta_{dq} \frac{|\tilde{\mathbf{V}}|^2 + 2\tilde{\mathbf{V}}^\top \mathbf{R}^\top \bar{\mathbf{v}}_r}{|\mathbf{V}| + |\bar{\mathbf{v}}_r|} (\tilde{\mathbf{P}} + m_2 \mathbf{R}^\top \bar{\mathbf{v}}_r) \\ &\quad + \alpha_r \mathbf{e}_{1 \times} \boldsymbol{\Omega} + \mathbf{R}^\top \mathbf{f}_p + T_p \mathbf{e}_1 \end{aligned} \quad (8.31)$$

where  $\alpha_r$  is now defined by (instead of (8.8))

$$\alpha_r \triangleq m_{12} \mathbf{e}_1^\top \mathbf{R}^\top \bar{\mathbf{v}}_r \quad (8.32)$$

and  $\mathbf{f}_p$  and  $T_p$  are defined by (instead of (8.11))

$$\begin{cases} \mathbf{f}_p \triangleq \beta_{gb} \mathbf{e}_3 - \beta_{dl} \mathbf{P} - \beta_{dq} |\bar{\mathbf{v}}_r| \mathbf{P} - m_2 \dot{\bar{\mathbf{v}}}_r \\ T_p \triangleq \bar{T} - \dot{\alpha}_r + \beta_{dq} (|\mathbf{V}| - |\bar{\mathbf{v}}_r|) \alpha_r \end{cases} \quad (8.33)$$

Then, similarly to Eq. (8.13), Eq. (8.31) can be rewritten as

$$\begin{aligned} \dot{\tilde{\mathbf{P}}} &= -\boldsymbol{\Omega}_\times \tilde{\mathbf{P}} - \mathbf{K}_P \tilde{\mathbf{P}} - \mathbf{M}^{-1} \mathbf{R}^\top \mathbf{K}_\xi (h(|\bar{\mathbf{y}}|^2) \bar{\mathbf{y}}) \\ &\quad - \beta_{dq} \frac{|\tilde{\mathbf{V}}|^2 + 2\tilde{\mathbf{V}}^\top \mathbf{R}^\top \bar{\mathbf{v}}_r}{|\mathbf{V}| + |\bar{\mathbf{v}}_r|} (\tilde{\mathbf{P}} + m_2 \mathbf{R}^\top \bar{\mathbf{v}}_r) \\ &\quad + \alpha_r \mathbf{e}_{1 \times} \boldsymbol{\Omega} + \mathbf{R}^\top \bar{\mathbf{f}}_p + \bar{T}_p \mathbf{e}_1 \end{aligned} \quad (8.34)$$

### 8.3. Simulation results

with  $\bar{\mathbf{y}} \triangleq \mathbf{K}_\xi \bar{\xi}$ ,  $\mathbf{K}_\xi$  a diagonal positive gain matrix,  $\mathbf{K}_P \triangleq \text{diag}(k_{p1} + k_{p2}, k_{p1}, k_{p1})$  (with  $k_{p1}, k_{p2} > 0$ ), and  $\bar{\mathbf{f}}_p$  and  $\bar{T}_p$  defined by (instead of (8.14))

$$\begin{cases} \bar{\mathbf{f}}_p \triangleq \mathbf{f}_p + k_{p1}(\mathbf{p} - m_2 \bar{\mathbf{v}}_r) + \frac{1}{m_2} \mathbf{K}_\xi (h(|\bar{\mathbf{y}}|^2) \bar{\mathbf{y}}) \\ \bar{T}_p \triangleq T_p - k_{p1} \alpha_r + k_{p2} \bar{P}_1 - \frac{m_{12}}{m_1 m_2} \mathbf{e}_1^\top \mathbf{R}^\top \mathbf{K}_\xi (h(|\bar{\mathbf{y}}|^2) \bar{\mathbf{y}}) \end{cases} \quad (8.35)$$

Interestingly, Eqs. (8.30) and (8.34) have identical form as Eqs. (8.6) and (8.13), respectively. Therefore, similar outer-loop control expressions together with associated stability result as in Proposition 8 can be straightforwardly stated.

**Proposition 9.** *Let  $\bar{T}_p$  and  $\bar{\mathbf{f}}_p$  be defined by (8.35)+(8.33) and  $\alpha_r$  be defined by (8.32). Apply the outer-loop controller (8.23) where the involved term  $\mathbf{u}$  is obtained by integration of (8.20) with the augmented control input  $\Omega_u$  given by (8.24). Choose  $k_{p1}$  and  $k_{p2}$  such that*

$$\begin{cases} k_{p1} > \left(1 + \frac{m_2}{2m_1}\right)^2 \beta_{dq} \left(\sup(|\mathbf{v}_r|) + \frac{\ddot{I}_{max}}{2k_{v1}}\right) \\ k_{p2} > \left(1 - \frac{m_2}{m_1}\right)^2 \beta_{dq} \left(\sup(|\mathbf{v}_r|) + \frac{\ddot{I}_{max}}{2k_{v1}}\right) \end{cases} \quad (8.36)$$

Assume that  $\alpha_r \neq 0$  and  $|\bar{\mathbf{f}}_p| > 0$  for all time. Assume that all conditions and assumptions in Lemma 4 hold. Then, the equilibrium  $(\mathbf{I}_{\bar{\xi}}, \dot{\mathbf{I}}_{\bar{\xi}}, \bar{\xi}, \mathbf{v}, \mathbf{R}^\top \gamma) = (\mathbf{0}, \mathbf{0}, \bar{\xi}_r, \mathbf{v}_r, \mathbf{u})$  is almost globally asymptotically stable.

**Proof.** The proof of this proposition is almost identical to that of Proposition 8. Indeed, Lemma 4 and the outer-loop control expressions (8.23)–(8.24) ensure the convergence of the term  $\alpha_r \mathbf{e}_{1 \times} \Omega + \mathbf{R}^\top \bar{\mathbf{f}}_p + \bar{T}_p \mathbf{e}_1$  involved in (8.34) to zero. Then, similarly to the proof of Lemma 3, using (8.36) and the fact that  $\sup(|\bar{\mathbf{v}}_r|) \leq \sup(|\mathbf{v}_r|) + \sup(\mathbf{I}_{\bar{\xi}}) \leq \sup(|\mathbf{v}_r|) + \ddot{I}_{max}/(2k_{v1})$  one easily deduces that the equilibrium  $(\bar{\xi}, \bar{\mathbf{P}}) = (\mathbf{0}, \mathbf{0})$  of the zero dynamics of (8.30)+(8.34) is globally asymptotically stable. Then, from the definition (8.29) of  $\bar{\xi}$  and  $\bar{\mathbf{v}}$  the proof of convergence of  $(\mathbf{I}_{\bar{\xi}}, \dot{\mathbf{I}}_{\bar{\xi}}, \bar{\xi}, \bar{\mathbf{v}})$  to zero follows the same lines as the proof of Lemma 3.2 in [32]. The remainder of the proof then directly follows.  $\square$

### 8.3 Simulation results

In this section the performance and robustness of the proposed control approach are validated through simulation conducted on a realistic model of a quasi-axisymmetric underactuated vehicle. The vehicle's body shape, as depicted in Fig. 8.3, is not perfectly symmetric along the longitudinal axis due to a large rudder and a lower base.

The simulated dynamics are given by (3.23). Physical parameters of the simulated

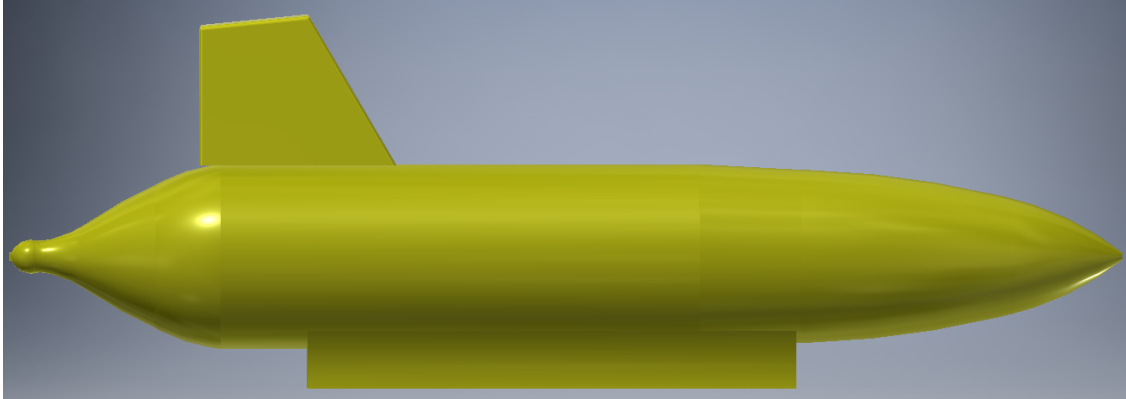


Figure 8.3: Quasi-axisymmetric shape of the simulated vehicle with the main body's dimension  $2.7[m] \times 0.45[m]$

Specification	Numerical value
Mass $m$ [kg]	100
$F_b$ [N]	$mg$
$\mathbf{r}_G$ [m]	$[0 \ 0 \ 0.01]^\top$
$\mathbf{J}_0$ [kg.m <sup>2</sup> ]	$\begin{bmatrix} 10 & 1 & 2 \\ 1 & 100 & 1 \\ 2 & 1 & 90 \end{bmatrix}$
$\mathbf{M}_a$ [kg]	$\begin{bmatrix} 32.6 & 3 & 4 \\ 3 & 484.8 & 1 \\ 4 & 1 & 394 \end{bmatrix}$
$\mathbf{J}_a$ [kg.m <sup>2</sup> ]	$\begin{bmatrix} 12.7 & 5 & 10 \\ 5 & 133.4 & 8 \\ 10 & 8 & 113.1 \end{bmatrix}$
$\mathbf{K}_{dl}$ [kg.s <sup>-1</sup> ]	diag(1.5, 7.5, 5.5)
$\mathbf{K}_{dq}$ [kg.m <sup>-1</sup> ]	diag(33, 341.8, 285.5)
$\mathbf{K}_{\Omega l}$ [kg.m <sup>2</sup> .s <sup>-1</sup> ]	diag(1, 35, 40)
$\mathbf{K}_{\Omega q}$ [N.m]	diag(10, 352, 437)

Table 8.1: Specifications of the simulated vehicle

vehicle are provided in Tab. 8.1, where the added-mass, added-inertia and damping coefficients are roughly identified from the given shape. Note that the second and third components of the added-mass matrix  $\mathbf{M}_a$  and of the damping matrix  $\mathbf{K}_{dq}$  are significantly different. This represents an opportunity to test the robustness of proposed controller w.r.t. such a violation of the axisymmetric assumption used for control design. For control implementation, an approximate axisymmetric model is used with the fol-

### 8.3. Simulation results

lowing estimated and approximated parameters:

$$\left\{ \begin{array}{l} \hat{\mathbf{M}}_a = \text{diag}(30, 440, 440) [kg] \\ \hat{\mathbf{J}} = \hat{\mathbf{J}}_0 + \hat{\mathbf{J}}_a = \text{diag}(20, 200, 190) [kg.m^2] \\ \hat{\mathbf{K}}_{dl} = \text{diag}(1, 6, 6) [kg.s^{-1}] \\ \hat{\mathbf{K}}_{dq} = \text{diag}(30, 310, 310) [kg.m^{-1}] \end{array} \right.$$

One can notice that these estimated terms are quite different from the corresponding “real” ones given in Tab. 8.1. In addition, a non-null current velocity  $\mathbf{v}_f = [-0.1 \ 0.2 \ 0.05]^\top [m.s^{-2}]$  is introduced, allowing us to test the control robustness w.r.t. both model uncertainties and external disturbances.

The simulated model of the dissipative torque  $\Gamma_d$  is given by  $\Gamma_d = -\mathbf{K}_{\Omega l}\Omega - \mathbf{K}_{\Omega q}|\Omega|\Omega$ , with the damping matrices  $\mathbf{K}_{\Omega l}$  and  $\mathbf{K}_{\Omega q}$  specified in Tab. 8.1, whereas in the inner-loop torque control expression (8.12) the estimate of this dissipative torque is simply set equal to zero (i.e.  $\hat{\Gamma}_d = \mathbf{0}$ ) so that no prior knowledge of this torque is required for control implementation.

The gains and parameters involved in the proposed controller are chosen as follows:

$$\left\{ \begin{array}{l} k_{p1} = 5.6154, k_{p2} = 8, \\ \mathbf{K}_\xi = \text{diag}(900, 1870, 1870), \mathbf{K}_I = 0.5\mathbf{I}_3, \\ h(s) = \frac{1}{\sqrt{1+s/\eta^2}}, \eta = \hat{m}_2 = 540, \\ k_u = 2, \\ \sigma(\cdot) \text{ given by (8.26) with } \varepsilon = 0.1, \\ \lambda = \mathbf{e}_1^\top (\mathbf{e}_3 \times \mathbf{R}^\top \mathbf{e}_3), \end{array} \right. \quad (8.37)$$

Note that the above expression of  $\lambda$  allows for maintaining roll angle near zero. Limitations of the actuators are also taken into account by saturating the applied thrust force and torque control inputs according to the following inequality constraints  $|T| \leq 200[N]$  and  $|\Gamma_{i=1,2,3}| \leq 160[N.m]$ .

The reference trajectory is a horizontal circular trajectory with radius  $20[m]$  and constant tangential speed  $1[m/s]$  (i.e.  $|\mathbf{v}_r| = 1[m/s]$ ). More precisely,

$$\boldsymbol{\xi}_r(t) = \left[ 20\sin\left(\frac{t}{20}\right) \quad 20\left(\cos\left(\frac{t}{20}\right) - 1\right) \quad 0 \right]^\top [m]$$

Note that  $\boldsymbol{\xi}_r(0) = \mathbf{0}$  and  $\mathbf{v}_r(0) = \dot{\boldsymbol{\xi}}_r(0) = \mathbf{e}_1$ . The initial conditions are chosen such that initial errors are relatively large, namely

$$\left\{ \begin{array}{l} \boldsymbol{\xi}(0) = [-20 \ 15 \ 10]^\top, \mathbf{v}(0) = \mathbf{0}, \\ \mathbf{R}(0) = \mathbf{R}_{\{0,0,\frac{75\pi}{180}\}}, \boldsymbol{\Omega}(0) = \mathbf{0}, \end{array} \right.$$

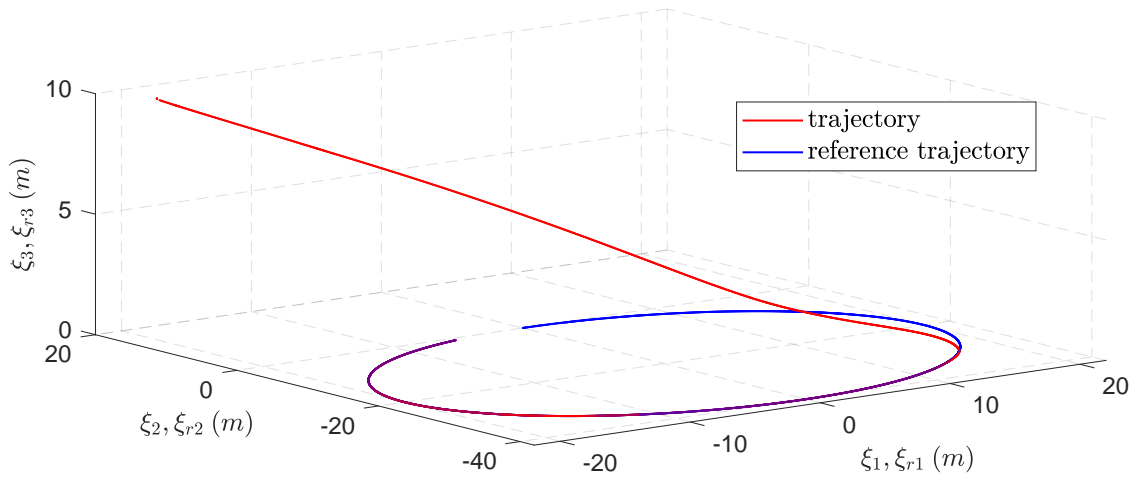


Figure 8.4: **(Proposed controller)** Actual and reference trajectories

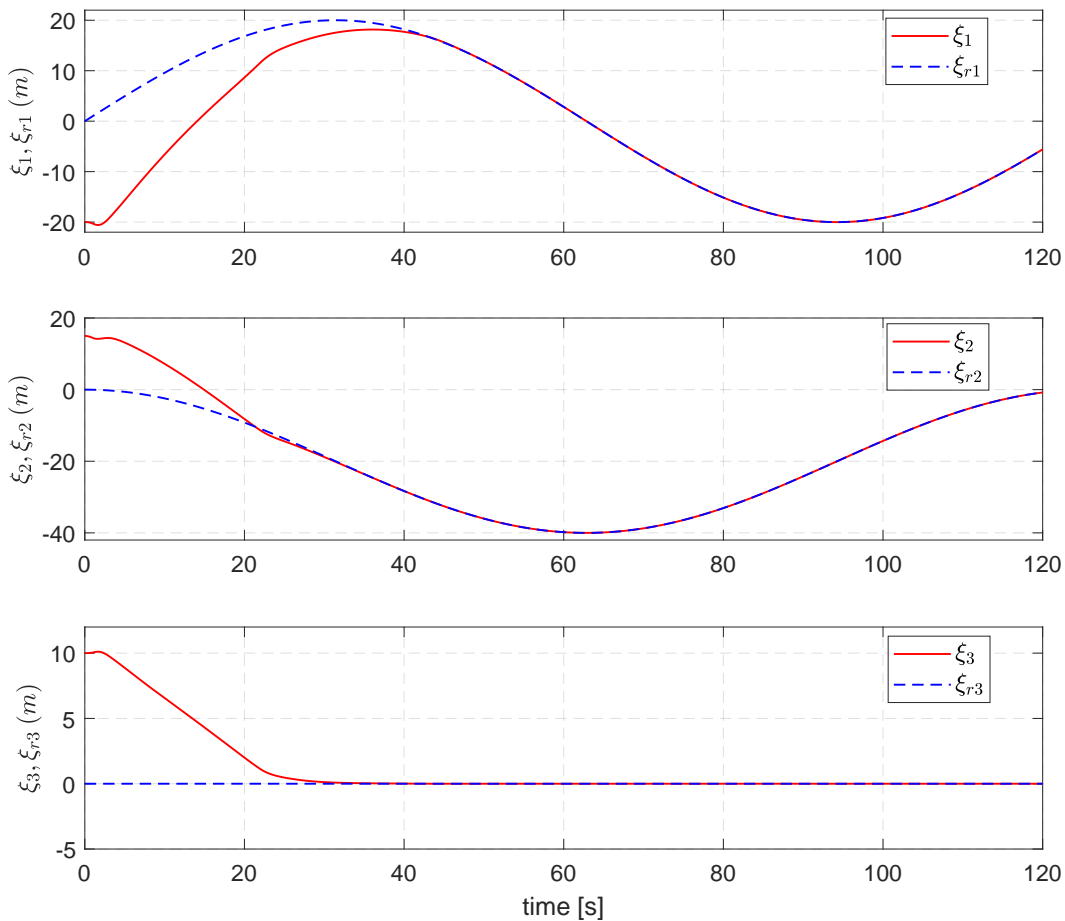


Figure 8.5: **(Proposed controller)** Vehicle's position and reference position components v.s. time.

• **Convincing behaviour of the proposed controller:** Simulation results are reported in Figs. 8.4–8.8. Fig. 8.4 illustrates the convergence in 3-dimensional space of the actual trajectory to the reference trajectory. The time evolutions of the vehicle's position

### 8.3. Simulation results

$\xi$  against the reference position  $\xi_r$ , of the position error  $\tilde{\xi}$ , of the vehicle's orientation (represented by Euler angles), and of the applied force and torque control inputs are respectively shown in Figs. 8.5, 8.6, 8.7, and 8.8. From both Figs. 8.5 and 8.6 one observes that despite large initial errors and significant external disturbances, the vehicle's position converges quickly to the reference one without much oscillations and overshoots. Saturation in force (resp. yaw torque) control input occurred during the first 23[s] (resp. 3[s]) as shown in Fig. 8.8 marginally affects the smooth convergence of the position error to zero. One can also observe from Fig. 8.7 that during the transient period the Euler roll angle always remains small (i.e. less than 5 degrees) and all the three Euler angles do not exhibit much oscillations. We find that the overall performance of the proposed controller is quite satisfactory.

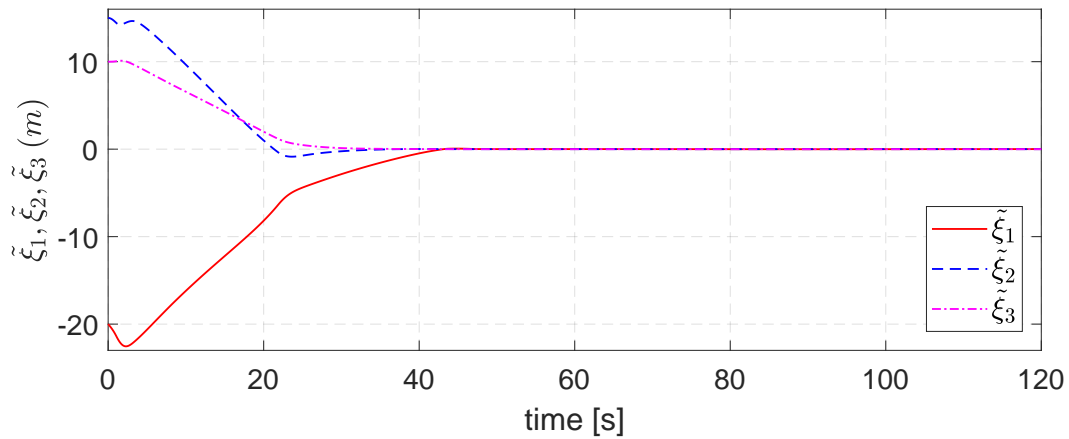


Figure 8.6: (**Proposed controller**) Position tracking error v.s. time.

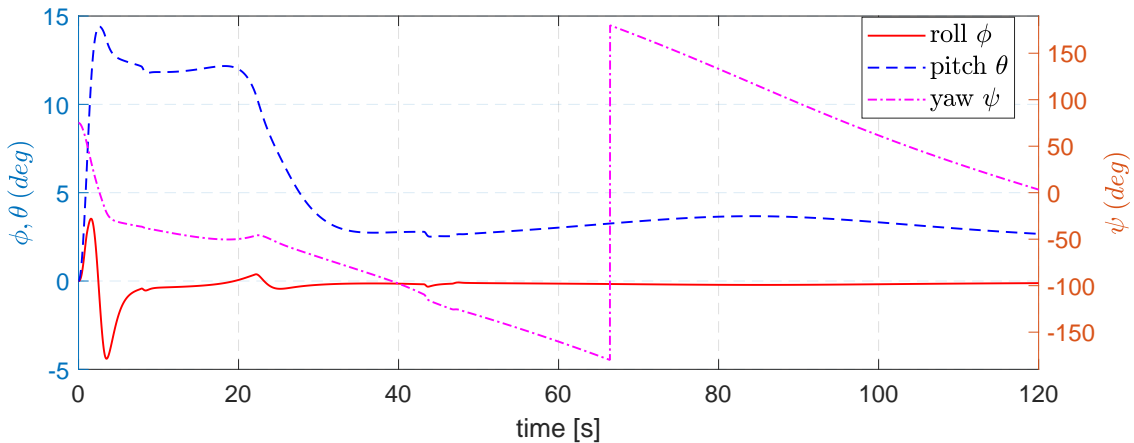


Figure 8.7: (**Proposed controller**) Vehicle's orientation represented by Euler roll, pitch, yaw angles v.s. time.

• **Oscillating behaviour of a simpler controller:** In order to illustrate the need of introducing the augmented variable  $\mathbf{u}$  and the associated control variable  $\Omega_u$  in the proposed control approach, simulation results using the simpler outer-loop controller (8.19) are

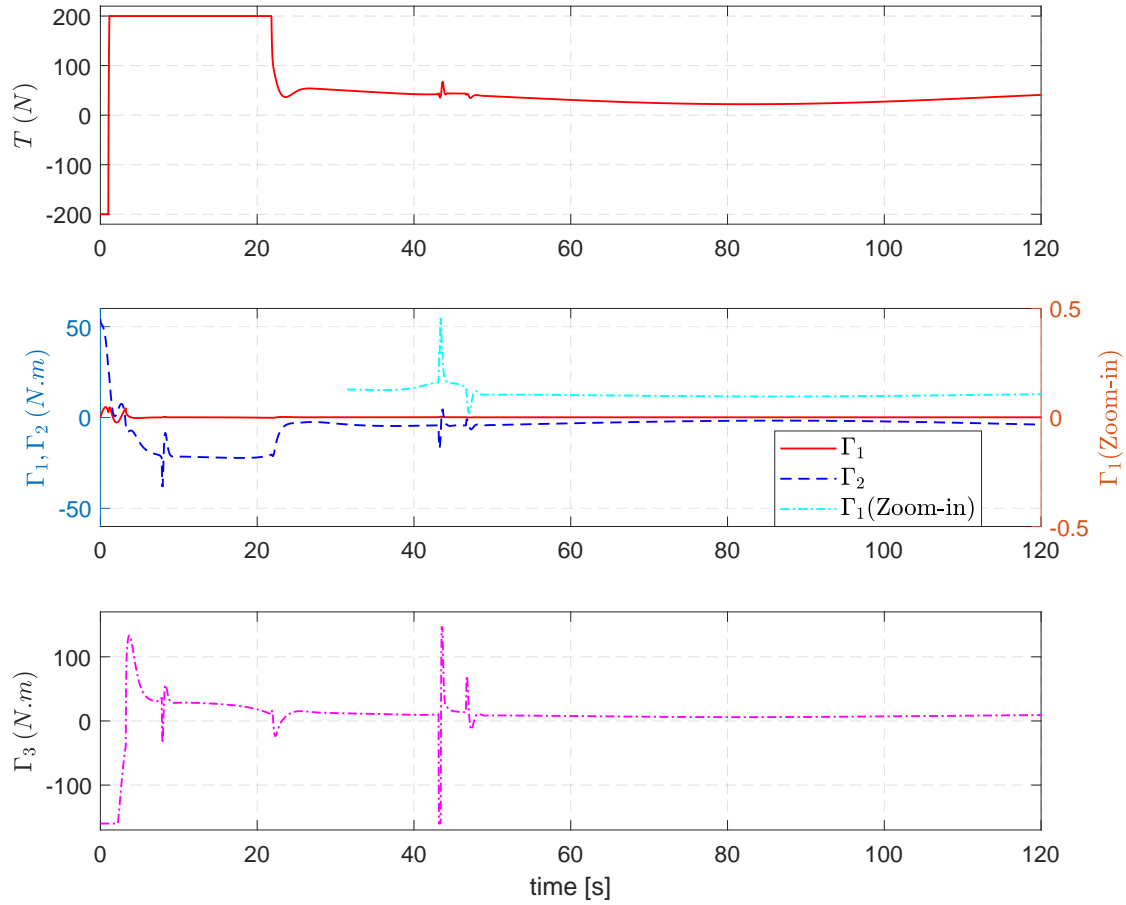


Figure 8.8: (**Proposed controller**) Control force and torque inputs v.s. time.

reported next. Similarly to the proposed outer-loop controller, the expression of  $\Omega_d$  given in (8.19) is slightly modified by adding a term  $\lambda e_1$ , with  $\lambda$  given in (8.37), so that the roll angle is also regulated near zero. The inner-loop controller is the same as the one used previously. All the gains and parameters involved in this controller are chosen identically to those used for the previously reported controller (i.e. given in (8.37)). Let us call this controller “**simple controller**” for distinguishing with the proposed one. One observes that although the position error still converges to zero (see Fig. 8.9) the vehicle’s orientation exhibits much more oscillations during the first 10 seconds of the transient phase (see Fig. 8.10) in contrast with the smooth behaviour of the proposed controller as shown in Fig. 8.7. This justifies the need of explicitly controlling the orientation rather than leaving the latter guided by the closed-loop system’s zero dynamics.

## 8.4. Conclusion

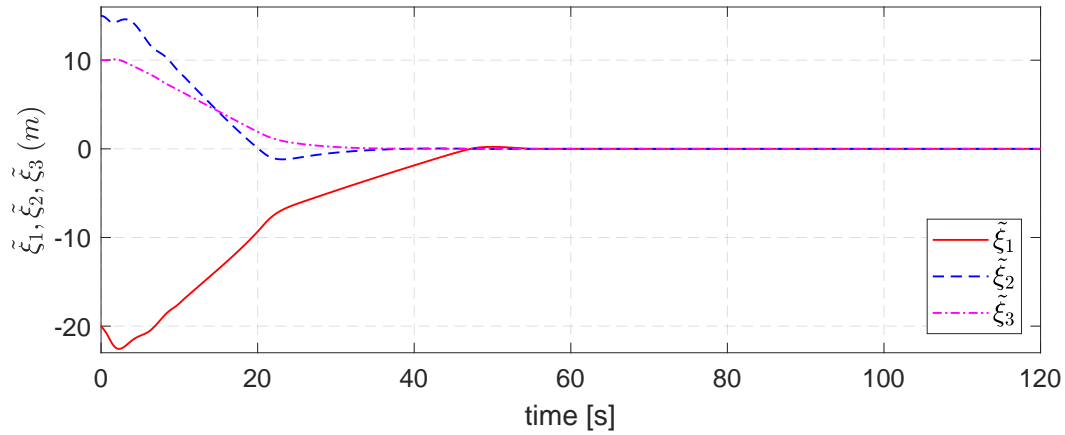


Figure 8.9: **(Simple controller)** Position tracking error v.s. time.

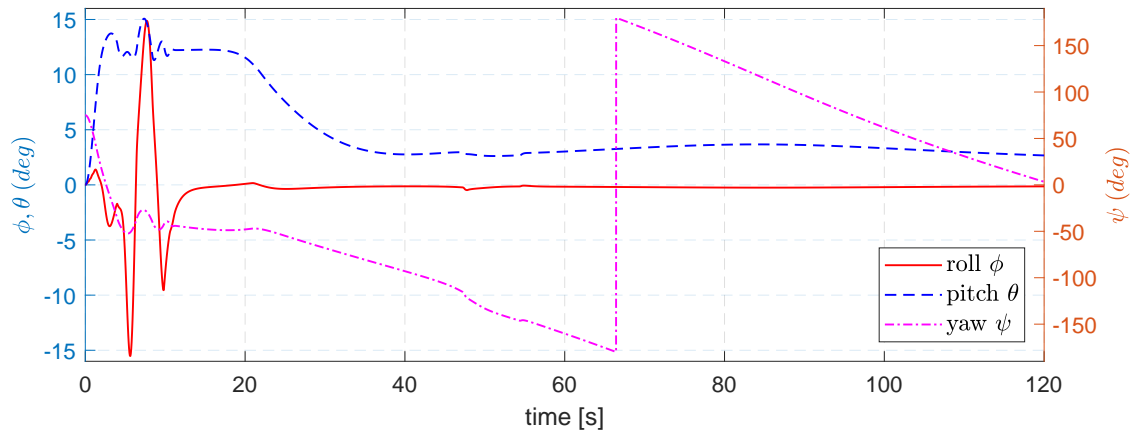


Figure 8.10: **(Simple controller)** Vehicle's orientation represented by Euler roll, pitch, yaw angles v.s. time.

## 8.4 Conclusion

A novel nonlinear control approach for slender-body axisymmetric underactuated underwater vehicles is proposed. Added-mass effects and dissipative hydrodynamic force are carefully taken into account via various adaptations, resulting in a modified apparent force no longer depending on the vehicle's orientation which is a good conditioning for control design. The proposed controller is also complemented with an integral correction term to enhance its robustness. Convincing simulation results conducted on a realistic model of a quasi-axisymmetric underwater vehicle illustrate the performance and robustness of the proposed controller.

# Conclusion

**T**HIS thesis addresses many aspects of the underwater robot control field. They range from system modeling, simplifying model for control design purposes to designing controllers for HBVS control of fully-actuated underwater vehicles and trajectory tracking of slender-body underactuated underwater vehicles.

## **Context and contributions of the thesis:**

The contributions reported in Part II constitute a continuation of prior work of the I3S-OSCAR team [44] on the topic of dynamic homography-based visual servoing. They contribute to the development of low-cost but still efficient vision-based control solutions for the stabilization of a class of fully-actuated underwater robotic vehicles. The use of costly DVL velocity sensors as in [44] is thus excluded due to their excessively high price. Instead only a suite of low-cost sensors consisting of a monocular camera and a MEMS IMU is required. In the context of monocular vision, the standard assumption on the planarity of the visual target is considered here, resulting in the meaningful involvement of the homography in control design. Despite such a restrictive assumption, the proposed solutions are still relevant for a number of AUV applications encompassing station-keeping or positioning using a downward-looking camera observing a (near) planar seafloor or using a forward-looking camera observing a subsea structure composing of planar surfaces for carrying out high-resolution imaging or manipulation tasks. Two algorithms have been proposed for these two cases in this thesis work and the results constitute the subject of the following publications or submissions [62], [63], [65]. The lack of linear velocity measurements has led us to make a certain number of simplifications of the model for control design, namely neglecting the dynamic couplings between the translational dynamics and the rotational dynamics and also considering the Munk

moment and hydrodynamic reaction forces and torques as constant disturbances. Discrepancies between the dynamic model used for control design and the vehicle's real dynamics due to these simplifications are dealt with by means of integral corrections. The development of the I3S-AUV platform and of the HomographyLab library has been a defining factor for successfully demonstrating the developed theories and concepts as an appealing success factor to the public, the specialized robotics community and industrial companies. We believe that the implemented works would become the key technology enablers for small-scale autonomous underwater robots devoid of expensive DVL velocity sensors.

The work presented in Part III is an extension of the I3S-OSCAR team's work on the control of rocket-like flying robots [70] to underactuated underwater vehicles with axisymmetric body shape. It contributes to the development of a novel and unified control framework for underactuated vehicles. The main contribution consists in designing a tracking control that exploits the full 3D nonlinear dynamics, allowing for achieving almost global asymptotical stability of the error dynamics. The simulation results showed the robustness of the control solution w.r.t model uncertainties and external disturbances (results are published in [64]).

#### **Perspectives:**

The work, already done in the thesis, on control design of underactuated AUVs with axisymmetric body shape have allowed us to have some preliminary understandings on how to deal with or exploit the added-mass effects and hydrodynamic forces acting on the translational dynamics of underactuated underwater vehicles. This constitutes the first step for us to address in the near future other challenging control design topics via the ongoing national projects involving the I3S-OSCAR team (ANR Astrid CONGRE and FUI GreenExplorer). For instance, the problem of degradation of actuator efficiency during a transition phase from low to high speed, which may naturally transforms a(n) (almost) fully-actuated AUV into an underactuated vehicle, is delicate to deal with and has seldom been addressed in the literature of underwater robotics. We will deal with this problem via the development of a continuous differentiable control law (i.e. without the need for switching between several control laws) allowing for monitoring smoothly such transition phases.

The second problem that we want to address would concern the asymptotic stabilization of a fixed reference pose by an underactuated AUV in the absence of a sea current. This problem is very challenging since classical control design methodologies do not provide solutions. The first reason is that the linearization of the system dynamics at the desired pose is not controllable. The second fact is that the system does not satisfy Brock-

ett's necessary condition [12] for the existence of a time-invariant feedback asymptotic stabilizer either linear or nonlinear. Specific and still prospective nonlinear techniques involving dynamic extensions are required to solve the stabilization problem (see, e.g., [75, 59, 60]).

By successfully developing novel and original control approaches for the two above difficult problems, we would like to advance the state-of-the-art of nonlinear control of AUVs in terms of fundamental methodologies to deal with the reduction in number of actuators (i.e. underactuated AUVs), the degradation of actuator efficiency during transition operating modes (i.e. transitions from fully-actuated to underactuated mode and vice-versa), and the highly nonlinear and coupled dynamics of underwater vehicles. The motivation is also that by developing original control solutions for the two above problems for the classical objective of trajectory tracking, these control approaches will also constitute a basic control pre-design framework to address many other objectives related to sensor-based control in a principled manner, knowing that extensions/adaptations should be carefully undertaken because sensor-based control design is often carried out in sensor spaces instead of state spaces and also due to the fact that some information may be unavailable to feedback control, thus, leading to the need of including dynamic augmentations or state observers in the control design process. Because sensor-based control of AUVs is a very wide topic, we will only tackle some relevant sensor-based control problems in relation to inspection and surveillance operations such as monocular vision-based stabilization or monocular vision-based pipeline following by either an underactuated AUV by conception or a fully-actuated AUV that may become underactuated at high speed motion. Besides these future conceptual and theoretical developments, developing a slender body underwater vehicle (based on the already developed software and control architecture of the I3S-UV platform) and then conducting experiments with these systems are indispensable to consolidate the future theoretical results and also the ones proposed in Part III of this thesis with respect to claims of robustness and performance in particular.



# Bibliography

- [1] Véhicule Ouvert et Reconfigurable pour les Techniques EXpérimentales (VORTEX). Online: accessed 29th September 2019.
- [2] Marine Technology Reporter magazine September 2019 issue, 2019. Online: accessed 29th September 2019.
- [3] A. Agarwal, C.V. Jawahar, and P.J. Narayanan. A survey of planar homography estimation techniques. Technical Report IIIT/TR/2005/12, IIIT, India, 2005.
- [4] A. P. Aguiar and J. P. Hespanha. Trajectory-tracking and path-following of underactuated autonomous vehicles with parametric modeling uncertainty. *IEEE Transactions on Automatic Control*, 52(8):1362–1379, 2007.
- [5] A. P. Aguiar and A. M. Pascoal. Dynamic positioning and way-point tracking of underactuated AUVs in the presence of ocean currents. *International Journal of Control*, 80(7):1092–1108, 2007.
- [6] G. Allibert, M.-D. Hua, S. Krupinski, and T. Hamel. Pipeline following by visual servoing for autonomous underwater vehicles. *Control Engineering Practice*, 82:151–160, 2019.
- [7] J. Antich and A. Ortiz. Development of the control architecture of an underwater cable tracker. *International Journal of Intelligent Systems*, 20(5):477–498, 2005.

- [8] S. Benhimane and E. Malis. Homography-based 2D visual tracking and servoing. *International Journal of Robotics Research*, 26(7):661–676, 2007.
- [9] S. Benhimane and E. Malis. Homography-based 2d visual tracking and servoing. *International Journal of Robotics Research*, 26(7):661–676, 2007.
- [10] J.-L. Blanco. A tutorial on SE(3) transformation parameterizations and on-manifold optimization. Technical Report 012010, University of Malaga, 2013.
- [11] L. Brignone, M. Perrier, and C. Viala. A fully autonomous docking strategy for intervention auvs. In *MTS/IEEE OCEANS'07*, pages 1–6, 2007.
- [12] R. W. Brockett. Asymptotic stability and feedback stabilization. In *Differential Geometric Control Theory*, pages 181–191. Birkhauser, 1983.
- [13] F. Chaumette and S. Hutchinson. Visual servo control, part ii: Advanced approaches. *IEEE Robotics and Automation Magazine*, 14(1):109–118, 2007.
- [14] C. Conomis. Conics-based homography estimation from invariant points and pole-polar relationships. In *IEEE Third International Symposium on 3D Data Processing, Visualization, and Transmission (3DPVT'06)*, pages 908–915, 2006.
- [15] X. Cufi, R. Garcia, and P. Ridao. An approach to vision-based station keeping for an unmanned underwater vehicle. In *IEEE/RSJ International Conference on Intelligent Robots and Systems (IROS)*, 2002.
- [16] H. de Plinval, P. Morin, and P. Mouyon. Stabilization of a class of underactuated vehicles with uncertain position measurements and application to visual servoing. *Automatica, Elsevier*, 77:155–169, March 2017.
- [17] O.A. Eidsvik. Identification of hydrodynamic parameters for remotely operated vehicles. Masters thesis, Norwegian University of Science and Technology, 2015.
- [18] T. I. Fossen. *Nonlinear Modelling and Control of Underwater Vehicles*. PhD thesis, Department of Engineering Cybernetics, Norwegian University of Science and Technology (NTNU), 1991.
- [19] T. I. Fossen. *Guidance and Control of Ocean Vehicles*. Wiley, 1994.

- [20] T. I. Fossen. *Handbook of Marine Craft Hydrodynamics and Motion Control*. John Wiley and Sons Ltd, 2011.
- [21] R. Garcia, J. Battle, X. Cufi, and J. Amat. Positioning an underwater vehicle through image mosaicking. In *IEEE International Conference on Robotics and Automation*, 2001.
- [22] T. F. Gonçalves, J. R. Azinheira, and P. Rives. Vision-based autonomous approach and landing for an aircraft using a direct visual tracking method. In *International Conference on Informatics in Control, Automation and Robotics*, pages 94–101, 2009.
- [23] F. Hamano. Derivative of rotation matrix - direct matrix derivation of well known formula. In *Green Energy and Systems Conference*, November 25 2013.
- [24] T. Hamel and R. Mahony. Visual servoing of an under-actuated dynamic rigid-body system: an image-based approach. *IEEE Transactions on Robotics and Automation*, 18(2):187–198, 2002.
- [25] T. Hamel, R. Mahony, J. Trumpf, P. Morin, and M.-D. Hua. Homography estimation on the Special Linear group based on direct point correspondence. In *IEEE Conference on Decision and Control (CDC)*, pages 7902–7908, 2011.
- [26] R. Hartley and A. Zisserman. *Multiple View Geometry in Computer Vision*. Cambridge University Press, 2003.
- [27] S. F. Hoerner. *Fluid dynamic drag*, 1965.
- [28] M.-D. Hua. *Contributions to the automatic control of aerial vehicles*. PhD thesis, I3S Laboratory, University of Nice Sophia Antipolis, 2009.
- [29] M.-D. Hua, G. Allibert, S. Krupinski, and T. Hamel. Homography-based visual servoing for autonomous underwater vehicles. In *IFAC World Congress*, pages 5729–5733, 2014.
- [30] M.-D. Hua, T. Hamel, R. Mahony, and G. Allibert. Explicit Complementary Observer Design on Special Linear Group  $SL(3)$  for Homography Estimation using Conic Correspondences. In *IEEE Conference on Decision and Control (CDC)*, pages 2434–2441, 2017.

- [31] M.-D. Hua, T. Hamel, P. Morin, and C. Samson. A control approach for thrust-propelled underactuated vehicles and its application to VTOL drones. *IEEE Transactions on Automatic Control*, 54(8):1837–1853, 2009.
- [32] M.-D. Hua and C. Samson. Time sub-optimal nonlinear PI and PID controllers applied to longitudinal headway car control. *International Journal of Control*, 84(10):1717–1728, 2011.
- [33] M.-D. Hua, J. Trumpf, T. Hamel, R. Mahony, and P. Morin. Point and line feature-based observer design on  $SL(3)$  for Homography estimation and its application to image stabilization. Technical Report hal-01628175, I3S, 2017.
- [34] M.-D. Hua, J. Trumpf, T. Hamel, R. Mahony, and P. Morin. Feature-based recursive observer design for homography estimation and its application to image stabilization. *Asian Journal of Control*, pages 1–16, 2019.
- [35] M.-D. Hua, J. Trumpf, T. Hamel, R. Mahony, and P. Morin. Nonlinear observer design on  $sl(3)$  for homography estimation by exploiting point and line correspondences with application to image stabilization. about to be published, 2019.
- [36] S. Hutchinson, G. Hager, and P. Cork. A tutorial on visual servo control. *IEEE Transactions on Robotics and Automation*, 12(5):651–670, 1996.
- [37] C.V. Jawahar and P.K. Jain. Homography estimation from planar contours. In *IEEE Third International Symposium on 3D Data Processing, Visualization, and Transmission (3DPVT'06)*, pages 877–884, 2006.
- [38] A. Joseph. Modern Torpedoes And Countermeasures, 2001. Online: accessed 29th September 2019.
- [39] J.-M. Kai, T. Hamel, and C. Samson. A nonlinear approach to the control of a disc-shaped aircraft. In *IEEE Conference on Decision and Control (CDC)*, pages 2750–2755, 2017.
- [40] J.Y. Kaminski and A. Shashua. Multiple view geometry of general algebraic curves. *International Journal of Computer Vision*, 56(3):195–219, 2004.
- [41] T. R. Kane and D. A. Levinson. *Dynamics: Theory and Applications*. McGraw-Hill, NY, 2005.

- [42] H. K. Khalil. *Nonlinear systems (3rd Edition)*. Prentice Hall, 2002.
- [43] S. Krupinski. *Offshore structure following by means of sensor servoing and sensor fusion*. PhD thesis, I3S Laboratory, University of Nice Sophia Antipolis, 2014.
- [44] S. Krupinski, G. Allibert, M.-D. Hua, and T. Hamel. An inertial-aided homography-based visual servoing control approach for (almost) fully actuated autonomous underwater vehicles. *IEEE Transactions on Robotics*, 33(5):1041–1060, 2017.
- [45] H. Lamb. *Hydrodynamics*. Cambridge University Press, 1932.
- [46] N. E. Leonard. Stability of a bottom-heavy underwater vehicle. *Automatica*, 33(3):331–346, March 1997.
- [47] J.-E. Lots, D. M. Lane, and E. Trucco. Application of 2 1/2 D visual servoing to underwater vehicle station-keeping. In *OCEANS 2000 MTS/IEEE Conference and Exhibition*, pages 1257–1264, 2000.
- [48] J.-E. Lots, D. M. Lane, E. Trucco, and F. Chaumette. A 2-d visual servoing for underwater vehicle station keeping. In *IEEE International Conference on Robotics and Automation (ICRA)*, pages 2767–2772, 2001.
- [49] K. N. Lwin, N. Mukada, M. Myint, D. Yamada, A. Yanou, T. Matsuno, K. Saitou, W. Godou, T. Sakamoto, and M. Minami. Visual docking against bubble noise with 3-D perception using dual-eye cameras. *IEEE Journal of Oceanic Engineering*, Early Access:1–24, 2018.
- [50] Y. Ma, J. Kosecka, and S. Sastry. Vision guided navigation for a nonholonomic mobile robot. *IEEE Transactions on Robotics and Automation*, 15(3):521–536, 1999.
- [51] Y. Ma, S. Soatto, J. Kosecka, and S.S. Sastry. *An Invitation to 3-D Vision: From Images to Geometric Models*. Springer Verlag, 2003.
- [52] R. Mahony, T. Hamel, P. Morin, and E. Malis. Nonlinear complementary filters on the special linear group. *International Journal of Control*, 85(10):1557–1573, 2012.
- [53] R. Mahony, J. Trumpf, and T. Hamel. Observers for kinematic systems with symmetry. In *9th IFAC Symposium on Nonlinear Control Systems*, pages 617–633, 2013.

- [54] F. Maire, D. Prasser, M. Dunbabin, and M. Dawson. A vision based target detection system for docking of an autonomous underwater vehicle. In *Australasian Conference on Robotics and Automation (ACRA)*, 2009.
- [55] E. Malis, F. Chaumette, and S. Boudet. 2 1/2d visual servoing. *IEEE Transactions on Robotics and Automation*, 15(2):238–250, 1999.
- [56] E. Malis and M. Vargas. Deeper understanding of the homography decomposition for vision-based control. *INRIA Research report*, RR-6303:90, 2007.
- [57] S. Matsumoto and Y. Ito. Real-time vision-based tracking of submarine-cables for AUV/ROV. In *Challenges of Our Changing Global Environment. MTS/IEEE OCEANS’95*, pages 1997–2002, 1995.
- [58] A. Micaelli and C. Samson. Trajectory tracking for unicycle-type and two-steering-wheels mobile robots. Technical Report 2097, INRIA, 1993.
- [59] P. Morin and C. Samson. Time-varying exponential stabilization of the attitude of a rigid spacecraft with two controls. In *IEEE Conference of Decision and Control (CDC)*, pages 3988–3993, 1995.
- [60] P. Morin and C. Samson. Practical stabilization of driftless systems on lie groups: the transverse function approach. *IEEE Transactions on Automatic Control*, 48(9):1496–1508, 2003.
- [61] J. Newman. *Marine Hydrodynamics*. MIT Press, 1977.
- [62] L.-H. Nguyen, M.-D. Hua, G. Allibert, and T. Hamel. Inertial-aided homography-based visual servo control of autonomous underwater vehicles without linear velocity measurements. In *21st International Conference on System Theory, Control and Computing (ICSTCC)*, pages 9–16, 2017.
- [63] L.-H. Nguyen, M.-D. Hua, G. Allibert, and T. Hamel. A homography-based dynamic control approach applied to station keeping of autonomous underwater vehicles without linear velocity measurements. *First revision of submission to IEEE Transactions on Control Systems Technology*, 2019.
- [64] L.-H. Nguyen, M.-D. Hua, and T. Hamel. A nonlinear control approach for trajectory tracking of slender-body axisymmetric underactuated underwater vehicles. In

*European Control Conference (ECC'19)*, pages 4053–4060, 2019.

- [65] L.-H. Nguyen, M.-D. Hua, and T. Hamel. A homography-based dynamic control approach of autonomous underwater vehicles observing a (near) vertical target without linear velocity measurements. *Submitted to European Control Conference (ECC'20)*, 2020.
- [66] N. Palomeras, S. Nagappa, D. Ribas, N. Gracias, and M. Carreras. Vision-based localization and mapping system for AUV intervention. In *MTS/IEEE OCEANS'13*, pages 1–7, 2013.
- [67] E. Panteley and A. Loria. Growth rate conditions for uniform asymptotic stability of cascaded time-varying systems. *Automatica*, 37:453 – 460, 2001.
- [68] H. Plinval, P. Morin, P. Mouyon, and T. Hamel. Visual servoing for underactuated VTOL UAVs: a linear, homography-based framework. *International Journal of Robust and Nonlinear Control*, 24(16):2285–2308, 2014.
- [69] S.J.D. Prince. *Computer Vision: Models Learning and Inference*. Cambridge University Press, 2012.
- [70] D. Pucci, T. Hamel, P. Morin, and C. Samson. Nonlinear feedback control of axisymmetric aerial vehicles. *Automatica*, 53:72–78, 2015.
- [71] J. E. Refsnes, A. J. Sorensen, and K. Y. Pettersen. Model-based output feedback control of slender-body underactuated AUVs: theory and experiments. *IEEE Transactions on Control Systems Technology*, 16(5):930–946, 2008.
- [72] F. Repoulas and E. Papadopoulos. Planar trajectory planning and tracking control design for underactuated AUVs. *Ocean Engineering*, 34(11):1650–1667, 2007.
- [73] P. Rives and J.-J. Borrelly. Underwater pipe inspection task using visual servoing techniques. In *IEEE International Conference on Intelligent Robots and Systems (IROS)*, pages 63–68, 1997.
- [74] D. L. Rudnick, R. E. Davis, C. C. Eriksen, D. M. Fratantoni, and M. J. Perry. Underwater gliders for ocean research. *Marine Technology Society Journal*, 38(1):48–59, 2004.

- [75] C. Samson. Control of chained systems application to path following and time-varying point-stabilization of mobile robots. *IEEE Transactions on Automatic Control*, 40(1):64–77, Jan 1995.
- [76] D. A. Smallwood and L. Whitcomb. Model-based dynamic positioning of underwater robotic vehicles: Theory and experiments. *IEEE Journal of Oceanic Engineering*, 29(1):169–186, 2004.
- [77] G. G. Stokes. On the effect of the internal friction of fluids on the motion of pendulums. *Transactions of the Cambridge Philosophical Society*, 9:8–106, 1851.
- [78] S. van der Zwaan, A. Bernardino, and J. Santos-Victor. Visual station keeping for floating robots in unstructured environments. *Robotics and Autonomous Systems*, 39(3):145–155, 2002.
- [79] M. Wirtz, M. Hildebrandt, and C. Gaudig. Design and test of a robust docking system for hovering AUVs. In *MTS/IEEE OCEANS'12*, pages 1–6, 2012.